Universitat
de les Illes Balears

DOCTORAL THESIS

2021

SYNCHRONIZATION AND COLLECTIVE PHENOMENA IN QUANTUM DISSIPATIVE SYSTEMS

Albert Cabot Martorell

Universitat
de les Illes Balears

DOCTORAL THESIS
2021

Doctoral Programme in Physics

SYNCHRONIZATION AND COLLECTIVE PHENOMENA IN QUANTUM DISSIPATIVE SYSTEMS

Albert Cabot Martorell

Thesis Supervisor: Roberta Zambrini
Thesis Supervisor: Gian Luca Giorgi
Thesis tutor: Pere Colet Rafecas

Doctor by the Universitat de les Illes Balears

Resum

Les passades dues dècades han viscut un gran progrés en l'habilitat experimental per a controlar i implementar sistemes complexes quàntics. Exemples d'aquestes plataformes experimentals són niguls atòmics atrapats en potencials de llum, o dins cavitats òptiques, sistemes optomecànics, o conjunts de qubits superconductors. Una de les motivacions darrera aquesta empresa, és la promesa de noves tecnologies quàntiques basades en sistemes fets de moltes unitats que podrien sobrepassar les capacitats de les tecnologies actuals per a la computació, telecomunicacions, o per fer mesuraments, fent us d'efectes quàntics. Cal mencionar també la simulació quàntica, on aquests sistemes experimentals precisos i controlables serien utilitzats per a estudiar fenòmens quàntics fonamentals que no poden esser estudiats d'altre manera.

Aquests sistemes experimentals són sistemes quàntics oberts ja que, inevitablement, estan acoblats a algun continu d'energia que indueix dissipació i decoherència. Aquesta interacció és inherent a la nostra habilitat per observar i controlar aquests sistemes, ja sigui a través de la radiació que a emeten, o que nosaltres els fem arribar. A més, pot constituir una limitació important a l'hora d'aprofitar efectes quàntics per a aplicacions tecnològiques. Tot i així, la naturalesa dissipativa i lluny de l'equilibri termodinàmic d'alguns d'aquests sistemes ha suposat una gran oportunitat per a estudiar fenòmens quàntics lluny de l'equilibri, amb interès tant fonamental com aplicat.

Aquesta tesis està enfocada a l'estudi de la sincronització i altres fenòmens dinàmics col·lectius en sistemes quàntics dissipatius. La sincronització és un fenomen paradigmàtic dels sistemes clàssics fora de l'equilibri, que ocorr en diferents contexts i adoptant diferents formes. Uns deu anys enrere, una sèrie d'articles van mostrar que fenòmens de sincronització podien ocórrer també en sistemes quàntics, donant peu al camp de la sincronització quàntica. En aquesta tesis, investigarem preguntes com ara a quins sistemes quàntics podem observar aquest fenomen, com es manifesta quànticament, o si mostra característiques eminentment quàntiques.

Després de la introducció, la segona part de la tesis es centra en el fenomen de la sincronització transitòria, on la relaxació de sistemes cap al seu estat estacionari ocorr d'una manera sincronitzada. Tal com mostrarem, aquest és un fenomen comú i robust, que ocorr en sistemes d'espins, sistemes lineals d'oscil·ladors harmònics, tant en presència de dissipació col·lectiva com independent, i també en presència de topologies complexes i sistemes inhomogenis. Mostrarem com aquest tipus de sincronització quàntica pot emergir en la física de baixes energies d'un sistema d'àtoms atrapats en un potencial de llum unidimensional, i n'identificarem diferents escenaris. A més, descriurem la sincronització deguda a la coalescència o punts excepcionals en sistemes estesos, estudiant-ne les carac-

terístiques espectrals especifiques, com ressonàncies estretes, finestres de transparència i altres efectes deguts a interferències.

La tercera part d'aquesta tesis es centra en estudiar la relació entre la sincronització a una senyal externa i altres fenòmens quàntics lluny de l'equilibri, considerant el cas particular de l'oscil·lador de van der Pol amb squeezing. La nostra investigació mostrarà que, de fet, la sincronització d'aquest sistema està íntimament relacionada al fenomen de la metaestabilitat quàntica. A més, a mesura que el sistema s'apropa al limit clàssic, es donen fenòmens de ruptura espontània de simetria, i la sincronització resulta estar relacionada també amb transicions dissipatives de fase i cristalls temporals. De fet, l'absència de sincronització correspon a un cristall temporal continu, mentre que la sincronització a un cristall temporal discret.

Finalment presentarem les conclusions d'aquesta tesis juntament amb possibles línies d'investigació futures. Els resultats principals d'aquesta tesis permeten identificar nous escenaris de sincronització quàntica i establir les seves connexions amb altres fenòmens fonamentals com la coalescència de modes col·lectius, les transicions de fase dissipatives, o els cristalls temporals.

Resumen

Las últimas dos décadas han sido testigo de un gran progreso experimental en cuanto a la habilidad de controlar e implementar sistemas complejos cuánticos. Ejemplos de dichos sistemas incluyen nubes de átomos atrapados en potenciales de luz, o en cavidades ópticas, sistemas optomecánicos, o conjuntos de qubits superconductores. Una de las motivaciones detrás de esta empresa, es la promesa de nuevas tecnologías basadas en sistemas de muchas unidades que podrían sobrepasar las capacidades de las tecnologías actuales para la computación, telecomunicaciones, o para realizar medidas, haciendo uso de efectos cuánticos. Cabe mencionar también la simulación cuántica, donde estos sistemas experimentales precisos y controlables serían utilizados para estudiar fenómenos cuánticos fundamentales que no pueden ser estudiados de otra forma.

Estos sistemas experimentales son sistemas cuánticos abiertos, ya que, inevitablemente, están acoplados a un continuo de energía que induce disipación y decoherencia. Esta interacción es inherente a nuestra habilidad de observar y controlar estos sistemas, ya sea a través de la radiación que emiten, o de la que nosotros les hacemos llegar. Además, esta puede constituir una limitación importante a la hora de aprovechar efectos cuánticos para aplicaciones tecnológicas. Por otra parte, la naturaleza disipativa y lejos del equilibrio termodinámico de algunos de estos sistemas ha supuesto una gran oportunidad para estudiar fenómenos cuánticos lejos del equilibrio, de interés tanto fundamental como aplicado.

Esta tesis está enfocada al estudio de la sincronización y otros fenómenos dinámicos colectivos en sistemas cuánticos disipativos. La sincronización es un fenómeno paradigmático de los sistemas clásicos lejos del equilibrio, que ocurre en diferentes contextos y adquiere diferentes formas. Unos diez años atrás, una serie de artículos mostró que fenómenos de sincronización podían ocurrir en sistemas cuánticos, dando paso al campo de la sincronización cuántica. En esta tesis, investigaremos preguntas como en qué sistemas cuánticos podemos observar este fenómeno, como se manifiesta cuánticamente, o si muestra características genuinamente cuánticas.

Después de la introducción, la segunda parte de la tesis se centra en el fenómeno de la sincronización transitoria, donde la relajación de sistemas hacia su estado estacionario ocurre de manera sincronizada. Enseñaremos que este es un fenómeno común y robusto, que ocurre en sistemas de espines, sistemas lineales de osciladores armónicos, tanto en presencia de disipación colectiva como independiente, y también en presencia de topologías complejas y sistemas inhomogéneos. Enseñaremos como este tipo de sincronización cuántica puede emerger en la física de bajas energías de un sistema de átomos en un potencial de luz unidimensional, e identificaremos los diferentes escenarios. Además, describiremos la sincronización debido a coalescencia o puntos excepcionales en

sistemas extendidos, estudiando las características espectrales específicas, como resonancias estrechas, ventanas de transparencia y otros efectos debidos a interferencias.

La tercera parte de esta tesis se centra en estudiar la relación entre la sincronización a una señal externa y otros fenómenos cuánticos lejos del equilibrio, considerando el caso particular del oscilador de van der Pol con squeezing. Enseñaremos que la sincronización de este sistema está íntimamente relacionada con el fenómeno de la metaestabilidad cuántica. Además, a medida que el sistema se acerca al límite clásico, se dan fenómenos de rotura espontánea de simetría, y la sincronización resulta estar relacionada también con transiciones disipativas de fase y cristales temporales. De hecho, la ausencia de sincronización se corresponde a un cristal temporal continuo, mientra que la presencia de sincronización a uno discreto.

Finalmente presentaremos las conclusiones de esta tesis junto con posibles lineas de investigación futuras. Los resultados principales de esta tesis permiten identificar nuevos escenarios de sincronización cuántica y establecer sus conexiones con otros fenómenos fundamentales como la coalescencia, las transiciones de fase disipativas, o los cristales temporales.

Abstract

The past two decades have witnessed huge experimental progress on the ability to control and engineer the dynamics of complex quantum systems. Experimental platforms range from large atomic clouds trapped in optical lattices, to few atoms trapped near photonic nanostructures, optomechanical systems, or arrays of superconducting qubits. An important driving force behind this venture has been the promise of new quantum technologies based on extended systems for computation, telecommunications, and sensing that might surpass the performance and capabilities of current ones by exploiting quantum effects. As well as the development of quantum simulation, in which highly-controllable experimental systems are aimed to study fundamental quantum phenomena currently unaddressable by other means.

All these experimental platforms are unavoidably open quantum systems: the system degrees of freedom are coupled to an environment made of a continuum of modes that induces dissipation and decoherence. This coupling is inherent to our ability to observe these systems, e.g. by observing their emitted radiation, or to control them through it, and it is often an ultimate limit for quantum technologies. Still, the driven-dissipative nature of many platforms has provided a great opportunity to explore non-equilibrium dynamics in quantum systems, to study quantum phenomena that have no equilibrium counterpart, and to widen the spectrum of achievable dynamical phenomena of fundamental and applied interest.

This thesis is devoted to the study of synchronization and related collective phenomena in dissipative quantum systems. Synchronization is a paradigmatic dynamical phenomenon of non-equilibrium classical systems, occurring in very different contexts and forms. About ten years ago a series of seminal works showed different forms of synchronization occurring in quantum systems, which gave birth to quantum synchronization. Here, we have addressed questions as how this phenomenon manifests in the quantum regime, which are the systems in which it can emerge, or whether it displays genuine quantum features.

After introducing the main topics of this thesis as well as the used methods and theoretical framework, in the second part of this thesis we focus on the phenomenon of spontaneous transient synchronization, in which systems relax towards their stationary state in a synchronized fashion. As we show, this is a common and robust phenomenon: it emerges in spin systems and even in linear systems of harmonic oscillators, both in the presence of collective and independent dissipation, and in the presence of complex topologies and inhomogeneous parameters. We propose a possible implementation of transient synchronization in the low-energy physics of a one-dimensional atomic lattice, a relevant system for

quantum simulation, and we identify different scenarios of synchronization. Furthermore, we establish synchronization enabled by coalescence or exceptional points in different extended systems, and we characterize specific spectral features of synchronization as narrow subradiant resonances as well as transparency windows and other interference effects.

In the third part, we address the relation of quantum entrainment with other driven-dissipative phenomena, considering the particular case of the squeezed quantum van der Pol oscillator. Our research shows that driven synchronization is related to quantum metastability. Moreover, as the classical limit is approached, spontaneous symmetry-breaking occurs, and entrainment turns out to be related to time-crystalline order and to a dissipative phase transition. Interestingly, synchronization is here related to a discrete time-crystal, while the absence of it to a continuous one.

We conclude this thesis with final remarks and outlook. The main original results of this thesis allow us to identify new scenarios of synchronization, to establish its robustness, and to unveil its connections with other important and fundamental phenomena as coalescence, dissipative phase transitions or time-crystals.

Acknowledgements

First I would like to thank my PhD supervisors Roberta Zambrini and Gian Luca Giorgi for their support and guidance during these last years in which I've had the pleasure to work with them closely and from whom I've learnt a lot. I also want to thank Roberta for her support and guidance since I finished my bachelor degree and I got to know her in the SURF and master programs. In this sense, I would like to thank Fernando Galve too, from whom I also had the opportunity to learn and work with those first years.

During my PhD I've also had the pleasure to collaborate with other experienced researchers from which I've also been able to learn from. I want to thank Stefano Longhi with whom I've collaborated on several projects during his visits at IFISC, in which I've become acquainted with many new and interesting topics. In this sense, I'm also grateful to Víctor Eguíluz, Konstantin Klemm, and Sabrina Maniscalco, with whom I've also had the pleasure to work and learn about classical and quantum networks. I also thank Salvatore Lorenzo with whom I could work with during his visit to IFISC in a very interesting project focused non-Markovian decay dynamics. Here I would also like to mention all the people with whom I discussed my ongoing projects or physics in general. This is a lot of people, from PhD and master students, to senior researchers. While I cannot mention them all (I would probably forget more than one person!), I have the general feeling that these discussions have usually been an enriching experience, as they have helped me to either get into something new, or to notice something I didn't have noticed.

Another experience of great value of my PhD has been the opportunity to visit other research centers. Here I want to thank again Roberta for having encouraged me to do so (Yes! I had to be encouraged to do so!). In particular, I was able to participate in the KITP program "Open Quantum System Dynamics: Quantum Simulators and Simulations Far From Equilibrium" at the Kavli Institute in Santa Barbara. This was a very stimulating experience for which I'm grateful to all the organizers and participants that made it possible. Special thanks also to Susana Huelga, with whom I had the opportunity to collaborate during this stay and from whom I could first learn about the interesting physics of quantum biology. Later on, I visited her group in Ulm, which was also a very stimulating experience. Here, I would also like to thank Jaemin Lim, with whom I also worked in Ulm, as well as Susana, Martin Plenio, and the members of their group for their hospitality during my visit. Finally, I want to send a hug to the people I had the pleasure to met and be friend of during my stays in Santa Barbara and Ulm, and that made these experiences really enjoyable. I hope our paths cross again at some point!

It is also the moment to have some nice words for the IFISC, the research institute in which I've spent the last six years. I'm thankful to all the people that have contributed to

– and keep contributing to – make of this institute such a great place to be. I would also like to send a hug to the people from the S07 room with whom I've shared so many great moments, as well as my master classmates with whom I also spent a lot of good times. I hope all of you are doing well! I will remember my days at the IFISC underground with great joy. From the illusion of the early days, to the moment when you realize that you are the next one to leave.

Finally, I'm thankful to my family for their love and support. This is also true for my friends. The days of my PhD were also the days in which many of us grew up together.

Last but not least, I would like to acknowledge the financial support from the CAIB FPI PhD and mobility program and also the QUAREC project; from the Horizon 2020 EU collaborative project QuProCS (Grant Agreement No. 641277); from MINECO/AEI/FEDER through projects NoMaQ FIS2014-60343-P, EPheQuCS FIS2016-78010-P, the QUARESC project (PID2019-109094GB-C21and-C22/AEI/10.13039/501100011033); and from the María de Maeztu Program for Units of Excellence in R&D (MDM-2017-0711). Finally, I acknowledge the use of the python library Qutip [11, 12] for performing some of the calculations presented in this thesis.

List of publications

During the course of this thesis the following articles have been published or submitted for publication:

P1. A. Cabot, F. Galve, and R. Zambrini, *Dynamical and quantum effects of collective dissipation in optomechanical systems*, New J. Phys. **19**, 113007 (2017).

P2. A. Cabot, F. Galve, V. M. Eguíluz, K. Klemm, S. Maniscalco, and R. Zambrini, *Unveiling noiseless clusters in complex quantum networks* npj Quantum Inf. **4**, 57 (2018).

P3. A. Cabot, G. L. Giorgi, F. Galve, and R. Zambrini, *Quantum Synchronization in Dimer Atomic Lattices*, Phys. Rev. Lett. **123**, 023604 (2019).

P4. A. Cabot, G. L. Giorgi, S. Longhi, and R. Zambrini, *Exceptional points in 1D arrays of quantum harmonic oscillators*, EPL **127**, 20001 (2019).

P5. G. L. Giorgi, A. Cabot, and R. Zambrini, *Transient synchronization in open quantum systems* in *Advances in Open Systems and Fundamental Tests of Quantum Mechanics* (Eds.: B. Vacchini, H.-P. Breuer, A. Bassi), Springer, Cham, CH 2019, pp. 73-89.

P6. G. L. Giorgi, S. Longhi, A. Cabot, and R. Zambrini, *Quantum probing topological phase transitions by non-Markovianity*, Ann. Phys. (Berl.) **531**, 1900307 (2019).

P7. A. Cabot, G. L. Giorgi, and R. Zambrini, *Synchronization and coalescence in a dissipative two-qubit system*, Proc. R. Soc. A **477**, 20200850 (2021).

P8. S. Lorenzo, S. Longhi, A. Cabot, R. Zambrini, and G. L. Giorgi, *Intermittent decoherence blockade in a chiral ring environment*, Sci. Rep. **11**, 12834 (2021).

P9. A. Cabot, G. L. Giorgi, and R. Zambrini, *Metastable quantum entrainment*, New J. Phys. **23**, 103017 (2021).

P10. A. Cabot, G. L. Giorgi, and R. Zambrini, *From a continuous to a discrete time-crystal and the entrainment transition*, in preparation.

In particular, Refs. [P2,P3,P4,P5,P7,P9,P10] are part of the thesis, while Refs. [P1,P6,P8]

will not be covered. However, in the following, we offer a brief summary of [P1,P6,P8] and our reasons for not to include them.

P1. Dynamical and quantum effects of collective dissipation in optomechanical systems. In this work we considered the effects of collective dissipation in an optomechanical system made of two optomechanical oscillations. We focused both on the classical synchronization dynamics as well as on the effects on quantum correlations between the oscillators. In the regime of classical self-sustained oscillations we found collective dissipation to enhance the emergence of mutual synchronization, especially favouring anti-phase synchronization between the mechanical oscillations. On the other hand, in the fixed point regime, the quantum fluctuations around the stable attractor displayed enhanced quantum correlations and a lower effective temperature when considering the collective dissipation case, as one of the mechanical normal modes was better isolated from the environment than in the case of independent dissipation. This reference will not be presented in this thesis as it was the topic of my master thesis and the main results were already presented there.

P6. Quantum probing topological phase transitions by non-Markovianity. In this work we considered a Su–Schrieffer–Heeger tight-binding (SSH) chain, one of the simplest systems displaying a topologically non-trivial phase and a topological phase transition. This model basically consists in a tight-binding chain (no matter the statistics of the constituents) displaying uniform frequencies and nearest-neighbor couplings alternating two different strengths. Depending on the relation between these two coupling strengths, the system can be in a topologically trivial phase or in a non-trivial phase, the latter displaying edge states (among other features). The main question on which we focused here is whether is it possible to assess the topological phase of the chain with a local probe, i.e. a system coupled to few sites of the chain, in the bulk, i.e. far from any edge state. As we showed, the answer is affirmative, and we provided a basic scheme to do so. This consists in coupling a two-level system (the probe) with a dephasing interaction to at least two neighboring tight-binding sites. The frequency of this probe needs to lay within the bandgap of the SSH chain. Then, studying the non-Markovian dynamics of the probe one can assess the topological phase transition as well as the topological phase of the system. In particular, we showed that a non-Markovianity quantifier acts as a witness of this transition, displaying two different behaviors in each phase and a non-analytical behavior at the transition. Furthermore, a scheme based on a dissipative coupling between the probe and the chain was also proposed; however, it was shown to be optimal just for certain parameter values. This reference will not be presented in this thesis as it is not related to synchronization and I am not the leading author.

P8. Intermittent decoherence blockade in a chiral ring environment. In this reference we considered the non-equilibrium decay dynamics of a two-level system coupled to a tight-binding ring environment displaying two chiral energy bands. This means that in a certain energy range, the modes of each of the bands propagate in just one direction, and it is the result of breaking the time reversal symmetry of the tight-binding chain by the introduction of an effective magnetic flux (as it can be engineered in modern photonic structures). In particular, the considered band structure displays a band-crossing point in which the two bands display an almost linear dispersion relation, with very disparate group velocities, and propagating in different directions. As we showed, if one couples a two-level system resonant with this band-crossing point, it turns out to display an exotic decay-dynamics. Specifically, if the two-level state is initially in the excited state it decays to the ground state following a stair-case dynamics in which short periods of decay

are interrupted by short dark periods in which there is no decay. We named this effect 'intermittent decoherence blockade', and we showed that it results from an interference between light emitted in the past into the fast modes with light emitted in the present. Moreover, it requires certain timescales of the system to display certain hierarchy: the group velocity of the fast modes needs to be much larger than that of the slow modes, while the typical system relaxation timescale needs to be much larger than the time the excitation in the fast modes needs for making a round trip along the chain. This is an example of non-Markovian dynamics due to the finite size of the bath, while other examples usually consider several units coupled to the same bath (as we will briefly comment in chapter 2) or an 'atom in front of a mirror' configuration. Notice that in both of these other examples there are usually bound states in the continuum, while in our case there are not. This reference will not be presented in this thesis as it is not related to synchronization and I am not the leading author.

List of abbreviations

1D	One-dimensional
CB	Common bath
DFS	Decoherence-free subspace
DPT	Dissipative phase transition
EIT	Electromagnetically induced transparency
EMS	Extreme metastable state
EP	Exceptional point
ER	Erdős-Rényi
GKLS	Gorini-Kossakovski-Lidnblad-Sudarshan
MI	Mott insulator
NS	Noiseless subsystem
QvdP	Quantum van der Pol
SB	Separate bath
SNIC	Saddle-node on an invariant circle
SSH	Su–Schrieffer–Heeger
SW	Small world
vdP	Van der Pol

Contents

PART I

Introduction

CHAPTER 1

Collective and non-equilibrium phenomena in quantum dissipative systems

Open quantum systems exhibit features beyond dissipation of energy and decoherence that cannot generally be found in the absence of losses. The investigation of the non-equilibrium dynamics of dissipative quantum systems has become a major research subject in the past decades, triggered by the huge progress in the development of experimental platforms for the study of driven-dissipative quantum systems: from individual components, to small arrays, and many-body systems [13, 14, 15, 16]. In the atomic realm, systems of cold atoms in optical potentials, trapped ions, and highly excited Rydberg atoms can be used to simulate far-from-equilibrium quantum dynamics [17], complementing their demonstrated capabilities in the simulation of equilibrium physics [18, 19]. Moreover, atomic systems can be interfaced with optical cavities [14] and photonic nanostructures [16], enabling the simulation of different forms of driving and dissipation. Collective and non-equilibrium phenomena also emerge in mesoscopic systems, beyond atomic platforms, as in superconducting circuits [20, 21], exciton-polariton condensates [13], non-linear photonic arrays [15, 22], optomechanical oscillators [23], and quantum dots embedded in photonic crystal structures [24].

In these far-from-equilibrium scenarios, the interplay between driving, dissipation, and interactions has been shown to enable the emergence of intriguing physical phenomena. Super- and subradiance constitute paradigmatic examples of cooperative light-matter non-equilibrium phenomena, occurring not only in large atomic systems [25, 26, 27], but also in small arrays of quantum emitters, as in superconducting qubits [28, 29], or color centers in diamond nano-cavities [30]. Cooperative effects also lead to the self-organization of atomic clouds and condensates, which form patterns that enhance light-scattering into cavity modes [14, 31, 32], and which can also be shaped by optomechanical interactions with the cavity mirrors [33]. These can be regarded as examples of non-equilibrium phases of matter emerging in driven-dissipative systems, which can spontaneously break the underlying symmetries of the system [34, 35], as translational symmetry [36], parity symmetry [37], or even time-translation symmetry [38, 39, 40], the latter being forbidden in equilibrium

[41]. Synchronization, a paradigmatic phenomenon of complex systems [42, 43], has also been reported for quantum systems [44]: from small arrays of qubits [45], to large clouds of atoms in optical cavities [46]. Besides these dynamical phenomena, topological phenomena have also been reported to occur in dissipative (non-Hermitian) systems, as topological energy transfer in an optomechanical system [47], and chiral dynamics in photonic systems [48]. These examples give account of the rich physics beyond equilibrium, and which has inspired researchers to explore intensely the non-equilibrium dynamics of complex quantum systems.

In this chapter, we provide a qualitative introduction to the non-equilibrium and collective phenomena on which this thesis will focus. We begin presenting the topic of quantum synchronization, which is central to this thesis, and around which much of the research had been oriented. Later on, we discuss the emergence of non-equilibrium phases in driven-dissipative systems, making emphasis on phenomena such as dissipative phase transitions, spontaneous symmetry breaking and time-crystals. Finally, we introduce the physics of exceptional points: spectral singularities that are ubiquitous in dissipative systems. We conclude the chapter with a summary of the plan that will be followed in the rest of the thesis.

1.1 Synchronization phenomena in quantum systems

The emergence of synchronization in quantum systems, or *quantum synchronization*, is a paradigmatic example of dynamical phenomenon that can emerge in the non-equilibrium dynamics of quantum dissipative systems, and it is generally related to the emergence of some "similarity" in the dynamical properties of coupled system components. This topic has attracted much interest in the past decade. Questions as fundamental as whether synchronization can even emerge in the quantum regime, which are its signatures, or whether it involves genuine quantum effects have been addressed [44]. In this section, we introduce some of these ideas and results that have been reported in the literature, and which motivate and contextualize the research done in this thesis about this topic to be presented in the forthcoming chapters. Before jumping into quantum synchronization, we must take a brief detour to explain some basic concepts and ideas of its parent field, namely classical synchronization, as we do in the following subsection.

1.1.1 Classical synchronization

The first observation of the phenomenon of *mutual synchronization* dates back to the seventeenth century when Christiaan Huygens noted that two pendulum clocks oscillated exactly in anti-phase when hanged on the same beam. Huygens not only reported for the first time on this intriguing phenomenon, but he already deduced that this "sympathy" between the pendula was due to their mutual interaction through the beam [43, 49]. Another breakthrough followed from the work by Edward Appleton and Balthasar van der Pol at the beginning of the twentieth century, when they observed that a non-linear electrical circuit could adjust its oscillation frequency to that of an external weak signal [50, 51]. These seminal observations of *entrainment*, or synchronization driven by an external source, were of great practical importance as they provided a way to stabilize the oscillation frequency of powerful electrical generators by using the signal of weaker but more precise ones [43]. This is an important application of synchronization that has transcended this particular system, and it is used in modern laser and optical communication systems [52]. Indeed, both mutual synchronization and entrainment have found wide application in modern telecommunication systems [53]. Since these early findings, synchronization has emerged as a paradigmatic dynamical phenomenon of complex systems, which has been

recognized in widespread contexts and forms, ranging from biological and social systems to engineered physical set-ups. Popular examples are fireflies flashing at once, cardiac pacemaker cells, clapping in an audience, arrays of lasers and Josephson junctions, or non-linear electrical circuits, to name a few [42, 43]. Here we will address the generalization of synchronization to the quantum regime, which constitutes a new frontier in which to explore this phenomenon.

Mutual synchronization and entrainment. In this thesis, we will consider both *spontaneous* or *mutual* synchronization phenomena and *entrainment* phenomena [44]. *Spontaneous synchronization* involves two or more systems that display different dynamics when uncoupled, but which can evolve coherently when mutually interacting. In the case of dynamical systems displaying regular oscillations, this means that, when mutually coupled, these systems oscillate at a common frequency and display phase-locking, i.e. the phase relation between their oscillations is fixed. Notice that other scenarios of mutual synchronization are possible, as commented at the end of this section. A crucial feature of spontaneous or mutual synchronization is the presence of a *mutual* interaction between different system components. This is precisely the key difference with entrainment, in which the interaction is unidirectional, as one system (the driver) is not influenced by the dynamics of the other (the driven). Hence, *entrainment* occurs when a system adapts its dynamics to that of an external forcing, which is itself unaffected by the action of the system. In the case of regular oscillatory dynamics, this usually involves the system changing its own intrinsic frequency to that of the forcing, while developing a fixed phase relation. Notice that unidirectional interactions arise in very different contexts and can be engineered in many different ways: the circadian rhythm results from the entrainment of biological internal clocks (the driven) by the environmental conditions, as illumination by the Sun (the driver) [43]; in laser systems one can use optical circulators and isolators to inject the signal of one laser to another, avoiding unwanted feedback in the opposite direction [52]; or quantum cascaded systems [54] implemented by interfacing quantum emitters with chiral photonic nanostructures [16, 24], in which, at certain frequencies, light is only allowed to propagate in one direction.

In Figure 1.1, we illustrate the mutual synchronization of two *self-sustained oscillators*. Self-sustained oscillators are autonomous systems in which the interplay between dissipation, energy gain, and non-linearities leads to the emergence of stable oscillations [55]. Here we consider two classical self-sustained oscillators that, when uncoupled, oscillate at their own intrinsic frequency, $\omega_{1,2}$, as shown in panel (a). Then, when mutually interacting with a strong enough coupling strength, ε, it can happen that the oscillators adjust their frequency to an intermediate value, $\Omega_1 = \Omega_2 = \Omega$, and they lock their relative phase as shown in panel (b). Notice that we have defined their *observed frequencies* ($\Omega_{1,2}$) as the oscillation frequencies that they display when coupled, which can of course differ from their intrinsic ones ($\omega_{1,2}$).

The importance of the coupling strength between the oscillators can be understood from panels (c) and (d). In panel (c) we keep fixed a non-zero coupling strength while we vary the intrinsic detuning, $\Delta\omega$, and we plot the difference of their observed frequencies, $\Delta\Omega$. We can see that if the intrinsic detuning is too large, the oscillators do not synchronize, and indeed $\Delta\Omega$ tends to $\Delta\omega$. In contrast, if the systems detuning is small, there is a synchronization region around $\Delta\omega = 0$ in which the difference in the observed frequencies vanishes. In panel (d), we show the whole synchronization region, i.e. the flat region of (c), varying the coupling strength and the intrinsic detuning. As we increase the detuning, larger coupling strengths are needed for synchronization to emerge. This is a first example of an *Arnold tongue* [42, 43], a ubiquitous feature of synchronizing systems. Indeed, while here we have introduced this synchronization feature for coupled system

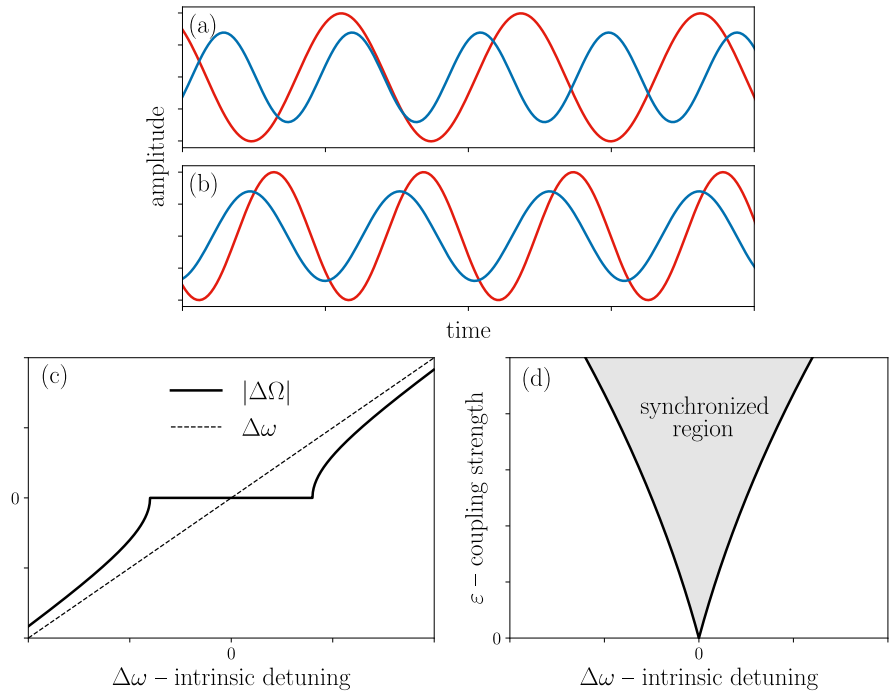

Figure 1.1: Cartoon of mutual synchronization between two classical self-sustained oscillators. (a) In the absence of mutual coupling each system oscillates at its own frequency $\omega_{1,2}$. (b) For large enough mutual coupling the oscillators synchronize and their observed frequencies adjust to a common one $\Omega_1 = \Omega_2 = \Omega$, while there is a fixed phase relation between the two oscillations (here close to zero). (c) When the coupling strength is fixed, increasing or decreasing the intrinsic detuning, $\Delta\omega = \omega_2 - \omega_1$, can take the system inside the synchronized region $\Delta\Omega = \Omega_2 - \Omega_1 = 0$ or outside it $\Delta\Omega = \Omega_2 - \Omega_1 \neq 0$. Notice that $\Delta\Omega$ and $\Delta\omega$ cross at the origin, where a vanishingly small coupling strength is enough to synchronize the system. (d) Synchronized region ($\Delta\Omega = 0$) varying the coupling strength ε and the intrinsic detuning $\Delta\omega$. This kind of shape is known as Arnold tongue and it is very common in synchronization phenomena for small coupling/driving strengths. Panels (c) and (d) can also be used to illustrate the entrainment of a system by an external driving if the detunings are reinterpreted as the mismatch between the frequency of the driving and that of the system and ε is reinterpreted as the driving strength.

components, the same kind of interplay is often found in the case of entrainment, where ε is to be reinterpreted as the external forcing strength while $\Delta\omega$ as the detuning between the intrinsic frequency of the oscillator and that of the external driving.

Beyond the illustrative example of synchronization and entrainment we have discussed, these phenomena can display different features, and they can be generalized and identified in more complex scenarios [56]. For instance, *higher-order mutual synchronization* occurs when systems spontaneously lock their frequencies to multiples/fractions of a common one [42]. In the same spirit, one can find *higher-order entrainment* in which the forced system locks to a multiple/fraction of the frequency of the forcing [42], as we shall see in chapters 6 and 7. Strikingly, synchronization has been generalized and studied in systems beyond limit cycles and self-sustained oscillations, lacking regular periodic orbits. This is the case of *synchronization in chaotic systems* [43], in which several new forms of synchronization have been reported [56], while important applications have been found for the implementation of secure telecommunication protocols [57]. Moreover, synchronization has also been studied in *stochastic dynamical systems*, i.e. dynamical systems in the presence of fluctuations, in which the signatures of this phenomenon are studied at the ensemble or average over realizations level [42, 43]. As we will see, this can provide physical insights to the study of synchronization in quantum systems where *quantum fluctuations* play an important role. These more general scenarios for synchronization as well as the examples we have commented illustrate the fact that synchronization is a paradigmatic

phenomenon of non-equilibrium systems [43]. Then, the next big question to be addressed is whether this phenomenon can actually be identified and generalized to the dynamics of quantum systems.

1.1.2 Quantum synchronization

When considering the dynamics of quantum (dissipative) systems, one is faced with fundamental differences with respect to classical dynamical systems, that can preclude an immediate generalization of synchronization and other dynamical phenomena in the quantum regime. In fact, classical synchronization is essentially rooted in the properties of the temporal trajectories of dynamical systems, in which the notion of a similar temporal evolution and phase-locking are generally easily recognizable [e.g. Fig. 1.1 (a)]. Moreover, in the most common examples of synchronization, one often deals with deterministic dynamical systems, neglecting the role of noise or fluctuations. In stark contrast, quantum mechanics is essentially a statistical theory, in which there is no direct analogue to the classical noiseless trajectories and generally departing also from classical stochastic systems. When studying the dynamics of quantum dissipative systems, one usually considers physical quantities at the ensemble level, i.e. as expectation values over the state of the system [58, 59]. While "individual" quantum trajectories can still be analyzed, as in photocounting experiments and other observation schemes, the presence of noise and fluctuations is here not only unavoidable but also *fundamental* [60]. Furthermore, these "individual realizations" depend strongly on the way one observes the quantum system, and hence, the dynamics at the ensemble level is not uniquely associated with a given stochastic process but it can be unravelled in many different ones [61]. Therefore, these fundamental differences not only challenge a direct comparison with classical noiseless synchronization but also limit the analogies with synchronization in classical stochastic systems. It is probably because of this conceptual gap that many different approaches to quantum synchronization have been adopted.

On the historical origins of quantum synchronization. The diversity in approaches to quantum synchronization can be already appreciated in the first works on the subject. More than a decade ago, the seminal works by Goychuk et al. [62] and Zhirov and Shepelyansky [63] reported for the first time on quantum entrainment and quantum spontaneous synchronization, respectively. In Ref. [62] the dynamics of a quantum-tunneling system was reported to synchronize to an external periodic drive, while in Ref. [63] a qubit and a driven-dissipative harmonic oscillator were shown to mutually synchronize. As early as in these works, some key quantities in which synchronization is manifested were identified, as the power spectrum [63], which we will explain in more detail below. A few years later, mutual transient synchronization emerging in systems of coupled dissipative spins [64] and harmonic oscillators [65] was reported, in which the dynamics of expectation values was central for the analysis. Moreover, Giorgi et al. [65] provided a first example in which quantum synchronization is accompanied by quantum correlations, a fundamental issue addressed in many later works [44]. Shortly after, quantum synchronization was addressed in the quantum counterpart of classical systems known to synchronize [66, 67, 68], providing the first examples in which to compare synchronization in the classical and quantum regimes. Since then, a growing research community has focused on different ways to generalize synchronization to the quantum realm, as well as in the search for genuine quantum features associated with it. In the following, we review some approaches to quantum synchronization and entrainment adopted in the literature, starting with approaches with an immediate classical analogue.

Generalization of classical synchronization into the quantum regime. It is pedagogical to begin our discussion by considering some important examples in which the quantum counterparts of well known classical synchronization models have been studied. These systems provide a rich playground where the transition from quantum to classical synchronization can be analyzed, which has yielded important physical insights. This is the case of the paradigmatic van der Pol oscillator (vdP), a non-linear dynamical system in which classical synchronization phenomena have been extensively analyzed [42, 43]. Its quantum counterpart, i.e. the quantum vdP oscillator (QvdP), consists of a non-linear driven-dissipative bosonic mode, where both entrainment and mutual synchronization have been addressed [67, 68, 69, 70]. Optomechanical systems [23] are also candidates in which classical spontaneous synchronization and entrainment have been studied, both theoretically [71, 72] and experimentally [73, 74, 75, 76], and in which the quantum regime has also been addressed [23, 66, 77]. In some of these systems [71, 72], the classical many-body synchronization dynamics can be understood in terms of the paradigmatic Kuramoto model [78], a reduced model that describes the coupled phase dynamics of arrays of self-sustained oscillators and which captures the transition to synchronization. Indeed, semiclassical generalizations of the Kuramoto model have been considered [79], in which the effect of quantum fluctuations has been analyzed. Furthermore, a variation of the Kuramoto model has been found to describe the mean-field mutual synchronization dynamics of atomic systems as clouds of interacting dipoles [80].

In these initial studies of quantum vdP oscillators [67, 68] and optomechanical systems [66], a far-reaching approach to quantum synchronization was adopted. This consists in studying *phase-space representations* of the stationary state of the system in a rotating frame [59, 60], also known as stationary quasipobability distributions. While these are "static" or time-independent quantities, if one already knows that the system displays a limit-cycle regime or self-sustained oscillations, this kind of quantities can be used to assess (at the ensemble-level) whether the phase of the limit cycle is free or rather there is some preferred phase. In fact, the stationary quasiprobability distribution of a quantum self-sustained oscillator is known to display a ring-like shape in the absence of any preferred phase [59, 66, 67, 81, 82], which is to be interpreted as the system displaying a stable non-zero oscillation amplitude and a free oscillation phase. In contrast, when these systems become synchronized, their quasiprobability distribution displays a localized lobe (or some other localized pattern), which signals the stabilization of a certain oscillation phase. Hence, the transition from one pattern to the other constitutes a signature of the onset of quantum synchronization in quantum self-sustained oscillators [66, 67, 68]. This is exemplified in Fig. 1.2 (a) and (b), in which we show the stationary Wigner quasiprobability distribution (see appendix A) for a driven QvdP oscillator when it is not entrained (a), and when it is (b). Notice that the analysis of phase-space representations of the stationary state of quantum systems parallels the analysis of the stationary probability distribution in classical stochastic systems displaying synchronization, which features similar changing patterns [42, 43, 82]. Since these early studies, and following a similar spirit, other ways to detect the emergence of a preferred phase in quantum self-sustained oscillators have been proposed, as the study of angular phase distributions [83, 84, 85], and order parameters for synchronization such as indicators based on stationary expectation values of amplitudes or amplitude correlations [86, 87].

In this regard, another important signature of quantum synchronization identified in these early studies [46, 63, 68, 70] is the *observed frequency*, or the frequency at which the emission/power spectrum [59, 88] of these systems takes its maximum value. Here, the basic idea is that quantum synchronization should imply a change in the characteristic dominant frequencies of the system, and this should be reflected in quantities related to the emission/absorption of energy by the system. In fact, as reported initially in [46, 68, 70],

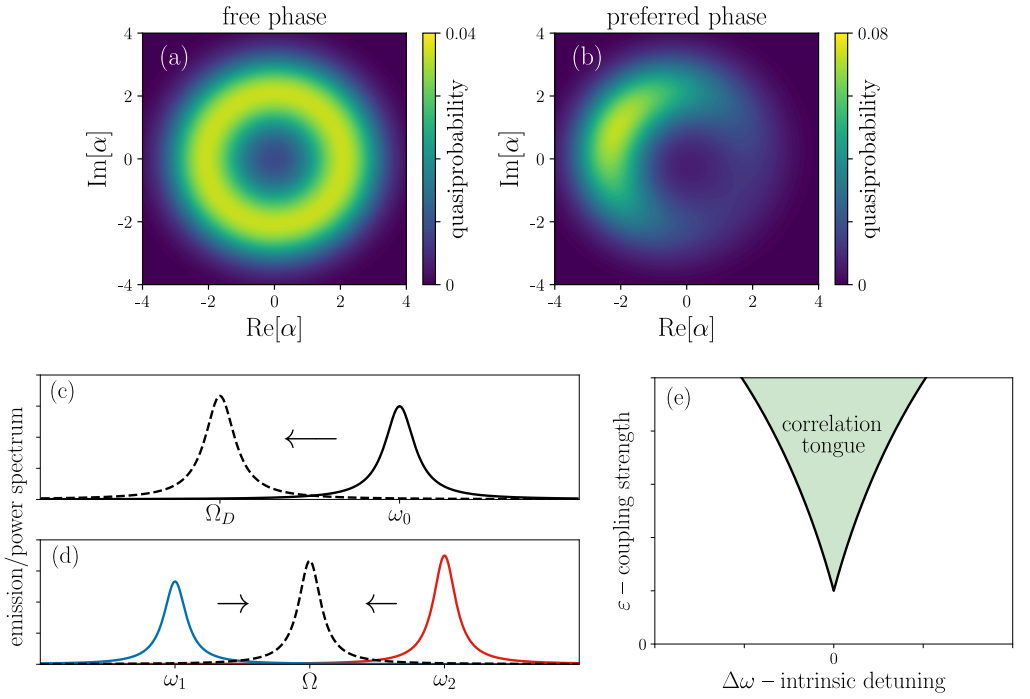

Figure 1.2: Schematic illustration of some important signatures of quantum synchronization. (a), (b) Phase-space representations: stationary quasiprobability (Wigner) distribution of a non-linear bosonic oscillator (the driven quantum vdP oscillator [67, 68]), where α is the amplitude of a coherent state. The transition from the ring-like shape in (a) to the localized lobe in (b) indicates the onset of phase-locking. (c) and (d), emission/power spectrum. (c) In the case of entrainment the peak of the maximum shifts from the intrinsic frequency of the system, ω_0, to that of the external forcing, Ω_D. (d) Spontaneous synchronization can be indicated by multiple peaks at different frequencies, $\omega_{1,2}$, shifting towards the same frequency, Ω, as for instance in [70]. (e) "Correlation tongue": in some systems mutual synchronization has been shown to be witnessed by quantum correlations between the units of the system computed at a single time, in which, varying the parameter values, a behavior similar to an Arnold tongue is reported.

the observed frequency is able to adjust to an external drive, in the case of quantum entrainment [68], or to shift to a common one, in the case of mutual synchronization [46, 63, 70]. This is schematically illustrated[1] in Fig. 1.2 (c) and (d), respectively. The analysis of the frequency at which the emission/power spectrum peaks can be compared with classical experimental studies of synchronization in the presence of thermal fluctuations [73, 74, 76]. Moreover, the study of this quantity can also be seen to be analogous to methods used in classical stochastic systems displaying entrainment, as the analysis of the "average frequency" [42, 43].

Synchronization in systems with no classical counterpart. The study of quantum synchronization has not been restricted to the generalization of classical synchronizing systems to the quantum realm. In fact, quantum systems with no classical counterpart have been addressed. This is the case of synchronization in dissipative spin-1/2 systems, from systems made of few qubits [45, 64, 89, 90], to mesoscopic clouds of atoms trapped in optical cavities [46, 80]. This is also the case of spin-1 [91, 92, 93] or other few level systems [94], as well as a one-dimensional Hubbard fermionic chain [93]. Moreover, phenomena differing from the paradigmatic classical cases had been reported deep in the quantum regime, as the synchronization blockade [95], in which small detuning does not favor

[1]Notice that this is the simplest scenario while in actual systems the emission/power spectrum can display more intricate features, as interference windows just at resonance, which can require a more detailed analysis in order to assess the emergence of synchronization, as we will see in the forthcoming chapters.

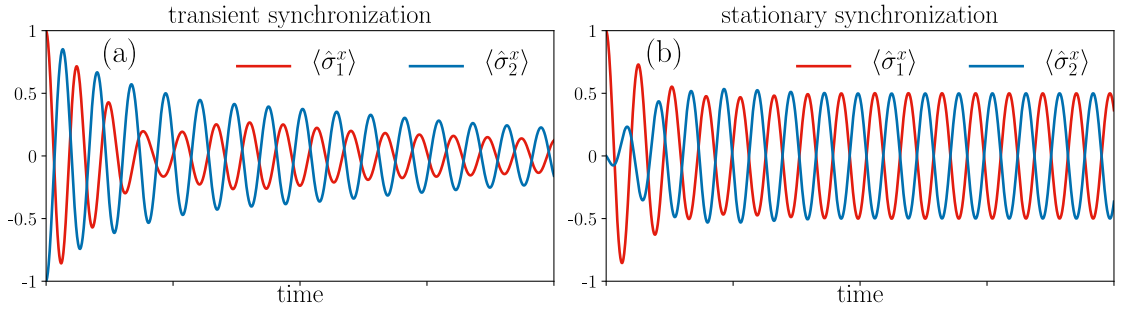

Figure 1.3: Example of quantum synchronization emerging in the dynamics of expectation values. Here we consider a system made of two coupled qubits dissipating collectively [90] in which one can find both transient synchronization, as shown in (a), and stationary synchronization, as shown in (b). The synchronous oscillation is manifested in the dynamics of the expectation values of the x- and y-components of the spins, encoded in the Pauli matrices $\hat{\sigma}_{1,2}^{x,y}$, in which both qubits oscillate at the same frequency with a locked phase difference close to π.

synchronization, as also reported in a spin system [89]. It is also interesting to recall that phase-space representations have been used also in spin-1/2 [96] and spin-1 [91, 92] systems in look for signatures of quantum synchronization.

Transient synchronization. This type of synchronization will be the topic of chapters 3, 4 and 5. A characteristic of transient synchronization is that it departs from the paradigm of self-sustained oscillations, and it can even emerge in linear dissipative systems [65]. Notice that, as we have mentioned, there are also classical synchronization scenarios departing from the paradigm of regular self-sustained oscillations, as it is the case of chaos synchronization [56]. Then, in such cases, the notion of mutual synchronization is not rooted in the dynamical landscape of coupled limit-cycle oscillators that acquire a preferred phase, but rather on the more general notion of spontaneous synchronization as the emergence of a strong temporal correlation or similitude in the dynamics of coupled (dissimilar) systems. In a transient synchronization scenario, the units of a dissipative system spontaneously synchronize in their transient towards the stationary state. This kind of synchronization is signaled by the emergence of a monochromatic long-lived oscillation in the dynamics of expectation values of coupled systems, which is rooted in the presence of a collective excitation that is long-lived with respect to the others and which dominates the long-time dynamics of the system [44, 65]. Thus, the characteristic temporal order of synchronization emerges because of a certain structure in the collective excitations of a system which allows the dominance of a (synchronizing) collective mode in a long transient towards the stationary state. The mechanism behind transient synchronization is rather general, and this phenomenon has been reported to manifest in many dissipative quantum systems: as systems of coupled spins [45, 89, 90, 93], fermionic lattices [93], arrays of coupled harmonic oscillators [65, 97] with complex geometries [98], or excitonic models [99]. Furthermore, the emergence of this kind of synchronization has been linked with the presence of long-lived quantum correlations [45, 98], as mentioned previously, and super/subradiance phenomena [90]. Moreover, some practical uses of transient synchronization have been already reported, as a synchronization-based scheme for probing the spectral density of an environment [89, 100]. In Figure 1.3 (a) we plot an example of transient synchronization of two dissipative spins. We can see how this synchronous oscillation emerges after a short transient of time and it slowly decays towards the stationary state.

Stationary synchronization and decoherence-free subspaces. A particular yet remarkable case of transient synchronization is that in which the collective excitation synchro-

nizing the system displays an infinite lifetime. This leads to the emergence of non-decaying coherent oscillations in the dynamics of expectation values and correlations [45, 65, 90, 93, 98, 101]. Furthermore, this kind of synchronization has been found to occur in highly-symmetrical configurations involving collective dissipation [45, 98, 101] or dynamical symmetries [102], and it is essentially rooted in the presence of decoherence-free subspaces (DFSs) and noiseless degrees of freedom [103, 104]. DFSs are parts of the system Hilbert space that are effectively uncoupled from the environment, and are thus not affected by decoherence and dissipation. They have been proposed as a way to circumvent the detrimental effects of the environment in quantum information and computation protocols [105, 106, 107], where coherence and quantum correlations play a fundamental role. Similarly to this form of synchronization, decoherence-free subspaces and noiseless degrees of freedom have been reported in situations in which the different units of a system dissipate into a common environment, as in systems of qubits [45, 108, 109] and harmonic oscillators [101, 110, 111], which enable the asymptotic preservation of quantum correlations. Hence, this form of synchronization is often accompanied by the asymptotic preservation of quantum correlations, as entanglement or discord, as reported in Refs. [45, 98, 101]. In Figure 1.3 we plot an example of this stationary synchronization: in (b) we can see how after a small transient both spins oscillate synchronously in anti-phase. Moreover, it is readily apparent the non-decaying nature of the coherent oscillations. Notice that this kind of synchronization is also known as "stationary" synchronization [5], a term that refers to the non-decaying nature of the coherent oscillations. This nomenclature also highlights the key difference of this case with that of transient synchronization, which in many cases both occur in the same systems [45, 65, 93, 98, 101].

Non-decaying oscillations vs. self-sustained oscillations. We should also carefully notice that the non-decaying oscillations associated with "stationary synchronization" are fundamentally different from those of a quantum self-sustained oscillator, as the QvdP oscillator [67, 68, 82]. In fact, the QvdP oscillator does not display non-decaying coherent oscillations, as the oscillation phase is free, and thus susceptible to phase diffusion induced by quantum fluctuations. This leads to the aforementioned ring-like shape of the quasiprobability distribution, as well as to the expectation value of the amplitude to display an exponentially damped temporal evolution [82]. In particular, a key difference between the two phenomena is the following: while in self-sustained oscillations a source of energy is needed to compensate dissipation and thus allow for a non-zero amplitude (e.g. as signaled by the non-zero radius of the ring-like shape), these non-decaying coherent oscillations do not need such energy source (e.g. as in Refs. [65, 90, 98, 101]) as dissipation, rather than being counteracted, simply does not affect the relevant collective degrees of freedom that constitute a DFS or a noiseless collective mode, and thus energy remains trapped in them. Furthermore, in the case of "stationary synchronization" the amount of energy or the amplitude trapped in the noiseless mode depends on the initial condition, while in self-sustained oscillators these quantities are dynamically fixed by the interplay between energy inputs and dissipation.

Synchronization and correlations. An important question is on the relation of synchronization with other (quantum) correlations, and whether one can be used to detect the other, or if one implies the other [44]. Here, we find that it is important to distinguish between correlations calculated *at a single time*, and correlations that contain information on *a whole time window* [44]. An example of the first would be the entanglement between two oscillators in the stationary state [69], while an example of the second would be the emission spectrum, which corresponds to the Fourier transform (i.e. it integrates over a whole time window) of certain two-time correlations computed in the stationary state

[46, 68]. The conclusions that can be drawn from one or the other are different and we will comment them separately.

Correlations and indicators computed at a single time. This refers to the analysis of correlations at a single snap-shot of the temporal evolution, or at the stationary state, as indicators of quantum synchronization. Here, one must bear in mind that, due to the *dynamical* nature of synchronization, the capacity to assess it with such "static" quantities computed at just one instant of time is in general limited [44]. Nevertheless, in some quantum systems, spontaneous synchronization has been shown *to be accompanied by* enhanced correlations [65, 80, 83, 98, 112], and in such cases these correlations at a single-time can be "crafted" as indicators or witnesses of quantum synchronization, as for instance the stationary mutual information between coupled QvdP oscillators [112] or spin-spin correlations in atomic systems [80, 83]. In fact, in some of these cases, one can observe that quantum correlations computed at some given time display a behavior with the parameters similar to an Arnold tongue [65, 69, 112], and one can generally speak of "correlation tongues", as schematically illustrated in Fig. 1.2 (e). Moreover, recent works have adopted powerful information-theoretical approaches to further refine and propose quantum synchronization measures based on quantities computed at a single time, as coherences in the stationary density matrix [113, 114]. However, it is important to keep in mind that quantum synchronization (i.e. a dynamical phenomenon) is not equivalent to quantum correlation [44], and indeed, different measures of synchronization based on different correlations computed at a single time need not to agree in the general case, as one can find examples in which different measures do not display the same behavior when varying the parameter values [44, 84]. Indeed, the particular results we will report in chapter 5 constitute a further example in which the whole synchronization scenario of a system cannot be captured by a correlation measure calculated at a single instant of time. Hence, while for some systems an "integral approach" has been adopted for the analysis of quantum synchronization (i.e. considering both "static" and dynamical indicators), as in the QvdP oscillator [68, 70], in some other systems with no classical counterpart or deep in the quantum regime, only indicators computed at a single time have been used for the assessment of synchronization, as in e.g. Refs. [69, 91, 92, 94, 113], which raises the question on which is the "dynamical face" of the reported quantum synchronization phenomena.

Correlations and indicators involving a whole time window. Here we will focus on two-time correlations and on the Pearson factor. As mentioned, several works have made use of the emission and power spectra in order to assess the presence of quantum synchronization, as in e.g. Refs. [46, 63, 68, 70]. These spectra are generally defined as the Fourier transform of some two-time correlations calculated in the stationary state of the system [59], and thus they yield information on the dynamics of the system, as for instance: which is the dominant frequency of the system, which are the lifetimes of the different collective modes, or how important is a collective mode for a particular unit. Indeed, the *observed frequency* introduced above is just a particular way to aggregate some of this important dynamical information in a single-valued quantity. Along this thesis, we will further illustrate the usage of this kind of quantities to assess the emergence of quantum synchronization. Moving beyond the analysis of the temporal dynamics in the long-time limit, synchronization can be assessed also in the dynamics after an arbitrary initial condition. In such cases, a useful indicator is the Pearson factor, a statistical correlator between temporal trajectories [44, 65]. This is especially useful in the analysis of the dynamics of expectation values and it has been used in the study of spontaneous transient synchronization, as in e.g. Refs. [44, 65, 93, 98, 99]. This correlator takes the temporal trajectories of two observables and computes their correlation over a whole time window, providing a numerical result in the range $[-1, 1]$, where -1 means perfect anti-correlation

(synchronization with a locked phase difference of π), while 1 corresponds to perfect correlation (perfect synchronization, for more details see appendix B). While other correlations and newly conceived quantum indicators (as the synchronization error [115]) have also been studied on an average over a whole time window, the main advantages of the Pearson factor are that it provides an *absolute* scale of the degree of temporal correlation, and that it can be computed between any two temporal trajectories [44].

Quantum synchronization beyond the ensemble-averaged level. Finally, it is interesting to mention some first results of the study of quantum synchronization analyzing the temporal dynamics of the system *beyond* the ensemble level, i.e. that of expectation values, in which the dynamics of quantum trajectories has been considered [63, 87, 116]. As observed in these works, quantum noise makes the phase between the synchronized systems to suddenly jump from time to time, similarly to what is observed in classical stochastic systems [43], and which can lead to an exponentially damped trajectory when averaging over many realizations.

Experiments on quantum synchronization. In the past years, the first experimental studies of quantum synchronization have been reported. Spontaneous synchronization has been reported in the dynamics of large clouds of cold atoms trapped inside an optical cavity [117]. The synchronization dynamics of this kind of systems can be understood at the semiclassical level, from the study of the truncated mean-field dynamics for the first and second order moments of the pseudospins that model the relevant atomic transitions [46]. Notice that the optical cavity provides a collective decay channel which is crucial for the emergence of synchronization. Moreover, the synchronized regime has been found to display interesting properties for practical applications, as an enhanced coherence time [46, 118], or the enhancement of laser cooling of the atomic ensemble [119]. On the side of entrainment, the quantum phase-locking of a spin-1 system to an external drive [91] has been recently reported in an experiment with trapped cold Rb atoms [120]. Interestingly, this system has also been simulated in the IBM quantum computer [121].

As we have seen, quantum synchronization has been reported in several systems and following different approaches [44]: some are inspired by the study of classical synchronization in fluctuating systems, and deal with phase-space representations [67, 66] or the observed frequency [62, 63, 68]; while some others are genuinely quantum, as the study of quantum correlations [65, 69, 115]. Moreover, we have seen that some first steps towards the experimental study of quantum synchronization have been achieved [117, 120]. In this thesis, we will explore several fronts of the emerging field of quantum synchronization. First we will focus on the emergence of transient and stationary synchronization in more complex systems, analyzing whether these stationary synchronized coherent oscillations can be found away from the reported highly symmetric configurations, and looking also for the prevalence of its transient counterpart. Later on, we will analyze whether synchronization can be found in systems implementable with cold atoms trapped in optical lattices and beyond collective dissipation. This is a paradigmatic platform of quantum simulation in which phenomena such as the superfluid-Mott insulator transition have been studied [18]. In this project, we will also address the connection between correlations and synchronization, analyzing whether one thing necessarily implies the other for this particular set-up. Finally, we will also consider a class of QvdP systems. There, we will analyze how the synchronization regime, as signaled by the stationary quasiprobability and the power spectrum, translates into the dynamics of expectation values, a question that remains largely unexplored.

1.2 Non-equilibrium phases in driven-dissipative quantum systems

When presenting the topic of quantum synchronization, it was implicit the notion that quantum systems can display several regimes (e.g. synchronized one vs. unsynchronized), which depend on the strength of the different processes occurring in the system. Indeed, driven-dissipative systems can display rich phase diagrams in which the interplay of different processes shapes the stationary properties of the system and its dynamical response. These non-equilibrium phases or regimes become sharply defined in the *thermodynamic limit* of infinite system units, or in the *infinite-excitation limit*, in which the number of excitations (e.g. photons) present in the system becomes macroscopic and the effect of quantum fluctuations becomes vanishingly small [35, 122, 123]. In these limits, observables of the system can display *non-analytical transitions* when crossing the phase boundaries, and these different regimes can be characterized by the spontaneous breakdown of underlying system symmetries [35]. This parallels the behavior of equilibrium quantum systems at zero temperature, in which the competition between non-commuting terms of the Hamiltonian can lead to quantum phase transitions, characterized by different properties and symmetries of the ground state [124]. The study of these non-equilibrium phases and of the dynamical phenomena near their boundaries has attracted much attention recently [35]. The focus has been set on the search for distinctive and genuine non-equilibrium phenomena, as time-crystals [38, 39, 40], on the analysis of the critical dynamics emerging in the transitions between different regimes, as well as on the spontaneous symmetry breaking phenomena occurring far-from-equilibrium [34, 35, 125]. In this section, we will introduce some of these topics that will be studied in the rest of the thesis.

1.2.1 Dissipative phase transitions and spontaneous symmetry breaking

It is a common scenario that quantum dissipative systems possess a stationary state described by a density matrix, $\hat{\rho}_{ss}$. This state plays the role of the stable attractor of the dynamics, as the state of the system at some time ends up converging towards it, i.e. $\hat{\rho}(t) \to \hat{\rho}_{ss}$. Naturally, the properties of this stationary state depend on the parameters of the system, as for instance the components interaction strength, or the detuning with an external driving. While the effect of the environment tends to induce an equilibrium state, i.e. the thermal state, in the presence of driving or energy pumping, $\hat{\rho}_{ss}$ generally describes a far-from-equilibrium state. Due to the interplay between driving, dissipation and interactions or non-linearities, the system often displays different stationary states when changing the parameters, with specific properties and symmetries, and that define a phase diagram [34, 35]. For finite-sized systems or in the presence of a finite number of excitations, the system generally features a smooth crossover between these regimes. In contrast, in the thermodynamic and in the infinite-excitation limits [35], they become sharply defined, and one can identify observables that undergo a non-analytical transition when crossing the phase boundaries by varying some control parameter (g around a critical point g_c). These observables play the role of order parameters, since their non-analytical behavior signals the occurrence of a *dissipative phase transition* (DPT) [34, 35]. Notice that, in contrast to classical (equilibrium) phase transitions [126, 127], these order parameters are not related to thermodynamic potentials or their derivatives, as the stationary state in these far-from-equilibrium situations is not governed by such thermodynamic quantities [34, 35].

The study of DPTs and the characterization of these non-equilibrium phases has

become a very active field of research in the past decade, in which a variety of systems have been considered: spin lattices [128, 129, 130, 131], arrays of non-linear photonic resonators [132, 133, 134, 135, 136, 137, 138, 139, 140], dissipative Dicke models [37, 141, 142, 143, 144], optically trapped systems of cold-atoms [125, 145, 146] and Rydberg atoms [36, 147, 148, 149, 150, 151], or optomechanical oscillators [66, 152]. However, notice that the earliest reports on this kind of phenomena can be traced back to the quantum-optical literature, in which the notion of far-from-equilibrium phase transitions occurring in driven-dissipative systems was already present, as in the laser phase transition analogy [153], in optical bistability [154, 155], or in cooperative resonance fluorescence [156], although some crucial features, as the closure of a spectral gap (see below), have been only identified recently [34].

Dynamics near a DPT. In the last decade, research efforts have focused on the critical dynamics near these DPTs, analyzing their common and distinctive features with respect to equilibrium phase transitions, as well as in look for non-equilibrium universal behavior [125, 131, 136, 138, 140, 143, 150, 151, 157, 158, 159, 160]. In fact, for some systems, it has been possible to analyze the spectral properties of the generator of the dynamics, i.e. the Liouvillian, near a DPT [34, 35, 136, 158, 161]. This has revealed that DPTs are associated to the closure of the Liouvillian spectral gap, either at the critical point or in a whole region, which results in the emergence of new stationary states [34, 35]. This parallels what can occur in closed equilibrium systems where the energy gap of the generator of the dynamics, i.e. the Hamiltonian, can close in the thermodynamic limit leading to a quantum phase transition [34, 124]. DPTs are an emergent phenomenon, i.e. they emerge progressively as one approaches some limit, and a strict closure of this gap occurs only in the thermodynamic or infinite-excitation limits [34, 35]. Nevertheless, its effects are evident even far from these limits, e.g. as manifested by the emergence of a very long dynamical timescale associated with the "quasi" closure of the gap. This can lead to a critical slowing of the dynamics near the phase boundaries [140], to dynamical hysteresis phenomena [135], and to metastability [162]. In fact, this kind of signatures of a DPT has been recently observed in experiments with Rydberg atoms [163], superconducting circuits [164] and cavity polaritons [165].

In Figure 1.4 we illustrate the typical scenario of a continuous DPT. For analogous plots for a first-order DPT we refer the reader to Refs. [35, 136]. In panel (a), we plot the order parameter (some appropriate observable calculated in the stationary state) varying a control parameter: when varying this parameter far from the thermodynamic limit or the infinite-excitation limit, a smooth crossover is observed in the behavior of the order parameter (see curves for finite N). The sharp DPT emerges only in these limits (i.e. N going to infinite), in which, for this example, the behavior of the system is well captured by the mean-field equations of motion that display a bifurcation between the different regimes at the critical value of the control parameter $g = g_c$ (black line) [35, 122, 134, 135, 136, 139, 152, 158]. When N is increased, the order parameter obtained from the quantum stationary state (color-broken lines) approaches the mean-field one (black solid line). At the same time, the Liouvillian spectral gap tends to zero in a whole region, as shown Fig. 1.4 (b). As we will see, the inverse of this gap defines a very-long characteristic timescale associated with the emergence of a metastable response (see chapter 6).

DPTs and spontaneous symmetry breaking. Dissipative phase transitions can lead to non-equilibrium phases that *spontaneously break* some symmetries of the system. This means that there emerge stable attractors that are less symmetric than the underlying equations governing the dynamical system. An illustrative example is found in Rydberg

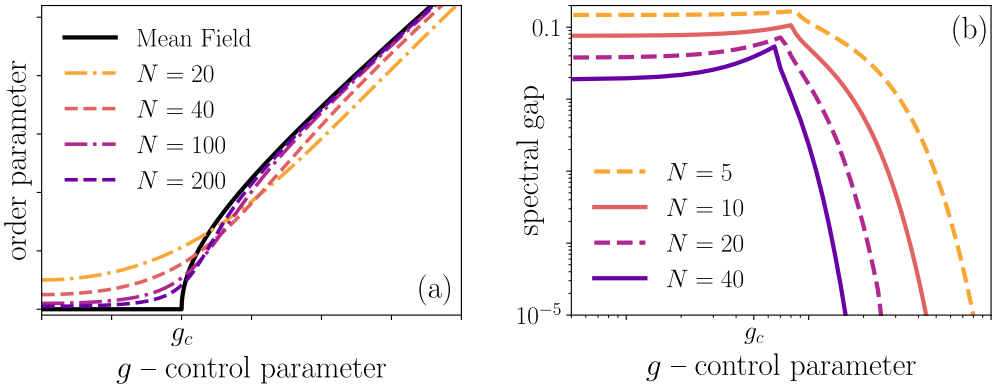

Figure 1.4: Illustrative example of a continuous DPT. In (a) the order parameter is shown as the control parameter g is varied. The mean-field result (black line) shows a non-analytical transition at g_c. The results from the stationary state of a full quantum treatment of the dynamics are plotted in color-broken lines. As the "thermodynamic limit" is approached (larger N), the results approach the mean-field ones, and the crossover becomes sharper. (b) (Liouvillian) spectral gap. Close to the critical point g_c, the behavior of the spectral gap changes abruptly and tends to zero in the whole regime $g > g_c$. The larger the N the more exaggerated is this trend. These results correspond to the squeezed van der Pol oscillator [166], a system consisting in a driven-dissipative non-linear bosonic mode that will be analyzed in detail in chapters 6 and 7.

atoms in optical lattices [36, 149], as well as in arrays of non-linear cavities [132, 133, 137], in which despite the arrays and lattices are uniform, i.e. all the units are equivalent, there are phases in which the observables break this translational symmetry by displaying checkerboard patterns or anti-ferromagnetic ordering. It is also common, while its consequences are more subtle, the spontaneous breakdown of parity symmetry, as reported for the dissipative Dicke model [37, 144] and other spin-boson models [158], as well as in non-linear bosonic models [35, 139, 152], as the squeezed QvdP oscillator (see chapter 7). Another intriguing case which has attracted a lot of attention recently is the spontaneous breakdown of time-translation symmetry, as we explain in the following subsection.

1.2.2 Time crystals: the breakdown of time-translation symmetry

It is well known that classical non-linear dynamical systems can evolve towards stable limit cycles [55], resulting in the emergence of stable self-sustained oscillations. This kind of attractors breaks the underlying *time-translation symmetry* of the dynamical system; from a time-independent set of equations there emerge time-dependent stable solutions. This can also happen in quantum driven-dissipative systems described by time-independent equations. Indeed, in the section about synchronization, we have already met some systems that display self-sustained oscillations in the classical or infinite-excitation limit, as vdP [168] and optomehcanical [167] oscillators, while in the quantum regime these attractors are affected by quantum fluctuations that generally lead to phase diffusion and the loss of temporal coherence, as signaled by a ring-like shaped stationary quasiprobability distribution and a Lorentzian emission/power spectrum, as in Fig. 1.2 [67, 68, 81, 82]. Self-sustained oscillations in many-body quantum systems have been also reported, as in systems of Rydberg atoms in optical lattices [36, 149], and other driven-dissipative spin lattices [129, 169], in arrays of non-linear photonic resonators [133], as well as in driven-dissipative spin-boson systems [171], as dissipative Dicke models [142]. However, in these works, stable limit cycles are reported only at the mean-field level. Then, one important question is to be answered [38]: does time-translation symmetry breaking actually survive in the presence of a full quantum treatment of the dynamics, or is it rather an artifact of

mean-field approximations? This question has triggered a lot of activity recently in the emerging topic of *dissipative time-crystals*, in which a careful assessment of the thermodynamic limit or the infinite-excitation limit of the quantum dynamics is performed in search for the emergence of self-sustained oscillations, i.e. looking for signatures that can confirm time-translation symmetry breaking.

The birth of time-crystals. While the huge activity of the past decade in the field of driven-dissipative quantum systems has naturally lead to the study of spontaneous time-translation symmetry breaking (as this is a ubiquitous and well known phenomenon in their classical counterpart, i.e. classical non-linear dynamical systems [55]), the wide interest on time-crystals has been actually triggered by a different community: that of closed, or Hamiltonian, many-body systems. In fact, almost a decade ago, Wilczek asked in a seminal work [172] whether the ground state of a many-body system can break time-translation symmetry, giving birth to the concept of time-crystal. The analogy is with solid-state crystal structures, where space-translation symmetry is spontaneously broken. This initial example of a time-crystal turned out to be incorrect [173], and other works challenged the possibility of time-crystals in equilibrium systems [174, 175, 176]. Indeed, a no-go theorem was proved that rules out the possibility of time-translation symmetry breaking in the equilibrium state of many-body systems with short-range interactions [41]. Then, the attention turned to non-equilibrium situations and time-crystalline phases were initially reported for driven *closed* systems [177, 178, 179, 180, 181]. In these phases, a set of observables of the system displays persistent oscillations with a period that is a multiple of the driving period, i.e. time-translation symmetry is broken *discretely* [182, 183]. Generally, the lifetime of this subharmonic response is found to diverge only in the thermodynamic limit, and thus these *discrete* or *Floquet* time-crystals emerge strictly in this limit. Notice that in these non-dissipative systems, the presence of disorder is crucial in order to prevent the system to reach a featureless state; since, due to the continued action of the external driving, this state would have infinite temperature [183]. Dissipation can counteract this energy divergence, and the first examples of dissipative discrete time-crystals were reported shortly after in Refs. [39, 40]. In parallel, *continuous* time-translation symmetry breaking was reported for another dissipative system [38]; a work in which the emergence of self-sustained oscillations from the quantum model was assessed by means of a finite-size analysis of the eigenspectrum of the generator of the dynamics, i.e. the Liouvillian, an approach that would be followed in later works on the subject. Remarkably, even if discrete time-crystals were predicted only few years ago, recent experiments with different quantum simulators and many-body systems have already reported on the observation of signatures of this non-equilibrium phase [184, 185, 186, 187, 188].

Dissipative time-crystals. In this thesis, we will only consider *dissipative* time-crystals, for which we can distinguish between two cases: those driven by a time-dependent field in which a stable subharmonic regime emerges, i.e. *discrete* time-crystals; and those governed by time-independent equations in which an oscillatory regime emerges, i.e. *continuous* time-crystals. Examples of both cases have been reported for driven-dissipative systems made of spins [38, 40, 170, 189, 190, 191, 192], atoms in a cavity and other spin-boson systems [39, 193, 194, 195], and non-linear photonic systems [168, 196, 197, 198, 199, 200, 201, 202]. Notice that while in discrete time-crystals the emerging oscillations are constrained to display a frequency that is a fraction of the one of the driving, in continuous time-crystals the frequency is generally determined by the strength of the underlying coherent and incoherent processes [168, 192, 193, 194, 195, 197, 199, 200, 203], in complete analogy to classical self-sustained oscillations [55]. Furthermore, in our context,

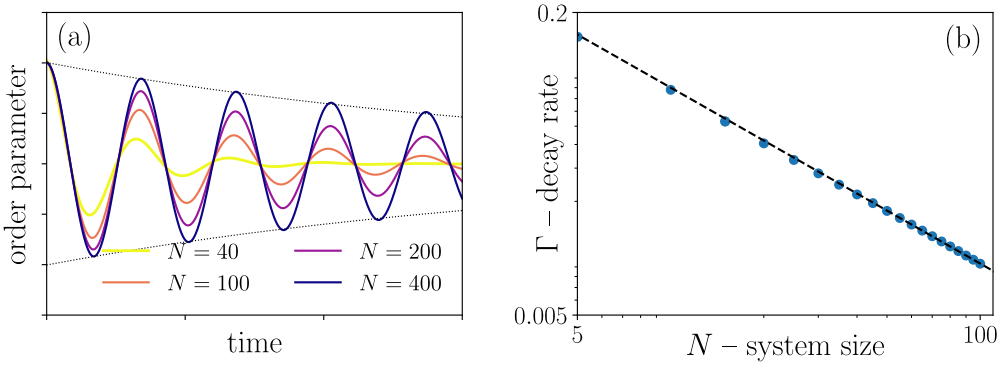

Figure 1.5: Illustrative example of a continuous time-crystal. (a) Some observables display oscillations whose lifetime increases with the "system size", N. The dotted envelopes indicate that their decay is well captured by an exponential decay with rate Γ. (b) The obtained decay rates Γ (points) follow accurately a scaling of the type $\Gamma \propto N^{-\alpha}$ with $\alpha > 0$. This suggests that the lifetime of the oscillations diverges in the "thermodynamic limit". All the results are obtained for the squeezed QvdP oscillator, and they will be explained in detail in chapter 7. However, notice that these results are quite generic of time-crystals and serve to illustrate the general case.

it will be important the notion of *semiclassical time-crystal* as introduced in Ref. [199]: this encompasses many-body systems with all-to-all interactions [39, 38, 192, 193, 195] as well as zero-dimensional systems (as non-linear oscillators) [168, 197, 199, 200], in which the thermodynamic or infinite-excitation limit where time-translation symmetry is spontaneously broken is well described by the mean-field semiclassical equations of motion. In other words, not only persistent oscillations emerge, but these are actually well captured by the mean-field model. This is not always the case, and time-crystalline phases have been reported for systems as dissipative spin chains [191], or the Dicke model with additional short-range interactions [194], in which the latter break the mean-field solvability of the model. Finally we notice that in some proposals [203], the stable oscillations can emerge away from the thermodynamic limit or infinite-excitation limit, in which case the time-crystalline phase is rooted in the presence of dynamical symmetries [102], similarly to some cases of stationary synchronization introduced previously [93].

In Figure 1.5 we illustrate the emergence of a continuous time-crystal. In (a) we show that an appropriate observable displays oscillations (quite regardless of the initial condition), whose lifetime increases with the system size, as parameterized by N. Notice that their envelope is well-captured by an exponential decay with rate Γ. In panel (b) we show that this decay rate scales as $\Gamma \propto N^{-\alpha}$ with $\alpha > 0$, i.e. it vanishes in the "thermodynamic limit". The divergence of the oscillation lifetime in the thermodynamic limit or in the infinite-excitation limit is the hallmark of time-crystalline phases. The major difference between this case and a discrete time-crystal is that in the latter the oscillation frequency is constrained to be a fraction of that of an external time-dependent field.

We conclude this section with a brief discussion of the aspects of DPTs and time-crystals that will be addressed in the forthcoming chapters. Provided that quantum synchronization is often studied in driven-dissipative systems while its classical counterpart is a paradigmatic phenomenon of non-equilibrium physics, in this thesis we will explore the relation of quantum synchronization with DPTs, spontaneous symmetry breaking and time-crystals. Indeed, connections between time-crystals and synchronization have been pointed out in some works, as in Refs. [38, 193], and we will further explore this venue. Moreover, we will also analyze the relation between DPTs and synchronization with the following question in mind: can the transition to a synchronized regime be understood as

a DPT? In such a case, is the quantum synchronized dynamics associated to some of the critical dynamics observed in driven-dissipative systems? And beyond synchronization, we will also address fundamental questions such as, can we find a transition between different types of time-crystalline order?

1.3 Non-Hermitian physics and exceptional points

In the previous section, we have discussed the emergence of non-equilibrium phases and DPTs in quantum dissipative systems, as the thermodynamic or infinite-excitation limits are approached. As we have seen, in these limits some observables computed in the stationary state undergo a non-analytical transition as a control parameter is varied. The spectrum of quantum dissipative systems can also undergo non-analytical transitions, far from the thermodynamic and infinite-excitation limits, and we introduce here some intriguing physical consequences of these *spectral singularities*, that we will study in different systems in this thesis and are connected to synchronization phenomena.

Exceptional points (EPs). The dynamics of quantum dissipative systems is often described by sets of equations that can be written as a *non-Hermitian* matrix, in stark contrast with closed (non-dissipative) quantum systems. This is the case of the Liouvillian superoperator, governing Markovian open quantum systems, or of non-Hermitian effective Hamiltonians, governing the dynamics of a set of expectation values. The eigenspectrum of these non-Hermitian matrices is complex-valued, and the real and imaginary parts of the eigenvalues correspond to the eigenfrequencies and decay rates of the dynamics[2]. The non-Hermitian character of these matrices can give rise to phenomena that have no equivalent in Hermitian (non-dissipative) systems, what has been dubbed as non-Hermitian physics [204, 205, 206, 207]. As for the phenomena we have introduced, namely synchronization, DPTs, and time-crystals, the enabling process is the interplay between the coherent and incoherent processes occurring in coupled dissipative systems; however, here the attention is set on the spectral origin of these phenomena, often rooted in the presence of non-Hermitian degeneracies or *exceptional points* (EPs) [208]. EPs are points in parameter space in which several eigenvalues become the same and their corresponding eigenvectors coalesce, making the dynamical system non-diagonalizable: i.e. they are spectral singularities of the system.

Non-Hermitian phenomena. The exploration of non-Hermitian physics, and more in particular of the dynamics of EPs, has been a very active field of research in photonics for the past decade, where engineered arrays of dissipative systems are ubiquitous, and models consisting of non-Hermitian effective Hamiltonians are common [204, 205, 206, 207]. Furthermore, in recent years the exploration of the effects of EPs in quantum dissipative systems has also received notable interest [205, 207, 208, 209]. The presence of these spectral singularities has been shown to be behind a variety of intriguing physical phenomena occurring in photonic systems, atomic systems, as well as in phononic and optomechanical arrays [204, 205, 206, 207], as parity-time symmetry breaking [210, 211, 212, 213], extreme sensitivity to perturbations [214, 215], chiral dynamics for adiabatic EP encircling [47, 48, 216], anomalous quantum decay [209, 217, 218], and topological phenomena [219]. Beyond the fundamental interest on these phenomena, applications such as novel functionalities based on parity-time symmetry phenomena have been drawn

[2]Depending on the definition of the matrix the eigenfrequencies correspond to the real or imaginary part of the eigenvalues. For the Liouvillian matrix they correspond to the imaginary part, while for effective Hamiltonians they correspond to the real part.

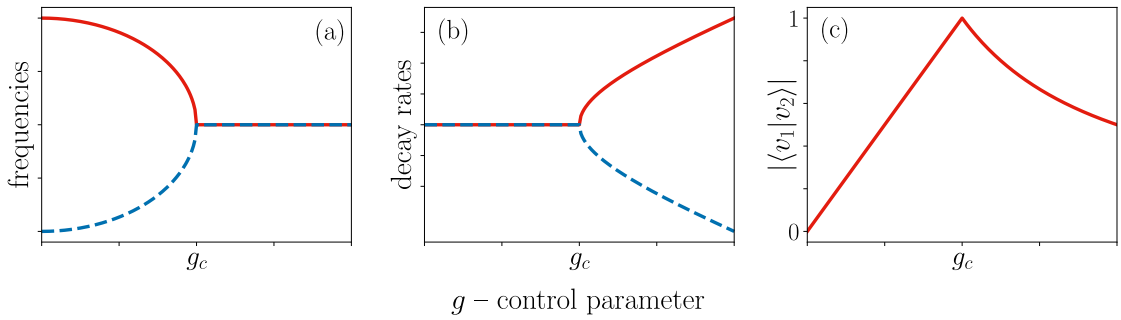

Figure 1.6: Illustrative example of a second order exceptional point occurring when varying the control parameter g through the critical point g_c. (a) For $g < g_c$ we have two different eigenfrequencies (red solid and dashed blue lines), while for $g > g_c$ they become the same. (b) The decay rates show the complementary behavior and bifurcate for $g > g_c$. (c) At the EP, i.e. at $g = g_c$, the two eigenvectors become parallel, i.e. the modulus of their inner product is one: $|\langle v_1|v_2\rangle| = 1$ (in Bra-Ket notation).

for photonic systems [204, 205, 206, 207, 220], as well as sensing applications based on the enhanced sensitivity of perturbations near EPs [207, 214].

Exceptional points and dynamical regimes. EPs can be seen as bifurcations of eigenvalues in the complex plane. The number of eigenvectors that coalesce defines the order of the EP [207]. In Figure 1.6 we illustrate a second order EP: we can appreciate how varying a control parameter, g, the real part and imaginary part of two eigenvalues "bifurcate" following complementary behaviors. Just at the critical point, $g = g_c$, the eigenvalues and the eigenvectors coalesce, the latter becoming parallel. This is the hallmark of this non-Hermitian degeneracy [208]: while in the Hermitian case the eigenvectors always remain orthogonal to each other, in the non-Hermitian case they do not necessarily do so.

In contrast to DPTs, these non-analytical changes of the excitation spectrum can occur far from the thermodynamic and infinite-excitation limits, and thus EPs can be found in finite-sized systems, as small qubit systems [209]. From figure 1.6 (a) and (b) it is readily apparent that these non-analytical points lead to a reorganization of the excitation eigenspectrum, as the number of different eigenfrequencies and decay rates changes at this point, and their qualitative behavior varying the parameters too. Indeed, this has been noted in some earlier works analyzing the dynamics of driven-dissipative quantum systems [34, 35, 46, 161], although an explicit connection with EPs has only been recently performed in [35]. In this thesis we will analyze the presence of EPs from this point of view, studying the different dynamical regimes that these points can separate, as well as looking for connections with the phenomena of synchronization and DPTs.

1.4 Plan of the thesis

In this thesis we will present in detail the results of Refs. [2, 3, 4, 5, 7, 9, 10] concerned with the topic of synchronization. In particular, the rest of the thesis is structured as follows:

– Chapter 2 is a brief introduction to the dynamics of open quantum systems, focusing on the methodological tools needed in the following works such as, for instance, the master equation description of dissipative quantum systems, the method to compute multi-time averages, or the Liouvillian approach.

– Chapters 3, 4 and 5 analyze the phenomenon of transient synchronization in different situations and also considering its relation to other collective phenomena. Specifically, in chapter 3 complex networks of quantum harmonic oscillators dissipating collectively are considered, and the presence of synchronization and noiseless collective modes is studied. In chapter 4 the presence of EPs is reported for two different systems, and dynamical phenomena associated to them, as synchronization, are analyzed. In chapter 5 the emergence of synchronization in atomic systems trapped in optical lattices is discussed, and the relation of this phenomenon to the emergence of quantum correlations is also addressed. The results presented in these chapters correspond to Refs. [2, 3, 4, 5, 7].

– Chapters 6 and 7 study the relation of quantum entrainment with other driven-dissipative phenomena. In particular, chapter 6 shows that entrainment in the squeezed QvdP oscillator is accompanied by a metastable dynamical response. While chapter 7 shows that the entrainment transition in this system corresponds to a DPT, while different symmetries (as parity symmetry or time-translation symmetry) are spontaneously broken in the different dynamical regimes. The results of these chapters correspond to Ref. [9] and a work in preparation [10].

– In each results chapter we include a short specific abstract and discuss the main achievements in concluding remarks. Appendices A to K contain technical details and additional results supplementing the results and discussions of the main text. Conclusions and outlook of this thesis are presented in chapter 8.

CHAPTER 2

Master equation and Liouvillian approach

The theory of open quantum systems provides the framework needed to describe the phenomena that we have introduced in the previous chapter and that will be treated in this thesis. This is a vast subject, as vast as it is its domain of application, a fact witnessed by the many different approaches and perspectives [58, 59, 60, 221, 222]. Here, we will provide a concise introduction focusing on the master equation and the Liouvillian approach, while a thorough discussion of technical details is generally avoided referring to the existing specialized literature [58, 59, 60, 221, 222]. With such a scope in mind, we start introducing the GKLS master equation, and the main approximations that enable such a description of a dissipative quantum system. We discuss some intriguing possibilities that emerge when several systems interact with the environment, as collective dissipation, or engineering dissipative dynamics through coupling to dissipative systems, placing special emphasis on modern realizations with quantum technologies. Finally, we present the specific techniques used to study the GKLS master equation in this thesis, as the basic rules to calculate one-time and multi-time expectation values. Then, we introduce the less known but powerful Liouvillian approach, which allows for a spectral analysis of dissipative dynamical systems that can provide important physical insights and understanding.

2.1 The GKLS master equation

The GKLS master equation is a time-local equation for the dynamics of the state of an open quantum system, as described by its density matrix $\hat{\rho}$. Its name stands for Gorini, Kossakowski, Lindblad and Sudarshan and acknowledges the fundamental contributions of these authors on the understanding of the mathematical properties of this equation [223, 224]. Its importance stems from these properties (e.g. maps states to states) as well as the fact that it describes accurately the physics of many dissipative quantum systems, as it is the case in quantum optics in which it is especially prevalent [58, 59, 88].

This master equation can be written in two equivalent forms: the non-diagonal form and the diagonal one. The choice between the different forms depends on the physical situation and it is a matter of taste and convenience. In its non-diagonal form it can be

written as ($\hbar = 1$) [58]:

$$\frac{d}{dt}\hat{\rho} = -i[\hat{H}, \hat{\rho}] + \sum_{j,k=1}^{M} \tilde{\gamma}_{jk}\Big(\hat{F}_j \hat{\rho} \hat{F}_k^\dagger - \frac{1}{2}\{\hat{F}_k^\dagger \hat{F}_j, \hat{\rho}\}\Big), \tag{2.1}$$

where the rates $\tilde{\gamma}_{jk}$ form a M-dimensional Hermitian and positive semi-definite matrix, $\tilde{\Gamma}$, while $\hat{F}_j$ are different system operators known as *jump operators*. Since $\tilde{\Gamma}$ is Hermitian and positive semi-definite we can diagonalize it by means of a unitary transformation obtaining a diagonal matrix $\Gamma = U\tilde{\Gamma}U^\dagger$, which contains the real non-negative rates γ_j. Similarly, we can define the corresponding set of new jump operators as $\hat{L}_j = \sum_{j,k=1}^{M} u_{kj}\hat{F}_k$, where u_{kj} are the matrix elements of the unitary matrix U. Then we obtain the Lindblad[1] master equation in its diagonal form [58]:

$$\frac{d}{dt}\hat{\rho} = -i[\hat{H}, \hat{\rho}] + \sum_{j=1}^{M} \gamma_j\Big(\hat{L}_j \hat{\rho} \hat{L}_j^\dagger - \frac{1}{2}\{\hat{L}_j^\dagger \hat{L}_j, \hat{\rho}\}\Big). \tag{2.2}$$

Notice that superoperators[2] provide a convenient way to work with master equations. In particular, we define the dissipator:

$$\mathcal{D}[\hat{L}_j]\hat{\rho} = \hat{L}_j \hat{\rho} \hat{L}_j^\dagger - \frac{1}{2}\{\hat{L}_j^\dagger \hat{L}_j, \hat{\rho}\}, \tag{2.3}$$

and the Liouville superoperator or *Liouvillian*:

$$\mathcal{L}\hat{\rho} = -i[\hat{H}, \hat{\rho}] + \sum_{j=1}^{M} \gamma_j \mathcal{D}[\hat{L}_j]\hat{\rho}, \tag{2.4}$$

from which we can write Eq. (2.2) as $\frac{d}{dt}\hat{\rho} = \mathcal{L}\hat{\rho}$ and its formal solution as

$$\hat{\rho}(t) = \mathcal{V}(t)\hat{\rho}(0), \quad \text{with} \quad \mathcal{V}(t) = \exp(\mathcal{L}t), \tag{2.5}$$

where we denote the initial condition as $\hat{\rho}(0)$. In Eq. (2.5) we have defined the quantum dynamical map $\mathcal{V}(t)$, which generates the dynamics corresponding to the master equations (2.1) or (2.2), and hence it satisfies the semigroup property [58, 222]:

$$\mathcal{V}(t_1 + t_2) = \mathcal{V}(t_1)\mathcal{V}(t_2), \quad \text{for} \quad t_{1,2} \geq 0. \tag{2.6}$$

The semigroup property of $\mathcal{V}(t)$ implies that the dynamics described by Eqs. (2.1) or (2.2) is *Markovian*, which essentially means that the evolution of the state of the system at a given time depends only on the state of the system at the same time[3]. Another basic property of the Lindblad master equation is that it maps states to states. More technically, $\mathcal{L}$ is a completely positive trace-preserving map [58, 222], and hence, when considering a system described by this type of equation, it is guaranteed that the state of the system remains physical at all times (i.e. $\hat{\rho}(t)$ remains Hermitian, positive semi-definite and with unit trace). On the other hand, not all physical situations in which dissipation is present in quantum systems can be described by Lindblad master equations, even when the dynamics is local in time. Markovian master equations which are not in the Lindblad form can be more accurate in some physical situations [58, 225]; however, at the cost that one must remain alert during the time evolution on possible violations of the properties of $\hat{\rho}$ that make it a physical state.

[1] We will usually denote the GKLS master equation as the 'Lindblad master equation' or as the 'master equation in the Lindblad form'. This is just a matter of custom, as we acknowledge the contribution of the other authors.

[2] Superoperators map operators of the Hilbert space to operators of the same Hilbert space.

[3] See Refs. [58, 222] for a more detailed discussion on Markovian quantum time-evolutions.

2.2 Microscopic origins of the Lindblad master equation

The purpose of this section is to illustrate the main physical conditions that can lead to a Lindblad description of the dynamics of a dissipative system. We first present a general derivation of this master equation using the canonical system plus environment approach [58, 59, 60, 221, 222] starting from the full Hamiltonian describing the system, the environment and their interaction. Here, we will follow closely the derivation of [58], as it enables to discuss the main approximations and physical conditions that can lead to a Markovian master equation while keeping the equations in a general form, which will be useful for the rest of the thesis. Later on, we illustrate this derivation with an elementary but important example: a harmonic oscillator coupled to a thermal bath.

2.2.1 System plus environment approach: main approximations

In a system plus environment approach one models a system of interest, as made for instance by several accessible[4] degrees of freedom, weakly coupled to the environment, as composed by a continuum of modes in a certain equilibrium state. This interaction enables the exchange of information and energy between the system and environment. Since the environment is a continuum with a macroscopically large number of degrees of freedom this interaction can lead to irreversible effects such as dissipation and decoherence [58, 59]. As we shall see, under certain physical conditions, the environment can be traced out of the description leading to a reduced description for the state of the system which can be well approximated by a Lindblad master equation.

Hamiltonian description. The total Hamiltonian describing this general situation is the following:

$$\hat{H}_T = \hat{H}_S + \hat{H}_E + \hat{H}_{SE}, \tag{2.7}$$

where $\hat{H}_S$ describes the degrees of freedom in which we are interested, or system, $\hat{H}_E$ describes the environment, and $\hat{H}_{SE}$ describes the weak system-environment interaction. This last term can be modeled in a general form as:

$$\hat{H}_{SE} = \sum_\alpha \hat{A}_\alpha \otimes \hat{B}_\alpha, \tag{2.8}$$

where $\hat{A}_\alpha$ and $\hat{B}_\alpha$ are Hermitian operators acting only on the system or the environment, respectively.

The starting point of the derivation is the von Neumann equation for the total state of the system plus environment $\hat{\chi}$ in the interaction picture[5] defined by $\hat{H}_S + \hat{H}_E$ [58] ($\hbar = 1$):

$$\frac{d}{dt}\hat{\chi}(t) = -i[\hat{H}_{SE}(t), \hat{\chi}(t)]. \tag{2.9}$$

Formal integration of this equation and insertion of the resulting $\hat{\chi}(t)$ back into it leads to an exact integro-differential equation, which is very convenient to identify and perform approximations:

$$\frac{d}{dt}\hat{\chi}(t) = -i[\hat{H}_{SE}(t), \hat{\chi}(0)] - \int_0^t ds[\hat{H}_{SE}(t), [\hat{H}_{SE}(s), \hat{\chi}(s)]]. \tag{2.10}$$

[4] That one can observe at least up to certain point (the one that enables to know the system indeed exists).

[5] Unless stated otherwise in this section we will work in this interaction picture.

In order to have a reduced description of the dynamics of the system we trace out the environment. In doing so, we assume that the total initial state is factorizable, i.e.:

$$\hat{\chi}(0) = \hat{\rho}(0) \otimes \hat{\mu}_R, \quad \text{with} \quad \hat{\rho}(t) = \mathrm{Tr}_E\{\hat{\chi}(t)\}, \tag{2.11}$$

where $\hat{\rho}(t)$ is the state of the system, and $\hat{\mu}_R$ is the reference state or equilibrium state of the environment. We now assume that this reference state and the environment operators $\hat{B}_\alpha$ are such that the condition

$$\mathrm{Tr}_E\{[\hat{H}_{SE}, \hat{\rho}(0) \otimes \hat{\mu}_R]\} = 0 \tag{2.12}$$

is satisfied. While this might seem a restrictive condition, it turns out to be broadly satisfied. Under these assumptions we obtain the still exact equation for the state of the system:

$$\frac{d}{dt}\hat{\rho}(t) = -\int_0^t ds\, \mathrm{Tr}_E\{[\hat{H}_{SE}(t), [\hat{H}_{SE}(s), \hat{\chi}(s)]]\}, \tag{2.13}$$

which is the basis of the approximate description that follows.

Born-Markov approximations. The *Born-Markov approximations* are two major approximations that lead to a time-local reduced description for the state of the system. However, notice that in the general case an extra approximation is needed for this equation to be of the Lindblad form. This is the *secular approximation* that will be introduced later [58]. The physical basis of these approximations resides on the following three general conditions [58, 59, 221, 222]; weak interaction between system and environment; the environment being constituted by a macroscopically large number of degrees of freedom; and a huge separation of timescales between system and environment dynamics. The latter condition means that the typical relaxation timescales of the environment, as characterized by τ_R, are much shorter than those of the dynamics of the system, as characterized by τ_S, i.e. $\tau_R \ll \tau_S$. We now proceed to show how making these approximations we can obtain a Lindblad master equation from Eq. (2.13).

The *Born approximation* exploits these conditions and assumes that the system essentially sees the bath in the reference state during all time evolution, i.e. that on the *relevant timescales* the environment has already re-equilibrated itself from the small perturbation caused by the system. Then, to leading order on the right-hand side of Eq. (2.13), the total state can be approximated as a product of the system state and the reference state of the environment: $\hat{\chi}(t) \approx \hat{\rho}(t) \otimes \hat{\mu}_R$. We then obtain the master equation in the Born approximation:

$$\frac{d}{dt}\hat{\rho}(t) = -\int_0^t ds\, \mathrm{Tr}_E\{[\hat{H}_{SE}(t), [\hat{H}_{SE}(s), \hat{\rho}(s) \otimes \hat{\mu}_R]]\}. \tag{2.14}$$

It is now convenient to work out the nested commutators. To do so, we first write in a more explicit fashion the system-environment Hamiltonian in the interaction picture. For this we write down the operators $\hat{A}_\alpha$ in terms of the eigenoperators of the system Hamiltonian[6]. These are defined as [58]:

$$\begin{gathered} \hat{A}_\alpha = \sum_\nu \hat{A}_\alpha(\nu), \quad [\hat{H}_S, \hat{A}_\alpha(\nu)] = \nu \hat{A}_\alpha(\nu), \\ [\hat{H}_S, \hat{A}_\alpha^\dagger(\nu)] = -\nu \hat{A}_\alpha^\dagger(\nu), \end{gathered} \tag{2.15}$$

which lead to:

$$\hat{H}_{SE}(t) = \sum_{\alpha,\nu} e^{-i\nu t} A_\alpha(\nu) \otimes \hat{B}_\alpha(t) = \sum_{\alpha,\nu} e^{i\nu t} A_\alpha^\dagger(\nu) \otimes \hat{B}_\alpha(t), \tag{2.16}$$

[6]This can always be done for systems residing in a finite Hilbert space or for systems described by quadratic Hamiltonians.

where the second equality is just a re-statement of the identity $\hat{A}^\dagger_\alpha(\nu) = \hat{A}_\alpha(-\nu)$ [58]. Inserting this expression into the Born master equation, developing the nested commutators, and performing the change of variables $s = t - \tau$, we arrive at:

$$\begin{aligned}\frac{d}{dt}\hat{\rho}(t) = \sum_{\alpha,\alpha'}\sum_{\nu,\nu'} e^{i(\nu-\nu')t}\int_0^t d\tau\big(\hat{A}_{\alpha'}(\nu')\hat{\rho}(t-\tau)\hat{A}^\dagger_\alpha(\nu) \\ -\hat{A}^\dagger_\alpha(\nu)\hat{A}_{\alpha'}(\nu')\hat{\rho}(t-\tau)\big)e^{i\nu'\tau}\langle\hat{B}^\dagger_\alpha(\tau)\hat{B}_{\alpha'}(0)\rangle_R + H.c.,\end{aligned} \tag{2.17}$$

where $H.c.$ stands for Hermitian conjugate and we have defined the environment two-time correlation functions:

$$\langle\hat{B}^\dagger_\alpha(\tau)B_{\alpha'}(0)\rangle_R = \mathrm{Tr}_E\{\hat{B}^\dagger_\alpha(t)B_{\alpha'}(t-\tau)\hat{\mu}_R\} \tag{2.18}$$

which only depend on the time difference of the arguments, τ, since $\hat{\mu}_R$ is assumed to be an equilibrium state [59]. Notice that these correlation functions characterize the response of the environment to the weak perturbation caused by the interaction with the system, and contain all the effects of the environment on the system. We are now in a good position to perform the *Markov approximation*. This exploits the assumptions of weak coupling and huge separation of timescales. Hence, the characteristic timescale on which $\hat{\rho}(t)$ changes appreciably in the interaction picture is given by τ_S, which is much larger than τ_R, the relaxation timescale of the environment. Therefore, the correlations given in Eq. (2.18) are expected to be non-zero only for times of the order of $\sim \tau_R$ in which essentially $\rho(t-\tau) \approx \rho(t)$, resulting in a dynamics well-approximated by a time-local master equation. Then, we arrive at the Born-Markov master equation:

$$\begin{aligned}\frac{d}{dt}\hat{\rho}(t) = \sum_{\alpha,\alpha'}\sum_{\nu,\nu'} e^{i(\nu-\nu')t}\Gamma_{\alpha\alpha'}(\nu')\big(\hat{A}_{\alpha'}(\nu')\hat{\rho}(t)\hat{A}^\dagger_\alpha(\nu) \\ -\hat{A}^\dagger_\alpha(\nu)\hat{A}_{\alpha'}(\nu')\hat{\rho}(t)\big) + H.c.,\end{aligned} \tag{2.19}$$

with:

$$\Gamma_{\alpha\alpha'}(\nu') = \int_0^\infty d\tau e^{i\nu'\tau}\langle\hat{B}^\dagger_\alpha(\tau)B_{\alpha'}(0)\rangle_R, \tag{2.20}$$

where Eq. (2.20) are the Fourier transformed (by the resonant frequencies of the system) two-time correlations of the environment. Notice that in Eq. (2.20) we have extended the integration limit to infinity as on the considered timescale, $t \gg \tau_R$, these correlations are already vanishingly small.

In physical terms, the master equation in the Born-Markov approximations is essentially a coarse-grained description of the system dynamics on a timescale much larger than τ_R. For $t \sim \tau_S \gg \tau_R$, the dissipative dynamics of the system starts to be evident as captured by this equation, while the microscopic processes leading to such an irreversible dynamics and occurring on a timescale τ_R (as the spreading through the environment of the energy and information given by the system) are not resolved by this equation. Hence, the existence of such disparate timescales, $\tau_{R,S}$, enables a much simpler and tractable effective description for the dynamics of the degrees of freedom in which we are interested.

Secular approximation and Lindblad form. While Eq. (2.19) is local in time, it is not generally of the Lindblad form (2.1). To achieve a Lindblad master equation we usually need to perform the additional *secular approximation*, which neglects fast rotating terms, and it is thus accurate when

$$|\nu - \nu'|^{-1} \ll \tau_S, \quad \text{for all} \quad \nu \neq \nu'. \tag{2.21}$$

This approximation is very well justified in some of the paradigmatic quantum optical situations [59], in which is also known as the rotating wave approximation. However,

notice that for coupled multipartite systems, whether to perform and how to perform this secular approximation can, in some cases, require a more careful analysis of the specific physical situation [225, 226], a topic that has received a renowned interest recently in the quantum thermodynamics community [227, 228, 229]. Then, if condition (2.21) is satisfied we obtain after the secular approximation:

$$\frac{d}{dt}\hat{\rho}(t) = -i[\hat{H}_{LS}, \hat{\rho}(t)] + \sum_{\nu,\alpha,\alpha'} \gamma_{\alpha\alpha'}(\nu)\Big(\hat{A}_{\alpha'}(\nu)\hat{\rho}(t)\hat{A}^{\dagger}_{\alpha}(\nu) - \frac{1}{2}\{\hat{A}^{\dagger}_{\alpha}(\nu)\hat{A}_{\alpha'}(\nu), \hat{\rho}(t)\}\Big), \tag{2.22}$$

with

$$\hat{H}_{LS} = \sum_{\nu,\alpha,\alpha'} S_{\alpha\alpha'}(\nu)\hat{A}^{\dagger}_{\alpha}(\nu)\hat{A}_{\alpha'}(\nu), \tag{2.23}$$

and

$$\begin{aligned} \gamma_{\alpha\alpha'}(\nu) &= \Gamma_{\alpha\alpha'}(\nu) + \Gamma^{*}_{\alpha\alpha'}(\nu), \\ S_{\alpha\alpha'}(\nu) &= \frac{1}{2i}\Big(\Gamma_{\alpha\alpha'}(\nu) - \Gamma^{*}_{\alpha\alpha'}(\nu)\Big). \end{aligned} \tag{2.24}$$

Otherwise, when the condition (2.21) is not fully satisfied some other terms have to be kept, what is known as the partial secular approximation [225]. Notice that the matrix formed by the rates $\gamma_{\alpha\alpha'}(\nu)$ can be generally proved to be positive for an equilibrium environment [58] and thus Eq. (2.22) is of the Lindblad form. Moreover, the environment, besides causing dissipation and decoherence, also introduces coherent energy shifts and interactions in the system, as modeled by the Lamb-shift Hamiltonian defined in Eq. (2.23).

2.2.2 A harmonic oscillator coupled to a thermal bath

We consider this paradigmatic elementary example to illustrate the fundamental ideas introduced in the previous subsection. In particular, we consider an harmonic oscillator of frequency ω_0 coupled to an infinite set of bosonic modes at thermal equilibrium, $\hat{\mu}_R = \hat{\mu}_{th}$, which form a thermal bath. The Hamiltonian describing this situation reads ($\hbar = 1$):

$$\begin{aligned} &\hat{H}_S = \omega_0 \hat{a}^{\dagger}\hat{a}, \quad \hat{H}_E = \sum_k \omega_k \hat{b}^{\dagger}_k \hat{b}_k, \\ &\hat{H}_{SE} = \sum_k (\hat{a} + \hat{a}^{\dagger})(\lambda_k \hat{b}_k + \lambda^{*}_k \hat{b}^{\dagger}_k), \end{aligned} \tag{2.25}$$

where the $\hat{a}$ and the $\hat{b}_k$'s are the annihilation operators of the bosonic modes that constitute the system and the environment, respectively. This bosonic model describes accurately high-quality factor optical [59], microwave, and mechanical resonators [23], and thus it is of wide application in the field of quantum technologies.

We observe that the assumption to drop the contribution from the initial condition in the reduced von Neumann equation, Eq. (2.12), is satisfied in this case. Comparing Eq. (2.25) with Eq. (2.8) we identify the coupling operators $\hat{A}_1 = \hat{a} + \hat{a}^{\dagger}$ and $\hat{B}_1 = \sum_k (\lambda_k \hat{b}_k + \lambda^{*}_k \hat{b}^{\dagger}_k)$. Moreover, it is clear that the eigenoperators are $\hat{A}_1(\omega_0) = \hat{a}$ and $\hat{A}_1(-\omega_0) = \hat{a}^{\dagger}$, so that comparing with Eq. (2.19) we can establish the approximation to drop the fast rotating terms proportional to $e^{\pm i 2\omega_0 t}$. In high-quality factor resonators the frequency is much larger than the decay rates, i.e. $\omega_0 \tau_S \gg 1$, and thus these terms can be safely neglected. In some cases these timescales can be separated by more than six orders of magnitude, both in optical and mechanical resonators, as for instance in some modern optomechanical systems [23].

The following step is to compute the rates appearing in Eq. (2.22), starting with the dissipation rate:

$$\gamma_{11}(\nu) = \int_{-\infty}^{\infty} d\tau \sum_k |\lambda_k|^2 \left(\bar{n}_k e^{i(\nu+\omega_k)\tau} + (\bar{n}_k + 1) e^{i(\nu-\omega_k)\tau}\right) \tag{2.26}$$

where $\bar{n}_k$ is the thermal occupation number for a bosonic mode of frequency ω_k and temperature T. The two-time correlations for an equilibrium environment only depend on the difference of time-arguments, i.e. τ, as anticipated. Moreover, for an infinite environment we can consider the continuum limit of bath modes:

$$\sum_k |\lambda_k|^2 \to \int_0^{\infty} d\omega g(\omega) |\lambda(\omega)|^2. \tag{2.27}$$

Here we have introduced the *density of states* of the environment, $g(\omega)$, which corresponds to the density of bath modes in the frequency interval $[\omega, \omega + d\omega]$. It is customary to also define the *spectral density* [58, 230] $J(\omega) = g(\omega)|\lambda(\omega)|^2$, which joins the spectral information of the density of modes and of the system-environment coupling strength. This fundamental quantity characterizes the effects of the environment in certain energy range. Then, making use of the mathematical identity [59]:

$$\lim_{\tau\to\infty} \int_0^{\tau} d\tau e^{i(\omega+\nu)\tau} = \delta(\omega + \nu) + iP\frac{1}{\omega + \nu} \tag{2.28}$$

where the second term is the Principal part of the integral, we arrive at

$$\begin{aligned} \gamma_{11}(\omega_0) &= 2\pi J(\omega_0)\left(\bar{n}(\omega_0) + 1\right) \equiv \gamma(\bar{n} + 1), \\ \gamma_{11}(-\omega_0) &= 2\pi J(\omega_0)\bar{n}(\omega_0) \equiv \gamma\bar{n}, \end{aligned} \tag{2.29}$$

where $\bar{n}$ denotes the occupation number of a bosonic mode of frequency ω_0 and temperature T. Importantly, within the Born-Markov approximations these rates only depend on the environment modes resonant with the system, as encoded in $J(\omega_0)$.

It is important to mention that both phenomenological and microscopic descriptions of the spectral density can be found in the literature. A well known phenomenological model is the Ohmic spectral density, in which one assumes $J(\omega) \propto \omega$ for small frequencies together with a high-frequency cutoff [58, 230, 231], while the effects of super- and sub-Ohmic spectral densities ($J(\omega) \propto \omega^s$ for small ω with $s > 1$ or $s < 1$, respectively) have also been thoroughly analyzed [230, 231]. As for microscopic descriptions, a paradigmatic example is that of spontaneous emission for atoms in free space, in which by accounting for the free space continuum of electromagnetic modes one can derive the Einstein spontaneous emission rate [58, 59, 221]. Detailed microscopic descriptions are also important for novel platforms in which quantum systems are coupled to engineered environments as quantum dots [24] or atoms [16] coupled to photonic nanostructures, or optomechanical systems coupled to tailored photonic-phononic crystals [232, 233], in which these environments are designed to display some desired spectral properties.

We finally consider the Lamb-shift contribution, $\hat{H}_{LS}$. This leads to a frequency shift Δ which, in stark contrast to the dissipation rates, resolves the whole energy continuum and not only resonant terms:

$$\Delta = P \int_0^{\infty} d\omega J(\omega) \left(\frac{1}{\omega_0 - \omega} + \frac{1}{\omega_0 + \omega}\right). \tag{2.30}$$

Then, we arrive to the following master equation for the harmonic oscillator in the Schrödinger picture:

$$\frac{d}{dt}\hat{\rho} = -i[(\omega_0 + \Delta)\hat{a}^\dagger\hat{a}, \hat{\rho}] + \gamma\bar{n}\mathcal{D}[\hat{a}^\dagger]\hat{\rho} + \gamma(\bar{n} + 1)\mathcal{D}[\hat{a}]\hat{\rho}. \tag{2.31}$$

The last two terms describe the (thermally) stimulated absorption of quanta from the environment (proportional to $\bar{n}$), and the stimulated and spontaneous emission of quanta to the environment (proportional to $\bar{n}+1$). Finally, we recall that the frequency shift caused by the environment is usually reabsorbed in the definition of ω_0 (as we do in the rest of the chapter), which is then interpreted as the measurable frequency instead of the bare one of the (fictious) isolated harmonic oscillator.

2.3 From one to many dissipative units

In the previous sections we have introduced the Lindblad master equation as well as the main physical conditions under which such a description can arise, together with an elementary but important example of its application. When the dissipative system is made of several units the treatment is more complex and specific issues need to be taken into account. We first discuss the possibility of the units of a system to interact with the same environment or with independent ones. Indeed, as we will see in this thesis, this can have major consequences on the dynamics of the dissipative systems, as the emergence of superradiance/subradiance effects, or the possibility to protect collective degrees of freedom from dissipation and decoherence. We later discuss the fact that in coupled dissipative systems, under the appropriate conditions, a subsystem can be used to engineer a dissipative dynamics for another subsystem. This has the advantage that can lead to general master equations not constrained by the equilibrium properties of the environment. All these situations will be encountered in this thesis.

2.3.1 Common versus separate environments

In multipartite open systems the units of the system can be coupled to a common environment or to independent or separate environments, as illustrated in Fig. 2.1 (a), (b). For instance, two quantum dots can be embedded in the same photonic environment or into different ones [24], or two atoms can be optically trapped near the same waveguide or onto different ones [16]. These different situations lead to deeply different open system dynamics. In fact, a common environment can lead to collective dissipation, in which the jump operators $\hat{L}_\alpha$ involve several of these units, and thus the environment mediates an interaction between them enabling bath induced cooperative effects. In this sense, collective dissipation enables intriguing phenomena as decoherence free subspace and noiseless subsystems [104], generation of entanglement between the units of the system [109, 111, 234, 235], super- and subradiance [25, 27, 28, 90, 236, 237], quantum synchronization [65, 70, 98], or tailored multiphoton emission [238, 239], to name a few. In fact, some of these phenomena are studied in this thesis and hence they will be encountered in the forthcoming chapters. Then, the purpose of this subsection is to briefly introduce the signatures of common or separate environments on the structure of the Lindblad master equation, to show how the former can lead to environment-mediated coherent and incoherent interactions, as well as to briefly overview some of the paradigmatic and modern situations in which such collective dissipation can emerge.

We will illustrate these features in the most elementary case of a system made of two units, either coupled to a common environment or to separate ones. The system-environment interaction Hamiltonian for these two situations reads:

$$H_{SE} = \sum_\alpha \hat{A}_{\alpha,1} \otimes \hat{B}_{\alpha,1} + \sum_\alpha \hat{A}_{\alpha,2} \otimes \hat{B}_{\alpha,2}, \tag{2.32}$$

where $\hat{A}_{\alpha,j}$ correspond to operators α of the subsystems $j = 1, 2$. For separate environments, $\hat{B}_{\alpha,1}$ correspond to operators of the first environment, while similarly for $\hat{B}_{\alpha,2}$ and

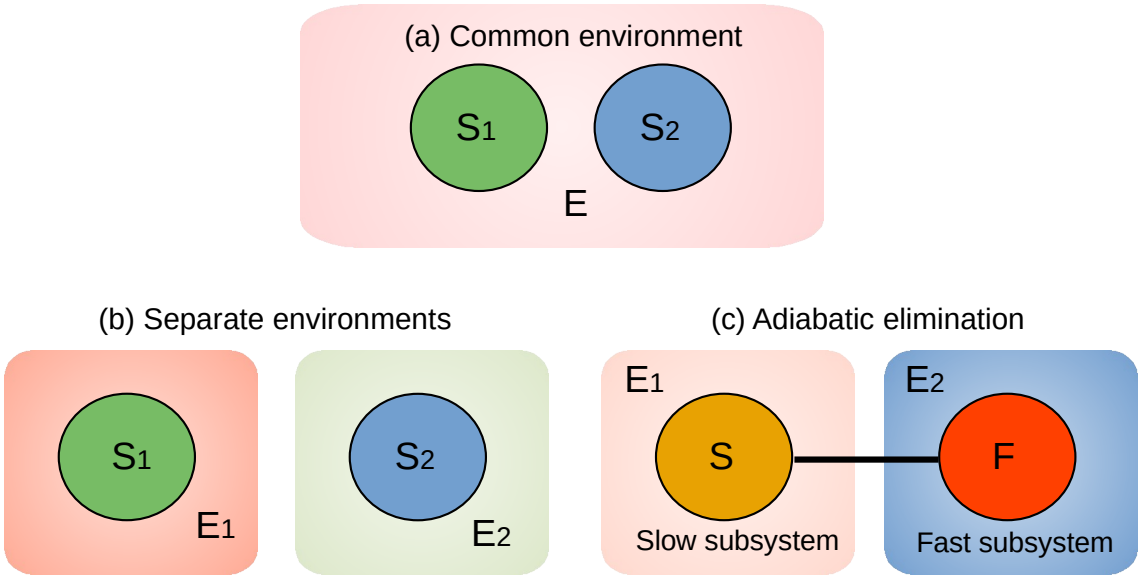

Figure 2.1: Scheme of the possible multipartite open quantum system scenarios that we consider. (a) Common environment scenario: two (or more) systems are coupled to the same environment and this induces incoherent and coherent couplings between them. This can happen when the distance between the systems is smaller than the characteristic correlation of the environment, $r \ll \xi$, or when coupling to an engineered environment as a photonic crystal (see Sect. 2.3.1). (b) Separate environments scenario: the systems are coupled to independent environments. This can correspond to physically different environments, as two different waveguides, but also to a common environment in which the separation between the systems is much larger than the environment correlation length, i.e. $r \gg \xi$ (see Sect. 2.3.1). (c) Adiabatic elimination of dissipative degrees of freedom: When coupling two (or more) dissipative systems, it can happen that one of them evolves much faster than the rest, to which it is weakly coupled. Then, the fast subsystem can be 'traced out' or adiabatically eliminated, leading to an effective dissipative dynamics for only the slow degrees of freedom (see Sect. 2.3.2). Examples of this situation are the optomechanical cooling master equation [251, 252] or collective dissipation of an atomic cloud induced by a common cavity mode [46].

the second environment. In contrast, for a common environment, $\hat{B}_{\alpha,j}$ correspond to operators of the same environment. In this case, we still use the label 'j' to account for possible differences in the way in which each subsystem is coupled to the environment. As an example, extending the case of Eq. (2.25) to two harmonic oscillators, the separate environment situation is described by:

$$\begin{aligned} \hat{H}_S &= \sum_{j=1,2} \omega_j \hat{a}_j^\dagger \hat{a}_j, \quad \hat{H}_{E,j} = \sum_k \omega_{j,k} \hat{b}_{j,k}^\dagger \hat{b}_{j,k}, \\ \hat{H}_{SE} &= \sum_{j=1,2} \sum_k (\hat{a}_j + \hat{a}_j^\dagger)(\lambda_{j,k} \hat{b}_{j,k} + \lambda_{j,k}^* \hat{b}_{j,k}^\dagger), \end{aligned} \tag{2.33}$$

while Eq. (2.33) can also describe the common environment situation if the bath operators, their frequency, and the system-environment coupling strength are made independent of j, i.e. $\omega_{j,k} = \omega_k$, $\lambda_{j,k} = \lambda_k$ and $\{\hat{b}_{j,k}, \hat{b}_{j,k}^\dagger\} = \{\hat{b}_k, \hat{b}_k^\dagger\}$.

In the Born-Markov approximations, the consequences of these two different situations are immediately appreciated on the Fourier transformed environment correlation functions. Hence, generalizing Eq. (2.20) to a multipartite system we obtain:

$$\Gamma_{\alpha,j;\beta,k}(\nu) = \int_0^\infty d\tau e^{i\nu\tau} \langle \hat{B}_{\alpha,j}^\dagger(\tau) B_{\beta,k}(0) \rangle_R. \tag{2.34}$$

For separate environments $\Gamma_{\alpha,j;\beta,k}(\nu) \propto \delta_{j,k}$, where $\delta_{j,k}$ is the Kronecker delta, as the two environments are independent of each other, and thus they cannot be correlated. On the other hand, for a common environment the Fourier transformed correlations can in

principle be non-zero for $j \neq k$, which can lead to cross-terms in the master equation as follows from the generalization of Eq. (2.22) to this multipartite case. In particular, in the secular approximation, incoherent interactions are encoded in the following terms of the multipartite master equation:

$$\sum_{\alpha,\beta,\nu} \gamma_{\alpha,1;\beta,2}(\nu)\big(\hat{A}_{\beta,2}(\nu)\hat{\rho}(t)\hat{A}^{\dagger}_{\alpha,1}(\nu) - \frac{1}{2}\{\hat{A}^{\dagger}_{\alpha,1}(\nu)\hat{A}_{\beta,2}(\nu), \hat{\rho}(t)\}\big) + H.c., \tag{2.35}$$

while coherent interactions in the following terms of the multipartite Lamb-shift Hamiltonian:

$$\sum_{\alpha,\beta,\nu} S_{\alpha,1;\beta,2}(\nu)\hat{A}^{\dagger}_{\alpha,1}(\nu)\hat{A}_{\beta,2}(\nu) + H.c. \tag{2.36}$$

where the rates $\gamma_{\alpha,j;\beta,k}(\nu)$ and $S_{\alpha,j;\beta,k}(\nu)$ are readily generalized from Eqs. (2.24) and (2.34). Hence, from Eq. (2.35) it follows that in a diagonal representation of the Lindblad master equation the jump operators will be generally collective.

These simple situations already illustrate that a common environment enables the possibility of environment-mediated interactions and hence collective dissipation, while separate environments do not. Interestingly, we remark that a common environment does not guarantee collective dissipation *per se*. Indeed, $\Gamma_{\alpha,1;\beta,2}(\nu)$ can generally depend on the distance between the two subsystems, as well as on the dimensionality and spectral characteristics of the environment. For isotropic two- and three-dimensional environments these cross-correlation functions decay with the distance r between the subsystems, and one can generally define a characteristic distance ξ such that for $r \ll \xi$ collective dissipation effects are significant, while for $r \gg \xi$ the subsystems essentially see independent environments[7] [240, 241, 242]. This is the case of atoms in free space, in which ξ corresponds to the wavelength of the electromagnetic modes resonant with the relevant atomic transition [242], and hence the cross-terms present for $r \ll \xi$ can lead to collective effects such as super- and subradiance [25, 90], while for $r \gg \xi$ the atoms essentially see independent or uncorrelated electromagnetic environments.

Anisotropic and engineered environments. This situation is significantly altered in presence of structured or anisotropic environments as well as in effectively one-dimensional environments. These cases have received a renewed interest as they play a major role for quantum systems interfaced with photonic and phononic crystals [16, 24, 233]. The distinct scenario emerging in anisotropic environments is well illustrated in Refs. [243, 244], in which it is shown that special 'crystal' directions can enable long-ranged coherent and dissipative interactions between quantum systems. Outstandingly, in one-dimensional environments the cross-correlations $\Gamma_{\alpha,1;\beta,2}(\nu)$ can even become periodic and non-decaying with the distance separating the system units [240, 241, 243, 244, 245], enabling long-range collective effects [16]. However, one must notice that the Lindblad description implicit in Eqs. (2.35) and (2.36) is no longer valid when the delay times due to the finite propagation velocity of excitations through the environment become appreciable (i.e. of the order of $\sim \tau_S$), eventually precluding a fully time-local Markovian description [244, 246, 247].

2.3.2 Adiabatic elimination of dissipative degrees of freedom

In coupled dissipative systems there is the possibility to engineer the dynamics of a subsystem by 'tracing out' another dissipative subsystem to which it is coupled, as illustrated in Fig. 2.1 (c). If the characteristic timescales of one of the dissipative subsystems are

[7] Thus a common environment situation in which $r \gg \xi$ can be *de facto* modeled as a separate environment situation in which each subsystem interacts with identical separate environments.

much shorter than those of the other subsystems, and the interaction between both is weak, one can actually obtain a reduced description only for the 'slow' subsystem. Indeed, on the relevant timescales of the slow subsystems, the fast subsystem essentially remains in its stationary state as its characteristic 're-equilibration' timescale is much shorter than those of the slow subsystem and of the weak coupling between them. This situation parallels the one we have met in the system-environment derivation of the Lindblad master equation, with the difference that in the present case the role of an environment is played by a dissipative subsystem.

In these conditions, 'tracing out' the fast dissipative subsystem leads to an effective dynamics for the slow subsystems alone. This effective dynamics might be described by a Lindblad master equation too, which can contain new Hamiltonian terms as well as new jump operators. This is generally known as *adiabatic elimination*[8] of the fast subsystem degrees of freedom, and provides an important route to engineer dissipative time evolutions and coherent dynamics that are not constrained by the properties of an equilibrium environment or a microscopic Hamiltonian.

Adiabatic elimination is the basis of paradigmatic phenomena such as ground state laser cooling of motional degrees of freedom of trapped ions [248, 249], polar molecules [250], or optomechanical oscillators [251, 252, 253, 254]; engineered two-level systems from driven multilevel systems [249, 255, 256]; or collective dissipation by adiabatic elimination of a cavity light (or microwave) mode [30, 29, 257, 258, 259]. Therefore, this situation is far from hypothetical and it is in fact found in many 'hybrid' quantum dissipative systems, in which the different units composing the system are of a different physical nature, as well as in driven multilevel scenarios.

The physical situation that we are considering can be schematically described as follows. The starting point is a multipartite dissipative system described by a Lindblad master equation in the Schrodinger picture:

$$\frac{d}{dt}\hat{\rho} = -i[\hat{H}_F(t) + \hat{H}_S + \hat{H}_{SF}, \hat{\rho}] + \sum_\alpha \gamma_{F,\alpha}\mathcal{D}[\hat{F}_\alpha]\hat{\rho} + \sum_\beta \gamma_{S,\beta}\mathcal{D}[\hat{S}_\beta]\hat{\rho}, \tag{2.37}$$

in which we have distinguished two subsystems: the fast subsystem, as described by $\hat{H}_F(t)$ and the jump operators $\hat{F}_\alpha$, and the slow subsystem as described by $\hat{H}_S$ and the jump operators $\hat{S}_\beta$, both weakly interacting through $\hat{H}_{SF}$. Notice that we have considered a time-dependent Hamiltonian for the fast subsystem, as it is often the case for these degrees of freedom to be driven, as for instance in Refs. [248, 251, 252, 255]. Then, adiabatically eliminating the fast subsystem leads to an effective master equation for the slow subsystem only:

$$\frac{d}{dt}\hat{\rho}_S = -i[\hat{H}_S + \hat{H}'_S, \hat{\rho}_S] + \sum_\beta \gamma_{S,\beta}\mathcal{D}[\hat{S}_\beta]\hat{\rho}_S + \sum_\beta \tilde{\gamma}_\beta\mathcal{D}[\hat{S}'_\beta]\hat{\rho}_S, \tag{2.38}$$

where $\hat{\rho}_S = \mathrm{Tr}_F[\hat{\rho}]$, and new coherent and incoherent processes are present in the dynamics, as modeled by $\hat{H}'_S$ and $\tilde{\gamma}_\beta\mathcal{D}[\hat{S}'_\beta]\hat{\rho}_S$, respectively. Notice that in many cases of interest, the rates characterizing the strength of these processes can be tuned *in situ* by varying the characteristics of an external driving source, as the frequency and intensity of an input laser [248, 251, 252, 255].

Optomechanical cooling. For a pedagogical example of this adiabatic elimination procedure, i.e. how to go from Eq. (2.37) to (2.38), we refer the reader to [260] in which the phenomenon of optomechanical cooling [23, 251, 252] is considered. There, the fast degrees

[8]This kind of situation is also found in classical (and semiclassical) stochastic dynamical systems in which elimination of fast variables receives the same name [59, 88].

of freedom correspond to a driven high-quality optical (or microwave) cavity mode, while the slow degrees of freedom correspond to a high-quality mechanical resonator. The resulting effective mechanical dynamics after adiabatically eliminating the optical degrees of freedom corresponds to a master equation with the same terms as the one of the harmonic oscillator coupled to a thermal bath, Eq. (2.31), i.e.:

$$\frac{d}{dt}\hat{\rho} = -i[(\omega_0 + \Delta + \Delta_{om})\hat{a}^\dagger\hat{a}, \hat{\rho}] + [\gamma\bar{n} + \gamma_\uparrow]\mathcal{D}[\hat{a}^\dagger]\hat{\rho} + [\gamma(\bar{n}+1) + \gamma_\downarrow]\mathcal{D}[\hat{a}]\hat{\rho}, \tag{2.39}$$

with the important difference that the rates of phonon emission and absorption are modified by the optically tunable ones, $\gamma_{\uparrow,\downarrow}$, enabling ground state laser cooling of the mechanical resonator when $\gamma_\downarrow \gg \gamma_\uparrow, \gamma\bar{n}$ [251, 252, 253, 254], while an optically tunable frequency renormalization term is also present, Δ_{om}, an effect known as the 'optical-spring effect' [23]. As a more mathematical remark, adiabatic elimination often makes use of the powerful projector operator techniques, e.g. [248, 250, 256, 260], which can also be applied to derive the Lindblad master equation in the system plus environment approach [58, 60, 222].

We finally overview some relevant examples of engineered dissipative time evolutions by adiabatic elimination of degrees of freedom. Besides the optically tunable master equation for a bosonic mode (2.39), optomechanical systems [23] constitute a versatile platform for the implementation of engineered time evolutions. In arrays of optomechanical oscillators, optical modes shared by various mechanical modes can be adiabatically eliminated leading to optically tunable coherent and incoherent interactions between the mechanical modes [261]. Indeed, these optically mediated interactions can be used to implement tight-binding bosonic lattices with synthetic Gauge fields leading to topological and non-reciprocal phenomena [262, 263]. Moreover, the effective mechanical dynamics can also be engineered to be non-linear, providing a route to implement parametric oscillators [152], or van der Pol oscillators [68, 70, 166]. Finally, adiabatic elimination of a common dissipative bosonic mode is a well known route to implement collective dissipation in spin systems. This is the case of atoms and ions trapped in an optical cavity[46, 257, 258, 259, 264], superconducting qubits coupled to a common microwave cavity [29], or silicon vacancy centers in a diamond nanophotonic cavity [30]. Complementarily, multilevel systems can be adiabatically eliminated to engineer the dissipative dynamics of bosonic modes, as in laser cooling of trapped ions [248, 249], or the implementation of van der Pol oscillators with trapped ions [67], as in laser-cooling of polar molecules [250], or tunable dissipation in one-dimensional lattices of trapped atoms [265].

In this thesis, we will find that adiabatic elimination is at the basis of some of the models that will be studied. In fact, in chapter 5 synchronization will be studied in an effective highly tunable spin system with local dissipation, which can be implemented in an atomic lattice adiabatically eliminating high-energy configurations and implementing laser cooling schemes [265]. Furthermore, in chapters 6 and 7, the quantum van der Pol oscillator will be studied, which, as we have mentioned, it can be implemented in platforms of trapped ions [67] or optomechanical oscillators [68] adiabatically eliminating the internal electronic dynamics or the optical degrees of freedom, respectively.

2.4 Dynamics of expectation values

Having already introduced the Lindblad master equation and some of the microscopic situations in which such a description for dissipative quantum systems can emerge, we now consider how to obtain from it equations for the time evolution of expectation values of system operators and multi-time correlations, as these represent the main indicators to assess the quantum system dynamics.

2.4.1 One-time expectation values

The expectation values of system operators at a given time describe the ensemble averaged observed dynamics of a system. These can be computed from the state of a system at a given time as [58]:

$$\langle \hat{O}(t) \rangle = \mathrm{Tr}[\hat{O}\hat{\rho}(t)], \tag{2.40}$$

where $\hat{O}$ denotes a system operator. From the Lindblad master equation one can obtain the state of the system at any time, from which the expectation values for system operators can be computed. Alternatively, one is sometimes interested in just a particular set of system operators, and thus it might be simpler and more practical to derive and solve the equations for the time evolution of just this set of expectation values. This can be done by simply taking the time derivative of the previous Schrödinger picture formula:

$$\frac{d}{dt}\langle \hat{O}(t) \rangle = \mathrm{Tr}[\hat{O}\frac{d}{dt}\hat{\rho}(t)]. \tag{2.41}$$

Inserting the Lindblad master equation on the right-hand side produces the desired equations of motion for the system expectation values. The advantage of this procedure is that it can lead, in some cases, to a closed set of first-order differential equations. However, in some other cases it can lead to an infinite hierarchy of equations.

Let us illustrate this with the simple example of the harmonic oscillator coupled a thermal bath as described by the master equation (2.31). In order to obtain equations for expectation values from Eq. (2.41) we just have to make use of the commutation relation $[\hat{a}, \hat{a}^\dagger] = 1$ and the cyclic property of the trace. Then, the equation of motion for $\langle \hat{a}(t) \rangle$ is obtained as follows:

$$\begin{aligned}
\frac{d}{dt}\langle \hat{a}(t) \rangle = & -i\omega_0 \mathrm{Tr}[\hat{a}\hat{a}^\dagger\hat{a}\hat{\rho}(t) - \hat{a}\hat{\rho}(t)\hat{a}^\dagger\hat{a}] \\
& + \gamma\bar{n}\mathrm{Tr}[\hat{a}\hat{a}^\dagger\hat{\rho}(t)\hat{a} - \frac{1}{2}(\hat{a}\hat{a}\hat{a}^\dagger\hat{\rho}(t) + \hat{a}\hat{\rho}(t)\hat{a}\hat{a}^\dagger)] \\
& + \gamma(\bar{n}+1)\mathrm{Tr}[\hat{a}\hat{a}\hat{\rho}(t)\hat{a}^\dagger - \frac{1}{2}(\hat{a}\hat{a}^\dagger\hat{a}\hat{\rho}(t) + \hat{a}\hat{\rho}(t)\hat{a}^\dagger\hat{a})] \\
= & -i\omega_0\langle \hat{a}(t) \rangle - \frac{\gamma}{2}\langle \hat{a}(t) \rangle,
\end{aligned} \tag{2.42}$$

which we recognize as the equation for the amplitude of a damped cavity or resonator [9]. We can similarly obtain the equation for the number of excitations, $\hat{n} = \hat{a}^\dagger\hat{a}$, which reads:

$$\frac{d}{dt}\langle \hat{n}(t) \rangle = -\gamma\langle \hat{n}(t) \rangle + \gamma\bar{n}, \tag{2.43}$$

from which we see that in the long-time limit the system equilibrates with the bath, displaying the thermal occupation number $\langle \hat{n} \rangle_{ss} = \bar{n}$ with

$$\langle \hat{n} \rangle_{ss} = \lim_{t\to\infty}\langle \hat{n}(t) \rangle. \tag{2.44}$$

The point is that we obtained closed sets of equations for the system expectation values as the time evolution described by Eq. (2.31) is quadratic or bilinear in the bosonic creation and annihilation operators [266, 267], that we can readily solve without need to explicitly find the solution $\hat{\rho}(t)$.

[9] Notice that we have reabsorbed the Lamb shift into the definition of the frequency.

2.4.2 Two-time correlations

Two-time correlations, and multi-time correlations in general, are some of the fundamental quantities characterizing the dynamics of quantum systems. In fact, in some contexts as quantum optics, multi-time correlations are useful quantities that one can experimentally access [59], and which can unveil the statistical differences in the light emitted from a quantum source from that emitted from a classical one [59, 221]. Thus, it is of utmost importance to have a method to compute them from the Lindblad master equation.

In this thesis we will encounter multi-time correlations of the type

$$\langle \hat{O}_1(t)\hat{O}_2(s)\rangle, \tag{2.45}$$

which consist in the expectation value of two operators at two different times. Then, the immediate question that arises is whether we can actually compute such a quantity from the state of the system at a single time and the Lindblad master equation which also involves just a single time. The answer is affirmative [58, 59, 221], and multi-time correlations can be computed just in terms of the state of the system and the master equation, *within the same Born-Markov approximations* that lead to the Lindblad master equation[10].

General formulas for two-time correlations. For the two-time correlations of the type (2.45) we can distinguish two cases: the one in which $s \geq t$ and the one in which $s < t$, for which different formulas are derived. For convenience, we set the time difference to the value τ, with $\tau \geq 0$. We then have two possible results [59]:

$$\begin{aligned} \langle \hat{O}_1(t)\hat{O}_2(t+\tau)\rangle &= \mathrm{Tr}\big[\hat{O}_2 e^{\mathcal{L}\tau}\big(\hat{\rho}(t)\hat{O}_1\big)\big], \\ \langle \hat{O}_1(t+\tau)\hat{O}_2(t)\rangle &= \mathrm{Tr}\big[\hat{O}_1 e^{\mathcal{L}\tau}\big(\hat{O}_2\hat{\rho}(t)\big)\big]. \end{aligned} \tag{2.46}$$

The superoperator $e^{\mathcal{L}\tau}$ applies to everything into the big rounded parenthesis, and it stands for time-evolving for a period of time τ and according to $\mathcal{L}$ the "initial condition" inside the parenthesis. Reading Eq. (2.46) we identify the following steps: compute the state at time t, apply the corresponding operator in the correct order, time-evolve the result for a period τ using the master equation, and finally use the time-evolved result to compute the expectation value including the other operator.

The quantum regression theorem. A particular but important case is that for which there exist a particular set of system operators whose equations of motion for the single-time expectation values form a closed system [59]. In particular, let us assume that we have a set of system operators denoted by $\hat{A}_j$ with $j = 1, 2, \ldots, m$, such that their closed system of equations of motion for their expectation values can be written as:

$$\frac{d}{dt}\langle \hat{A}_j(t)\rangle = \sum_{k=1}^{m} M_{jk}\langle \hat{A}_k(t)\rangle, \tag{2.47}$$

where M_{jk} are the coefficients defining the dynamical system. This system of equations can be rewritten in matrix form by defining the m-dimensional vector $\vec{A}(t)$ and the corresponding square matrix $\mathbf{M}$ whose entries are the coefficients M_{jk}:

$$\frac{d}{dt}\langle \vec{A}(t)\rangle = \mathbf{M}\langle \vec{A}(t)\rangle. \tag{2.48}$$

[10] For a pedagogical derivation of this result the reader is referred to the book by Carmichael [59].

Then, as shown in Ref. [59], the two-time correlations $\langle \hat{O}(t)\vec{A}(t+\tau)\rangle$ and $\langle \vec{A}(t+\tau)\hat{O}(t)\rangle$, where $\hat{O}$ can be any system operator, obey the following system of equations:

$$\begin{aligned} \frac{d}{d\tau}\langle \hat{O}(t)\vec{A}(t+\tau)\rangle &= \mathbf{M}\langle \hat{O}(t)\vec{A}(t+\tau)\rangle, \\ \frac{d}{d\tau}\langle \vec{A}(t+\tau)\hat{O}(t)\rangle &= \mathbf{M}\langle \vec{A}(t+\tau)\hat{O}(t)\rangle. \end{aligned} \tag{2.49}$$

This means that the dynamics of two-time correlations in this particular circumstances corresponds essentially to the dynamics of single-time expectation values with a particular fixed initial condition, as given by $\langle \vec{A}(t)\hat{O}(t)\rangle = \mathrm{Tr}[\vec{A}\hat{O}\hat{\rho}(t)]$ or by $\langle \hat{O}(t)\vec{A}(t)\rangle = \mathrm{Tr}[\hat{O}\vec{A}\hat{\rho}(t)]$. This is the basic statement of the *quantum regression theorem* [88].

As an elementary example of the application of the quantum regression theorem, let us consider again the case of the harmonic oscillator coupled to a thermal bath. Moreover, let us analyze the stationary amplitude two-time correlation $\langle \hat{a}^\dagger(0)\hat{a}(\tau)\rangle_{ss} = \lim_{t\to\infty} = \langle \hat{a}^\dagger(t)\hat{a}(t+\tau)\rangle$, where '0' denotes an arbitrary time-origin in the stationary state of the system. Then, applying the above results we see that $m = 1$ and $\hat{A}_1 = \hat{a}$ while $M_{11} = -i\omega_0 - \gamma/2$. Hence:

$$\frac{d}{dt}\langle \hat{a}^\dagger(0)\hat{a}(\tau)\rangle_{ss} = -\big(i\omega_0 + \frac{\gamma}{2}\big)\langle \hat{a}^\dagger(0)\hat{a}(\tau)\rangle_{ss}, \tag{2.50}$$

which results in:

$$\langle \hat{a}^\dagger(0)\hat{a}(\tau)\rangle_{ss} = \bar{n}e^{-i\omega\tau-\frac{\gamma}{2}\tau} \tag{2.51}$$

as follows from integrating the equation of motion with the initial condition $\langle \hat{n}\rangle_{ss} = \bar{n}$. This is a very simple illustration of our previous statement that in these conditions two-time correlations follow the dynamics of single-time expectation values with a particular initial condition. Notice that a more involved example of the application of Eq. (2.49) will be met in chapter 4 in which arrays of quantum harmonic oscillators are studied.

As we will see, two-time correlations play a relevant role in this thesis, and we will meet them in most of the following chapters. Their importance resides in the fact that we can use them to characterize the collective modes governing the dynamics of a system and thus, they can be useful indicators for the emergence of synchronization and other dynamical phenomena.

2.5 The Liouvillian approach

In this section we introduce some powerful techniques to study the dynamics of a system based on the spectral decomposition of the Liouvillian. As we shall see, the eigenspectrum of the Liouvillian provides a complete picture of the characteristic timescales and frequencies of the system, and hence, when applicable, provides important insights on the behavior of a system. In the following subsections we introduce the main theoretical formulas that we will apply in some of the forthcoming chapters.

2.5.1 Spectral properties of the Liouvillian

The Liouvillian superoperator maps operators to other operators as defined in Eq. (2.4). In this sense, we can find eigenoperators (also called eigenmatrices or eigenmodes) that are invariant up to a complex constant, i.e. the eigenvalue, to the action of this superoperator. The set of right and left eigenmatrices as well as the corresponding eigenvalues constitute the eigenspectrum of the Liouvillian. These are defined as:

$$\mathcal{L}\hat{\rho}_j = \lambda_j\hat{\rho}_j, \quad \mathcal{L}^\dagger\hat{\sigma}_j = \lambda_j^*\hat{\sigma}_j, \tag{2.52}$$

where λ_j is the eigenvalue corresponding to the right (left) eigenmatrix $\hat{\rho}_j$ ($\hat{\sigma}_j^\dagger$). Since the Liouvillian is non-Hermitian, i.e. $\mathcal{L} \neq \mathcal{L}^\dagger$, right and left eigenmatrices are generally different. Importantly, for time-independent Liouvillians and for finite-dimensional Hilbert spaces, it can be shown that the system has at least one stationary state, $\hat{\rho}_{ss}$, that satisfies $\mathcal{L}\hat{\rho}_{ss} = 0$. That is, it corresponds to a right eigenmatrix of the Liouvillian with zero eigenvalue [35, 268]. While for infinite-dimensional systems (as bosonic ones) the existence of such stationary state is not guaranteed, it does usually exist, and this is certainly the case for the systems considered in this thesis (i.e. arrays of harmonic oscillators and the quantum van der Pol oscillator).

If the Liouvillian is diagonalizable, that is away from possible exceptional points [35, 208, 268] (defined in Sect. 1.3), its set of right and left eigenoperators form a complete basis of the system's Hilbert space that can be used to decompose any system operator [35, 268]. In particular, the right and left eigenmatrices form a biorthogonal basis that can be normalized such that $\mathrm{Tr}[\hat{\sigma}_j^\dagger \hat{\rho}_k] = \delta_{jk}$. This can be used to decompose the state of the system at any time in terms of the Liouvillian eigenspectrum [35, 268]:

$$\hat{\rho}(t) = \sum_j \mathrm{Tr}[\hat{\sigma}_j^\dagger \hat{\rho}(0)] \hat{\rho}_j e^{\lambda_j t} \tag{2.53}$$

where j runs over all the eigenvalues. This formula follows from the formal solution of the master equation, $\hat{\rho}(t) = e^{\mathcal{L}t}\hat{\rho}(0)$, from the fact that when considering eigenmatrices $e^{\mathcal{L}t}\hat{\rho}_j = e^{\lambda_j t}\hat{\rho}_j$, and the mentioned biorthogonality of the eigenmatrices.

Properties of the eigenspectrum. From Eq. 2.53 it is clear that a number of properties of the Liouvillian eigenspectrum follow directly from the properties of the master equation [35, 268]:

i) The eigenvalues are non-positive, i.e. their real part is either negative or zero: $\mathrm{Re}[\lambda_j] \leq 0 \ \forall j$. Physically, this property prevents Eq. (2.53) to diverge exponentially with time. Moreover, it is customary to order the eigenvalues according to their real part such that $\mathrm{Re}[\lambda_0] \geq \mathrm{Re}[\lambda_1] \geq \mathrm{Re}[\lambda_2] \geq \ldots$ In which case there is a stationary state that corresponds to the zero-eigenmatrix: $\lambda_0 = 0$, $\hat{\rho}_{ss} = \hat{\rho}_0/\mathrm{Tr}[\hat{\rho}_0]$, and $\hat{\sigma}_0 = \mathbb{1}$, where $\mathbb{1}$ is the identity matrix.

ii) The eigenvalues λ_j are either real or appear in complex conjugate pairs, as follows from the fact that the master equation is Hermiticity preserving [35, 268]. Moreover, for a real eigenvalue, the right and left eigenmatrices can be constructed to be Hermitian [35]. Instead, for a complex conjugate pair of eigenvalues $\lambda_j = \lambda_k^*$, the corresponding eigenmatrices are Hermitian conjugates of each other $\hat{\rho}_j = \hat{\rho}_k^\dagger$ and $\hat{\sigma}_j = \hat{\sigma}_k^\dagger$ [35].

iii) For eigenvalues with negative real part the eigenmatrices are traceless, as follows from the fact the master equation is trace preserving [35]. This last important property illustrates the fact that the eigenmatrices $\hat{\rho}_j$ do not need to be physical states (being $\hat{\rho}_{ss}$ a notable exception) keeping in mind, however, that in decompositions of the type of Eq. (2.53) they are combined in such a way to yield a physical state at all times.

Eigendecomposition of the dynamics. The usefulness of the Liouvillian eigendecomposition can be readily intuited from the state decomposition of Eq. (2.53), that we can recast as:

$$\hat{\rho}(t) = \hat{\rho}_{ss} + \sum_{j \geq 1} \mathrm{Tr}[\hat{\sigma}_j^\dagger \hat{\rho}(0)] \hat{\rho}_j e^{\lambda_j t}. \tag{2.54}$$

Hence, the eigenspectrum of the Liouvillian reveals how the system approaches its stationary state, as well as the different characteristic timescales of the dynamics, as encoded in the real part of the eigenvalues, or the possible oscillating frequencies, as encoded in the imaginary part of the eigenvalues. Furthermore, this can also be used to understand the dynamics of expectation values and multi-time correlations. Hence, from Eq. (2.54) we can straightforwardly obtain the expression for single-time expectation values:

$$\langle \hat{O}(t) \rangle = \langle \hat{O} \rangle_{ss} + \sum_{j \geq 1} \mathrm{Tr}[\hat{\sigma}_j^\dagger \hat{\rho}(0)] \mathrm{Tr}[\hat{O} \hat{\rho}_j] e^{\lambda_j t}, \tag{2.55}$$

while from Eq. (2.46) two-time correlations can also be obtained from the state decomposition of Eq. (2.53). Here we will focus on the most important case for this thesis which is that of two-time correlations in the stationary state, i.e.:

$$\begin{aligned} \langle \hat{O}_1(0) \hat{O}_2(\tau) \rangle_{ss} &= \lim_{t \to \infty} \langle \hat{O}_1(t) \hat{O}_2(t+\tau) \rangle, \\ \langle \hat{O}_1(\tau) \hat{O}_2(0) \rangle_{ss} &= \lim_{t \to \infty} \langle \hat{O}_1(t+\tau) \hat{O}_2(t) \rangle. \end{aligned} \tag{2.56}$$

Then, from Eqs. (2.46) and (2.53) we obtain:

$$\begin{aligned} \langle \hat{O}_1(0) \hat{O}_2(\tau) \rangle_{ss} &= \langle \hat{O}_1 \rangle_{ss} \langle \hat{O}_2 \rangle_{ss} + \sum_{j \geq 1} \mathrm{Tr}[\hat{\sigma}_j^\dagger \hat{\rho}_{ss} \hat{O}_1] \mathrm{Tr}[\hat{O}_2 \hat{\rho}_j] e^{\lambda_j \tau}, \\ \langle \hat{O}_1(\tau) \hat{O}_2(0) \rangle_{ss} &= \langle \hat{O}_1 \rangle_{ss} \langle \hat{O}_2 \rangle_{ss} + \sum_{j \geq 1} \mathrm{Tr}[\hat{\sigma}_j^\dagger \hat{O}_2 \hat{\rho}_{ss}] \mathrm{Tr}[\hat{O}_1 \hat{\rho}_j] e^{\lambda_j \tau}, \end{aligned} \tag{2.57}$$

which illustrate again the importance of operator ordering in two-time correlations. These results will be fundamental in the forthcoming chapters, when we will apply these formulas to understand the dynamics of the system in terms of the Liouvillian spectrum.

2.5.2 Matrix representation of the Liouvillian

In the previous subsection we have kept the discussion at the general level of operators and superoperators, while in practice one normally resorts on a particular matrix representation of the Liouvillian in order to perform calculations. Here, we present such a matrix representation for the Liouvillian superoperator, which is very useful for the calculation of its eigenspectrum either analytically or numerically.

In the matrix representation one works in an enlarged Hilbert space in which the density matrix is represented by a vector and the Liouvillian by a matrix. This implies that if the dimension of the system Hilbert space is D, the density matrix is represented by a D^2-dimensional vector and the Liouvillian is represented by a $D^2 \times D^2$ matrix. For this reason, a spectral analysis of the Liouvillian generally requires more computational resources than numerical integration of the master equation, which can ultimately hinder it. Nevertheless, as we shall see in the following chapters, such an spectral analysis provides important physical insights on the dynamics of quantum systems, which motivates the use of this technique.

The matrix representation of the Liouvillian is based on the following isomorphism in which the density matrix is mapped to a vector in an enlarged Hilbert space [35, 90, 268]:

$$\hat{\rho} = \sum_{i,j=1}^{D} \rho_{ij} |i\rangle\langle j| \leftrightarrow |\rho\rangle\!\rangle = \sum_{i,j=1}^{D} \rho_{ij} |ij\rangle\!\rangle, \tag{2.58}$$

with $|ij\rangle\!\rangle = |i\rangle \otimes |j\rangle$. In this enlarged space we use a "Bra-Ket" notation in which vectors are denoted by a "Ket" $|\cdot\rangle\!\rangle$, while the "Bra" $\langle\!\langle\cdot|$ corresponds to their Hermitian conjugate partners. Then, it follows that the action of operators on the density matrix maps as:

$$\hat{O}_1 \hat{\rho} \hat{O}_2 \leftrightarrow (\hat{O}_1 \otimes \hat{O}_2^\intercal) |\rho\rangle\!\rangle, \tag{2.59}$$

where $\hat{O}^\top = (\hat{O}^\dagger)^*$, i.e. it denotes the transpose of an operator. Moreover, the "Bra-Ket" product in the enlarged space corresponds to:

$$\mathrm{Tr}[\hat{O}_2^\dagger \hat{O}_1] \leftrightarrow \langle\langle O_2 | O_1 \rangle\rangle, \tag{2.60}$$

Making use of this isomorphism the Lindblad master equation (2.2) can be written in matrix form in the enlarged Hilbert space:

$$\frac{d}{dt}|\rho\rangle\rangle = \bar{\bar{\mathcal{L}}}|\rho\rangle\rangle, \tag{2.61}$$

where the matrix representation of the Liouvillian is denoted by $\bar{\bar{\mathcal{L}}}$ and reads:

$$\bar{\bar{\mathcal{L}}} = -i(\hat{H} \otimes \mathbb{1} - \mathbb{1} \otimes \hat{H}^\top) + \sum_{j=1}^{M} \gamma_j \Big(\hat{L}_j \otimes \hat{L}_j^* - \frac{1}{2}[\hat{L}_j^\dagger \hat{L}_j \otimes \mathbb{1} + \mathbb{1} \otimes \hat{L}_j^\top \hat{L}_j^*] \Big). \tag{2.62}$$

Now that we have represented the Liouvillian by a matrix, it is clear that the eigenoperators presented in the previous subsection correspond to the right and left eigenvectors of a non-Hermitian matrix:

$$\bar{\bar{\mathcal{L}}}|\rho_j\rangle\rangle = \lambda_j |\rho_j\rangle\rangle, \quad \bar{\bar{\mathcal{L}}}^\dagger |\sigma_j\rangle\rangle = \lambda_j^* |\sigma_j\rangle\rangle, \tag{2.63}$$

and thus standard matrix methods can be used to obtain them. Away from EPs, these vectors form a biorthogonal basis $\langle\langle \sigma_j | \rho_k \rangle\rangle = \delta_{jk}$ which can be used to write the state decomposition of Eq. (2.54) and the equations for the expectation values and two-time correlations of Eqs. (2.55) and (2.57) in a vectorized form (see for instance [90, 268]).

This approach applies to finite-dimensional systems. Then, an important question is what happens with infinite-dimensional bosonic systems. In this case, numerical techniques are generally based on truncation of the number of considered states. With the exception of some particular cases, as when one deals with Gaussian states and quadratic Lindblad master equations [266, 267]. Away from these cases, truncation of the Hilbert space to a finite dimension D_T allows one to represent the Liouvillian with a $D_T^2 \times D_T^2$ matrix and the density matrix with a D_T^2-dimensional vector. Then, the above results apply, but are only valid if they are convergent with the considered truncation dimension D_T, i.e. if the truncated Hilbert space is large enough so that it does not affect the physics of the system. This can be checked considering a larger truncation dimension, i.e. $D_T' > D_T$, to establish that results in both cases converge.

2.5.3 Symmetries of the Liouvillian

The Lindblad master equation describing the dynamics of a dissipative system can display symmetries [35, 268]. A Liouvillian symmetry is defined by a unitary transformation, $\mathcal{U}\hat{\rho} = \hat{U}\hat{\rho}\hat{U}^{-1}$, whose action commutes with that of the Liouvillian:

$$[\mathcal{U}, \mathcal{L}]\hat{\rho} = 0. \tag{2.64}$$

As we will see, these symmetries introduce particular constraints in the dynamics generated by the Liouvillian. Thus, identifying and characterizing the symmetries of a dissipative system can provide important insights about the dynamics and the properties of the system. In stark contrast with the Hamiltonian case, the symmetries of the Liouvillian do not need to be accompanied by conserved quantities (i.e. Noether's theorem does not apply), as discussed in detail in Ref. [268].

A first fundamental consequence of the Liouvillian displaying a symmetry is that its eigenmatrices inherit this symmetry [35, 268]. Then, if $\hat{U}$ has a set of eigenvalues or

symmetry sectors u, each of the Liouvillian eigenmatrices must belong to one of these symmetry sectors, i.e.:

$$\mathcal{U}\hat{\rho}_j = u_j\hat{\rho}_j \tag{2.65}$$

where $u_j \in u$, i.e. it takes one of the possible values of the possible set of symmetry eigenvalues. Moreover, as the symmetry corresponds to a unitary transformation, there must be an eigenvalue that takes the value 1, and the stationary state of the system must belong to this symmetry sector since it has unit trace, as can be seen by inserting $\hat{\rho}_{ss}$ in Eq. (2.65) and taking the trace. Furthermore, from Eq. (2.64) it also follows that the Liouvillian displays a direct sum structure:

$$\mathcal{L} = \bigoplus_u \mathcal{L}_u \tag{2.66}$$

and thus the different symmetry sectors are not coupled by the dynamics of the system [35, 268, 269]. In a matrix representation of the Liouvillian this structure makes the Liouvillian to be a block-diagonal matrix, in which each block corresponds to a symmetry sector, and thus it does not couple different parts of the state vector. Notice that this can be used to reduce significantly the computational resources needed for studying numerically quantum dissipative systems, as it is the case for spin systems displaying permutation symmetry [35, 270].

Dissipative harmonic oscillator and U(1) symmetry. We now exemplify these results considering the simple case of the harmonic oscillator coupled to a thermal bath. This system displays a $U(1)$ symmetry defined by the unitary transformation

$$\mathcal{U}_\phi\hat{\rho} = e^{-i\phi\hat{a}^\dagger\hat{a}}\hat{\rho}e^{i\phi\hat{a}^\dagger\hat{a}} \tag{2.67}$$

for any real ϕ [168]. Notice that this unitary transformation acts as

$$\mathcal{U}_\phi(\hat{a}^\dagger)^l\hat{a}^m = e^{i\phi(m-l)}(\hat{a}^\dagger)^l\hat{a}^m \tag{2.68}$$

on the system operators, which can be used to check that the master equation (2.31) is indeed invariant under such a transformation, i.e. $[\mathcal{U}_\phi, \mathcal{L}]\hat{\rho} = 0$. Then, the Liouvillian eigenmatrices are also eigenmatrices of this unitary transformation, $\mathcal{U}_\phi\hat{\rho}_j = u_j\hat{\rho}_j$, and the Liouvillian is block-diagonal in the different symmetry sectors. In fact, as shown in Ref. [168], due to this symmetry, the eigenmatrices take the following general form in the Fock basis:

$$\hat{\rho}_j = \sum_n C_n^{(j)}|n\rangle\langle n-k|, \tag{2.69}$$

where k is an integer and $C_n^{(j)}$ are complex coefficients. Then, the particular value of k determines the symmetry sector to which the eigenmode belongs, as $\mathcal{U}_\phi\hat{\rho}_j = e^{-i\phi k}\hat{\rho}_j$. Furthermore, the stationary state belongs to the $k = 0$ sector which corresponds to the eigenvalue one, and it is thus diagonal in the Fock basis.

Another consequence of this symmetry is that the contribution to the dynamics of an observable from eigenmodes that belong to a different symmetry eigensector vanish identically. This means that, since the operators satisfy Eq. (2.68), only eigenmatrices of the sector $k = m - l$ contribute to the dynamics of this operator. This can also be deduced using the general form (2.69) from which it is clear that a necessary condition for $\mathrm{Tr}[(\hat{a}^\dagger)^l\hat{a}^m\hat{\rho}_j] \neq 0$ is that $k = m - l$. Formally, we can write

$$\langle(\hat{a}^\dagger)^l\hat{a}^m(t)\rangle = \sum_{j\in u_k}\mathrm{Tr}[\hat{\sigma}_j^\dagger\hat{\rho}(0)]\mathrm{Tr}[(\hat{a}^\dagger)^l\hat{a}^m\hat{\rho}_j]e^{\lambda_j t}, \tag{2.70}$$

where $j \in u_k$ means that the sum is restricted to the eigenmodes of the symmetry sector $k = m - l$. This tells us that the dynamics of operators of different symmetry sectors can not be coupled. Moreover, we see that only the operators belonging to the symmetry sector $k = 0$ can display a non-zero stationary value: this is in agreement with our previous results in which we have found the $\langle \hat{a} \rangle_{ss} = 0$ while $\langle \hat{n} \rangle_{ss} = \bar{n}$. Therefore, this elementary example already illustrates how the presence of a symmetry in the Liouvillian constrains the dynamics of the system, and how with symmetry considerations one can deduce some of the characteristic features of the dynamics of the system [168, 268].

As introduced in Sect. 1.2, the symmetries of a model can be spontaneously broken in the thermodynamic and infinite-excitation limits when, for instance, a dissipative phase transition occurs. Then, despite the quantum model described by a $\mathcal{L}$ displays a symmetry, one can find that in these limits stable solutions do not respect it. This will be illustrated in chapter 7, in which we will analyze spontaneous symmetry breaking phenomena occurring in the quantum van der Pol oscillator.

PART II

Collective phenomena in coupled dissipative systems

CHAPTER 3

Synchronization and noiseless clusters in complex quantum networks

The contents of this chapter have been adapted from the works entitled *Unveiling noiseless clusters in complex quantum networks* [2] and *Transient synchronization in open quantum systems* [5]. The main results presented here are concerned with the presence of noiseless modes and synchronization in complex networks of harmonic oscillators dissipating into a common environment. The main goal is to assess the effects of complex topologies on the abundance and characteristics of these collective modes, either effectively decoupled from the environment (i.e. noiseless), or that synchronize the system (slow relaxing modes). First we introduce the basic case of two harmonic oscillators dissipating either into a common or into separate environments [5]. This pedagogical example will enable us to introduce some of the basic physics of transient synchronization and noiseless modes before addressing the complex extended networks of Ref. [2].

3.1 Introduction

Noiseless modes and synchronization in complex scenarios. The emergence of synchronization and the presence of noiseless modes are two examples of intriguing phenomena enabled by collective dissipation. Noiseless modes and DFSs are collective degrees of freedom that are effectively uncoupled from the environment and have been reported for few-body and highly symmetric systems coupled to a common environment, as systems of few harmonic oscillators [101, 110, 111, 271], or few qubits [105, 108, 109, 234]. Indeed, it was commonly believed that such a symmetric scenario, e.g. similar frequencies and fine-tuned couplings or geometries [101], was necessary for the presence of such modes or subspaces effectively decoupled from the environment. In this sense, a fundamental question was whether these noiseless modes and DFSs could be present in more *complex scenarios*, as systems with disordered topologies or with random parameter values. For synchronization induced by collective dissipation more complex arrays were reported in

Ref. [98]. Still, the resilience of this phenomenon to such topological complexity and parameter disorder was not addressed. These questions are at the heart of the analysis presented in the following sections and a main motivation for the work reported in Ref. [2].

Complex quantum networks. Complex networks provide a rich playground in which to explore the effects of a non-trivial topological structure on dynamical phenomena, moving beyond the scenarios of regular lattices or all-to-all interactions [272]. In the past decades, they have been intensively studied in very diverse scientific disciplines ranging from ecology, economics and socio-technical systems, to physics [272, 273]. Formally, complex *quantum* networks are distinguished from their classical counterpart by the physical nature of the nodes and links composing them [274]. In particular, one can distinguish between two broad classes of complex quantum networks, depending on the type of connections between the units or nodes of the quantum system: in the first category, we can find quantum networks whose connections are represented by entangled states [275, 276, 277, 278, 279]; while in the second category, we find quantum networks in which the links correspond to interactions between the different units [280, 281, 282, 283, 284, 285, 286, 287, 288, 289]. The interest in the first type of quantum networks has been triggered in part by possible applications in quantum technologies, such as secure quantum communication [280, 283, 290, 291, 292]. On the other hand, the study of networks of the second type is of relevance for understanding quantum transport and dynamical phenomena in both biological and artificial complex systems [282, 293, 294, 295, 296, 297, 298, 299, 300, 301], in which fundamental questions as whether coherence play a role in excitation transfer through networks [296, 298], or what happens to emergent phenomena known in classical complex networks when moving into the quantum regime [45, 65, 98, 115], have begun to be addressed. In this sense, in this chapter we will analyze the effects of such complex topological structures on the presence of noiseless modes and the emergence of synchronization.

Complex networks of harmonic oscillators in a common environment. In the following, we will introduce complex networks of harmonic oscillators embedded into a common environment and assess the resilience of synchronization and noiseless modes in more complex and less symmetric scenarios. These quantum networks belong to the second broad category as the links correspond to interactions between the oscillators. Specifically, we will consider the topology of the paradigmatic example of a random Erdős-Rényi quantum network [277, 281] and also of small-world networks [273], and we will also extend our analysis by looking at the resilience for inhomogeneities in parameters, as it happens in experimental situations [289, 302]. As we will show, random quantum networks are able to support noiseless clusters where quantum coherences can survive indefinitely. This allows one to either store or transport quantum states, excitations or, e.g., entanglement in a virtually error-free way even in presence of environmental noise [106, 285, 303, 304, 305]. We will analyze in detail the abundance, the extension and the composition of these noiseless sub-structures, in connection to the specific characteristics of the complex network topological regimes.

In the case of synchronization, we will see how collective dissipation enables both the emergence of *transient synchronization* and *stationary synchronization*, due to the presence of a normal mode with a lifetime much longer than the rest of collective modes [65, 98, 101]. In this case, before analyzing the complex network scenario, we will review the basic example of two harmonic oscillators dissipating independently or collectively, and we will show that only in the latter case synchronization is possible [65]. This will provide us with physical intuition and with the necessary tools to tackle the more complex

scenario of large arrays of harmonic oscillators dissipating collectively.

3.2 Minimal model: two coupled harmonic oscillators

In this section, we consider the dynamics of two coupled harmonic oscillators either dissipating into separate environments or into a common environment, which represents the minimal model to observe mutual synchronization. This is not only because we consider two oscillators, but more surprisingly, because these are both linear, contrasting with the known scenarios for classical synchronization in which only nonlinear dynamical systems are considered [42, 43]. First, we analyze the crucial differences between the master equations describing each scenario. Later, we show that only in the common environment case the emergence of synchronization in the dynamics of first and second moments is possible, as well as the presence of non-decaying noiseless normal modes. Moreover, we make use (for the first time in this thesis) of some important tools to assess the emergence of synchronization: as (i) the Pearson factor (see appendix B) and (ii) the ratio between decay rates of the collective modes. Hence, this section will pave the way to the more complex scenario of networks of oscillators of the following section, and it will also provide important insights for the subsequent chapters.

3.2.1 Harmonic oscillators coupled to common or separate environments

Spontaneous synchronization for two coupled harmonic oscillators in the presence of common environment was first shown in Ref. [65]. The Hamiltonian describing two coupled harmonic oscillators with equal mass ($m = 1$) and different frequency is given by ($\hbar = 1$):

$$\hat{H}_S = \frac{\hat{p}_1^2}{2} + \frac{\hat{p}_2^2}{2} + \frac{\omega_1^2}{2}\hat{x}_1^2 + \frac{\omega_2^2}{2}\hat{x}_2^2 + \lambda\hat{x}_1\hat{x}_2, \tag{3.1}$$

where $\hat{x}_j$ and $\hat{p}_j$ are the position and momentum operators[1] of the harmonic oscillator j satisfying $[\hat{x}_j, \hat{p}_k] = i\delta_{jk}$. The coupling term $\lambda\hat{x}_1\hat{x}_2$ is not written in the rotating wave approximation, as coupling strengths of the order of the frequencies are considered, i.e. $\lambda \sim \omega_j^2$ [65, 98, 101]. This Hamiltonian can be diagonalized in the normal mode basis as defined by the following canonical transformation [65]:

$$\begin{aligned} \hat{X}_+ &= \sin\theta\hat{x}_1 + \cos\theta\hat{x}_2, \quad \hat{P}_+ = \sin\theta\hat{p}_1 + \cos\theta\hat{p}_2, \\ \hat{X}_- &= \cos\theta\hat{x}_1 - \sin\theta\hat{x}_2, \quad \hat{P}_- = \cos\theta\hat{p}_1 - \sin\theta\hat{p}_2, \end{aligned} \tag{3.2}$$

with the angle given by

$$\tan(2\theta) = 2\lambda/(\omega_2^2 - \omega_1^2). \tag{3.3}$$

Then, the Hamiltonian for the normal modes reads:

$$\hat{H}_S = \frac{1}{2}\big(\hat{P}_+^2 + \hat{P}_-^2 + \Omega_+^2\hat{X}_+^2 + \Omega_-^2\hat{X}_-^2\big), \tag{3.4}$$

with [65]

$$2\Omega_\pm^2 = \omega_1^2 + \omega_2^2 \pm \sqrt{4\lambda^2 + (\omega_2^2 - \omega_1^2)^2}. \tag{3.5}$$

[1] These can be defined in terms of the creation and annihilation operators as $\hat{x}_j = \sqrt{1/(2\omega_j)}(\hat{a}_j^\dagger + \hat{a}_j)$ and $\hat{p}_j = i\sqrt{\omega_j/2}(\hat{a}_j^\dagger - \hat{a}_j)$, where $[\hat{a}_j, \hat{a}_k^\dagger] = \delta_{jk}$.

Common versus separate baths. We now consider these two harmonic oscillators coupled either to a common environment or to identical separate environments, and we analyze the differences in the resulting master equations describing the dissipative time-evolution of the system. As it is usual [58, 231], we can model the environments as an infinite collection of harmonic oscillators as given by the following Hamiltonian (see also Sect. 2.2.2):

$$\hat{H}_E = \frac{1}{2}\sum_{k=1}^{\infty}\left(\frac{\hat{K}_k^2}{M_k} + \nu_k^2\hat{Q}_k^2\right), \tag{3.6}$$

where M_k and ν_k are the mass and frequency of the environment mode k, with position and momentum operators $\hat{Q}_k$ and K_k, respectively. These environmental modes are assumed to be in a thermal state such that they constitute a thermal bath (see chapter 2 or [58]). In the common bath (CB) situation, the system is coupled to a unique bath (3.6), and the system-bath interaction is modeled by [65, 98, 101]:

$$\text{CB:}\quad \hat{H}_{SE} = (\hat{x}_1 + \hat{x}_2)\hat{B}\ ,\ \text{with}\ \hat{B} = \sum_{k=1}^{\infty} c_k\hat{Q}_k, \tag{3.7}$$

such that the system oscillators couple symmetrically to the bath ones. On the other hand, in the separate baths (SB) situation, each harmonic oscillator is coupled to an independent environment and each of the environments can be modeled by a Hamiltonian of the type of (3.6). The system-bath interaction term reads:

$$\text{SB:}\quad \hat{H}_{SE} = \sum_{j=1}^{2}\hat{x}_j\hat{B}_j\ ,\ \text{with}\ \hat{B}_j = \sum_{k=1}^{\infty} c_{k,j}\hat{Q}_{k,j}. \tag{3.8}$$

Here, $\hat{Q}_{k,j}$ and $\hat{K}_{k,j}$ correspond to the position and momentum operators of mode k of the bath j, each with a Hamiltonian like (3.6). Under the standard Born-Markov and secular approximations, a Lindblad master equation describing the dissipative dynamics of the system can be derived [65, 98, 101] (see also Sect. 2.2). Importantly, since the considered interaction strengths are of the order of the frequencies of the harmonic oscillators $\lambda \sim \omega_j^2$, in the master equation derivation is prominent the role of the normal modes that diagonalize the system Hamiltonian (what is known as a global master equation) [65, 98, 101, 225].

In order to understand the differences arising between the common environment and the separate environment cases, it is useful to rewrite the system-environment interaction Hamiltonian in terms of these normal modes. Then, for the CB scenario, the system-environment interaction term in the normal mode basis reads:

$$\text{CB:}\quad \hat{H}_{SE} = \kappa_+\hat{X}_+\hat{B} + \kappa_-\hat{X}_-\hat{B}, \tag{3.9}$$

where $\kappa_\pm = \cos\theta \pm \sin\theta$. Importantly, as generally $\kappa_+ \neq \kappa_-$, the interaction between one of the normal modes and the environment is enhanced while the one for the other is suppressed. As we will see, this have important dynamical consequences. On the other hand, for the SB situation we have:

$$\text{SB:}\quad \hat{H}_{SE} = \hat{X}_+(\sin\theta\hat{B}_1 + \cos\theta\hat{B}_2) + \hat{X}_-(\cos\theta\hat{B}_1 - \sin\theta\hat{B}_2). \tag{3.10}$$

In this case, each normal mode couples to a different linear combination of the two baths. Nevertheless, we anticipate that these two different linear combinations do not lead to observable effects. This is because the two baths are assumed identical and uncorrelated, and hence, the decay rates of the resulting master equation turn out to depend only on the sum of the squared coefficients, i.e. $\cos^2\theta + \sin^2\theta = 1$, which is the same for both terms.

Lindblad master equation. The resulting master equation for both CB and SB can be written in a general fashion as [98, 101]:

$$\begin{aligned}\frac{d}{dt}\hat{\rho} = &-i[\hat{H}_S,\hat{\rho}] + \sum_{j=\pm}\Bigg[\frac{D_j}{2}\mathcal{D}[\hat{X}_j]\hat{\rho} + \frac{D_j}{2\Omega_j^2}\mathcal{D}[\hat{P}_j]\hat{\rho} \\ &- i\frac{\Gamma_j}{2}\big(\hat{X}_j\hat{\rho}\hat{P}_j - \frac{1}{2}\{\hat{P}_j\hat{X}_j,\hat{\rho}\}\big) + i\frac{\Gamma_j}{2}\big(\hat{P}_j\hat{\rho}\hat{X}_j - \frac{1}{2}\{\hat{X}_j\hat{P}_j,\hat{\rho}\}\big)\Bigg],\end{aligned} \tag{3.11}$$

where the difference between the two cases resides in the definition of the rates. For the CB case we have [98, 101]:

$$\text{CB:}\quad \Gamma_\pm = \gamma\kappa_\pm^2, \quad D_\pm = \gamma\kappa_\pm^2\Omega_\pm\coth\left(\frac{\Omega_\pm}{2T}\right). \tag{3.12}$$

where T accounts for the bath temperature (we set both $\hbar = 1$ and $k_B = 1$). Note that the dissipation rates, $\Gamma_\pm$, and the diffusion coefficients, $D_\pm$, depend on $\kappa_\pm^2$ and thus can be generally unbalanced. In stark contrast, for SB we have:

$$\text{SB:}\quad \Gamma_\pm = \gamma, \quad D_\pm = \gamma\Omega_\pm\coth\left(\frac{\Omega_\pm}{2T}\right), \tag{3.13}$$

which are independent of the angle θ, as anticipated. While the dissipation rates are identical $\Gamma_+ = \Gamma_-$, the diffusion coefficients, $D_\pm$, depend on the normal mode frequency. In both cases we have introduced the parameter γ that controls the overall dissipation strength. As we have seen in chapter 2, an expression for γ in terms of the spectral density can be obtained [58, 65].

Equation (3.11) takes the form of a non-diagonal Lindblad master equation (2.1), where the jump operators are $\hat{F}_1 = \sqrt{\Omega_+}\hat{X}_+$, $\hat{F}_2 = \hat{P}_+/\sqrt{\Omega_+}$, $\hat{F}_3 = \sqrt{\Omega_-}\hat{X}_-$, $\hat{F}_4 = \hat{P}_-/\sqrt{\Omega_+}$. Then, the matrix of coefficients $\tilde{\Gamma}$ defined in chapter 2 takes a block diagonal form, where each of the blocks corresponds to one of the normal modes[2]:

$$\tilde{\Gamma} = \bigoplus_{j=\pm}\tilde{\Gamma}_j, \quad \tilde{\Gamma}_j = \frac{1}{2}\begin{pmatrix} D_j/\Omega_j & -i\Gamma_j \\ i\Gamma_j & D_j/\Omega_j\end{pmatrix}. \tag{3.14}$$

To ensure this equation is actually of the Lindblad form this matrix needs to be positive semi-definite, which can be assessed by studying its determinant. This translates in the condition $(D_\pm/\Omega_\pm)^2 - \Gamma^2 \geq 0$, which introducing the explicit expressions for these rates reads: $\coth^2(\Omega_\pm/(2T)) - 1 \geq 0$. This condition is always satisfied confirming that Eq. (3.11) is a Lindblad master equation[3].

Finally, it is interesting to write down this master equation in the basis of the oscillators, i.e. using $\hat{x}_{1,2}$ and $\hat{p}_{1,2}$ (see appendix C). Then, we observe that in the CB case there are both cross-damping and cross-diffusion terms, i.e. terms in the master equation that involve the two oscillators, as $\Gamma_+ \neq \Gamma_-$, and $D_+ \neq D_-$. On the other hand, for the SB case the cross-damping terms vanish identically, as $\Gamma_+ = \Gamma_-$. The cross-diffusion terms are generally non-zero but, when considering the equations for the expectation values for the first and second moments, they do not lead to couplings between the two oscillators (see appendix C). Thus, the oscillators only experiment *collective dissipation* in the CB scenario which, as we discuss below, enables the emergence of synchronization.

[2]Notice that we have reabsorbed some constants in the definition of the jump operators in order for the rates to have units of one over time.

[3]In fact, the master equation (3.11) for each normal mode is formally equivalent to Eq. (2.31). However, since the rotating wave approximation is not performed in the Hamiltonian term $\lambda\hat{x}_1\hat{x}_2$, it is more convenient to write (3.11) in terms of the position and momentum operators.

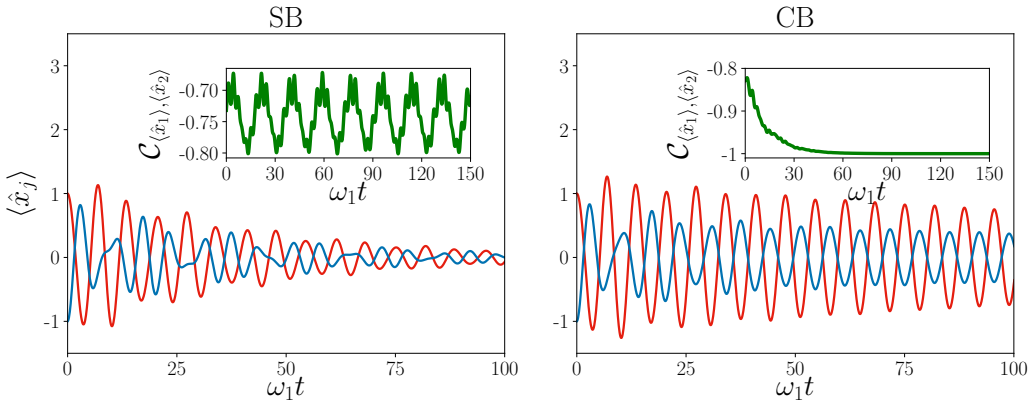

Figure 3.1: In red $\langle \hat{x}_1(t) \rangle$, in blue $\langle \hat{x}_2(t) \rangle$ for SB (left panel) and CB (right panel), with $\omega_2/\omega_1 = 1.2$, $\lambda/\omega_1^2 = 0.3$, and $\gamma/\omega_1 = 0.05$. Initial conditions: $\langle \hat{x}_1(0) \rangle = -\langle \hat{x}_2(0) \rangle = 1$ and zero momenta. In the insets we plot the synchronization measure: $\mathcal{C}_{\langle \hat{x}_1^2 \rangle, \langle \hat{x}_2^2 \rangle}(\omega_1 t | \omega_1 \Delta t = 15)$.

3.2.2 Equations of motion for the first and second moments

The linearity of the dynamics, coming from the fact that the Hamiltonian is quadratic, implies that if the initial state is Gaussian, it will remain so at all times [266, 267]. Then, in this case, the dynamics can be fully described through the first and second moments of the system, whose dynamical equations can be derived from the above master equation as we have explained in chapter 2. In particular, the equations of motion for the first moments in the normal mode basis read:

$$\frac{d}{dt}\langle \hat{X}_\pm \rangle = \langle \hat{P}_\pm \rangle - \frac{\Gamma_\pm}{2}\langle \hat{X}_\pm \rangle, \tag{3.15}$$

$$\frac{d}{dt}\langle \hat{P}_\pm \rangle = -\Omega_\pm^2 \langle \hat{X}_\pm \rangle - \frac{\Gamma_\pm}{2}\langle \hat{P}_\pm \rangle, \tag{3.16}$$

while the ones in the oscillators basis can be recovered by means of the canonical transformation defined in Eq. (3.2) (see also appendix C). From this equation it becomes clear that $\Gamma_\pm$ correspond to the damping rates of the normal modes. For the second moments we have the following system of equations:

$$\begin{aligned}\frac{d}{dt}\langle \hat{X}_j \hat{X}_k \rangle =& \frac{1}{2}\langle \{\hat{P}_j, \hat{X}_k\} + \{\hat{P}_j, \hat{X}_k\} \rangle \\ &- \frac{(\Gamma_j + \Gamma_k)}{2}\langle \hat{X}_j \hat{X}_k \rangle + \frac{D_j}{2\Omega_j^2}\delta_{jk},\end{aligned} \tag{3.17}$$

$$\begin{aligned}\frac{d}{dt}\langle \hat{P}_j \hat{P}_k \rangle =& -\frac{\Omega_j^2}{2}\langle \{\hat{P}_k, \hat{X}_j\} \rangle - \frac{\Omega_k^2}{2}\langle \{\hat{P}_j, \hat{X}_k\} \rangle \\ &- \frac{(\Gamma_j + \Gamma_k)}{2}\langle \hat{P}_j \hat{P}_k \rangle + \frac{D_j}{2}\delta_{jk},\end{aligned} \tag{3.18}$$

$$\frac{d}{dt}\langle \{\hat{X}_j, \hat{P}_k\} \rangle = \langle \hat{P}_j \hat{P}_k \rangle - 2\Omega_k^2 \langle \hat{X}_j \hat{X}_k \rangle - \frac{(\Gamma_j + \Gamma_k)}{2}\langle \{\hat{X}_j, \hat{P}_k\} \rangle. \tag{3.19}$$

This system of equations can be written in matrix form as

$$\frac{d}{dt}\vec{R} = \mathsf{M}\vec{R} + \vec{N}, \tag{3.20}$$

where $\vec{R}$ is the vector that contains the second moments of the system, M is the matrix that yields the homogeneous part of the system of equations, while $\vec{N}$ is the vector that contain

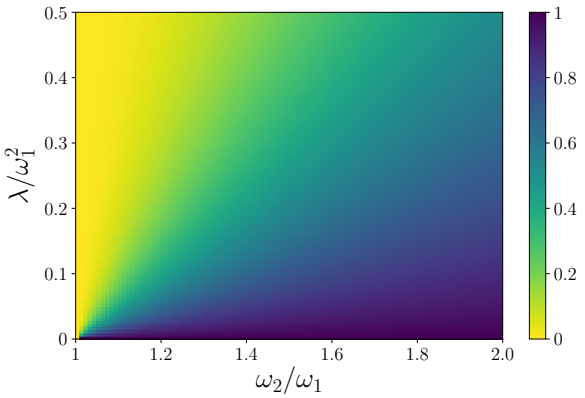

Figure 3.2: In color: ratio $\Gamma_-/\Gamma_+ = (\kappa_-/\kappa_+)^2$ for the common environment case varying ω_2/ω_1 and λ/ω_1^2.

the source terms, i.e. those proportional to the diffusion coefficients $D_\pm$. Notice that for the present case of two oscillators there are ten independent second moments. From the first and second moments equations we can see that (if both decay rates are non-zero) the stationary state of the first moments is zero, while the one for the second moments depends on the bath temperature through the diffusion terms in $\vec{N}$. This generalizes what we have already found for the elementary case of an harmonic oscillator coupled to a thermal bath, as described in chapter 2.

3.2.3 Transient synchronization

Here we analyze the emergence of transient synchronization in the dynamics of the first and second moments of the system of harmonic oscillators with common or separate environments. As introduced in chapter 1, transient synchronization emerges when there is a collective mode that dissipates much slower than the rest, as then, after an initial transient in which the rest of collective modes decay out, only this long-lived mode survives and the oscillators reach the stationary state in a synchronized fashion, oscillating at this normal mode frequency with a locked mutual phase-relation [44, 65, 5].

Synchronization in the first moments. The dynamics of the first moments of this system of two harmonic oscillators provides a first elementary illustration of this idea. In particular, the dynamics of $\langle \hat{x}_{1,2}(t) \rangle$ corresponds to a linear superposition of the dynamics of two independent dissipative modes $\langle \hat{X}_\pm(t) \rangle$, which follow Eq. (3.15) and (3.16). In order for transient synchronization to be possible, the decay rates $\Gamma_\pm$ need to be sufficiently different. Therefore, we see that synchronization of the first moments is not possible in the separate environment situation, as the decay rates of the two normal modes are identically the same $\Gamma_+ = \Gamma_-$, leading to the dynamics of $\hat{x}_1$ and $\hat{x}_2$ to oscillate asynchronously displaying multiple frequencies. On the other hand, for the common environment situation, we have that generally $\Gamma_+ \neq \Gamma_-$ and transient synchronization is possible if $\Gamma_+ \gg \Gamma_-$ or $\Gamma_+ \ll \Gamma_-$, as then one of the modes is long-lived with respect to the other [65, 98, 101]. In Fig. 3.1 we illustrate this first result, by plotting the time evolution of the expectation value of the position of the two oscillators. For the SB case (left panel), we see that the oscillators display an asynchronous relaxation dynamics, in spite of their coherent mutual coupling. In stark contrast, for the CB case, the oscillators quickly synchronize after a short initial transient, and they approach the stationary state oscillating synchronously with a locked-phase difference close to π.

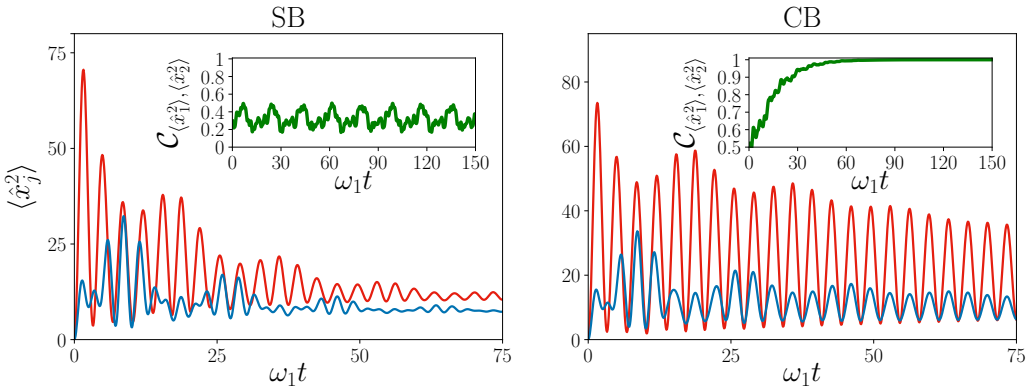

Figure 3.3: In red $\langle \hat{x}_1^2(t) \rangle$, in blue $\langle \hat{x}_2^2(t) \rangle$ for SB (left panel) and CB (right panel), with $\omega_2/\omega_1 = 1.2$, $\lambda/\omega_1^2 = 0.3$, $\gamma/\omega_1 = 0.05$ and $T/\omega_1 = 10$. The initial condition is a separable vacuum state with $r_1 = 2.5$ and $r_2 = 1.8$. In the insets we plot the synchronization measure: $\mathcal{C}_{\langle \hat{x}_1^2 \rangle, \langle \hat{x}_2^2 \rangle}(\omega_1 t | \omega_1 \Delta t = 15)$.

Pearson factor. The emergence or the absence of synchronization can be assessed using the Pearson factor [44, 65, 5]; this is a temporal correlation function introduced in appendix B, which takes as input the trajectories of two observables over a time window, and it computes their correlation. The Pearson factor can be calculated on a sliding time window such that it shows how synchronization eventually emerges in the dynamics. This quantity is defined as:

$$\mathcal{C}_{A_1(t),A_2(t)}(t|\Delta t) = \frac{\int_t^{t+\Delta t} ds[A_1(s) - \bar{A}_1][A_2(s) - \bar{A}_2]}{\sqrt{\prod_{j=1}^2 \int_t^{t+\Delta t} ds[A_j(s) - \bar{A}_j]^2}}, \tag{3.21}$$

where $\bar{A}_j = \frac{1}{\Delta t} \int_t^{t+\Delta t} ds A_j(s)$ and $A_{1,2}(t) = \langle \hat{O}_{1,2} \rangle$ are the input observables at time t, with a time window Δt over which the temporal correlation measure is computed. This measure takes values between -1 and 1, the two extreme values corresponding to synchronization with a π locked-phase difference, and with a zero locked-phase difference, respectively. In the insets of Fig. 3.1, the Pearson factor is shown: in the absence of synchronization, it typically displays intermediate values and an oscillatory temporal evolution; in contrast, when synchronization emerges, it reaches a stationary value close to ± 1. Notice that the Pearson factor can be generalized to account for arbitrary locked-phase differences (see appendix B).

Ratio of the collective decay rates. Based on the previous discussion, we can assess the emergence of synchronization analyzing the disparity between the decay rates of the collective modes. In Fig. 3.2 we address the emergence of synchronization in the first moments for the common bath case, by plotting the ratio Γ_-/Γ_+ varying the coupling strength and the detuning between the two oscillators. We can see that this ratio displays the typical Arnold-tongue behavior: the more detuned are the oscillators, the more coupling strength is needed for Γ_-/Γ_+ to be small, enabling the emergence of transient synchronization [65, 98, 101]. Hence, synchronization emerges when the coupling strength is large enough to compensate for the detuning between the oscillators [65]. Intuitively, this can be understood from the theoretical expressions for θ and $\Omega_\pm$ that we have reported in Eqs. (3.3) and (3.5). Notice that the larger is the detuning compared to the coupling strength, the closer is θ to zero, and thus the normal modes are essentially localized onto just one oscillator. Similarly, in this limit, the eigenfrequencies tend to the intrinsic ones, and the collective damping rates are almost balanced. Hence, for detunings that are too large compared to the coupling strength, the oscillators essentially do not talk to each other, precluding synchronization.

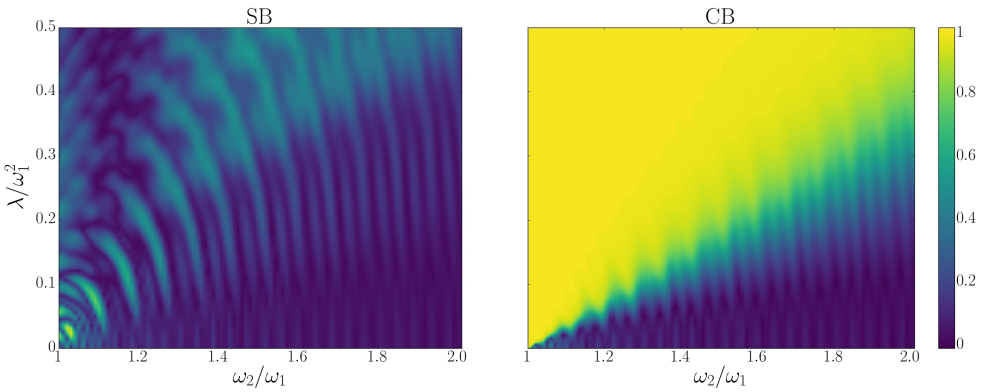

Figure 3.4: In color $|\mathcal{C}_{\langle\hat{x}_1^2\rangle,\langle\hat{x}_2^2\rangle}|$ at $\omega_1 t = 75$ and for a time window $\omega_1\Delta t = 20$. Here we vary the coupling strength λ/ω_1^2 and frequency ω_2/ω_1. The initial condition is a separable vacuum state with $r_1 = 2$ and $r_2 = 1$. We fix $T/\omega_1 = 10$ and $\gamma/\omega_1 = 0.05$.

Synchronization in the second moments. We now consider the dynamics of the second moments. Here the possible emergence of transient synchronization is, in principle, not so straightforward to analyze, as we deal with a more complicated system of coupled differential equations (3.20). For this reason, we perform a more careful numerical analysis making use of the Pearson factor. As initial conditions we consider vacuum squeezed states:

$$\langle\hat{x}_j^2(0)\rangle = \frac{e^{-2r_j}}{2\omega_j}, \quad \langle\hat{p}_j^2(0)\rangle = \frac{\omega_j e^{2r_j}}{2}, \quad j = 1, 2, \tag{3.22}$$

the rest of first and second moments being initially zero. However, we anticipate that synchronization, when present, is largely independent of the initial conditions. As observed in Ref. [65], if the baths are separate and identical, synchronization never emerges. In Fig. 3.3, we compare CB and SB and show how synchronization emerges in one case and not in the other. Notice how the Pearson factor progressively reaches a value closer to one in the CB case, while in the SB case it oscillates around small values indicating the lack of synchronization. Besides $\langle\hat{x}_1^2(t)\rangle$, $\langle\hat{x}_2^2(t)\rangle$, synchronization is observed in the other second moments too, as it is based on the disparity of the decay rates of the collective modes, which are also behind the dynamics of these other moments. In Fig. 3.4 the Pearson indicator is drawn for different detunings and coupling strength. We observe how synchronization never emerges in the SB case, despite increasing the coupling strength for a given detuning. On the contrary, in the CB case we observe the typical Arnold tongue behavior: as coupling strength increases, synchronization emerges for larger detunings.

A detailed analysis of the eigenvalues of M can be performed in order to have a complete picture of the different eigenmodes of this matrix that characterize the dynamics of the second moments [65]. This provides the same synchronization scenario that can be predicted characterizing the ratio Γ_-/Γ_+ [98], as we have done for the case of the first moments. In fact, comparing Fig. 3.2 with Fig. 3.4 we can see that there is a good correspondence between the synchronized regions with those in which Γ_-/Γ_+ takes small values. The damping rate imbalance provides a simple but powerful criterion which can be used to assess the emergence of synchronization in more complex scenarios, in which a complete analysis of the dynamical system (3.20) might not be so feasible. This is the case of the next sections, in which this ratio is used to analyze the presence of synchronization in complex networks of harmonic oscillators dissipating in a common environment.

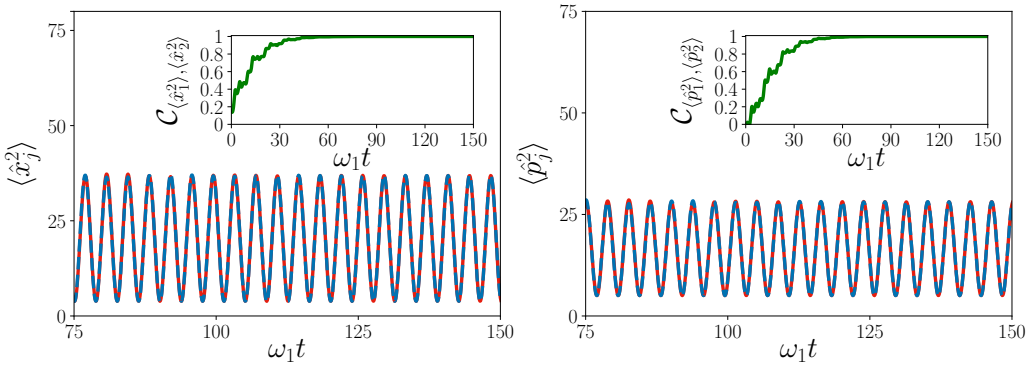

Figure 3.5: Example of stationary synchronous state. In red $\langle \hat{x}_1^2(t) \rangle$ (left panel) $\langle \hat{p}_1^2(t) \rangle$ (right panel), in dashed blue lines $\langle \hat{x}_2^2(t) \rangle$ (left panel) $\langle \hat{p}_2^2(t) \rangle$ (right panel), in the CB case with $\omega_2/\omega_1 = 1.0$, $\lambda/\omega_1^2 = 0.3$, $\gamma/\omega_1 = 0.05$ and $T/\omega_1 = 10$. The initial condition is a separable vacuum state with $r_1 = 2.5$ and $r_2 = 1.8$. In the insets we plot the synchronization measure: $\mathcal{C}_{\langle \hat{x}_1^2 \rangle, \langle \hat{x}_2^2 \rangle}(\omega_1 t | \omega_1 \Delta t = 15)$ (left panel) and $\mathcal{C}_{\langle \hat{p}_1^2 \rangle, \langle \hat{p}_2^2 \rangle}(\omega_1 t | \omega_1 \Delta t = 20)$ (right panel) .

3.2.4 Noiseless mode and stationary synchronization

Beyond transient spontaneous synchronization, when considering two or more oscillators, in the CB case it can happen that one or more normal modes are effectively uncoupled from the bath, as it happens here for $\omega_1 = \omega_2$ in which $\kappa_- = 0$. These states are effectively shielded from the environment and evolve freely. Then, depending on the initial conditions, the system does not fully thermalize and the asymptotic state itself can exhibit a synchronous dynamics and asymptotic correlations. This *stationary synchronization* due to the presence of decoherence free subspaces was shown in detail in small systems of coupled harmonic oscillators in [101]. In the present CB case, when $\omega_1 = \omega_2$ and $\kappa_- = 0$ we have that the evolution of $\hat{X}_-$ is only ruled by the Hamiltonian. Then, for any initial condition overlapping with $\hat{X}_-$, the dynamics of the system will be initially a mixture of modes, but eventually, only this non-decaying mode will survive, resulting in asymptotic synchronous oscillations. We stress that this asymptotic synchronization does not correspond to a limit-cycle due to the linear character of the oscillators, and it rather stems from the effective decoupling of a collective mode from the environment. In Fig. 3.5, we show the time-evolution of different second order moments in which the non-decaying synchronous oscillations can be appreciated. Moreover, in the inset the Pearson factor is shown from the beginning, which illustrates the spontaneous emergence of the synchronous oscillations. Interestingly, this form of synchronization is accompanied by non-decaying quantum correlations, as analyzed in [101].

3.3 Complex networks of harmonic oscillators in a common bath

We have seen that a common bath can induce synchronization and noiseless modes in a system of two coupled harmonic oscillators, showing that the symmetric system (i.e. with the same intrinsic frequencies) is the most favorable. What happens when extending the network to larger and more complex configurations? In the following, we will consider both Erdős-Rényi random complex networks and small-world networks. Before to present the results, we introduce the generalization of the CB model to many oscillators.

3.3.1 From two to many oscillators in a common bath

We now consider the generalization of the previous system to the case of many quantum harmonic oscillators coupled to a common bath. The network of harmonic oscillators can be described by the following Hamiltonian:

$$\hat{H}_S = \frac{1}{2}\sum_{i=1}^{N}\left(\hat{p}_i^2 + \omega_i^2\hat{x}_i^2\right) + \sum_{i=1}^{N}\sum_{j=1}^{N}\lambda_{ij}(1-\delta_{ij})\hat{x}_i\hat{x}_j, \tag{3.23}$$

where $\hat{x}_i$ and $\hat{p}_i$ are position and momentum operators of the quantum harmonic oscillators with intrinsic frequencies ω_i, and λ_{ij} is the coupling strength between oscillator i and j. As before, the common bath is modeled by an infinite collection of harmonic oscillators described by the Hamiltonian (3.6), which are assumed to be in thermal equilibrium. Then, the system-environment interaction is described by:

$$\hat{H}_{SE} = \sum_{n=1}^{N}\hat{x}_n\hat{B}, \text{ with } \hat{B} = \sum_{k=1}^{\infty}c_k\hat{Q}_k, \tag{3.24}$$

from which we can appreciate that the system interacts with the environment through the center of mass (c.m.) coordinate, $\hat{x}_{cm} = \sum_{n=1}^{N}\hat{x}_n$. As before, it is insightful to write the system bath Hamiltonian in terms of the normal modes of the system defined as:

$$\hat{x}_n = \sum_{m=1}^{N}\mathsf{F}_{nm}\hat{X}_m, \quad \hat{X}_n = \sum_{m=1}^{N}\mathsf{F}_{mn}\hat{x}_m, \quad \forall n \tag{3.25}$$

or in matrix notation:

$$\vec{x} = \mathsf{F}\vec{X}, \quad \vec{X} = \mathsf{F}^T\vec{x}, \tag{3.26}$$

where $\vec{X} = (\hat{X}_1, ..., \hat{X}_N)^T$, $\vec{x} = (\hat{x}_1, ..., \hat{x}_N)^T$, and F is the $N \times N$ matrix with elements F_{nm} that defines the canonical transformation between the oscillator basis, encoded in $\vec{x}$ and the normal mode basis, encoded in $\vec{X}$. F is a rotation matrix, and thus its inverse corresponds to its transpose, i.e. $\mathsf{F}^{-1} = \mathsf{F}^T$. However, for complex topologies we will generally resort to numerical diagonalization of the system, as analytical expressions for the eigenvalues of F are not available. Then, the Hamiltonian (3.23) is diagonalized as:

$$\begin{aligned}\hat{H}_S = \vec{p}^T\frac{\mathbb{1}}{2}\vec{p} + \vec{x}^T\mathsf{M}\vec{x} &= \vec{P}^T\frac{\mathbb{1}}{2}\vec{P} + \vec{X}^T\mathsf{V}\vec{X} \\ &= \frac{1}{2}\sum_{n=1}^{N}(\hat{P}_n^2 + \Omega_n^2\hat{X}_n^2),\end{aligned} \tag{3.27}$$

where $\mathbb{1}$ is the identity matrix, M is the matrix containing the frequencies and couplings as prescribed in (3.23), and $\mathsf{V} = \mathsf{F}^T\mathsf{M}\mathsf{F}$ is the diagonal matrix containing the system squared eigenfrequencies, i.e. $\Omega_n^2/2$. In the normal mode basis the system bath Hamiltonian reads as:

$$\hat{H}_{SE} = \sum_{n=1}^{N}\kappa_n\hat{X}_n\hat{B}, \quad \kappa_n = \sum_{m=1}^{N}\mathsf{F}_{mn}. \tag{3.28}$$

Hence, each normal mode is coupled to the bath with its own rate (proportional to κ_n) that depends on the matrix diagonalizing the system (and thus on the topology and parameters of the system), generalizing the case of two oscillators coupled to a common bath. Importantly, if $\kappa_n = 0$ the mode n is uncoupled from the bath, which can be stated equivalently as the normal mode n being perpendicular to the center of mass. Recall that $\hat{X}_n = \sum_{m=1}^{N}\mathsf{F}_{mn}\hat{x}_m$, and hence if the coefficients F_{mn} are represented as a vector, the scalar product of this vector with that representing $\hat{x}_{cm}$ is proportional to κ_n [98, 101].

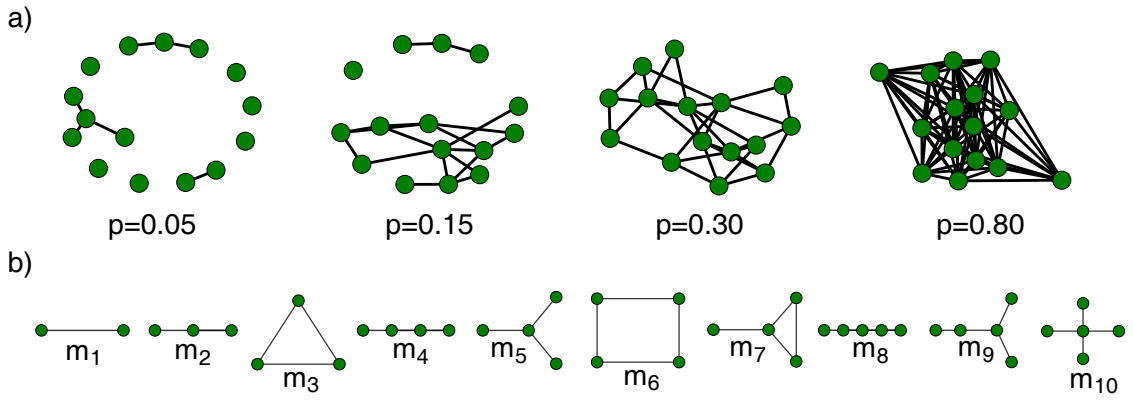

Figure 3.6: a) Realizations of Erdős-Rényi (ER) random networks with 15 nodes, and for different probabilities of connection p. For $p = 0.05$, and $p = 0.10$ the networks are composed of many components, while for $p = 0.30$ and $p = 0.80$ there is only one component spanning all the nodes. b) Motifs with less than five connections. For small probabilities of connection the motifs with few connections dominate.

In the normal mode basis, the full Hamiltonian describing the system, the bath, and their interaction is given by adding the terms (3.6), (3.27), and (3.28). From this total Hamiltonian, we can appreciate that when $\kappa_n = 0$ the mode n, i.e. $\hat{X}_n$ and $\hat{P}_n$, commute with the system-bath interaction term (3.28). Therefore, the reduced dynamics of this mode is not influenced by dissipation; indeed it is unitary and evolves with the Hamiltonian term $\frac{1}{2}(\hat{P}_n^2 + \Omega_n^2 \hat{X}_n^2)$. Hence, the *noiseless condition* stems out of a symmetry of the total Hamiltonian, and it is independent of the subsequent approach used to approximate the dynamics of those normal modes which are coupled to the thermal bath.

From these Hamiltonians, and under the standard Born-Markov and secular approximations, we can obtain the master equation describing the dissipative dynamics of the system [98]. This consists of the generalization of Eq. (3.11) to the N normal modes case, i.e.:

$$\begin{aligned}\frac{d}{dt}\hat{\rho} = &-i[\hat{H}_S, \hat{\rho}] + \sum_{j=1}^{N}\Bigg[\frac{D_j}{2}\mathcal{D}[\hat{X}_j]\hat{\rho} + \frac{D_j}{2\Omega_j^2}\mathcal{D}[\hat{P}_j]\hat{\rho} \\ &- i\frac{\Gamma_j}{2}\Big(\hat{X}_j\hat{\rho}\hat{P}_j - \frac{1}{2}\{\hat{P}_j\hat{X}_j, \hat{\rho}\}\Big) + i\frac{\Gamma_j}{2}\Big(\hat{P}_j\hat{\rho}\hat{X}_j - \frac{1}{2}\{\hat{X}_j\hat{P}_j, \hat{\rho}\}\Big)\Bigg],\end{aligned} \tag{3.29}$$

with

$$\Gamma_n = \kappa_n^2\gamma, \quad D_n = \kappa_n^2\gamma\Omega_n \coth(\Omega_n/2T). \tag{3.30}$$

Notice that here we have also introduced the phenomenological parameter γ that characterizes the overall dissipation strength, while the expressions for the decay rates and diffusion coefficients are the direct generalization of the two oscillator case. From this master equation, we could derive the equations of motion for the first and second moments of the whole system, as done in Ref. [98], and similarly to what we have done for two oscillators. Nevertheless, it will be sufficient to assess the form of the full Hamiltonian, and in particular of $\hat{H}_S$ and $\hat{H}_{SE}$, for the analysis of the following sections.

3.3.2 Erdős-Rényi quantum networks

In this chapter, we mainly focus on the analysis of Erdős-Rényi (ER) random networks [272, 306, 307] of quantum harmonic oscillators. Further results for small-world networks [273] are presented in appendix D. Erdős-Rényi (ER) random graphs [figure 3.6 (a)] are generated with a stochastic mechanism. Despite being based on minimal assumptions, they exhibit a rich phenomenology regarding their structure and connectivity [306, 307]. Fixing N and $0 < p < 1$ as parameter values, the ER statistical ensemble $\mathcal{G}(N, p)$ contains

networks with exactly N nodes, assigning probability

$$P(M) = p^M (1-p)^{\frac{N(N-1)}{2}-M} \tag{3.31}$$

to a network with M connections. In practice, one draws a network from the ensemble by independently considering each of the $N(N-1)/2$ unordered node pairs $\{i,j\}$ and establishing the connection between i and j with probability p. For not too small N, this random and uncorrelated creation of connections typically produces a network without obvious symmetries. The small-world model by Watts and Strogatz [273] instead was proposed to capture some properties of real networks and it is an interpolation between the two extremes of random networks and regular lattices (see appendix D).

For the present context, connectedness is a crucial network property. A network is connected if it consists of a single component: for all nodes i and j there is a path or walk from i to j. In ER random graphs, the probability of connectedness $P_{\text{conn}}(N,p)$, i.e. the probability to obtain a connected network from the ensemble of random networks for a given value of N and p, increases with p, see Fig. 3.6(a). In fact, the increase of P_{conn} is steepest around the critical value $p_c = N^{-1}\ln N$. For large N, the p-dependence of P_{conn} is close to a step function with value close to zero for $p < p_c$ and close to 1 for $p > p_c$, while this transition is smoothened for finite networks. Here, random networks are introduced to reveal how the complexity of the connectivity influences the decoherence and the emergence of synchronization across medium size networks of N nodes.

In our system, the nodes of the network correspond to the different harmonic oscillators of Hamiltonian (3.23), while the topology of the network is encoded in the coupling coefficients: λ_{ij}. The network is undirected which means that $\lambda_{ij} = \lambda_{ji}$. Inhomogeneity of frequencies and couplings will be also considered:

$$\omega_i = \omega_0 + 2k_m + \Delta\omega_i, \quad \lambda_{ij} = \lambda_{ji} = -\lambda + \Delta\lambda_{ij}, \tag{3.32}$$

where $\Delta\omega_i$ ($\Delta\lambda_{ij}$) are zero mean Gaussian numbers with standard deviation σ_ω (σ_λ), and ω_0 and λ are the mean values. Notice that we have introduced the frequency shift $2k_m$ to ensure that the eigenfrequencies of Hamiltonian (3.23) are always positive. A sufficient condition adopted here is to set k_m equal to the largest degree of a given network times λ, where the degree of a node corresponds to the number of nodes to which it is connected [272]. Furthermore, we consider these networks to be embedded in a common bath, as described in the previous subsection, such that the system-environment Hamiltonian (3.28) and the master equation (3.29) can be used to identify the presence of noiseless modes and synchronization. As commented, noiseless modes correspond to those eigenmodes that are perpendicular to the c.m. mode mode ($\hat{x}_{cm}$), i.e. those with

$$\text{Noiseless condition:} \quad \kappa_n = 0, \tag{3.33}$$

while synchronization will be analyzed by considering the ratio of the smallest decay rates.

3.4 Noiseless clusters in complex networks with a common bath

In the following we study how collective dissipation and the topology of the open network can concur in shielding part of the network form dissipation and decoherence. This will enable decoherence-free subspaces and noiseless subsystems or noiseless modes (NSs) (see for example [103] and the references therein). Well known examples are the simplest cases of two or few qubits [105, 108, 109, 234] and oscillators [101, 110, 111, 271], as described in Sect. 3.2, while here we well consider complex networks of many oscillators.

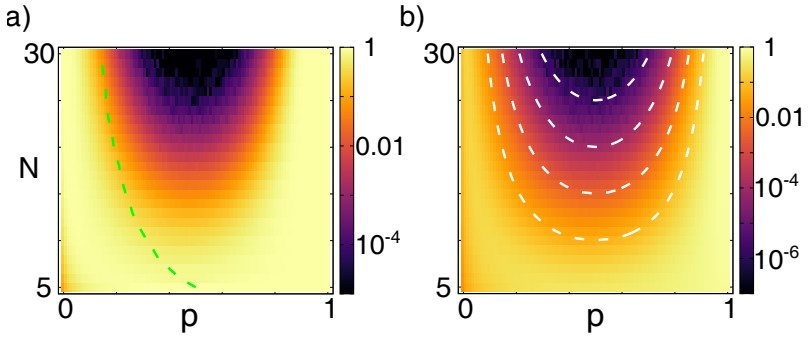

Figure 3.7: Probability to find at least one NS (a) and fraction of noiseless normal modes out of the total (b) as a function of the probability of connections in ER network p and its size N. Increasing values appear in lighter color. Green dashed line corresponds to the transition probability above which the probability of connectedness overcomes 50%. White dashed lines are contour plots of the variance of the degree distribution. Parameters are fixed to: $\omega_0 = 2$, $\lambda = 1$. Each point is evaluated over 10^5 realizations.

Being all network nodes (oscillators) identically coupled to the common bath. Therefore, the normal modes perpendicular to $\hat{x}_{cm}$, i.e. with (3.33), define the noiseless clusters. Hence, the results presented in the following subsections are concerned with the analysis of the existence and abundance of such normal modes varying the network topology and parameters. We first present the results for uniform parameters (so that λ_{ij} is either zero or λ), in which the effects of the underlying topology can be discerned most easily, and later on we move to the case with detunings and non-uniform coupling strengths. We first present the obtained results, while Sect. 3.4.4 is devoted to the discussion about their physical interpretation.

3.4.1 Networks with uniform frequency and coupling strength

We start our analysis by addressing the case of a network with homogeneous parameters (i.e. $\sigma_\lambda = \sigma_\omega = 0$) and focusing on the network topology. A convenient property of this model is that the particular values of ω_0 and λ do not influence the shape of the eigenvectors. This follows from the fact that the constant diagonal elements do not affect the diagonalization of the Hamiltonian, and the remaining λ can be factorized out of the adjacency matrix (the matrix of connections defining the network [272]). Hence, our analysis is independent of the coupling strength and these system parameters only play a role in determining the eigenfrequencies. Our results are therefore determined solely by the topology of the underlying Erdős-Rényi network which depends only on p and N. Furthermore, the same analysis holds for a tight-binding Hamiltonian with uniform parameters and ER network topology, as the adjacency matrix in this case is defined in a equivalent way (see appendix D).

Important limit cases are those in which the Hamiltonian matrix is in a *shifted* Laplacian form, i.e. the sum of all the elements of any column or row takes the same constant value. In fact, this leads to the c.m. being always an eigenvector of the Hamiltonian (3.23). Then for shifted Laplacian Hamiltonians there are always $N-1$ normal modes perpendicular to the c.m. and thus uncoupled from the bath. Each of these eigenvectors constitutes an NS. It can be easily shown that this is the case for highly symmetric systems described by Hamiltonian (3.23) and (3.32) with uniform parameters (i.e. $\omega_i = \omega_0 + 2k_m$ and $\lambda ij = \lambda$, $\forall i, j$) in either fully connected networks or regular lattices[4]. In general, however, the problem of the existence of NSs beyond these highly symmetric configurations is not trivial. This motivates the study of abundance and structure of NSs in random

[4]In this case, some of the couplings are zero $\lambda_{ij} = 0$, but the system displays translational invariance.

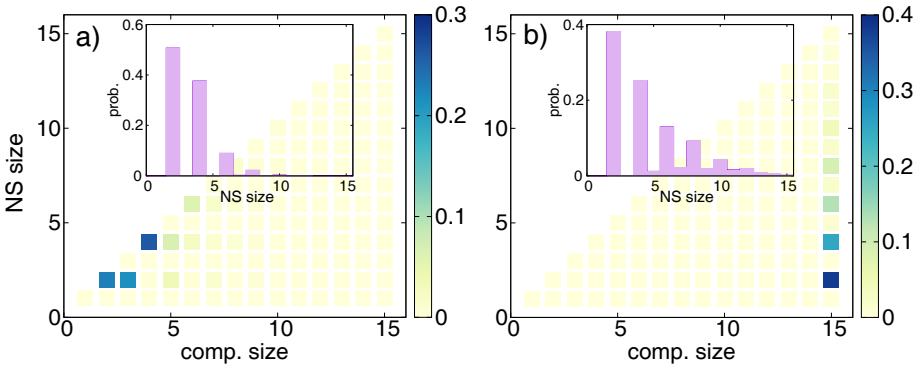

Figure 3.8: In color: probability that a NS of a given size (vertical axis) is located in a component of a particular size (horizontal axis), with $N = 15$, and $p = 0.05$ (a) or $p = 0.80$ (b). Both in (a) and in (b) we have not taken into account degenerate subspaces. Both insets show the distribution of sizes of NSs, obtained by summing all the contributions from different component sizes to the same NS size.

networks for $0 < p < 1$.

In Figure 3.7 (a) we encode in the color scale the probability to find at least one NS in a network, varying the probability of connection p and the network size N. We remind that in ER networks the average degree is given by the product pN. For small networks there is a significant probability to find a NS for all the range of p's (bright regions); however, as we increase the size of the networks this region shrinks and it remains significant only at the extreme values of p. The case of $p = 1$ corresponds to the fully connected network limit anticipated above (with $N - 1$ noiseless eigenvectors), while for independent oscillators ($p = 0$) the system is fully degenerate and can be always initialized to evolve in a NS. These features are robust when looking at the total fraction of NSs with respect to the N degrees of freedom and we find similar results in Fig. 3.7 (b).

An interesting issue is about the relation between the underlying topology and the abundance of noiseless normal modes. The green dashed line in Fig. 3.7 (a) indicates the transition probability to a one large component. In particular, we numerically determine a threshold $\tilde{p}_c$ as the value of p for which $P_{\text{conn}}(N, p) = 1/2$. For networks of $N = 15$ nodes we observe $\tilde{p}_c \approx 0.23$ (see appendix D). White dashed lines in Fig. 3.7 (b) represent contour plots of the variance of the degree distribution, i.e. the probability distribution that governs the degree for the ER network ensemble [272], with inner lines corresponding to higher values. Both quantities give insight on the relevant topological features to have NSs as will be discussed in detail in Sect. 3.4.4. In particular, the green line separates the parameter region in which NSs are made of disconnected motifs from that in which they are embedded in a large component. The white contours are an indicator of topological disorder (the bigger the variance the less degree homogeneity) which seems to be detrimental for the abundance of NSs.

For the NSs that are not degenerate we can characterize their features starting from their extension, i.e. their number of nodes within the network. Thus, we introduce the noiseless subsystem size (NS size) as the number of oscillators spanned by a given noiseless eigenvector. Due to the non-degeneracy and with each component's submatrix diagonalizable separately, each NS spans oscillators inside only one connected component. The distribution of sizes of connected components is an important characteristic of ER random networks with fixed p as it indicates different topological regimes [Fig. 3.6 (a)]. In Figure 3.8 we represent the probability to find a NS of a particular size (vertical axis) embedded in a network component of a given size (horizontal axis) below the connectedness transition [$p = 0.05$ (a)] and for a connected network [$p = 0.80$ (b)].

For small p, NSs with few nodes predominate as expected, Fig. 3.8(a), while for

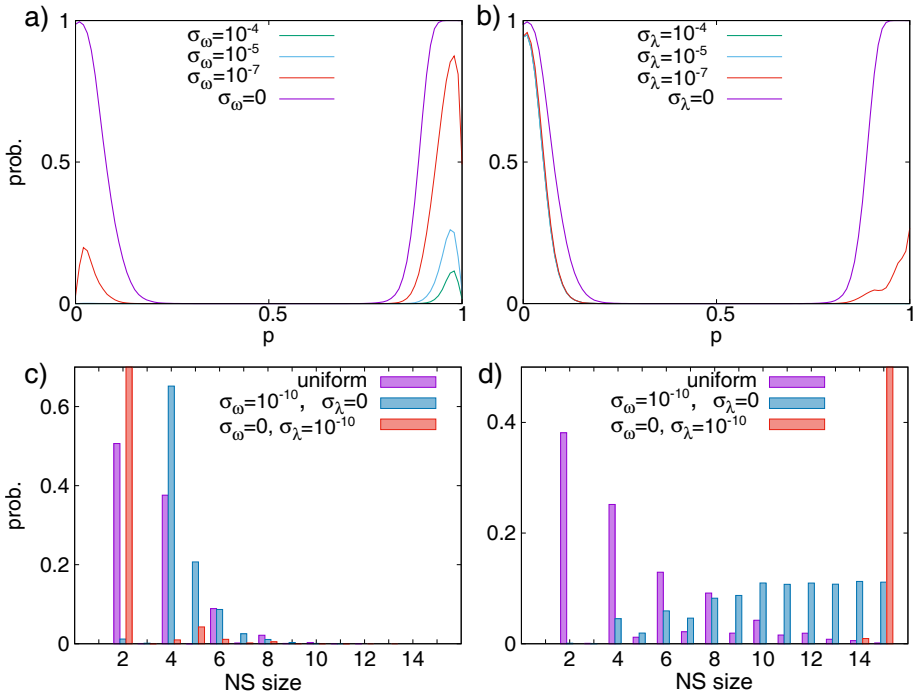

Figure 3.9: (a,b) Probability to find at least one decoherence free normal mode for N=30, for inhomogeneous frequencies with different σ_ω values (a), for inhomogeneous couplings with different σ_λ (b). (c,d) Probability distribution of NSs of different sizes (i.e. number of nodes of the noiseless eigenvector) for nonuniform frequencies (in blue, for $\sigma_\omega = 10^{-10}$) and couplings (in red, for $\sigma_\lambda = 10^{-10}$), in purple uniform parameters. Parameters $N = 15$ and $p = 0.05 < \tilde{p}_c$ (c), $p = 0.80 > \tilde{p}_c$ (d).

$p = 0.80$ there is only one component spanning all the oscillators, Fig. 3.8(b). What is surprising is the abundance of NSs spanning over an *even* number of oscillators [e.g. $2, 4, 6$ in Fig. 3.8 (a)] with respect to the scarce ones that span over an odd number of oscillators. This happens independently from the parity of the size of connected components [look for instance at components of sizes 4 and 5 in Fig. 3.8 (a)] and of N (not shown). In the case of components of odd size (for example of size 5), this implies that at least one of the oscillators is not involved in its largest NS (with 4 nodes in this example). Interestingly this characteristic parity symmetry in the NS size distribution is rather robust, and also observed for large probabilities of connection, as in (b) and also in small-world networks (see appendix D). The origin of this parity feature of NSs will be shown to be related to the presence of breathing modes and discussed in Sect. 3.4.4.

3.4.2 Resilience in the presence of imperfections

The study of homogeneous networks –with identical local frequencies and coupling strengths– allows to isolate the importance of the topological features for the existence of NSs. Here, we consider their resilience in presence of not uniform parameters, as they would occur for instance in biological complexes or any experimental set-up, inevitably characterized by inhomogeneity and imperfections. We consider Gaussian distributions either in frequencies or couplings ($\sigma_{\omega,\lambda} \neq 0$). Very small inhomogeneities ($\sigma_{\omega,\lambda} \sim 10^{-10}$) are enough to remove degeneracy in normal modes, while the probability to find NSs does not significantly change. In Figure 3.9 (a,b) we show the results of increasing differences on frequencies (a) and couplings (b) for the probability to find at least one NS. NSs can be very fragile even for small deviations from the uniform parameters. Important exceptions occur for inhomogeneous *couplings* that do not affect NSs for small components (Fig. 3.9 (b) for $p \lesssim 0.2$). Otherwise, large components are more resilient to the presence of

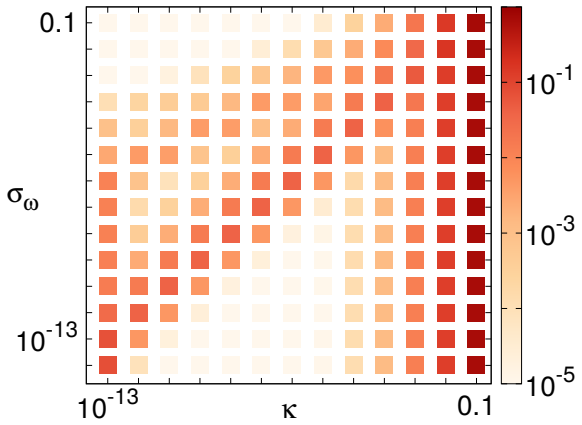

Figure 3.10: Probability to find a normal mode with a certain overlap with the dissipative mode (κ) and in presence of detuning across the network with variance σ_ω. The values for κ are binned according to their order of magnitude, i.e. the column 0.01 corresponds to normal modes with κ of the order of 0.01. The results have been obtained for networks of size $N = 30$ and $p = 0.9$.

detunings across the network, Fig. 3.9 (a).

The structure of NSs is strongly influenced by inhomogeneous parameters (Fig. 3.9). Looking at the regime where small components dominate [for $p = 0.05$, Fig.3.9 (c)], detuning (blue) leads to the disappearance of NSs of just pairs of nodes, as expected; decoherence free normal modes spanning over four oscillators are the most common (even if embedded in motives of five oscillators, not shown). In the regime of one large component [for $p = 0.8$, Fig. 3.9 (d)], NSs can have different sizes spanning from four oscillators to the whole network. In both cases, detuning removes the even-odd asymmetry. In networks with non-uniform coupling strengths [red histograms in Fig. 3.9], NSs of two oscillators survive and predominate for small p (c), while for high p the decoherence free mode is extended over almost all the network (d). In Sect. 3.4.4 we will present some mechanisms that can explain these differences in the results for non-uniform frequencies and non-uniform coupling strengths.

3.4.3 Quasi-noiseless clusters

We have seen that in general inhomogeneity in the parameters across the network is detrimental for NSs. On the other hand, for practical purposes it can be more interesting to establish if there are some modes with very long (even if not infinite) decoherence times. In this spirit, we ask whether, in spite of inhomogeneity, there is still a well defined set of modes which, although not perfectly decoupled from the bath, dissipate more weakly than the rest, being then effectively frozen over long timescales [98, 271].

We introduce then quasi-noiseless clusters that can be identified looking at their overlap, named κ, with the lossy mode $\hat{q}_{cm}$. Figure 3.10 represents the probability to have quasi-noiseless modes depending on detuning (σ_ω on vertical axis) and on their overlap κ (horizontal axis). Then, decoherence free modes do correspond to the first column ($\kappa \leq 10^{-13}$, our numerical zero), and the uniform ER network case to the lowest row. We observe that uniform networks exhibit two very well defined sets of normal modes (left and right in Fig. 3.10), separated by a huge gap in their respective dissipation rates (as quantified by κ): this gap allows to properly distinguish (and characterize even numerically) NSs with respect to the others.

As we increase the spread in detunings σ_ω, NSs tend to become slightly more noisy, with predominance of modes for $\kappa \sim \sigma_\omega$ (diagonal in Fig. 3.10). The gap between quasi-noiseless and dissipating normal modes decreases. Despite strict decoherence free modes

tend to disappear for increasing inhomogeneity, two well separated sets of normal modes (with a significant gap in κ) survive up to a certain strength σ_ω. This allows to identify *quasi* NSs up to a certain degree of disorder in frequencies. Analogous results are found for nonuniform couplings, i.e. for non-zero σ_λ.

3.4.4 Discussion: noiseless clusters in complex networks

In the following, we present and discuss the mechanisms that can explain the main results for NSs in complex network presented above. Moreover, we establish connections with the literature and with the results obtained studying another type of complex networks, namely small-world networks (see appendix D).

Insight about our results on the abundance and structure of NSs (Figs. 3.7 and 3.8) can be gained considering the underlying network topology and regimes, dominated by small and large size components (small and large p's in Fig. 3.8). Above a certain value of p, networks are composed predominantly by a single component (see appendix D for distributions of component sizes for different p's). The corresponding disappearance of small components is what crucially hinders the existence of noiseless modes for small p as clear by the comparison in Fig. 3.7 (a): below the threshold probability $\tilde{p}_c$ (green dashed line), several small components exist. Furthermore the most abundant *linear* motifs (such as $m_1, m_2, m_4...$) in ER networks [Fig.3.6 (b)] represent in this case noiseless modes (see [101] and appendix D), determining the abundance of NSs.

Network topological uniformity. We now move to networks with a larger average degree. The degree distribution of Erdős-Rényi networks is known to be binomial, with variance $(N-1)\,p(1-p)$ [307]. A spread of the degree distribution is a good measure of the inhomogeneity of the network topology being maximal at $p = 0.5$ (with maximum value increasing with the size of the network N) and minimal at 0 and 1 (see also appendix D). The comparison of this variance with the NSs abundance in Fig. 3.7 (b) (with inner contours corresponding to larger values of this variance) allows to establish a clear quantitative connection. The *network topological uniformity* is indeed found to be a crucial ingredient for the abundance of noiseless modes also when looking at other networks. Small-world networks, for instance, also display a transition to disorder starting from a regular lattice with a certain degree and randomly rewiring the nodes until becoming a random network (appendix D). Also in this case, as disorder in the topology increases, noiseless mode abundance diminishes, indicating a robust relation between homogeneity in network topology and presence of NSs (appendix D).

Breathing normal modes. A main and intriguing feature of NSs in uniform ER networks is the parity of their sizes, that is the fact that decoherence free normal modes tend to be composed by an *even* number of oscillators, Fig. 3.8 (a), (b). The absence of NSs with odd sizes, independently on the odd or even size of the embedding component, can be traced back to the fact that, for small values of p, string-like components of the network prevail, like motifs $m_{1,2,4,8}$ in Fig. 3.6 (b). In this kind of motifs we can actually identify stretching or *breathing normal modes* which are decoherence free and which involve all the nodes for an even motif, while they do not involve the central node for an odd motif, as discussed in the case of three oscillators in Ref. [101] and in appendix D. The presence of these breathing modes of even size allows to explain the predominance of even NSs below the connectedness transition. Above the connectedness transition, Fig. 3.8 (b), we can show (appendix D) that by embedding the small motifs of Fig. 3.6 (b) (and also those of Fig. D.4 of the appendix D) into the network with the proper symmetries in the connections, the noiseless eigenvectors of these motifs become noiseless eigenvectors of the

whole system. This enables us to clarify why we observe a similar structure in the NSs size when considering very connected ER networks [Fig. 3.8 (b)], where homogeneity in the degree distribution can enable the necessary symmetries in the couplings to be satisfied frequently. It is important to stress that we find this peculiar even modes dominance also for small-world networks (appendix D), which are composed mainly by one component, and which tend to display bigger noiseless modes than ER networks. As a further remark, detuning is known to introduce deviation from breathing modes [101], and this is consistent with the absence of even-odd asymmetry for NSs shown in Fig. 3.9 (d). Finally there is a noteworthy resemblance between the small NSs observed here, and the compact localized states that can be found in certain tight-binding lattices [308]. Also these localized states are often perpendicular to the c.m., and the enabling mechanism is the proper local topology of connections between the involved nodes and the neighboring lattice (see illustrative examples in Refs. [309, 310, 311]). The exploration of the connections between these two different contexts could constitute an interesting future extension to our work.

Inhomogeneous parameters and quasi-noiseless modes. Beyond topological features, we have considered inhomogeneous parameters for nodes and links as these can actually be unavoidable in experiments, as in a circuit QED system [289] or with optical frequency combs [312]. For the frequency combs platform [312], this experimental analysis has not yet been reported but the possibility to achieve identical nodes is discussed in [313] through chirping of the pump optical mode (i.e. a multimode light pulse in which the phase depends functionally on the frequency). On the other hand, a small amount of disorder has been measured in circuit QED lattices [302] and modeled as Gaussian as in our analysis. Frequency disorder up to $\sigma_\omega \sim 10^{-4}$ has been reported, that would significantly hinder NSs (Fig. 3.9), while inhomogeneities in (small) coupling rates are mainly induced by detunings and can be neglected in circuit QED networks [302]. We have analyzed both frequency and couplings disorder: for small connection probabilities NSs are fragile against detuning but not against inhomogeneities in couplings, and the opposite trend is found for large components (Fig. 3.9). This can be understood to follow from the fact that small decoherence free normal modes are more sensitive to inhomogeneity in frequencies. Motifs of two oscillators, for instance, are NSs independently of the value of the coupling and only if their frequencies are identical [65], while NSs for m_2 motifs appear only for special values of detunings [101], consistently with the NSs resilience found for small p's and inhomogeneous coupling strengths. For both detuning and couplings inhomogeneities, Fig. 3.9, the drop in the probability at $p = 1$ follows from the fact that the corresponding fully connected network, in the case of Gaussian distributed parameters, has no NSs. The presence of even small inhomogeneities allows also to avoid degenerate eigenvectors particularly abundant for $p \sim 0$ and $p \sim 1$.

Despite the fragility of NSs to inhomogeneities in parameters observed in Figs. 3.9, we have seen in Fig. 3.10 the existence of *quasi-noiseless* components up to moderate values of disorder ($\sigma_\omega > 0$). The gap in the coupling with the environment of two sets of normal modes, allows one to clearly identify quasi-noiseless subspaces dissipating much slower than other modes. The closure of the gap for $\kappa \sim \sigma_\omega$ can be understood considering that in the limit of small detuning, normal modes will deviate linearly in σ_ω from the NSs found for uniform ER networks. These quasi-NSs that persist in inhomogeneous networks can be useful for practical applications: even if manufacturing imperfections would prevent the existence of asymptotically decoherence free modes, the long coherence time of quasi NSs can serve the purpose of preserving coherences on timescales proportional to the degree of inhomogeneity of the device.

Extension to other models. Finally, it is interesting to comment on the results for other types of system Hamiltonians. In this sense, one can wonder if similar results would hold if we consider instead systems with spring like coupling Hamiltonian $\hat{\mathcal{H}} = \frac{1}{2}\sum_{i=1}^{N}\left(\hat{p}_i^2 + \omega_0^2\hat{q}_i^2\right) + \sum_{i=1}^{N}\sum_{j=1}^{N}\lambda_{ij}(\hat{q}_i - \hat{q}_j)^2$, where all the oscillators have the same frequency and the coupling λ_{ij} can take the values λ or zero. Remarkably, it can be shown (see appendix D) that in this case there are always $N-1$ NSs whatever is the underlying topology. We can also consider a tight-binding model, in which the rotating wave approximation is performed in the coupling term, and hence the number of excitations is conserved by the Hamiltonian. In this case our results would still hold in the case of networks with homogeneous parameters (appendix D). Moreover, for this case, in the presence of a single excitation, our analysis would also apply to spin or fermionic networks while the case of more excitations remains an open question.

3.5 Synchronization in complex networks with collective dissipation

In this section we focus on the emergence of a synchronous dynamics induced by collective dissipation in the complex networks of harmonic oscillators. As we have seen in Sect. 3.2, coupling to the common bath leads to a disparity in the decay rates of the normal modes that enables the emergence of synchronization; after a transient in which each node oscillates irregularly in a superposition of eigenfrequencies, all normal modes, except the one with the slowest decay, relax to equilibrium. Then, this slowest mode fixes the common rhythm of the corresponding nodes within the system either during a long transient or – when the slowest mode is actually noiseless– asymptotically. Moreover, we have seen that this synchronization dynamics emerges both in the first and second moments of the system, and the synchronization region, i.e. the parameter region in which synchronization emerges, is indeed well signaled by the ratio of normal mode decay rates taking a small value (see Fig. 3.2).

When considering the dynamics of our complex networks, we recall that the master equation (3.29) is the direct generalization of the one for the two oscillator case in a common bath (3.11). Then, in complete analogy to this simpler case, we see that the decay rates and diffusion coefficients given in Eq. (3.30) also depend on the squared normal mode overlap with the c.m. mode, i.e. κ_n^2. Therefore, the exact same mechanism enabling synchronization in the case of two oscillators is also present in this more complex scenario. In fact, in Ref. [98] the dynamics of random networks of harmonic oscillators governed by this master equation was considered, showing the emergence of synchronization when one of the normal modes displays a decay rate much smaller than the rest. In this reference, the possibility of transient and stationary synchronization to emerge in random networks with collective dissipation was unveiled. Moreover, it was shown that the synchronized regime is accompanied by long-lived correlations as in smaller arrays [65]. Nevertheless, the role of the network structure was not addressed before Ref. [2].

Here, we follow the results of Ref. [2] that address this question, analyzing how the possibility for transient and stationary synchronization to emerge varies with the parameters of the ER network ensemble, and also considering the prevalence of synchronization in the presence of frequency detunings and inhomogeneous coupling strengths. In order to do so in a systematic fashion, we will take advantage of the fact that the ratio of the smallest and second smallest normal mode decay rates is a witness of synchronization. This is a very convenient quantity, as it can be computed from the overlap of the eigenvectors with the c.m. mode, and hence, we can benefit from a statistical analysis analogous to that of the previous subsections.

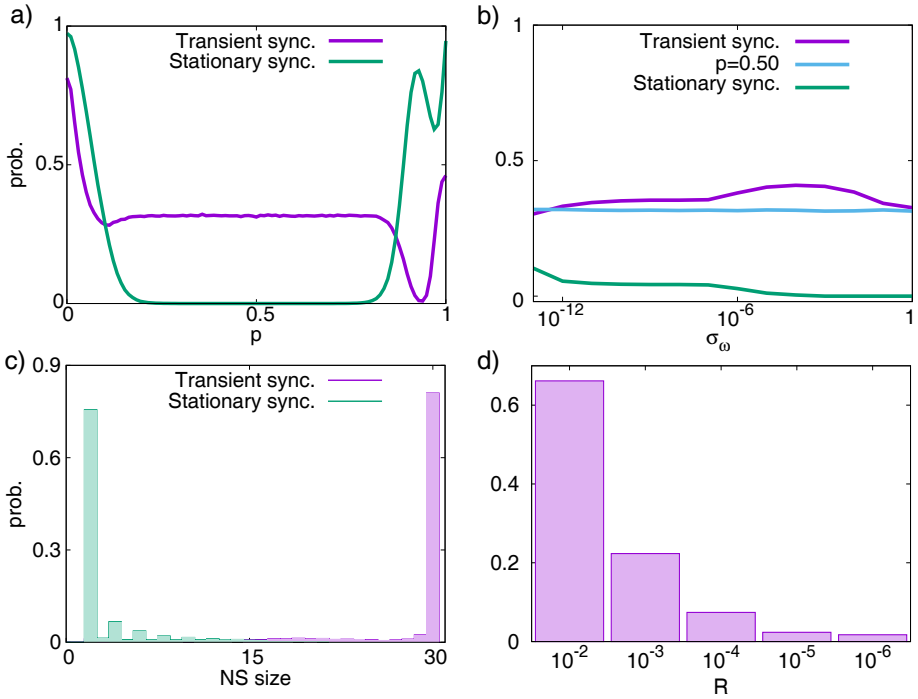

Figure 3.11: For all the panels we consider ER networks of size $N = 30$. a) Probability to find at least one synchronized normal mode which is stationary (green) or transient (purple), varying p, and with uniform parameters. b) Probability to find at least one synchronized normal mode per network as a function of the detunings spread σ_ω: for transient synchronization when $p = 0.5$ (blue, dashed) and when averaging over all p's (purple) and for stationary synchronization when averaging over all p's (green). c) Distribution of sizes for the case of stationary and transient synchronized normal modes, for $\sigma_\omega = 0$ and all the range of p's. d) Distribution of values of R for dissipating normal modes (avoiding completely NSs) for all the range of p's, and again for $\sigma_\omega = 0$.

3.5.1 Prevalence of transient and stationary synchronization in ER networks

First we recall the conditions for which a motif of any network of harmonic oscillators synchronizes: i) when one of the normal modes covering the particular subset of oscillators is coupled more weakly to the bath than the others (significant separation of dissipative timescales), leading to *transient* synchronization [65]; or ii) when there is only one decoherence free normal mode covering the particular subset of oscillators, leading to *stationary* synchronization [98, 101]. In case i) we can set as a significant separation of dissipative timescales when the smallest and second smallest dissipation rates are separated by an order of magnitude [98], i.e. their ratio, $R = (\kappa_1/\kappa_2)^2$, takes values at most of order $R \sim 0.1$, where we denote the normal mode with the smallest decay rate as '1', and the one with the second smallest decay rate as '2'. When this condition is satisfied, after most normal modes dissipate out, there remains only the slowest one, i.e. the one with the smallest coupling to the bath, and the oscillators spanned by this normal mode synchronize and can retain robust quantum correlations [65, 98, 101]. If R is small there is a significant time period in which the network is synchronous before full thermalization. Conditions i) and ii) refer to a particular subset of the network, and of course in the whole network there might be parts of it in which there is synchronization due to mechanism i), and parts of it in which it is due to ii), since both mechanisms are not excluding as long as the synchronizing normal modes span over different subsets of oscillators or oscillate at the same frequency. This is a key observation to take into account in our systematic analysis.

Resilient transient synchronization. In figure 3.11 we analyze the prevalence of dissipative synchronization for ER networks, both with uniform parameters and with detuning $\sigma_\omega \neq 0$. The appearance of stationary synchronization shown in Fig. 3.11 (a) (green line) behaves similarly to the abundance of NSs (see Fig. 3.9) except for p close to 1 where a dip appears. On the other hand, transient synchronization (Fig. 3.11(a) purple line) is a rather robust feature of the network, present with a significant probability (about in one over three networks) in all the range of p's except for a dip appearing again at p close to 1, where stationary synchronization dominates. In panel (b), we look at the effect of detuning, both for a specific average degree (for $p = 0.5$) and on average over all values of p. Transient synchronization is found to be rather *resilient to detuning* (purple line) while stationary synchronization (ii) is more fragile, as expected knowing results about NSs resilience reported in previous section. Analogous results are found for nonuniform couplings (not shown here).

Transient synchronization of the whole network. We now analyze the structure of the synchronous modes. Decoherence free synchronized normal modes (ii) tend to span small number of oscillators and the even-odd asymmetry reported before persists (Fig.3.11 (c) green histogram). More surprising is the fact that transient synchronization (i), beyond being a rather frequent phenomenon for several p and detunings, it does also tend to span all the network (Fig.3.11 (c) purple). This means that a *large set of oscillators synchronize* and will therefore, as previously reported in Refs.[65, 98], share enhanced quantum correlations. The timescale to observe this phenomenon can be assessed through the decays ratio R: the fastest rise of synchronization corresponds to smallest R values [98]. A significant synchronous transient is predicted before thermalization: in Fig.3.11 (d) the distribution of ratios R for $\sigma_\omega = 0$ shows in fact significant fractions of networks with more than two orders of magnitude of separation between the slowest decaying modes. This is weakly influenced by the network structure and displayed aggregating data for different p values.

Discussion. We now discuss in more detail the physical interpretation of these results. We have seen that the probability of transient synchronization is large and resilient in the presence of detunings. Surprisingly it can even be favored by *increasing the detuning* (as shown in Fig. 3.11 (b), purple line) and this might be caused by the corresponding disappearance of stationary synchronization. The fact that this increase is seen when looking at the aggregated data in p, while for $p = 0.5$ (blue line) is not observed, is consistent with this explanation, as for $p = 0.5$ there are no NSs independently of σ_ω. We have also observed that there is a dip in the probability to find synchronization for p close to 1 [Fig. 3.11 (a)]. These dips appearing for high p, both for stationary and transient synchronization, are related to the increasing probability to find large NSs of modes in the same network, of *different* frequencies, diminishing the overall synchronizability of networks. As p is further increased, degeneracy also grows, and overlap between synchronizable modes is no longer detrimental as they exhibit the same frequency, hence explaining the final increase in the synchronization probability.

3.6 Concluding remarks

In this chapter, we have considered the dynamics of coupled dissipative harmonic oscillators, focusing on the emergence of synchronization and on the presence of noiseless degrees of freedom, i.e. normal modes that become effectively uncoupled from the environment. We have started considering a system of just two oscillators, coupled either to separate

baths or to a common bath. Here, we have met the crucial difference between both scenarios: under the standard approximations, in the SB scenario the normal modes of the system display identical decay rate, while in the CB scenario, these decay rates can be different. In fact, we have shown how this disparity enables the emergence of transient synchronization in the common bath case, a phenomenon that can be appreciated in both the dynamics of the first and second moments, and which is known to be accompanied by long-lived correlations [65, 98, 101]. Moreover, it can even happen that, for the CB case, one of the decay rates becomes zero, leading to asymptotic synchronization and to the asymptotic preservation of quantum correlations and coherence [101].

The existence of these mechanisms enabled by the coupling to a common bath was explored in a more complex scenario in which *complex networks* of harmonic oscillators are coupled to a common bath [2]. Here, we have focused on the effects of the complex topology on the presence of noiseless modes, i.e. those with zero decay rate, and synchronization. Moreover, we have also considered the effects of random inhomogeneities in both the frequencies and coupling strengths along the network.

As a first important result, we have found that network topological uniformity is a crucial feature for the presence of noiseless modes. Both for ER and small-world networks, as disorder increases the probability to find NSs is suppressed. Hence, for ER networks, we have found NSs to be abundant for small and large probability of connection p. In the case of small-world networks, these are more abundant for small rewiring probability p_{rw}. Furthermore, by analyzing the structure of the NSs we have unveiled some intriguing features. In particular, we have found that NSs spanning over an odd number of nodes are strongly suppressed, while the structure of these NSs is very similar for the very different cases of ER networks with small p and large p. As we have seen, these two features can be understood considering the normal modes of small motifs (see Figs 3.6 (b) and D.4), in which *breathing* modes are prevalent (involving only an even number of oscillators). These small motifs are dominant in ER networks for small p, while they are also important for large p, as when properly embedded into the whole network (appendix D), their NSs become NSs of the whole network.

Finally, we have considered the effect of inhomogeneous frequencies and detunings along the network. While this variability is generally quite detrimental for the presence of exact noiseless modes, we have found that up to moderate values of parameter inhomogeneities we can still identify a family of quasi-noiseless modes with a lifetime orders of magnitude larger than the rest. This is especially relevant for experimental platforms, as circuit QED systems [289], in which experimental imperfections lead to variability in the system parameters [302].

As for the emergence of synchronization enabled by collective dissipation, we have addressed the effects of network topology on this phenomenon. In order to do so, we have considered the ratio between the smallest normal mode decay rates. As we have seen in Sect. 3.2, this quantity witnesses synchronization: when it is small the timescale separation enabling synchronization is present [65, 98, 101], while when it is not, synchronization cannot emerge as all normal modes relax on a similar timescale. This simple quantity can be efficiently studied in complex scenarios as the one considered here. Our analysis has revealed that stationary synchronization behaves, in general, similarly to the presence of NSs, and thus it is suppressed by topological disorder and parameter variability. On the other hand, transient synchronization has been revealed as a very robust phenomenon, as it is also common in ER networks with intermediate values of p, and even in the presence of parameter inhomogeneities. Moreover, quite remarkably, the transient synchronous modes tend to span the whole network. Therefore, we conclude that transient synchronization can be expected to emerge quite generally in coupled systems with collective dissipation.

CHAPTER 4

Dynamics and synchronization in the presence of coalescence

The contents of this chapter have been adapted from the works entitled *Exceptional points in 1D arrays of quantum harmonic oscillators* [4] and *Synchronization and coalescence in a dissipative two-qubit system* [7]. Here, the presence of exceptional points in the dynamics of two different dissipative systems is analyzed: a chain of coupled harmonic oscillators, and a system of two spins dissipating collectively. We will show that these spectral singularities (EPs) separate different dynamical regimes of these systems, as characterized by the evolution towards the stationary state, the emission spectrum, or the response to an external forcing. One of our main results is that, for both systems, EPs enable a monochromatic regime in which all the collective modes display the same frequency. Moreover, for the spin system, we will analyze the synchronization dynamics emerging in this regime, comparing this peculiar scenario of synchronization in the presence of coalescence with the more known scenarios of transient synchronization.

4.1 Introduction

Exceptional points are singular points in the parameter space of the eigenspectrum of non-Hermitian matrices in which several eigenvalues become the same and the corresponding eigenvectors coalesce, making the matrix non-diagonalizable at these points of parameter space. Non-Hermitian matrices commonly underlay the description of linear photonic arrays with dissipation and gain, in which an effective Hamiltonian with complex energies can be drawn to model the coherent processes as well as the decay/gain of energy occurring in the system. Consequently, the physics of EPs has been extensively studied in this kind of systems in the past decade [204, 205, 206, 207]. On the other hand, non-Hermitian matrices and superoperators are also ubiquitous in the description of quantum dissipative systems, while only recently, the peculiarities of EPs occurring in the Liouvillian, i.e. the full quantum dynamical system, have begun to be addressed [209].

As we have reviewed in chapter 1, EPs have been shown to be behind intriguing phenomena in classical systems, as for instance extreme sensitivity to perturbations [214,

215] or chiral dynamics when performing adiabatic parameter loops around them [47, 48, 216]. This rich phenomenology [204, 205, 206, 207] motivates their study in quantum dissipative systems, where fundamental questions regard how the quantum nature of the system can affect these phenomena or whether there are new and genuine non-Hermitian *quantum* effects to be disclosed. In this sense, in this chapter, we will analyze in detail the dynamical consequences of EPs in two dissipative quantum systems. In particular, the fact that at these EPs the dynamics of the quantum system cannot be fully decomposed in terms of collective modes leads us to a first question: is such a spectral singularity accompanied by a singular behavior of the temporal dynamics of the system? Moreover, many of the best known examples of systems with EPs are systems made of two coupled modes [207], which also raises the question of whether we can find coalescence in extended systems. These questions are tackled in the next section, based on [4], in which we address the dynamics of a one-dimensional (1D) array of dissipative harmonic oscillators with staggered losses. We show that the right interplay between coherent coupling and staggered losses leads to a cascade of EPs in the collective delocalized modes governing the dynamics of the system. Indeed, one of our main findings is that there is a dynamical regime characterized by all the collective modes displaying the same frequency. This single frequency regime is also present in a spin system with collective dissipation [7], as we report in the next section, in which we focus on the connection of this regime with synchronization, comparing this single-frequency dynamics with transient synchronization emerging in similar spin systems [45, 90].

The presence of these non-analytical points in the eigenspectrum is associated with a characteristic branching behavior of the eigenvalues (see next sections or [207], for instance), which is at the heart of the qualitative differences that can be observed in the dynamics of the system, and that characterize the different dynamical regimes separated by EPs. In fact, after this chapter, coalescence will also appear fundamental to understand the dynamics of the squeezed van der Pol oscillator, discussed in chapters 6 and 7.

4.2 Exceptional points in arrays of harmonic oscillators

In this section, we study how the interplay between coherent interactions and dissipation arising independently on each unit of an extended system can lead to coalescence of the normal modes of the system, and we analyze the dynamical consequences of this phenomenon. Specifically, we consider a 1D array of coherently coupled identical bosonic systems each of which dissipates independently with staggered rates. This kind of model can be regarded as a generalization of simpler two resonator models in which coalescence has been already investigated [206, 207, 208], and allows one to study the effects of an extended topology on the physics of EPs. Interestingly, our system shows a set of EPs in both first and second moments dynamics which separate different dynamical regimes characterized by a rich phenomenology, such as qualitative distinct temporal behaviors towards the stationary state and the emergence of interference effects in the transmission and emission spectra.

4.2.1 Tight binding chain of quantum harmonic oscillators

We consider a 1D tight-binding chain of quantum harmonic oscillators with uniform frequencies ω_0 and nearest neighbour coupling rates λ. The units are weakly coupled to independent baths in a staggered way, such that the system is composed of N cells of two dissipative modes each, with open boundary conditions. The Hamiltonian and master equation in the standard Born-Markov approximations describing the system and in the

rotating frame with ω_0 read ($\hbar = 1$):

$$\hat{H} = -\lambda \sum_{n=1}^{N} (\hat{a}_n^\dagger \hat{b}_n + h.c.) - \lambda \sum_{n=1}^{N-1} (\hat{a}_{n+1}^\dagger \hat{b}_n + h.c.), \tag{4.1}$$

$$\frac{d}{dt}\hat{\rho} = -i[\hat{H}, \hat{\rho}] + \sum_{n=1}^{N} \sum_{o=a,b} \left(2\gamma_o^c \mathcal{D}[\hat{o}_n]\hat{\rho} + 2\gamma_o^h \mathcal{D}[\hat{o}_n^\dagger]\hat{\rho}\right), \tag{4.2}$$

with local dissipation in each oscillator ($\hat{o}_n = \{\hat{a}_n, \hat{b}_n\}$). Notice that in principle we consider general out-of-equilibrium environments in which the rates $\gamma_{a(b)}^c$ and $\gamma_{a(b)}^h$ are not constrained to satisfy detailed balance. This dissipation can be achieved in several ways and in chapter 2 we mentioned the case of optomechanical systems used to engineer both coherent couplings and dissipation rates, by proper adiabatic elimination of the optical degrees of freedom [251, 252, 261]. The model described by Eqs. (4.1) and (4.2) is quadratic in the creation and annihilation operators of the bosonic modes. Consequently, if one considers Gaussian initial states, the state of the system is completely characterized by the first and second moments, while the stationary state of the system is Gaussian, independently of such initial condition [266, 267].

4.2.2 Dynamics of the first moments

Let us start our analysis considering the first moments, whose dynamics can be understood as the superposition of N independent pairs of interacting modes. Each of these pairs, from now on referred to as k-modes, displays two dynamical regimes separated by an EP. These regimes are characterized by the number of dynamical frequencies of the system and the way it decays (Fig. 4.1). The equations of motion of the first moments read

$$\frac{d}{dt}\langle \hat{a}_n \rangle = -\gamma_a \langle \hat{a}_n \rangle - i\lambda\left(\langle \hat{b}_{n-1} \rangle (1 - \delta_{n,1}) + \langle \hat{b}_n \rangle\right), \tag{4.3}$$

$$\frac{d}{dt}\langle \hat{b}_n \rangle = -\gamma_b \langle \hat{b}_n \rangle - i\lambda\left(\langle \hat{a}_n \rangle + \langle \hat{a}_{n+1} \rangle (1 - \delta_{n,N})\right), \tag{4.4}$$

with $n \in [1, N]$, $\gamma_{a(b)} = \gamma_{a(b)}^c - \gamma_{a(b)}^h$, and $\delta_{n,n'}$ the Kronecker delta. Equations (4.3) and (4.4) can be conveniently written in matrix notation as

$$\frac{d}{dt}\vec{u} = \mathsf{M}\vec{u} + \vec{F}, \tag{4.5}$$

where $\vec{u} = \left(\langle \hat{a}_1 \rangle, \langle \hat{b}_1 \rangle, \ldots, \langle \hat{a}_N \rangle, \langle \hat{b}_N \rangle\right)^T$ and we have introduced the term $\vec{F} = \big(\alpha_1(t), \beta_1(t), \ldots, \alpha_N(t), \beta_N(t)\big)^T$ that represents a possible additional driving term and which will be considered to be nonzero only in Sect. 4.2.3.

Exceptional points. Let us introduce the vector of moments via the orthogonal transformation $\vec{\tilde{u}} = \mathsf{P}^T \vec{u}$, where $\vec{\tilde{u}}$ is the vector that contains the expectation values of the k-modes $\hat{a}_{k_l}, \hat{b}_{k_l}$ defined by:

$$\hat{a}_{k_l} = \sum_{n=1}^{N} \hat{a}_n \mathcal{S}_{n,k_l}^{(a)}, \quad \hat{a}_n = \sum_{l=1}^{N} \hat{a}_{k_l} \mathcal{S}_{n,k_l}^{(a)}, \tag{4.6}$$

$$\mathcal{S}_{n,k_l}^{(a)} = \sqrt{\frac{2}{N+\frac{1}{2}}} \sin[k_l(n - \frac{1}{2})], \quad \mathcal{S}_{n,k_l}^{(b)} = \sqrt{\frac{2}{N+\frac{1}{2}}} \sin(k_l n), \tag{4.7}$$

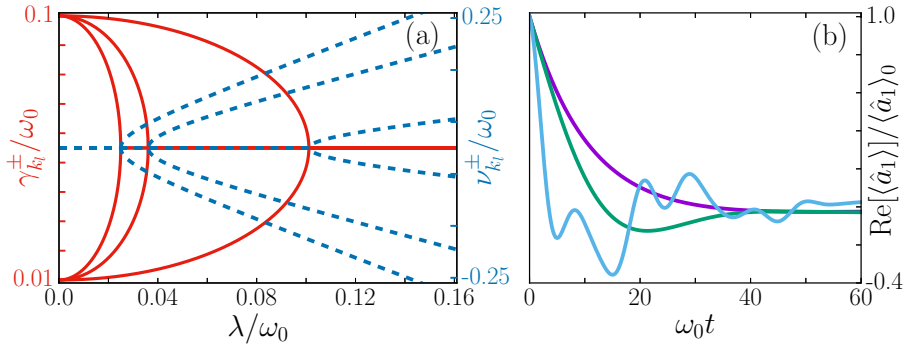

Figure 4.1: (a) Real and imaginary parts of $\Omega^{\pm}_{k_l}$ in red solid lines and blue dashed lines, respectively. (b) Real part of $\langle\hat{a}_1\rangle$ as a function of time. In magenta $\lambda/\omega_0 = 0.025$ in which all k-modes are in the single-frequency regime except for k_1. In green $\lambda/\omega_0 = 0.1$ in which all modes are in the two-frequency regime except those of k_3. In blue $\lambda/\omega_0 = 0.5$ and all modes are well into the two-frequency regime. Initial condition corresponds to excitation of the first site solely. In both panels $N = 3$, $\gamma_a/\omega_0 = 0.1$ and $\gamma_b/\omega_0 = 0.01$.

with $k_l = \pi l/(N+1/2)$, $\quad l = 1,\ldots,N$, and similarly for $\hat{b}_n, \hat{b}_{k_l}$. This transformation preserves the commutation relations since

$$\sum_{n=1}^{N} \mathcal{S}^{(x)}_{n,k_l}\mathcal{S}^{(x)}_{n,k_{l'}} = \delta_{l,l'}, \quad \sum_{l=1}^{N} \mathcal{S}^{(x)}_{n,k_l}\mathcal{S}^{(x)}_{n',k_l} = \delta_{n,n'} \tag{4.8}$$

with $x = a, b$. Then, $\widetilde{\mathsf{M}} = \mathsf{P}^T\mathsf{M}\mathsf{P}$ [with M of Eq. (4.5)] with $\widetilde{\mathsf{M}} = \bigoplus_{l=1}^{N}\widetilde{\mathsf{M}}_{k_l}$ and

$$\widetilde{\mathsf{M}}_{k_l} = \begin{pmatrix} -\gamma_a & -i\lambda_{k_l} \\ -i\lambda_{k_l} & -\gamma_b \end{pmatrix}, \tag{4.9}$$

with $\lambda_{k_l} = 2\lambda\cos(k_l/2)$. The eigenvalues of the whole system are obtained by diagonalizing the 2×2 blocks and read:

$$\Omega^{\pm}_{k_l} = \frac{\bar{\gamma}}{2} \pm \frac{1}{2}\sqrt{(\gamma_a-\gamma_b)^2 - 4\lambda^2_{k_l}}, \tag{4.10}$$

with $\bar{\gamma} = \gamma_a + \gamma_b$. Therefore, we obtain that, as the coupling λ is varied, below a certain threshold the eigenvalues are real, while above they become complex. The eigenvalues real and imaginary parts are defined^{-} as $\gamma^{\pm}_{k_l}$ and $\nu^{\pm}_{k_l}$ respectively [Fig. 4.1 (a)]

When the imaginary parts vanish (moving from the rotating frame to the lab one) all units oscillate at their bare frequencies, ω_0, in spite of their mutual interactions. This is in stark contrast to what one observes in the corresponding closed system where, for any coupling strength, the eigenfrequencies differ from the intrinsic frequency ω_0. At the threshold point the square root in Eq. (4.10) vanishes and the two eigenvalues with the corresponding *eigenvectors* coalesce [208, 314]. This point is thus an EP, at which $\widetilde{\mathsf{M}}_{k_l}$ (and thus M) becomes non-diagonalizable. Therefore, our system displays N EPs [Fig. 4.1 (a)], one for each k_l. The EPs separate different regimes in which the number of frequencies varies from 1 to $2N$, a feature that can not be observed for any closed or homogeneously dissipating system. In the case of balanced loss rates $\gamma_a = \gamma_b$, the bath would only introduce a uniform dissipation decay, while the frequencies would depart from ω_0 and be modified by λ as in the absence of the environment. EPs are indeed enabled by the staggered losses we have introduced, when their absolute imbalance take certain values with respect to the chain coupling strength λ.

Decay dynamics. To study the decay dynamics near an EP, we proceed to solve directly the block-diagonal system of equations using Laplace transform method, i.e. considering the Laplace transformed expectation values $\langle \hat{x}(s)\rangle = \int_0^\infty \langle \hat{x}(t)\rangle e^{-st} dt$. The equations for the k-modes are:

$$\frac{d}{dt}\langle \hat{a}_{k_l}\rangle = -\gamma_a \langle \hat{a}_{k_l}\rangle - i\lambda_{k_l}\langle \hat{b}_{k_l}\rangle, \tag{4.11}$$

$$\frac{d}{dt}\langle \hat{b}_{k_l}\rangle = -\gamma_b \langle \hat{b}_{k_l}\rangle - i\lambda_{k_l}\langle \hat{a}_{k_l}\rangle. \tag{4.12}$$

Solving their Laplace transformed version we obtain in the s-domain:

$$\langle \hat{a}_{k_l}(s)\rangle = \frac{(s+\gamma_b)\langle \hat{a}_{k_l}\rangle_0 - i\lambda_{k_l}\langle \hat{b}_{k_l}\rangle_0}{(s+\Omega^+_{k_l})(s+\Omega^-_{k_l})}, \tag{4.13}$$

$$\langle \hat{b}_{k_l}(s)\rangle = \frac{(s+\gamma_a)\langle \hat{b}_{k_l}\rangle_0 - i\lambda_{k_l}\langle \hat{a}_{k_l}\rangle_0}{(s+\Omega^+_{k_l})(s+\Omega^-_{k_l})}, \tag{4.14}$$

where the initial condition is given by $\langle \hat{a}_{k_l}(\hat{b}_{k_l})\rangle_0$. The poles $\Omega^\pm_{k_l}$ correspond to the eigenvalues of M, which displays an EP in each k-block at

$$|2\lambda_k| = |\gamma_a - \gamma_b|. \tag{4.15}$$

Here, an EP appears as a double pole, which clearly indicates that the decay dynamics is not purely exponential but displays polynomial corrections.

Dynamical regimes. From Eqs. (4.10), (4.13) and (4.14) we identify two dynamical regimes for each k-mode, separated by an EP. i) *Single-frequency regime* $|\gamma_a - \gamma_b| > |2\lambda_{k_l}|$: we have two different real poles and no oscillations (in the rotating frame). ii) *Exceptional point* $|\gamma_a - \gamma_b| = |2\lambda_{k_l}|$: we have a real second order pole, yielding polynomial corrections to the exponential decay without oscillations. iii) *Two-frequency regime* $|\gamma_a - \gamma_b| < |2\lambda_{k_l}|$: we have two different complex poles, yielding oscillations with equal damping. In the time domain the dynamics in each regime read as:
i) *Single-frequency regime*:

$$\langle \hat{a}_{k_l}\rangle = \left\{ \langle \hat{a}_{k_l}\rangle_0 \frac{(\gamma_b - \gamma^+_{k_l})e^{-\gamma^+_{k_l}t} - (\gamma_b - \gamma^-_{k_l})e^{-\gamma^-_{k_l}t}}{\gamma^-_{k_l} - \gamma^+_{k_l}} - i\lambda_{k_l}\langle \hat{b}_{k_l}\rangle_0 \frac{e^{-\gamma^+_{k_l}t} - e^{-\gamma^-_{k_l}t}}{\gamma^-_{k_l} - \gamma^+_{k_l}} \right\}\theta(t), \tag{4.16}$$

where $\theta(t)$ is the Heaviside step function. Notice that in all cases the solution for $\langle \hat{b}_{k_l}\rangle$ is obtained from the one of $\langle \hat{a}_{k_l}\rangle$ by exchanging the labels $a \leftrightarrow b$ and the initial conditions. In this regime the poles are real and read as $2\gamma^\pm_{k_l} = \bar{\gamma} \pm \sqrt{(\gamma_a - \gamma_b)^2 - 4\lambda^2_{k_l}}$.
ii) *Exceptional point*:

$$\langle \hat{a}_{k_l}\rangle = e^{-\frac{\bar{\gamma}}{2}t}\left\{ \langle \hat{a}_{k_l}\rangle_0 [1 + \frac{\gamma_b - \gamma_a}{2}t] - i\lambda_{k_l} t \langle \hat{b}_{k_l}\rangle_0 \right\}\theta(t), \tag{4.17}$$

iii) *Two-frequency regime*:

$$\langle \hat{a}_{k_l}\rangle = e^{-\frac{\bar{\gamma}}{2}t}\left\{ \langle \hat{a}_{k_l}\rangle_0 \big[\frac{\gamma_b - \gamma_a}{2\nu_{k_l}} \sin(\nu_{k_l}t) + \cos(\nu_{k_l}t) \big] - i\frac{\lambda_{k_l}}{\nu_{k_l}} \langle \hat{b}_{k_l}\rangle_0 \sin(\nu_{k_l}t) \right\}\theta(t), \tag{4.18}$$

Here the poles are complex, and the oscillation frequencies are given by the imaginary part of the eigenvalues, i.e. $\nu_{k_l} = \frac{1}{2}\sqrt{4\lambda^2_{k_l} - (\gamma_a - \gamma_b)^2}$.

The solution in the site basis is obtained reversing the orthogonal transformation, i.e. $\vec{u} = \mathsf{P}\vec{\tilde{u}}$ [Eq. (4.6)]. Hence, in the site basis, the local dynamics is a combination of the

different k-modes ones. As anticipated, the number of frequencies at which the modes can oscillate changes depending on the regime. Below the first EP, the modes oscillate monochromatically, despite the finite coherent coupling. This region of monochromatic evolution of all units occurs in a parameter window that depends on the size of the system: in the limit of large N the decay imbalance $|\gamma_a - \gamma_b| > 4\lambda$ is required to overcome the coupling, while for just a pair of oscillators one would get a smaller imbalance $|\gamma_a - \gamma_b| > 2\lambda$.

When the previous condition is not fulfilled, for instance increasing the coupling λ between elements, more k-modes enter in the two-frequency regime and, in the site basis, up to $2N$ frequencies are observed (Fig. 4.1). At the EP, the first moments present an exponential-power law decay [218]. The exponent of the polynomial corrections can be at most $h-1$, where h is the number of eigenvalues that coalesce, i.e. the order of the EP. For higher order EPs, more frequencies merge at the EP, and the variability in the number of frequencies displayed by the system is magnified. This could occur in our system when periodically modulating losses over larger cells. Finally notice that, despite the peculiar behavior at the EP and its singular spectral character, the solutions are continuous in the transition from one regime to the other, as also observed in other physical contexts (see below).

4.2.3 Driven system and transmission spectrum

Let us now move to the case of a system with driving, i.e. nonzero F. The details on the general solutions are provided in appendix E. Here we focus on the particular case in which we only drive one oscillator with an oscillatory input of frequency ω_n starting at time zero, i.e. $\alpha_n(t) = \eta_c \alpha e^{i\Delta_n t}\theta(t)$ with $\Delta_n = \omega_n - \omega_0$. Then in the k-basis the driving terms read as $\alpha_{k_l}(t) = \eta_c \alpha \mathcal{S}^{(a)}_{n,k_l} e^{i\Delta_n t}\theta(t)$ and $\beta_{k_l}(t) = 0 \ \forall l$, where α is the driving strength and η_c characterizes the input channel. Assuming vanishing initial conditions (see appendix E), the solution in the s-domain is given by:

$$\langle \hat{a}_{k_l}(s)\rangle = \frac{(s+\gamma_b)\eta_c \alpha \mathcal{S}^{(a)}_{n,k_l}}{(s-i\Delta_n)(s+\Omega^+_{k_l})(s+\Omega^-_{k_l})}, \tag{4.19}$$

$$\langle \hat{b}_{k_l}(s)\rangle = \frac{-i\lambda_{k_l}\eta_c \alpha \mathcal{S}^{(a)}_{n,k_l}}{(s-i\Delta_n)(s+\Omega^+_{k_l})(s+\Omega^-_{k_l})}. \tag{4.20}$$

Notice that the only pure imaginary pole is $s = i\Delta_n$. Hence, in the transient dynamics towards the steady state, the different dynamical regimes are manifested in the dynamical response of the system to the oscillatory drive through $\Omega^{\pm}_{k_l}$. In fact, in the steady state, the intrinsic dynamics of the system appears through the residue of $s = i\Delta_n$, which leads to the following stationary amplitudes for the k-modes:

$$\langle \hat{a}_{k_l}\rangle_{ss} = \frac{(i\Delta_n+\gamma_b)\eta_c \alpha \mathcal{S}^{(a)}_{n,k_l} e^{i\Delta_n t}}{(i\Delta_n+\Omega^+_{k_l})(i\Delta_n+\Omega^-_{k_l})}, \tag{4.21}$$

$$\langle \hat{b}_{k_l}\rangle_{ss} = \frac{-i\lambda_{k_l}\eta_c \alpha \mathcal{S}^{(a)}_{n,k_l} e^{i\Delta_n t}}{(i\Delta_n+\Omega^+_{k_l})(i\Delta_n+\Omega^-_{k_l})}. \tag{4.22}$$

It is useful for the discussion that follows to particularize the expression for $\langle \hat{a}_{k_l}\rangle_{ss}$ in the two dynamical regimes, making use of the explicit expression of $\Omega^{\pm}_{k_l}$. In the single-frequency regime we have:

$$\langle \hat{a}_{k_l}\rangle_{ss} = \frac{\eta_c \alpha \mathcal{S}^{(a)}_{n,k_l} e^{i\Delta_n t}}{\gamma^+_{k_l} - \gamma^-_{k_l}}\left[\frac{\gamma^+_{k_l}-\gamma_b}{i\Delta_n+\gamma^+_{k_l}} - \frac{\gamma^-_{k_l}-\gamma_b}{i\Delta_n+\gamma^-_{k_l}}\right], \tag{4.23}$$

while in the two-frequency regime we have:

$$\langle \hat{a}_{k_l} \rangle_{ss} = \frac{\eta_c \alpha \mathcal{S}^{(a)}_{n,k_l} e^{i\Delta_n t}}{2i\nu_{k_l}} \left[\frac{\frac{\gamma_a - \gamma_b}{2} + i\nu_{k_l}}{i(\Delta_n + \nu_{k_l}) + \frac{\bar{\gamma}}{2}} - \frac{\frac{\gamma_a - \gamma_b}{2} - i\nu_{k_l}}{i(\Delta_n - \nu_{k_l}) + \frac{\bar{\gamma}}{2}} \right]. \tag{4.24}$$

Hence, the steady amplitudes display a multi-resonance character with the driving detuning: i.e. the steady amplitude is strongly modulated by the frequency of the driving and the collective modes that can resonate with this frequency.

Signatures of the different dynamical regimes of a driven system can be identified in the transmission/reflection spectra, as done for instance in investigations of optomechanically induced transparency [315, 316]. In this sense, the input-output relation connecting the field that enters the driven mode with the field that comes out from it can be written as [23, 60]:

$$\hat{a}^{\text{out}}_n = \hat{a}^{\text{in}}_n - \eta_c \hat{a}_n. \tag{4.25}$$

Here, $\hat{a}^{\text{out}}_n$ represents the output field going outwards the resonator n (i.e. the field that leaks to the environment from the resonator), while $\hat{a}^{\text{in}}_n$ represents the input field going inwards the resonator n, and η_c the coupling strength of the system to this particular input-output channel. Then, within the assumption that the input-output channel is exactly the same as the decay channel described in the master equation (i.e. there is only one input-output channel per mode), we have that $\eta_c = \sqrt{\gamma_a}$ [60] [1]. Notice that in the presence of coherent driving $\langle \hat{a}^{\text{in}}_n \rangle = \alpha e^{i\Delta_n t}\theta(t)$, while in the absence of it, and for this kind master equation, the input field is quantum white noise with $\langle \hat{a}^{\text{in}}_n \rangle = 0$ [60]. We define the *transmission coefficient* as the ratio between the output and the input field of the driven resonator, i.e. $T = \langle \hat{a}^{\text{out}}_n \rangle / \langle \hat{a}^{\text{in}}_n \rangle$, which in the steady state reads:

$$T_{ss} = 1 - \sqrt{\gamma_a} \sum_{l=1}^{N} \frac{\mathcal{S}^{(a)}_{n,k_l} \langle \hat{a}_{k_l} \rangle_{ss}}{\langle \hat{a}^{\text{in}}_n \rangle}. \tag{4.26}$$

The different regimes described explicitly by Eq. (4.23) and (4.24) translate into different behaviors of the transmission spectrum. In particular, the multi-resonance character of the steady amplitude will translate into a transmission spectrum with multiple resonances and with possible interference effects between them. This can be observed in Fig. 4.2, in which we plot Eq. (4.26) (red solid lines) for three different cases: in (a) [and (b)] $\lambda/\omega_0 = 0.02$ all k-modes are in the single-frequency regime, in (c) $\lambda/\omega_0 = 0.1$ (only the two modes with wavevector k_3 are in the single-frequency regime), while in (d) $\lambda/\omega_0 = 0.35$ (all k-modes are well into the two-frequency regime).

Transparency window. A surprising feature of this spectrum is that, in cases (a-b-c), the system displays a transparency window centered at ω_0, despite the presence of k-modes of this frequency that naively should resonate perfectly with the driving. This can be understood by analyzing the stationary amplitude of the k-modes in the single-frequency

[1] Notice that, consistently with the input-output relation and our choice for η_c, the output field can correctly represent either the reflected field outside a Fabry-Pérot cavity (with only one leaky mirror), or the transmitted field in a unidirectional waveguide-resonator system (e.g. a whispering-gallery resonator evanescently coupled to a waveguide) [23]. Further generalizations to many input-output channels are possible [60], and they indeed describe other experimental situations [23, 317]. As we do not focus on any specific platform, we have analyzed the simplest scenario of only one input-output channel per resonator, i.e. $\eta_c = \sqrt{\gamma_a}$, and we have interpreted it as the transmitted field through an unidirectional waveguide-resonator system. Qualitative changes are not expected in these more general scenarios, as the reported results emerge due to the interference between the collective modes of the system [i.e. Eqs. (4.23) and (4.24)] and not because of the specific input-output geometry. In fact, the presence of more channels usually induces a loss of contrast in the transmission or reflection spectrum (e.g. transmission or reflection are not perfectly blocked) as illustrated in Ref. [315], in which the observation of interference windows in an experiment with optomechanical oscillators is discussed in detail.

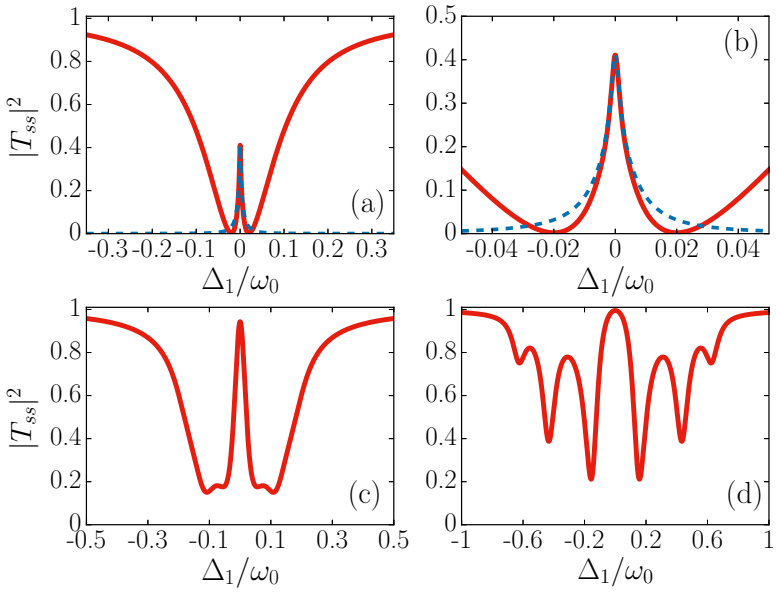

Figure 4.2: Spectral transmission $|T_{ss}|^2$ for mode $\hat{a}_1$ driven at frequency ω_1/ω_0 with $\Delta_1 = \omega_1 - \omega_0$. (a) $\lambda/\omega_0 = 0.02$. (b) Zoom in of the interference window. (c) $\lambda/\omega_0 = 0.1$ and (d) $\lambda/\omega_0 = 0.35$. In all cases $N = 3$, $\gamma_a/\omega_0 = 0.1$, and $\gamma_b/\omega_0 = 0.001$. In red solid lines, exact expression. In blue dashed lines, approximate expression.

regime. Indeed, from Eq. (4.23) we see that these amplitudes have two contributions that interfere destructively, both centered at the same frequency but with different decay rate. In fact, for weak coupling $\gamma_a \gg \lambda_{k_l}$, large disparity $\gamma_a \gg \gamma_b$, and near the resonant driving $\gamma_a \gg |\Delta_n|$, we can approximate the transmission spectrum as:

$$T_{ss} \approx \sum_{l=1}^{N} \frac{(\lambda_{k_l}^2/\gamma_a)(\mathcal{S}_{n,k_l}^{(a)})^2}{i\Delta_n + \gamma_b + \lambda_{k_l}^2/\gamma_a}, \tag{4.27}$$

where we have made the replacements $\gamma_{k_l}^+ \approx \gamma_a$, $\gamma_{k_l}^- \approx \gamma_b + \lambda_{k_l}^2/\gamma_a$ and $\gamma_a + i\Delta_n \approx \gamma_a$, accordingly to the above assumptions. In Fig. 4.2 (b) we compare this approximate expression (blue dashed lines) with the exact one, finding good agreement in the expected region. Thus Eq. (4.27) enables us to clearly visualize the Lorentzian transparency window that emerges in the single-frequency regime. Notice that the height and width of this window increase with the coupling strength, as it is clear from this expression and panels (a) and (c). Similar *interaction induced* transparency windows have been already observed in different systems and configurations, as for instance in optical resonators [318, 319] or optomechanical systems [315, 316, 320], and can be ultimately traced back to the rather general phenomena of Fano interference and electromagnetic induced transparency (EIT) [321, 322]. Therefore, remarkably, the interference between multiple resonances with the same frequency limits the capacity of the system to absorb the energy of a resonant input.

In the two-frequency regime we find the more intuitive result that each k-mode contributes to the transmission spectrum with a Lorentzian absorption line centered at its frequency [see Eq. (4.24) and Fig.4.2(d)]. In this case it is no surprise that the system is fully transparent at $\Delta_1 = 0$ as there are no k-modes resonant to this frequency. Furthermore, a distinctive feature of our system (enabled by this extended geometry) is that it can work in both regimes simultaneously, as in case of Fig.4.2 (c), in which there is the transparency window due to the k_3 modes, but there are also two double peak Lorentzian absorption lines due to the other k-modes. Finally we observe that the transmission coefficient is continuous along the different dynamical regimes, as it follows from Eqs. (4.21)

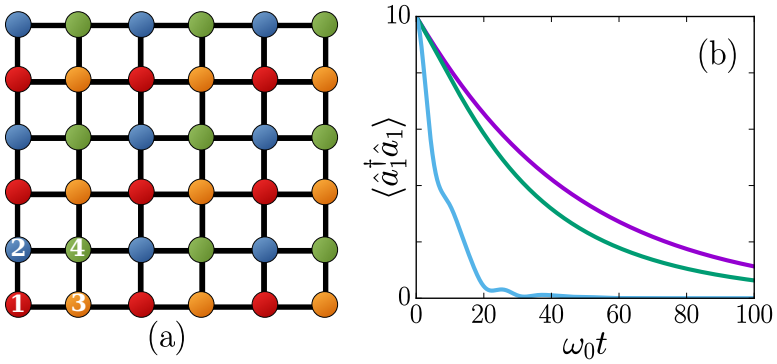

Figure 4.3: (a) Lattice model for $N = 3$, red dots (1) $\langle \hat{a}_n^\dagger \hat{a}_m \rangle$, green dots (4) $\langle \hat{b}_n^\dagger \hat{b}_m \rangle$, blue dots (2) $\langle \hat{a}_n^\dagger \hat{b}_m \rangle$, orange dots (3) $\langle \hat{b}_n^\dagger \hat{a}_m \rangle$. (b) Population of the first site for $\lambda/\omega_0 = 0.01$ (magenta), $\lambda/\omega_0 = 0.025$ (green), and $\lambda/\omega_0 = 0.2$ (blue), with $N = 3$, $\gamma_a/\omega_0 = 0.01$, $\gamma_b/\omega_0 = 0.1$, $\gamma_a^h/\gamma_a = \gamma_b^h/\gamma_b = 0$, $n_a = 10$, $n_b = 1$.

and (4.26) and the fact that $\Omega_{kl}^{\pm}$ are continuous. This is in spite of the singular character of the EPs and in accordance with what we have commented previously in Sect. 4.2.2.

4.2.4 Dynamics of the second moments

Let us now consider the dynamics of the second moments. We will first discuss the general method to solve the set of coupled equations of motion, showing that in general the dynamical scenario becomes more complex. Nevertheless, the same dynamical regimes will be shown to emerge in some special instances. Then we will compute the steady state, which will be used to analyze signatures of the EPs in the fluctuation emission spectrum of the system.

Equations for the second moments. The system of differential equations describing the dynamics of the second moments is divided into two uncoupled blocks: a homogeneous set of equations for the dynamics of all possible moments of the kind $\langle \hat{a}_n^\dagger \hat{a}_{n'}^\dagger \rangle$, $\langle \hat{b}_n^\dagger \hat{b}_{n'}^\dagger \rangle$, $\langle \hat{a}_n^\dagger \hat{b}_{n'}^\dagger \rangle$ and their Hermitian conjugates, and an inhomogeneous system of equations set for the dynamics of all terms of type $\langle \hat{a}_n^\dagger \hat{a}_{n'} \rangle$, $\langle \hat{b}_n^\dagger \hat{b}_{n'} \rangle$, $\langle \hat{a}_n^\dagger \hat{b}_{n'} \rangle$ together with their conjugates. The inhomogeneous block of equations (the only relevant part in our analysis) can be readily written from Eqs. (4.1) and (4.2):

$$\dot{A}_{n,m} = i\lambda\big[D_{n,m} + D_{n-1,m}(1-\delta_{n,1}) - C_{n,m} - C_{n,m-1}(1-\delta_{m,1})\big] - 2\gamma_a A_{n,m} + 2\gamma_a^h \delta_{n,m}, \tag{4.28}$$

$$\dot{B}_{n,m} = i\lambda\big[C_{n,m} + C_{n+1,m}(1-\delta_{n,N}) - D_{n,m} - D_{n,m+1}(1-\delta_{m,N})\big] - 2\gamma_b B_{n,m} + 2\gamma_b^h \delta_{n,m}, \tag{4.29}$$

$$\dot{C}_{n,m} = i\lambda\big[B_{n-1,m}(1-\delta_{n,1}) - A_{n,m} + B_{n,m} - A_{n,m+1}(1-\delta_{m,N})\big] - \bar{\gamma} C_{n,m}, \tag{4.30}$$

$$\dot{D}_{n,m} = i\lambda\big[A_{n,m} - B_{n,m-1}(1-\delta_{m,1}) - B_{n,m} + A_{n+1,m}(1-\delta_{n,N})\big] - \bar{\gamma} D_{n,m} m, \tag{4.31}$$

where we have defined $A_{n,m} = \langle \hat{a}_n^\dagger \hat{a}_m \rangle$, $B_{n,m} = \langle \hat{b}_n^\dagger \hat{b}_m \rangle$, $C_{n,m} = \langle \hat{a}_n^\dagger \hat{b}_m \rangle$, and $D_{n,m} = \langle \hat{b}_n^\dagger \hat{a}_m \rangle$, with $n, m \in [1, N]$, and we have used the dot in place of the time derivative. Notice that the structure of this system of equations is that of a square lattice with four different sites per unit cell, Fig. 4.3(a). This suggests that the system of equations can be brought to a block diagonal form by means of the orthogonal transformation P generalized to a 2D lattice. Thus, two wave-vectors are needed, k_x and k_y, and each block reads:

$$\dot{A}_{k_x,k_y} = i(\lambda_{k_x} D_{k_x,k_y} - \lambda_{k_y} C_{k_x,k_y}) - 2\gamma_a A_{k_x,k_y} + 2\gamma_a^h \delta_{k_x,k_y}, \tag{4.32}$$

$$\dot{B}_{k_x,k_y} = i(\lambda_{k_x} C_{k_x,k_y} - \lambda_{k_y} D_{k_x,k_y}) - 2\gamma_b B_{k_x,k_y} + 2\gamma_b^h \delta_{k_x,k_y}, \tag{4.33}$$

$$\dot{C}_{k_x,k_y} = i(\lambda_{k_x} B_{k_x,k_y} - \lambda_{k_y} A_{k_x,k_y}) - \bar{\gamma} C_{k_x,k_y}, \tag{4.34}$$

$$\dot{D}_{k_x,k_y} = i(\lambda_{k_x} A_{k_x,k_y} - \lambda_{k_y} B_{k_x,k_y}) - \bar{\gamma} D_{k_x,k_y}, \tag{4.35}$$

where we have defined $A_{k_x,k_y} = \langle \hat{a}^\dagger_{k_x} \hat{a}_{k_y} \rangle$, $B_{k_x,k_y} = \langle \hat{b}^\dagger_{k_x} \hat{b}_{k_y} \rangle$, $C_{k_x,k_y} = \langle \hat{a}^\dagger_{k_x} \hat{b}_{k_y} \rangle$, and $D_{k_x,k_y} = \langle \hat{b}^\dagger_{k_x} \hat{a}_{k_y} \rangle$. Hence, we have transformed a general set of $4N$ coupled differential equations into a reduced one of only 4 coupled equations, which can readily be solved. In the following we calculate explicitly the general solution of Eqs. (4.32-4.35) in the cases in which EPs are observed and the stationary state of the system.

EPs in the second moments. Let us take an initial condition that is uniform along each sublattice, $\langle \hat{a}^\dagger_n \hat{a}_m \rangle_0 = n_a \delta_{n,m}$, $\langle \hat{b}^\dagger_n \hat{b}_m \rangle_0 = n_b \delta_{n,m}$ and $\langle \hat{b}^\dagger_n \hat{a}_m \rangle_0 = \langle \hat{a}^\dagger_n \hat{b}_m \rangle_0 = 0 \ \forall n, m$, and analyze the evolution of the population of each mode. Using the orthogonality properties of the canonical transformation defined in Eq. (4.6), we can show that in the k-basis the initial condition reads:

$$\langle \hat{a}^\dagger_{k_x} \hat{a}_{k_y} \rangle_0 = n_a \delta_{k_x,k_y}, \quad \langle \hat{b}^\dagger_{k_x} \hat{b}_{k_y} \rangle_0 = n_b \delta_{k_x,k_y} \tag{4.36}$$

and the rest of second moments are zero. Then, all sectors of Eqs. (4.32-4.35) with $k_x \neq k_y$ vanish identically at all times. The solutions in the k-basis and in s-domain are:

$$A_{k_l,k_l}(s) = \frac{[2\lambda_{k_l}^2 + (s+2\gamma_b)(s+\bar{\gamma})]A(s) + 2\lambda_{k_l}^2 B(s)}{(s+\bar{\gamma})(s+2\Omega^+_{k_l})(s+2\Omega^-_{k_l})}, \tag{4.37}$$

$$B_{k_l,k_l}(s) = \frac{[2\lambda_{k_l}^2 + (s+2\gamma_a)(s+\bar{\gamma})]B(s) + 2\lambda_{k_l}^2 A(s)}{(s+\bar{\gamma})(s+2\Omega^+_{k_l})(s+2\Omega^-_{k_l})}, \tag{4.38}$$

$$C_{k_l,k_l}(s) = \frac{i\lambda_{k_l}[(s+2\gamma_a)B(s) - (s+2\gamma_b)A(s)]}{(s+\bar{\gamma})(s+2\Omega^+_{k_l})(s+2\Omega^-_{k_l})}, \tag{4.39}$$

with $D_{k_l,k_l}(s) = C^*_{k_l,k_l}(s)$, $A(s) = n_a + 2\gamma_a^h/s$ and $B(s) = n_b + 2\gamma_b^h/s$. As before, the dynamics of the second moments in the site basis can be obtained transforming back to time domain and writing

$$\begin{aligned} \langle \hat{a}^\dagger_n \hat{a}_m \rangle &= \sum_{l=1}^{N} A_{k_l,k_l} S^{(a)}_{m,k_l} S^{(a)}_{n,k_l}, \quad \langle \hat{b}^\dagger_n \hat{b}_m \rangle = \sum_{l=1}^{N} B_{k_l,k_l} S^{(b)}_{n,k_l} S^{(b)}_{m,k_l}, \\ \langle \hat{a}^\dagger_n \hat{b}_m \rangle &= \sum_{l=1}^{N} C_{k_l,k_l} S^{(a)}_{n,k_l} S^{(b)}_{m,k_l}, \quad \langle \hat{b}^\dagger_n \hat{a}_m \rangle = \sum_{l=1}^{N} D_{k_l,k_l} S^{(b)}_{n,k_l} S^{(a)}_{m,k_l}. \end{aligned} \tag{4.40}$$

From Eqs. (4.37-4.39) it is clear that A_{k_l,k_l}, B_{k_l,k_l} and C_{k_l,k_l} display the same dynamical regimes as the first moments, and thus the time evolution of the second moments presents also the characteristic features of each regime: only one frequency (ω_0) and multiple decay rates in the single-frequency regime, polynomial corrections in the decay just at the EP, and multiple frequencies with the same decay rate in the two-frequency regime. Indeed, here at the EP three poles coalesce, which makes the polynomial corrections to be quadratic in time. Examples of the emergent dynamics in the site basis are plotted in Fig. 4.3 (b).

Stationary state. Two key observations are needed to find the stationary state: only the equations for the blocks with $k_x = k_y$ have sources, and all blocks described by a

homogeneous system of equations go to zero in the stationary state. Then, setting the time derivatives of Eqs. (4.32-4.35) to zero and solving the algebraic equations, we can obtain the nonzero moments in the stationary state[2]. In this way the obtained stationary second moments recombined in the site basis read as:

$$\langle \hat{a}_n^\dagger \hat{a}_m \rangle_{ss} = \sum_{l=1}^{N} \left[\frac{(\gamma_b \bar{\gamma} + \lambda_{k_l}^2)\gamma_a^h + \lambda_{k_l}^2 \gamma_b^h}{\bar{\gamma}\lambda_{k_l}^2 + \gamma_a \gamma_b \bar{\gamma}} \right] \mathcal{S}_{n,k_l}^{(a)} \mathcal{S}_{m,k_l}^{(a)}, \tag{4.41}$$

$$\langle \hat{b}_n^\dagger \hat{b}_m \rangle_{ss} = \sum_{l=1}^{N} \left[\frac{(\gamma_a \bar{\gamma} + \lambda_{k_l}^2)\gamma_b^h + \lambda_{k_l}^2 \gamma_a^h}{\bar{\gamma}\lambda_{k_l}^2 + \gamma_a \gamma_b \bar{\gamma}} \right] \mathcal{S}_{n,k_l}^{(b)} \mathcal{S}_{m,k_l}^{(b)}, \tag{4.42}$$

$$\langle \hat{a}_n^\dagger \hat{b}_m \rangle_{ss} = \sum_{l=1}^{N} \left[\frac{i\lambda_{k_l}(\gamma_a \gamma_b^h - \gamma_b \gamma_a^h)}{\bar{\gamma}\lambda_{k_l}^2 + \gamma_a \gamma_b \bar{\gamma}} \right] \mathcal{S}_{n,k_l}^{(a)} \mathcal{S}_{m,k_l}^{(b)}, \tag{4.43}$$

and $\langle \hat{b}_n^\dagger \hat{a}_m \rangle_{ss}$ follows from Eq. (4.43) exchanging the labels $a \leftrightarrow b$. In case that sublattice effective temperatures are the same, $n_0 = \gamma_a^h/\gamma_a = \gamma_b^h/\gamma_b$, we recover the familiar scenario induced by the presence of local losses in the Lindblad equation (2) in which the only nonzero moments are $\langle \hat{a}_n^\dagger \hat{a}_n \rangle_{ss} = \langle \hat{b}_n^\dagger \hat{b}_n \rangle_{ss} = n_0 \ \forall n$. However, in the general case off-diagonal terms are also present, which can lead to the presence of correlations in the stationary state of the system. Indeed, as the master equation (2) is bilinear in the mode operators, if the initial state is Gaussian the stationary state too, and we can fully describe it constructing the covariance matrix, σ, from the above solutions [266, 267], which displays the characteristic block diagonal structure of our system: $\sigma = \bigoplus_{l=1}^{N} \sigma_{k_l}$. Notice that even though the difference in sublattice effective temperature can induce non-local correlations in the steady states, such correlations are not related to the transient dynamics and to the presence of EPs and will not be reported here.

4.2.5 Emission spectrum.

As described by Eq. (4.2), our open quantum system is subjected to the influence of the environments, which cause fluctuations and fluxes of energy. These effects can be characterized by means of the emission and absorption fluctuation spectrum which can be computed from two-time correlation functions in the stationary state [59, 60]. In this section we show that in these quantities, we also find signatures of the different dynamical regimes, and thus of the presence of EPs.

In Fig. 4.4 we plot the emission spectrum $S(\Delta) = 2\mathrm{Re}[\langle \hat{a}_1^\dagger \hat{a}_1(\Delta) \rangle]$ versus the coupling strength for a chain of six elements ($N = 3$) and with $n_0 = \gamma_a^h/\gamma_a = \gamma_b^h/\gamma_b$. This quantity is defined from

$$\langle \hat{a}_1^\dagger \hat{a}_1(\Delta) \rangle = \lim_{t\to\infty} \int_0^\infty d\tau \langle \hat{a}_1^\dagger(t) \hat{a}_1(t+\tau) \rangle e^{i\Delta\tau} \tag{4.44}$$

with $\Delta = \omega - \omega_0$, which can be computed from the previous results following the quantum regression theorem [59] (see appendix E). In panels (b) and (d) we show two limiting cases in which: for $\lambda/\omega_0 = 0.02$ the system response is characterized by one frequency (all k-modes are in the single-frequency regime) and for $\lambda/\omega_0 = 0.35$ the system response is characterized by six frequencies (all k-modes are in the two-frequency regime). In panel (a) one can observe the progressive emergence of EPs with the coupling, i.e. a continuous splitting of peaks as the coupling λ increases. As before, despite the singular character of EP, the dynamical behavior is continuous in the transition from one regime to the other.

In order to better understand these results, we look at the spectrum

$$S(\Delta) = \sum_{l=1}^{N} \mathcal{S}_{1,k_l}^{(a)} \mathrm{Re}[\langle \hat{a}_1^\dagger \hat{a}_{k_l}(\Delta) \rangle] \tag{4.45}$$

[2]This can also be obtained from the residue of the pole $s = 0$ of Eqs. (4.37-4.39).

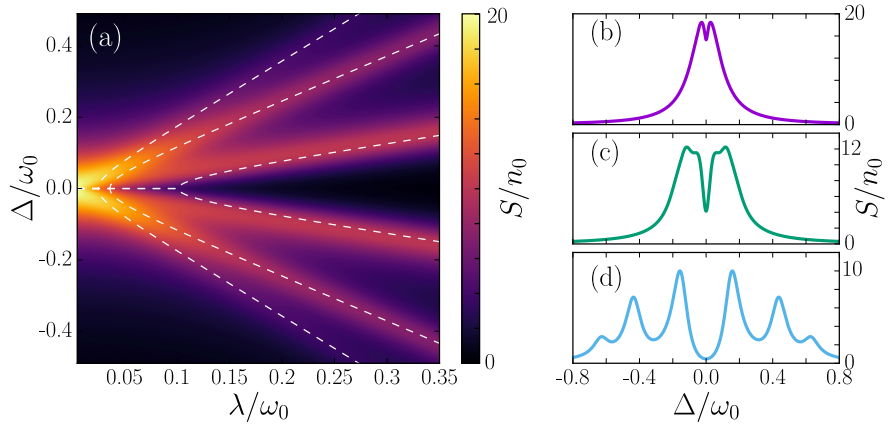

Figure 4.4: (a) In color emission spectrum, $S(\Delta/\omega_0)/n_0$, of the first site. Dashed white lines correspond to the eigenfrequencies of the system given by the imaginary part of Eq. (4.10). (b-d) $S(\Delta/\omega_0)/n_0$ of the first site for different coupling strengths: (b) $\lambda/\omega_0 = 0.02$, (c) $\lambda/\omega_0 = 0.1$, (d) $\lambda/\omega_0 = 0.35$. In all figures $N = 3$, $\gamma_a/\omega_0 = 0.1$, $\gamma_b/\omega_0 = 0.01$ and $n_0 = \gamma_a^h/\gamma_a = \gamma_b^h/\gamma_b$.

considering its components in the k-basis and for the different regimes. In the single-frequency regime we find:

$$\langle \hat{a}_1^\dagger \hat{a}_{k_l}(\Delta)\rangle = \frac{n_0 \mathcal{S}^{(a)}_{1,k_l}}{(\gamma^+_{k_l} - \gamma^-_{k_l})}\left[\frac{(\gamma^+_{k_l} - \gamma_b)(\gamma^+_{k_l} + i\Delta)}{\Delta^2 + \gamma^{+2}_{k_l}} - \frac{(\gamma^-_{k_l} - \gamma_b)(\gamma^-_{k_l} + i\Delta)}{\Delta^2 + \gamma^{-2}_{k_l}}\right], \tag{4.46}$$

while in the two-frequency regime we find:

$$\langle \hat{a}_1^\dagger \hat{a}_{k_l}(\Delta)\rangle = \frac{n_0 \mathcal{S}^{(a)}_{1,k_l}}{2i\nu_{k_l}}\left[\frac{(\frac{\gamma_b-\gamma_a}{2} + i\nu_{k_l})(\frac{\bar{\gamma}}{2} + i(\Delta + \nu_{k_l}))}{\frac{\bar{\gamma}^2}{4} + (\Delta + \nu_{k_l})^2} - \frac{(\frac{\gamma_b-\gamma_a}{2} - i\nu_{k_l})(\frac{\bar{\gamma}}{2} + i(\Delta - \nu_{k_l}))}{\frac{\bar{\gamma}^2}{4} + (\Delta - \nu_{k_l})^2}\right]. \tag{4.47}$$

It is remarkable the similitude between the expressions given in Eqs. (4.23) and (4.24) and the ones obtained here, for the same regimes. In fact, in panels (b) to (d) of Fig. 4.4 one can observe the same characteristic features of each regime: the interference windows in the single-frequency regime, and the expected Lorentzians in the two-frequency regime. These features can be clearly identified in Eqs. (4.46) and (4.47). In the single-frequency regime we always have $\gamma^+_{k_l} > \gamma^-_{k_l} \geq \gamma_b$. Hence, from Eq. (4.46), we clearly see that the spectrum is made of a Lorentzian dip with the smallest decay rate on top of a Lorentzian with the larger one. In Fig. 4.4 (b) all k-modes are in this regime, which explains the observed shape. This dip is also observed in panel (c) as λ_{k_3} is still below the critical value (EP). Thus, in Eq. (4.46) we recognize a clear manifestation of the interference effect also found in the transmission spectrum: in the single-frequency regime two modes with the same frequency but different damping rate $\gamma^\pm_{k_l}$ interfere destructively and inhibit (in the present case) thermal emission at a frequency in which the system is actually resonant.

In contrast, this interference effect is not present in the two-frequency regime. From Eq. (4.47) we see that the spectrum is composed of different frequencies which, for large enough coupling strength, can be observed as well defined resonance peaks in the spectrum [Fig. 4.4 (d)]. These two different regimes have been observed in different physical systems, as for instance inhibited emission in a system of two coupled mechanical modes [323] (single-frequency regime) or the so called parametric normal mode splitting in optomechanical systems [324, 325] (two-frequency regime).

4.3 Synchronization and coalescence in a spin system

One of the most striking results of the previous section is that the interplay between coherent and incoherent processes enables a regime in which all the modes of the array display a single frequency, before the occurrence of the first EP. Indeed, this raises the question on the relation of this regime with synchronization. In this sense, it is interesting to comment on the case of a system of two detuned atomic clouds dissipatively coupled (through a cavity mode) and incoherently pumped [46] (this is a system of the family of "superradiant lasers" [264, 326, 327]). In a semiclassical approximation, a synchronization regime is identified from the light emitted by this cloud; varying the coupling between the two clouds, a bifurcation of the frequencies of light emission is observed, similar to what we have observed for each k-mode in the previous section, which also leads to a monochromatic regime that is interpreted as the two detuned clouds becoming synchronized [46]. In fact, following the analysis of this chapter, we can identify an EP in the non-Hermitian matrix (approximately) governing the emission of light by this system.

In this section, we consider the simplest case of two qubits with the basic coherent and incoherent processes of this mesoscopic cloud. By doing so, we intend to tackle several questions. First, considering just two qubits we will be able to explore the full quantum dynamical system, and analyze the presence of EPs in the Liouvillian. Second, if we find monochromatic regimes, we can compare the synchronized dynamics in these regimes enabled by coalescence with the phenomenon of transient synchronization occurring in the presence of multiple frequencies, and known to occur in between slightly detuned spin systems with collective dissipation [5, 45, 90].

4.3.1 Spin qubit dimer with collective dissipation and incoherent pumping

We consider a dissipative system of two qubits described by the following Born-Markov master equation for their density matrix $\hat{\rho}$ ($\hbar = 1$)

$$\frac{d}{dt}\hat{\rho} = -i[\hat{H}, \hat{\rho}] + 2\gamma\mathcal{D}[\hat{L}]\hat{\rho} + w(\mathcal{D}[\hat{\sigma}_1^+]\hat{\rho} + \mathcal{D}[\hat{\sigma}_2^+]\hat{\rho}), \tag{4.48}$$

where the rising and lowering operators $\hat{\sigma}_j^{\pm}$ for spin $j = 1, 2$ are defined as usual from the Pauli matrices $\hat{\sigma}_j^{x,y,z}$ [59], and $\hat{L} = (\hat{\sigma}_1^- + \hat{\sigma}_2^-)/\sqrt{2}$. Two types of incoherent processes are taken into consideration: the qubits dissipate collectively through $\hat{L}$ and with rate 2γ, and a local incoherent pumping acts on each spin with rate w. The Hamiltonian part of this model reads as

$$\hat{H} = \frac{\omega_1}{2}\hat{\sigma}_1^z + \frac{\omega_2}{2}\hat{\sigma}_2^z + s_{12}(\hat{\sigma}_1^-\hat{\sigma}_2^+ + \hat{\sigma}_1^+\hat{\sigma}_2^-), \tag{4.49}$$

and describes two detuned spins with $\delta = \omega_1 - \omega_2$, and central frequency $\omega_0 = (\omega_1 + \omega_2)/2$, which interact coherently through the exchange term with rate s_{12}.

The phenomenological model that we consider lies can describe recent experiments in which a small number of two-level systems interact and display signatures of collective dissipation as subradiant and superradiant effects. The nature of the two-level systems and the origin of these interactions are diverse, as for instance: trapped atoms [237, 259] and ions [257] interacting through waveguides or cavity modes, or photon-mediated interactions between color centers in diamond [30], or superconducting qubits with photon-mediated interaction in 1D lines [28] or in the bad cavity limit [29]. Some theoretical works dealing with collective dissipation, as in our work, analyze the coupling to a common cavity mode in the bad cavity limit [46], the coupling to a common structured bath [243, 244] or to an effective one-dimensional bath as in waveguides [328], photonic nanostructures [245] or

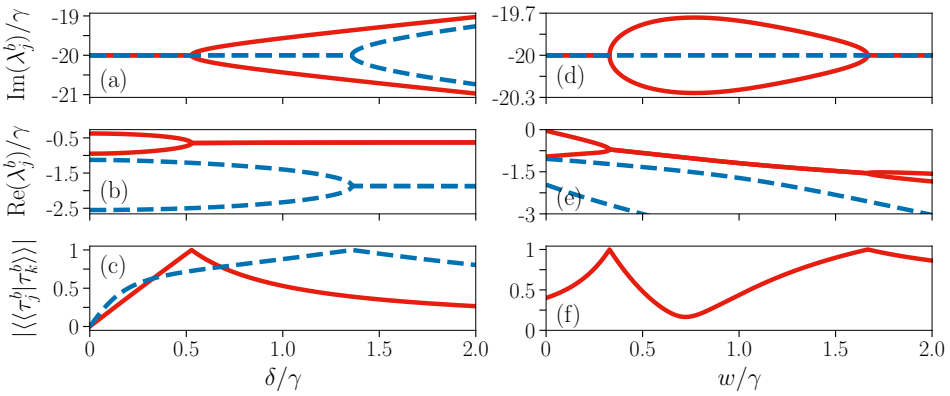

Figure 4.5: All panels: analysis of coalescence in $\bar{\bar{\mathcal{L}}}_b$ for $\omega_0/\gamma = 20$ and $s_{12} = 0$. (a) Imaginary part of the eigenvalues (eigenfrequencies) varying δ/γ, for $w/\gamma = 0.25$. In solid red and dashed blue the two different pairs of eigenvalues that coalesce. (b) The real part of the corresponding eigenvalues (decay rates). (c) Product of the corresponding pair of eigenvectors that coalesce. (d)-(f) Same quantities as in (a)-(c) but fixing $\delta/\gamma = 0.4$ and varying w/γ. Notice that the smallest (in absolute value) decay rate is not zero for $w/\gamma = 0$ as it can be checked from Eq. (E.17). Here only a pair of eigenvectors coalesce (twice).

microwave transmission lines [329]. Furthermore, tailored local incoherent processes such as the incoherent pumping can be realized addressing auxiliary energy levels of the spin system [46, 255].

Finally, an important remark on the parameter values is that we consider them to follow a hierarchy given by $\omega_0 \gg \delta, s_{12}, \gamma, w$ and $w, \delta, s_{12} \sim \gamma$, as it is a usual requirement for this kind of phenomenological models to have a microscopic origin [90, 225], while mutual dependencies between the values of these parameters are not considered, allowing for their independent variation.

4.3.2 Exceptional points in the Liouvillian

In spite of its simplicity, the model of Eqs. (4.48) and (4.48) displays several regimes separated by exceptional points, as conveniently described within the Liouville formalism. Indeed, as explained in chapter 2, an isomorphism can be adopted which maps $\hat{\rho}$ into the 16-dimensional vector $|\rho\rangle\!\rangle$, and the Liouville super-operator $\mathcal{L}$ into a 16×16 matrix $\bar{\bar{\mathcal{L}}}$. The time evolution of the density matrix can then be rewritten as a vector equation $|\dot{\rho}\rangle\!\rangle = \bar{\bar{\mathcal{L}}}|\rho\rangle\!\rangle$. How to explicitly build $\bar{\bar{\mathcal{L}}}$ is detailed in appendix E, where we generalize the results of [90] to the case of incoherent driving. This matrix is block diagonal, $\bar{\bar{\mathcal{L}}} = \oplus_\mu \bar{\bar{\mathcal{L}}}_\mu$, with $\mu \in \{a, b, c, d, e\}$, the different blocks being related to the dynamics of different observables (in appendix E we give the explicit expressions of such matrices). For instance, the dynamics of populations $\langle\hat{\sigma}_j^z\rangle$ is entirely described by $\bar{\bar{\mathcal{L}}}_a$, while the dynamics of coherences $\langle\hat{\sigma}_j^{x,y}\rangle$ by $\bar{\bar{\mathcal{L}}}_b$ and $\bar{\bar{\mathcal{L}}}_c = \bar{\bar{\mathcal{L}}}_b^*$. Such a block structure is a direct consequence of a symmetry on the superoperator level, that is, the invariance of the Liouvillian under the action of the total-number-of-particles superoperator, and appears every time the (partial) secular approximation holds. Thus, it can be found in a very broad class of systems, as detailed in Ref. [269].

Within this formalism, the general solution of the master equation at time t can be formally written as (see chapter 2):

$$|\rho(t)\rangle\!\rangle = \sum_\mu \sum_k p_{0\,k}^\mu \, |\tau_k^\mu\rangle\!\rangle \, \mathrm{e}^{\lambda_k^\mu t}, \tag{4.50}$$

where μ runs over the five blocks of $\bar{\bar{\mathcal{L}}}$ and k between 1 and the dimension of the corresponding block (where the block dependence μ of k_μ is omitted). In Eq. (4.50), we

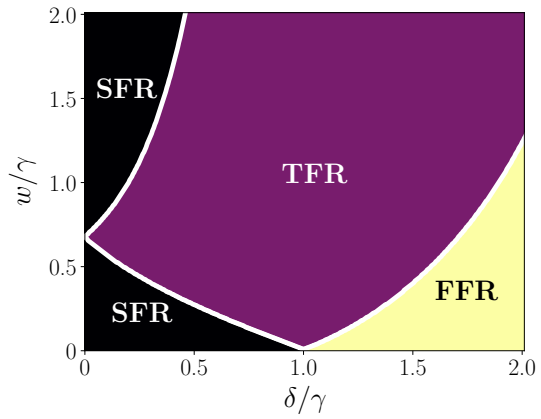

Figure 4.6: Diagram of eigenfrequencies of $\bar{\bar{\mathcal{L}}}_b$ for $\omega_0/\gamma = 20$ and $s_{12} = 0$. The white lines stand for second order EPs and separate the regions with different number of eigenfrequencies and decay rates. The lines $\delta/\gamma = 0$ and $w/\gamma = 0$ are not resolved in this plot, but analytical expressions are available (appendix E). In black, we have the SFR in which there is only one eigenfrequency ($-\omega_0$) and four decay rates. In purple, the TFR where there are three eigenfrequencies and three decay rates. In yellow the FFR where four eigenfrequencies and two decay rates are found. The most prominent features are displayed in this range of detunings and pumping rates.

have introduced the right (left) eigenvectors of the Liouvillian $|\tau_k^\mu\rangle\!\rangle$ ($|\bar{\tau}_k^\mu\rangle\!\rangle$), their respective eigenvalues λ_k^μ, defined through $\bar{\bar{\mathcal{L}}}|\tau_k^\mu\rangle\!\rangle = \lambda_k^\mu|\tau_k^\mu\rangle\!\rangle$ ($\bar{\bar{\mathcal{L}}}^\dagger|\bar{\tau}_k^\mu\rangle\!\rangle = \lambda_k^{\mu*}|\bar{\tau}_k^\mu\rangle\!\rangle$) and the weight of the initial conditions $p_{0\,k}^\mu = \frac{\langle\!\langle\bar{\tau}_k^\mu|\rho(0)\rangle\!\rangle}{\langle\!\langle\bar{\tau}_k^\mu|\tau_k^\mu\rangle\!\rangle}$, where we use the Bra-Ket notation. Notice that left and right eigenvectors form a biorthogonal basis: $\langle\!\langle\bar{\tau}_j^\mu|\tau_k^\nu\rangle\!\rangle \propto \delta_{\mu\nu}\delta_{jk}$.

Vanishing coupling ($s_{12} = 0$). Being the system open, $\bar{\bar{\mathcal{L}}}$ is non-Hermitian, so it is actually possible to have EPs in which the matrix is non-diagonalizable [209, 268]. Here, we focus on the EPs occurring in $\bar{\bar{\mathcal{L}}}_{b(c)}$, as they are relevant for the emergence of synchronization [5, 90]. However, we notice that $\bar{\bar{\mathcal{L}}}_a$ is also able to display EPs (see appendix E). In Figures 4.5 and 4.6 we analyze the presence of EPs in $\bar{\bar{\mathcal{L}}}_b$ for $s_{12}/\gamma = 0$. We first show particular examples of the EPs by tuning δ/γ (a)-(c) and w/γ in (d)-(f). Then, in Fig. 4.6, the overall picture is presented as a function of both detuning and pumping, showing the parameter regions where the Liouvillian displays from one to four frequencies: single-frequency regime (SFR), and similarly for three (TFR) and four (FFR).

In Figs. 4.5 (a) and (d), we plot the imaginary part of the eigenvalues (eigenfrequencies), in (b) and (e) their real part (decay rates), and in (c) and (f) the absolute value of the product of the coalescing (normalized) eigenvectors $|\langle\!\langle\tau_j^b|\tau_k^b\rangle\!\rangle|$ that is going to reach value one in the presence of coalescence. Both EPs appearing in $\bar{\bar{\mathcal{L}}}_{b(c)}$ are second order: two eigenvalues become the same and the corresponding eigenvectors become linearly dependent. Both varying detuning [as shown in Figs. 4.5 (a)-(c)] and incoherent pumping [in panels (d)-(f)] we show coalescence of different modes. As detailed in appendix E, in the absence of incoherent pumping $w/\gamma = 0$, all eigenvalues [Eq. (E.17)] depend on the coherent coupling through the term

$$V = \sqrt{(\gamma + i2s_{12})^2 - \delta^2} \tag{4.51}$$

Hence, for $s_{12} = 0$ (as in Fig. 4.5), we can see the two EPs arise for the same value $\delta = \gamma$ where Eq. (4.51) vanishes. In this special case, $w/\gamma = 0$, the emerging frequencies are degenerate and given by $\omega_0 \pm \mathrm{Im}(V)/2$. The physical intuition in this case is that the detuning needs to overcome the dissipation in order to induce the oscillatory behavior of

the system, somehow analogously to an overdamped to underdamped transition in the case of oscillators, but keeping in mind that here $\omega_0/\gamma \gg 1$.

The importance of EPs in the present context is that they separate dynamical regimes characterized by a different number of frequencies when varying w/γ and δ/γ (Fig. 4.6). Three different regimes are found: SFR, TFR and FFR, all of them separated by lines of second order EPs (white lines). We will see that the presence of EPs, enabling different frequency regions (SFR, TFR and FFR), leads to a regime with spontaneous synchronization. Finally, here we have focused in the case of zero coherent coupling, as when $s_{12}/\gamma \neq 0$ numerical analysis reveals that the system generally displays four frequencies and four decay rates as EPs are not present.

4.3.3 Synchronization of the coherences

Having established the presence of a monochromatic regime enabled by coalescence, we now address the synchronization dynamics associated with it, looking at the spin coherences (living in the $\bar{\bar{\mathcal{L}}}_{b(c)}$ sectors). As we will see, synchronization emerges as a transient monochromatic oscillation in which the coherences of both qubits remain phase-locked, until they finally reach the non-oscillatory stationary state of the system. Moreover, we will compare this scenario with that in which synchronization emerges in presence of multiple frequencies, happening for $s_{12}/\gamma \neq 0$. This is the more usual scenario for transient synchronization [90], also studied in chapter 3, for which we also study the unexplored effects of incoherent pumping.

Synchronization in the SFR. The dynamics of the coherences (e.g. $\langle\hat{\sigma}^x_{1,2}\rangle$) displays an oscillatory decay towards the stationary state. We aim to establish if this SFR dynamics can be understood as synchronization. We make use of the Pearson factor and its maximized version, optimized over all possible phase shifts, which are well known measures of synchronization [44, 90] (see Eq. (3.21) and appendix B). As a first remarkable result, and in spite of the presence of just one frequency, we find that phase-locking between the dynamics of the coherences is not guaranteed from the beginning. This is evident in Fig. 4.7 (a) in which the phase between the trajectories slips from zero to almost π at $\gamma t \approx 4$, where it remains locked until the oscillation completely decays out. The Pearson factor accounting for delay (purple dashed line) is a good measure of the final synchronous oscillation, while we can appreciate the transient phase slip as signaled by the bare indicator (green solid line).

The slip of the relative phase can be understood by analyzing the formal solution of $\langle\hat{\sigma}^x_{1,2}\rangle$ (see appendix E). Indeed, we can particularize Eq. (E.22) to the SFR in which $\mathrm{Im}(\lambda^b_k) = -\omega_0 \ \forall k$ and hence

$$\langle\hat{\sigma}^x_j(t)\rangle = \sum_{k=1}^{4} 2|p^b_{0k}\langle\tau^b_k\rangle_{xj}|e^{\mathrm{Re}(\lambda^b_k)t}\cos[\psi^b_{k,xj} - \omega_0 t], \tag{4.52}$$

the coefficients being defined in the appendix and $j = 1, 2$. Importantly, both the weight (p^b_{0k}) and phase ($\psi^b_{k,xj}$) associated with each eigenvalue depend on the initial condition. Then, from Eq. (4.52) we find that there are multiple terms oscillating at the same frequency but with different phases. The relative importance of each term changes in time due to the time dependent part of the weight factor $e^{\mathrm{Re}(\lambda^b_k)t}$, where the eigenvalues of $\bar{\bar{\mathcal{L}}}_b$ are ordered such that λ^b_4 is the one with the smallest real part in absolute value. This makes the relative phase between the qubits slip from the initial value determined by the initial condition to $\Delta\psi = \psi_{4,x1} - \psi_{4,x2}$ in a timescale related to $\mathrm{Re}(\lambda^b_3)$, in which all terms in Eq. (4.52) except the less damped one ($k = 4$) are damped out. Notice

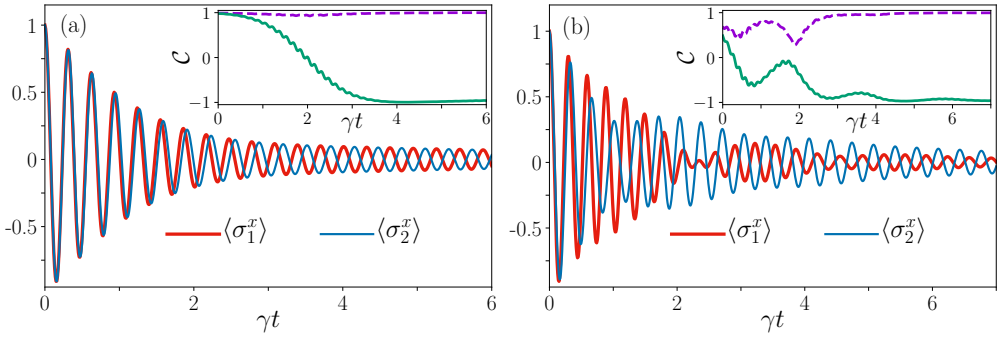

Figure 4.7: Main panels: $\langle\hat{\sigma}_1^x\rangle$ (red thick line) and $\langle\hat{\sigma}_2^x\rangle$ (blue thin line) for the initial condition $|\phi_0\rangle = (|ee\rangle + |eg\rangle + |ge\rangle + |gg\rangle)/2$. Insets: $\mathcal{C}_{\langle\hat{\sigma}_1^x(\gamma t)\rangle,\langle\hat{\sigma}_2^x(\gamma t)\rangle}(\gamma\Delta t)$ (green solid line) and $\mathcal{C}_{\max}$ (purple dashed line) with $\Delta t = 1.2/\gamma$ and delay range $\delta\tau = 0.35/\gamma$. (a) SFR with parameters $\omega_0/\gamma = 20$, $s_{12}/\gamma = 0$, $w/\gamma = 0.1$, $\delta/\gamma = 0.3$. (b) FFR with parameters $\omega_0/\gamma = 20$, $s_{12}/\gamma = 1$, $w/\gamma = 0.1$, $\delta/\gamma = 2$.

that, the more similar $\mathrm{Re}(\lambda_{3,4}^b)$ are, the more damped the oscillations when the relative phase eventually locks will be, although the relative phase shift between the qubits will be generally more difficult to appreciate. The dependence of the weights on the initial condition can be illustrated considering the same parameters as in Fig. 4.7 but with the initial condition $|\phi_0\rangle = (|ee\rangle - |eg\rangle + |ge\rangle - |gg\rangle)/2$, in which the relative phase is almost π from the beginning (not shown here). We conclude that in spite of the monochromatic spectrum, synchronization still emerges after a transient as in other scenarios described before, as a progressive *phase-locking*.

It is also interesting to comment on the general effect of increasing the incoherent pumping rate w/γ. As we have shown in Fig. 4.6 the SFR involves a wide range of values of w/γ, which implies that frequency degeneracy is present for large w/γ too. Nevertheless, the decoherence rate increases significantly with w/γ (as also appreciated in panel (e) of Fig. 4.5), strongly damping the coherent oscillations of $\langle\hat{\sigma}_{1,2}^x\rangle$. Thus, the amplitude of the synchronous oscillation decreases significantly with increasing incoherent pumping, which makes the phenomenon harder to be observed and finally hinders it.

Synchronization in the presence of multiple frequencies. We now consider the case where multiple frequencies are present ($s_{12}/\gamma \neq 0$) since the early stage of the dynamics. In this case, synchronization can only emerge in the presence of a slowly dissipating eigenmode, i.e. when $\mathrm{Re}(\lambda_4^b)/\mathrm{Re}(\lambda_3^b) \ll 1$, which leads to *frequency selection*, analogously to what we have found in chapter 3. This statement can be understood analyzing the formal solution of $\langle\hat{\sigma}_{1,2}^x\rangle$ given in Eq. (E.22): at the beginning the four different frequencies are involved and thus the qubits oscillate irregularly; however, as each frequency component decays with a different rate given by $\mathrm{Re}(\lambda_k^b)$, after a transient time, if $\mathrm{Re}(\lambda_4^b)/\mathrm{Re}(\lambda_3^b) \ll 1$, there is a significant oscillation governed by the eigenmode with the smallest decay rate $\mathrm{Re}(\lambda_4^b)$, making the qubits to oscillate synchronously with the phase difference locked to $\Delta\psi = \psi_{4,x1} - \psi_{4,x2}$. An example of such phenomenon is shown in Fig. 4.7 (b), where we can observe that after a time of about $\gamma t \approx 4$ the two qubits oscillate synchronously with a difference of phase of about π. The Pearson factor maximized to allow for a phase shift reaches a stationary value close 1. When comparing panels (a) and (b), we notice that in both cases synchronization emerges after a transient of a similar duration and the lasting amplitudes are of similar magnitude, while in the latter case the transient to synchronization displays beatings related to the presence of multiple frequencies.

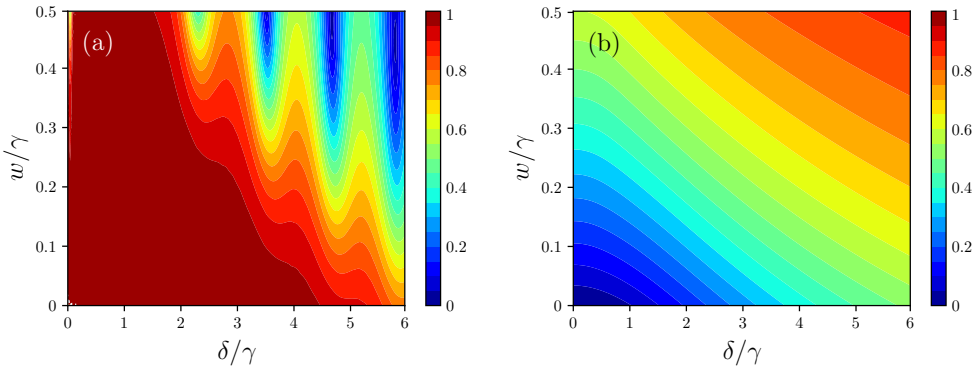

Figure 4.8: (a) In color: maximized Pearson factor measure $\mathcal{C}_{\max}$ at time $\gamma t = 6$ considering $\langle \hat{\sigma}_1^x \rangle$ and $\langle \hat{\sigma}_2^x \rangle$ for the initial condition $|\phi_0\rangle = (|ee\rangle + |eg\rangle + |ge\rangle + |gg\rangle)/2$. The dark red regions indicate the emergence of synchronization. (b) In color: ratio of the two smallest decay rates $\mathrm{Re}(\lambda_4^b)/\mathrm{Re}(\lambda_3^b)$ varying w/γ and δ/γ, with the other parameters fixed to $\omega_0/\gamma = 20$ and $s_{12}/\gamma = 1$.

Effects incoherent pumping. The influence of the different parameters on the synchronization behavior can be analyzed systematically by studying the ratio of the two smallest eigenmode decay rates (as in chapter 3). Indeed, the case with $w/\gamma = 0$ was already studied in Ref. [90], in which it was shown that the more detuned are the qubits, the more coherent coupling is needed for synchronization to emerge, analogously to the classical Arnold-tongue behavior. Here, we find that a nonzero w/γ preserves this overall behavior but decreases the capacity of the qubits to synchronize. The detrimental effect of the incoherent pumping can be understood by recalling that it constitutes an additional decoherence channel acting locally on each qubit, and thus as w/γ is increased, the effect of the common environment is counteracted by local decoherence which decreases the disparity between the two smallest decay rates. In this sense, its detrimental effects parallel those of pure dephasing, which is known to decrease the disparity of the eigenmode decay rates, as reported in Refs. [5, 45, 90].

The effects of incoherent pumping on synchronization are studied systematically in Figures 4.8 in which the maximized Pearson factor after an initial transient, (a), and the ratio of the two smallest eigenmode decay rates, (b), are plotted varying w/γ and δ/γ. Focusing on panel (b), for small enough w/γ, we can see that there is one decay rate significantly smaller than the rest, enabling the emergence of synchronization [as in Fig. 4.7(b)]. However, as w/γ increases this ratio tends to one and synchronization no longer emerges. This is also captured by the maximized Pearson factor, (a), which indicates that, for a given detuning, increasing w/γ eventually destroys synchronization. Indeed, the region of panel (a) in which this indicator takes the largest values is well correlated with the region in panel (b) in which $\mathrm{Re}(\lambda_4^b)/\mathrm{Re}(\lambda_3^b)$ takes the smallest values, indicating good agreement between both indicators of synchronization (as also observed in chapter 3 for two harmonic oscillators). Moreover, notice that the overall magnitudes of the decay rates increase with w/γ causing also a faster damping of the coherent oscillations.

Synchronization and subradiance. A common aspect of both synchronization scenarios (SFR and multiple frequencies) is that they are intimately related to subradiance, as in both cases there is a collective mode that can display a significantly smaller damping rate. In the SFR, this mode is the one that phase-locks the qubits, and since all of them have the same frequency, we find that this scenario is accompanied by sub/superradiance in the presence of *frequency degeneracy*. Otherwise, in the presence of multiple frequencies, synchronization is intimately related to *non-degenerate* subradiance, as also reported in Ref. [90] in which this spin system is considered in the absence of pumping.

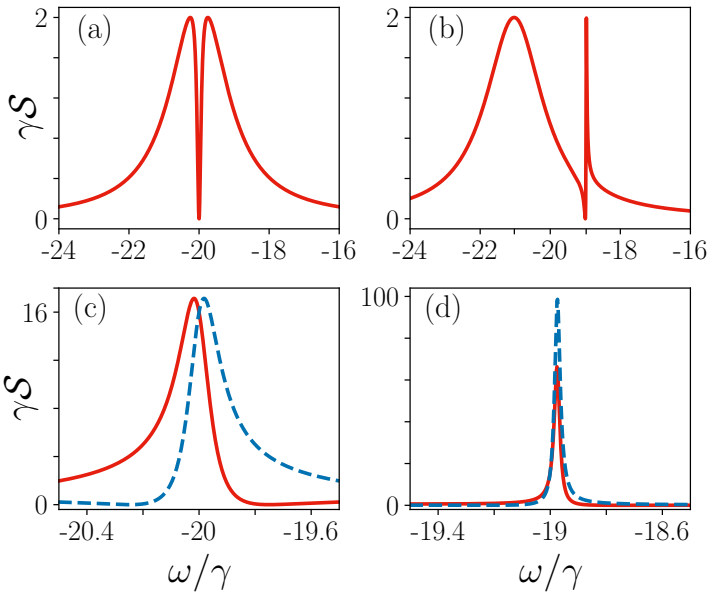

Figure 4.9: (a) and (b) Fourier transform of $\langle\hat{L}(\tau)\hat{L}^\dagger(0)\rangle_{ss}$. (c) and (d) Fourier transform of $\langle\hat{\sigma}^-_{1(2)}(\tau)\hat{\sigma}^+_{1(2)}(0)\rangle_{ss}$ in red solid (blue dashed) lines. In all panels $\omega_0/\gamma = 20$, $\delta/\gamma = 0.5$. The rest of parameters: (a), (c) $w/\gamma = 0$, $s_{12}/\gamma = 0$ and (b), (d) $w/\gamma = 0$, $s_{12}/\gamma = 1$.

4.3.4 Signatures of synchronization in the correlation spectrum

We now present a complementary view of the phenomenon of synchronization, analyzing its signatures in the two-time correlation spectrum, an indicator relevant when probing the system and accessible in many setups. This approach to characterize synchronization better illustrates the relation between synchronization and super/subradiance phenomena, and was taken for instance in Ref. [46], and it will also enable us to establish connections with the results presented for the harmonic oscillators (Sect. 4.2.1).

The correlations considered here lie in the same Liouvillian sectors $\bar{\bar{\mathcal{L}}}_{b(c)}$ as the local observables considered in the previous subsection. In particular, we consider two-time correlations for collective spin operators $\langle\hat{L}(t+\tau)\hat{L}^\dagger(t)\rangle$ [we remind that $\hat{L} = (\hat{\sigma}_1^- + \hat{\sigma}_2^-)\sqrt{2}$] as well as for local ones, $\langle\hat{\sigma}_j^-(t+\tau)\hat{\sigma}_j^+(t)\rangle$, and we illustrate the signatures of synchronization and coalescence. We will illustrate the main ideas considering the case with $w/\gamma = 0$, as we can guide the numerical results with analytical expressions (appendix E). Finally, we will comment on the main effects of a non-zero incoherent pumping.

Collective two-time correlations. We start analyzing the correlation spectrum for collective operators $\mathcal{S}_{\hat{L}\hat{L}^\dagger}(\omega)$ in the SFR [Fig. 4.9 (a)] induced by coalescence. From this panel, we clearly observe signatures of super- and subradiant behavior, the latter being related to the eigenmode synchronizing the qubits. Moreover, we immediately observe that the spectrum is made of a combination of several Lorentzians that interfere at a certain point. In the SFR the interference occurs just at the resonance frequency ω_0/γ.

Considering the exact expressions for $\mathcal{S}_{\hat{L}\hat{L}^\dagger}(\omega)$ we find that (appendix E), in the SFR

$$\mathcal{S}_{\hat{L}\hat{L}^\dagger}(\omega) = \frac{2}{V}\left[\frac{(\omega+\omega_0)^2}{(\omega+\omega_0)^2 + \frac{1}{4}(\gamma - V)^2} - \frac{(\omega+\omega_0)^2}{(\omega+\omega_0)^2 + \frac{1}{4}(\gamma + V)^2}\right]. \tag{4.53}$$

This corresponds to two superposed (interfering) resonances, opposite in sign and each centered at the same frequency ω_0 but with a different decay rate (in this case V is real), which yield a broad peak with a transparency window whose width is given by the narrow

resonance. Notice that the width of the narrow and broad resonance can be quite disparate for small enough detuning, leading to pronounced *degenerate* subradiant and superradiant eigenmodes, the former enabling phase-locking of the coherences.

In the case $s_{12}/\gamma \neq 0$, V becomes complex, and we denote its real and imaginary parts as V_R and V_I respectively. The exact results now read as

$$\mathcal{S}_{\hat{L}\hat{L}^\dagger}(\omega) = \frac{2(\omega+\omega_0-s_{12})}{|V|^2}\left[\frac{\gamma\frac{V_I}{2}+V_R(\omega+\omega_0-V_I)}{(\omega+\omega_0-\frac{V_I}{2})^2+\frac{1}{4}(\gamma-V_R)^2}-\frac{\gamma\frac{V_I}{2}+V_R(\omega+\omega_0+V_I)}{(\omega+\omega_0+\frac{V_I}{2})^2+\frac{1}{4}(\gamma+V_R)^2}\right], \quad (4.54)$$

in which we observe again the interference of two resonances, but now centered at different frequencies $\omega = \omega_0 \pm V_I/2$ and with different decay rates. Notice that here completely destructive interference occurs at $\omega = -\omega_0 + s_{12}$. Moreover, for $s_{12}/\delta \gg 1$, $V_R \approx \gamma$ while $V_I \approx 2s_{12}$, which implies that there is a significantly superradiant eigenmode and a significantly subradiant one, the latter being the one synchronizing the spins. This is clearly observed in Fig. 4.9 (b), in which the superradiant eigenmode is centered around $\omega \approx -\omega_0 - s_{12}$ and the subradiant one at around $\omega \approx -\omega_0 + s_{12}$.

Local two-time correlations. We now compare these results with the ones for local correlation spectra (for each spin) $\langle\hat{\sigma}^-_{1(2)}(\tau)\hat{\sigma}^+_{1(2)}(0)\rangle_{ss}$. In Fig. 4.9 (c) we can observe that $\mathcal{S}_{\hat{\sigma}^-_{1(2)}\hat{\sigma}^+_{1(2)}}(\omega)$ displays a Fano-like resonance, as we can clearly appreciate an asymmetric peak slightly displaced at the left (right) of ω_0. This is still an interference effect as the exact results show:

$$\mathcal{S}_{\hat{\sigma}^-_{1(2)}\hat{\sigma}^+_{1(2)}}(\omega) = \frac{2}{V}\left[\frac{(\omega+\omega_0)[\omega+\omega_0\mp\frac{\delta}{2}]+\frac{\gamma}{4}(\gamma-V)}{(\omega+\omega_0)^2+\frac{1}{4}(\gamma-V)^2}-\frac{(\omega+\omega_0)[\omega+\omega_0\mp\frac{\delta}{2}]+\frac{\gamma}{4}(\gamma+V)}{(\omega+\omega_0)^2+\frac{1}{4}(\gamma+V)^2}\right], \quad (4.55)$$

where the upper sign corresponds to spin 1 and the lower sign to spin 2. Here, we find the peaks of each spin to be centered at slightly shifted frequencies: the two-time correlations of each spin are affected by the presence of the other one, that is detuned, and each spectrum experiences a pushing effect. Of course these self-correlations enter also in the collective spectra described above but there the cross-correlations between spins also play a major role.

In the case of $s_{12}/\gamma \neq 0$, Fig. 4.9(d), we see that the self-correlations mainly display the sharp peak also present in the collective spectrum of correlations: the superradiant eigenmode is barely visible in this case while the subradiant one is the main contribution. The main reason for the difference between Figs. 4.9 (d) and 4.9 (b) is that the collective operator in the former is almost orthogonal to the subradiant eigenmode. In fact $\hat{L}$ is exactly the superradiant eigenmode in the absence of detuning. Therefore, the contributions of both eigenmodes acquire the same importance in the collective spectrum. In this case the analytical results are too cumbersome to provide additional insights.

As anticipated, we have found that synchronization is intimately related to the emergence of subradiance: as the long-lived subradiant mode is the one synchronizing the qubits, and which dominates the dynamics towards the stationary state of the system. Moreover, we have found that the results for the SFR and collective correlations parallel the ones we have found in the case of the array of harmonic oscillators, both for the transmission and the emission spectra, in which the monochromatic regime is signaled by an interference window just at resonance.

Effects of the incoherent pumping. When allowing for incoherent pumping, i.e. $w/\gamma \neq 0$, we observe a progressive smoothing out of the signatures of super/subradiant behavior in the spectrum (Fig. 4.10). In particular, we can see how the visibility of the interference effects decreases. In the SFR and for the collective correlation, the depth of the central dip decreases and its width increases, while for local correlations the resonance

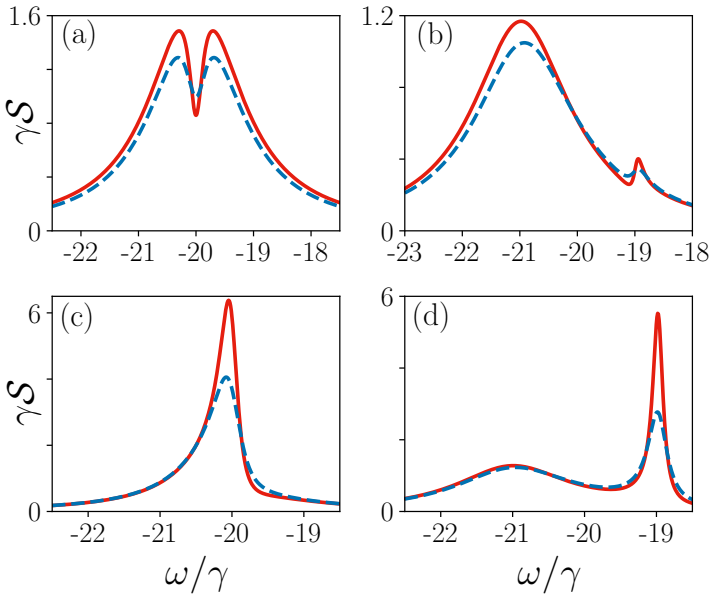

Figure 4.10: (a) and (b) Fourier transform of $\langle \hat{L}(\tau)\hat{L}^{\dagger}(0)\rangle_{ss}$. (c) and (d) Fourier transform of $\langle \hat{\sigma}_1^{-}(\tau)\hat{\sigma}_1^{+}(0)\rangle_{ss}$, $w/\gamma = 0.05$ in red solid lines and $w/\gamma = 0.1$ in blue dashed lines.. In all panels $\omega_0/\gamma = 20$, $\delta/\gamma = 0.5$. The rest of parameters: (a), (c) $s_{12}/\gamma = 0$. (b), (d) $s_{12}/\gamma = 1$.

becomes less asymmetric. In the case of $s_{12}/\gamma = 1$ [panels (b) and (d)], we see that the width of the subradiant eigenmode increases significantly. Indeed, for the collective correlation, the corresponding peak becomes barely visible, while for the local correlations it still dominates but with a significant decrease (increment) of the height (width) [compare with Fig. 4.9 (d)]. These effects are a clear manifestation of the fact that this local incoherent process counteracts collective dissipation, the latter being the mechanism behind strong disparities in the decay rates of the eigenmodes in the model described by Eqs. (4.48) and (4.49).

4.4 Concluding remarks

In this chapter we have reported the presence of EPs in the dynamics of two very different systems: a 1D array of quantum harmonic oscillators with staggered losses [4], and a system of two detuned spins with collective dissipation and incoherent pumping [7]. In both cases, we have found that the right interplay between coherent and incoherent processes enables the presence of such spectral singularities and of the dynamical phenomenon that follows them. Indeed, EPs have been reported for other open quantum systems recently, as in Refs. [35, 209, 330, 331], and we will meet them again in chapters 6 and 7, in which they play an important role. This suggests that this kind of spectral singularities might be a common feature of the non-equilibrium dynamics of dissipative quantum systems in which non-Hermitian matrices are ubiquitous.

Monochromatic regime. As discussed in chapter 2, EPs are behind intriguing physical phenomena such as parity-time symmetry breaking or chiral effects for adiabatic EP encircling [207]. Here, we have focused on the fact that these spectral non-analycities separate different dynamical regimes. The 1D scenario that we have studied constitutes a many-oscillator generalization of simpler two-mode systems in which EPs were known to occur [207]. Moreover, the fact that the system is extended does not hinder the presence of coalescence: this is present as long as there is the right interplay between coherent

and incoherent processes. Indeed, the topology of this array enables a cascade of successive EPs for increasing coupling strength. As a result, there emerges a *monochromatic regime* in which the $2N$ collective modes display the same frequency, which leads to interference windows when probing the system, and which parallel those generally identified in the context of EIT, coupled resonator induced transparencies, and Fano resonances [315, 316, 318, 319, 321, 322, 325]. On the other hand, as we have shown in several occasions, the fact that EPs are singular points does not lead to a singularity in the temporal dynamics of expectation values: rather the considered quantities evolve continuously from one regime to another. This also occurs in the spin system, and it remains an open question to find a dynamical quantity in which such singular character can be identified, or even whether such a quantity exists.

Synchronization and coalescence. The reported monochromatic regime for the two spins naturally connects with the topic of synchronization. Here, we have established the emergence of mutual synchronization in this regime, and we have compared this scenario with the one in the presence of multiple frequencies, occurring in the same system for different parameter values and also in other similar spin systems [45, 90]. In particular, we have found that in the SFR, synchronization generally emerges after a transient in which the qubits display a sort of dephasing between their oscillations. While this might seem surprising in a monochromatic regime, we have traced it back to the presence of several collective modes with the same frequency but different decay rate. Then, this effective dephasing can be regarded as the temporal counterpart of the interference effects observed in the power spectrum, as an interference window at the resonant frequency in the case of collective operators. In this sense, synchronization is thus favored by one of the modes having a lifetime much larger than the rest, as in these conditions, when this is the only mode not damped out and the qubits phase-lock, the oscillation amplitudes are larger. This is certainly similar to the general case of transient synchronization in the presence of multiple frequencies that we have reported when $s_{12}/\gamma \neq 0$. Thus, the results enabled by coalescence parallel the general scenario of transient synchronization, in which *both* frequency- and phase-locking emerge after a transient, due to a long-lived subradiant mode [5, 7, 90]. Therefore, we conclude that synchronisation in the presence of coalescence can be regarded as a peculiar scenario within this more general context of transient synchronization [7].

Finally, it is interesting to briefly discuss the results of Ref. [46] in which synchronization is reported for a system made of two detuned atomic clouds with collective dissipation and incoherent pumping. In Ref. [46], synchronization is assessed by analyzing the frequencies of the emitted light, which is found to be monochromatic in the synchronized regime. This system is described at the semiclassical level, considering the mean-field equations for the first and second moments. In this approximate treatment, the emission of light is governed by a non-Hermitian matrix, and we can identify an EP just at the transition between the synchronized (monochromatic) regime and the unsynchronized one. Hence, despite one deals with a more complicated many-body scenario, one can still appreciate how the right interplay between coherent and incoherent processes leads to coalescence and to the reported monochromatic regime.

CHAPTER 5

Quantum synchronization in dimer atomic lattices

The contents of this chapter have been adapted from Ref. [3] entitled *Quantum synchronization in dimer atomic lattices*. The goal is to assess the possibility of synchronization in a spin system that can be simulated in a platform of cold atoms in optical lattices. We show that several forms of synchronization are possible, even though the kind of dissipation that can be engineered is local and not collective. Moreover, we also address the relation between synchronization and spin-spin correlations, finding that two-time correlations are good witnesses of synchronization, while single-time spin-spin correlations fail to capture the transition between the different possible synchronization regimes.

5.1 Introduction

Atoms trapped in optical lattices represent a rich platform to study many-body physics, entanglement and state engineering, as well as for quantum simulation of condensed matter phenomena [18, 332]. Prior to Ref. [3], synchronization was not reported in extended atomic lattices but it had been studied in mesoscopic atomic clouds in which collective dissipation was reported to be a crucial ingredient [46, 80]. In these atomic clouds, the synchronization dynamics can be understood at the semiclassical mean-field level, as we have mentioned before. This raises the question of whether synchronization can also emerge in the quantum dynamics of lattice and strongly correlated atomic systems. In fact, effective spin Hamiltonians often capture the low-energy physics of atomic lattices [333]. In this sense, synchronization had been previously reported for theoretical models of two spins with collective dissipation [45, 64, 90], or a non-dissipative spin coupled to a dissipative one [89]. However, can synchronization still emerge in extended spin systems and within the constraints imposed by the atomic lattice? This is one of the main questions that we addressed in Ref. [3] on which this chapter is based.

Building on the proposed experimental scheme of Ref. [265], we design a modified set-up, consisting of a one-dimensional atomic lattice in a dimer configuration, where we show that synchronization can emerge even in the absence of collective dissipation. This

contrasts with many of the previously discussed results in which collective dissipation is a key ingredient for synchronization [45, 64, 65, 98, 90, 101]. The dynamics of this atomic system is well described by an effective spin model with staggered dissipation rates. As we show, the spatial modulation of dissipation is what enables synchronization, which can emerge in two different forms, while it disappears in the limit of homogeneous chains similarly to synchronization blockade [95, 89].

Once established the emergence of synchronization, we address the question of whether this is witnessed by spin-spin correlations, which is an important open issue in the literature of quantum synchronization [44] (see also chapter 1). Interestingly, we will show that both single-time and multi-time spin-spin correlations accompany synchronization; however, only the latter can be taken as faithful measures of synchronization, as single-time correlations fail to capture the transition between the different synchronization regimes.

5.2 Dissipative spin chain

Cold atoms in optical lattices are suitable platforms for quantum simulation. In general, atomic systems allow for high experimental control, and cold atomic lattices provide a route to engineer highly adjustable spin models [18, 333, 334, 335, 336], for which trapped ions [337] and highly excited Rydberg atoms [338, 339] are also relevant set-ups. In fact, oscillation frequencies and coupling strengths can be tuned in these effective spin systems. On the other hand, we have seen that a crucial ingredient for synchronization is also dissipation, while in these proposals one essentially deals with closed Hamiltonian systems. Collective dissipation can be engineered and tuned in mesoscopic atomic clouds [46, 80], but what about engineered dissipation in extended atomic lattices? In Ref. [265] a proposal for implementing an effective spin chain with tunable dissipation is presented, as based on cold atomic lattices. As we will see, by properly modifying this proposal, we can engineer the effective spin model of Eqs. (5.4) and (5.5), which consists of a one-dimensional spin chain with nearest-neihbour couplings and two alternating frequencies and decay rates. The emergence of synchronization in this system will be assessed in Sec. 5.3.2. Before, we overview the main ingredients to implement the dissipative spin system of Eqs. (5.4) and (5.5).

Atoms in an optical lattice with engineered dissipation. As we have commented, one-dimensional optical lattices can also be used to simulate an Ising-like dissipative spin chain, where spins are the two lowest vibrational levels $|0\rangle$ and $|1\rangle$ of the atoms trapped in the optical potential [265]. The system can be described as a two-band Bose-Hubbard model in the Mott-insulator regime, in which the atoms are well localized at each site of the optical lattice, and tunneling between lattice sites is strongly suppressed [340]. Such a system can be modeled by a Hamiltonian of the following type [265] ($\hbar = 1$):

$$\begin{aligned}\hat{H}_{\text{atomic}} = \sum_{j=1}^{N} \Big\{ &\frac{\omega_0}{2}(\hat{d}_j^\dagger \hat{d}_j - \hat{c}_j^\dagger \hat{c}_j) + U_{01}\hat{c}_j^\dagger \hat{c}_j \hat{d}_j^\dagger \hat{d}_j + \frac{U_{00}}{2}\hat{c}_j^\dagger \hat{c}_j(\hat{c}_j^\dagger \hat{c}_j - 1) \\ &+ \frac{U_{11}}{2}\hat{d}_j^\dagger \hat{d}_j(\hat{d}_j^\dagger \hat{d}_j - 1)\Big\} + \sum_{j=1}^{N-1}(t_0 \hat{c}_j^\dagger \hat{c}_{j+1} + t_1 \hat{d}_j^\dagger \hat{d}_{j+1} + H.c.),\end{aligned} \tag{5.1}$$

where the bosonic operators $\hat{c}_j^\dagger$ and $\hat{c}_j$ ($\hat{d}_j^\dagger$ and $\hat{d}_j$) create and annihilate an atom in the lowest $|0\rangle$ (second lowest $|1\rangle$) motional state of site j of the optical lattice, separated by the largest energy scale of the system given by ω_0 [340, 341]. When the atoms are at the same site, they experiment repulsive interactions with strengths U_{00}, U_{11}, and U_{01} [265]. In the Mott-insulator regime, these repulsive interactions are much stronger than the tunneling rates, i.e. $U_{00}, U_{11}, U_{01} \gg t_{0,1}$, such that the atoms tend to be localized at each site, preferably sharing site with the minimum possible amount of other atoms [340, 341].

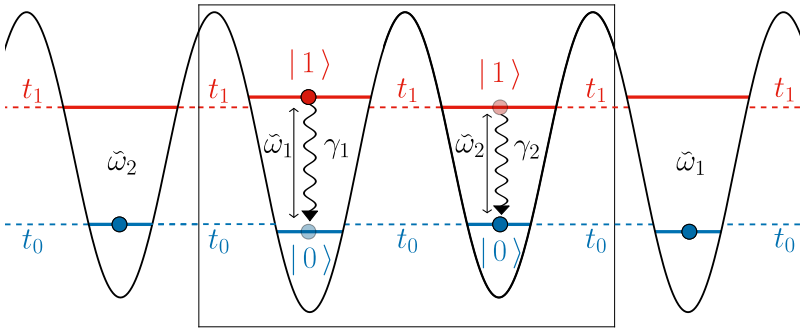

Figure 5.1: Schematic illustration of the atomic lattice. A dimeric configuration is considered in which there are two alternating energy separations between the ground and first motional excited state, given by $\tilde{\omega}_{1,2}$. Atomic tunneling between different sites occurs with rates $t_{0,1}$, in which the motional state remains unchanged. Strong same-site repulsive interactions ensure the system is in the Mott-insulator regime with just one atom per site, which enables the implementation of an effective spin Hamiltonian. Finally, engineered dissipation with rates $\gamma_{1,2}$ can be implemented by laser cooling techniques that address the internal electronic structure of the atoms.

The strong lattice anharmonicity that allows a two band description, the strong on-site repulsion, and the perturbative contributions due to weak tunneling among lattice sites enable the approximation of an XXZ spin-1/2 chain Hamiltonian with highly adjustable parameters, that captures accurately the low-energy physics of the atomic system given in Eq. (5.1) in the regime of one atom per site [265] (see also appendix F).

The importance of the proposal [265] stems from the fact that it enables one to engineer a tunable local Lindblad dissipation too. This is introduced by optically addressing the internal (three level 'Λ') structure of the atomic states in the Lamb-Dicke regime [248, 255]. Then, the decay from the first excited motional state of the optical lattice potential $|1\rangle$ towards the motional ground state $|0\rangle$ can be engineered to take the usual form $\sum_i \gamma_j(2\hat{\sigma}_j^- \hat{\rho}\hat{\sigma}_j^+ - \{\hat{\sigma}_j^+\hat{\sigma}_j^-, \hat{\rho}\})$, where $\hat{\sigma}_j^{\pm}$, $\hat{\sigma}_j^z$ are the pseudospin operators describing the effective spin-1/2 of site j, as made by this atom being either at the sate $|0\rangle$ or the state $|1\rangle$ (see [265] and appendix F). Importantly, the amount of dissipation can be locally tuned by addressing the parameters of the laser cooling scheme (e.g. detuning, driving strength, driving phase) [265], also enabling an effective suppression of the opposite transitions from $|0\rangle$ to $|1\rangle$, i.e. heating can be experimentally made several orders of magnitude lower than cooling and then neglected.

Using standard techniques to produce double wells [342, 343, 344, 345], the dissipative model of [265] can be modified such that the lattice results in dimer arrangement where, in each well, the motional states have different (staggered) energy separation $\tilde{\omega}_{1,2}$. This is done by considering a small dimeric modulation of the optical potential, as described by the following Hamiltonian:

$$\hat{H}_{\text{mod}} = \sum_{j\in\text{odd}} \frac{\omega_1}{2}(\hat{d}_j^\dagger \hat{d}_j - \hat{c}_j^\dagger \hat{c}_j) + \sum_{j\in\text{even}} \frac{\omega_2}{2}(\hat{d}_j^\dagger \hat{d}_j - \hat{c}_j^\dagger \hat{c}_j), \tag{5.2}$$

where we have defined the small frequency modulations $\omega_{1,2} = \tilde{\omega}_{1,2} - \omega_0$, and the detuning

$$\delta = \omega_1 - \omega_2. \tag{5.3}$$

For this modulation to be a perturbation it should satisfy $\omega_0 \gg \omega_1, \omega_2$, while in order to be able to engineer the desired spin effective Hamiltonian, we also need that $U_{00}, U_{11}, U_{01} \gg \delta$ (see appendix F). In Fig. 5.1, we represent the system described by (5.1) and (5.2) in the relevant Mott-insulator regime with one atom per site together with the engineered source of dissipation.

Effective spin model. Under the conditions described above, a dimer effective spin model is found to capture the low-energy physics of this atomic system (further details are presented in appendix F). This spin model is described by the following Hamiltonian:

$$\hat{H} = \sum_{j=1}^{N} \frac{\omega_j}{2} \hat{\sigma}_j^z + \sum_{j=1}^{N-1} \lambda(\hat{\sigma}_j^+ \hat{\sigma}_{j+1}^- + H.c.), \tag{5.4}$$

where $\omega_j = \omega_{1(2)}$ is the frequency of spin j with j odd (even) and λ is the spin-spin coupling strength, which can be tuned by adjusting the parameters of the optical lattice [265].

The use of a bichromatic lattice will also affect the engineered dissipation, as the corresponding decay rates also depend on the trap frequency through the detuning with the cooling laser [265]. In the weak dissipation regime, the reduced density matrix $\hat{\rho}$ of the chain obeys a local master equation:

$$\frac{d}{dt}\hat{\rho} = -i[\hat{H}, \hat{\rho}] + \sum_j 2\gamma_j \mathcal{D}[\hat{\sigma}_j^-]\hat{\rho}. \tag{5.5}$$

Because of the presence of a bichromatic lattice, the decay rates γ_j also assume staggered values and, they can be chosen such that $\gamma_1/\omega_1 = \gamma_2/\omega_2$ (see appendix F). Hence, the model first described in Ref. [265], and here modified to allow for detuning and staggered losses, goes beyond the standard simulation of closed spin systems [18, 333, 334, 335, 336], and provides a dissipative set-up to explore the emergence of quantum synchronization.

5.3 Synchronization dynamics

In this section we analyze the emergence of transient synchronization in the engineered spin system described by Eqs. (5.4) and (5.5). Indeed, in the proper parameter region, the spins progressively evolve towards the non-oscillatory stationary state of the system (all spins down or all atoms in the ground state) oscillating monochromatically and with a locked phase difference.

5.3.1 Long-time dynamics and one-excitation sector

As in the previous chapter, the analysis of the eigenspectrum of the Liouvillian will enable us to understand the emergence of synchronization. In this sense, a key observation is that the Liouvillian spectrum can be calculated from the spectrum of the superoperator associated to the non-Hermitian effective Hamiltonian [see Eq. (5.7)]:

$$\hat{K} = \hat{H} - i \sum_j^N \gamma_j \hat{\sigma}_j^+ \hat{\sigma}_j^-. \tag{5.6}$$

where $\hat{H}$ is the spin Hamiltonian given in (5.4). This non-Hermitian Hamiltonian defines the master equation without the 'jump' terms, i.e. Eq. (5.5) without $\sum_j 2\gamma_j \hat{\sigma}_j^- \hat{\rho} \hat{\sigma}_j^+$:

$$\frac{d}{dt}\hat{\rho} = -i(\hat{K}\hat{\rho} - \hat{\rho}\hat{K}^\dagger) \equiv \mathcal{K}\hat{\rho} \tag{5.7}$$

where we have defined the superoperator $\mathcal{K}$. The importance of the non-Hermitian Hamiltonian (5.6) resides in the fact that $\mathcal{L}$ has an upper triangular form in the eigenbasis of $\mathcal{K}$, and the Liouvillian diagonal elements correspond to the eigenvalues of $\mathcal{K}$ (and then of $\mathcal{L}$ itself), while the jump operators $\sum_j 2\gamma_j \hat{\sigma}_j^- \hat{\rho} \hat{\sigma}_j^+$ only contribute to off-diagonal elements. Hence, since the eigenvalues of $\mathcal{K}$ can be obtained from those of $\hat{K}$ and $\hat{K}^\dagger$, the full Liouvillian spectrum can be obtained from that of (5.6) and its conjugate. This special (and

convenient) Liouvillian structure follows from certain features of the master equation, as proved for the general case in Ref. [346], and which in our case translate into the following features: (i) $\hat{H}$ conserves the total number of up (down) spins; (ii) the jump operators $\hat{\sigma}_j^-$ only change the number of up (down) spins by one; (iii) there are no driving processes, such that the final state is all spins down (or the vacuum, in terms of the collective excitations).

Therefore, the first step in the study of $\mathcal{L}$ is to analyze the collective excitations of $\hat{K}$, which can be readily obtained from those of $\hat{H}$ replacing the real frequencies $\omega_{1,2}$ by the complex valued ones $\Omega_{1,2}$, that incorporate the staggered decay rates:

$$\Omega_{1(2)} = \omega_{1(2)} - i\gamma_{1(2)}. \tag{5.8}$$

That is, in the presence of the non-Hermitian dissipation term, the collective excitations of $\hat{H}$ acquire a finite lifetime. Then, in complete analogy to what can be done for $\hat{H}$, its non-Hermitian counterpart can be diagonalized by Jordan-Wigner transformation (i.e. fermionization of the spin chain) [347], a Fourier sine transform (as the one of chapter 4) plus a final rotation within the same wavevector blocks (see appendix G for the details). This yields the two-band elementary[1] complex eigenvalues:

$$\Omega_k^{\pm} = \frac{\Omega_1 + \Omega_2}{2} \pm \frac{1}{2}\sqrt{(\Omega_1 - \Omega_2)^2 + 16\lambda^2 \cos^2\frac{k}{2}}, \tag{5.9}$$

with the allowed wavevectors $k = 2\pi l/(N+1)$, $l = 1, 2, ..., N/2$. These complex eigenvalues correspond to the one-excitation sector of $\hat{K}$, i.e. they contain the frequencies and decay rates of each one of its elementary collective excitations, while the full eigenspectrum is obtained by making all the possible 'multi-particle' combinations taking into account that, due to the fermionic character of the collective modes, each of them can display an excitation number of either zero or one.

In the one-excitation sector, the collective modes can be easily written in the basis of the spins:

$$\begin{aligned} |u_k\rangle &= \sqrt{\frac{4}{N+1}} \sum_{j=1}^{N/2} \Big(\cos\theta_k \sin\left[k(j-\frac{1}{2})\right] |\uparrow_{2j-1}\rangle - \sin\theta_k \sin\left[kj\right] |\uparrow_{2j}\rangle \Big), \\ |v_k\rangle &= \sqrt{\frac{4}{N+1}} \sum_{j=1}^{N/2} \Big(\sin\theta_k \sin\left[k(j-\frac{1}{2})\right] |\uparrow_{2j-1}\rangle + \cos\theta_k \sin\left[kj\right] |\uparrow_{2j}\rangle \Big), \end{aligned} \tag{5.10}$$

where $|u_k\rangle(|v_k\rangle)$ correspond to the modes of the '+(−)' band, and $|\uparrow_j\rangle$ denotes the state with spin j in the up state and the rest in the down state (i.e. a state of the one-excitation sector). For the expression of θ_k and the derivation of these results see appendix G. From (5.10), we can clearly appreciate the delocalized nature of the collective modes, similarly to what we have found in chapter 4 for the 1D array of harmonic oscillators.

As anticipated, the eigenvalues of $\mathcal{L}$ are obtained by combining $\Omega_k^{\pm}$ and their complex conjugates $\Omega_k^{\pm *}$ (corresponding to $\hat{K}^\dagger$) as prescribed in [346], so that their imaginary part (decay rates) *always add together*. Moreover, $-i\Omega_k^{\pm}$ and $i\Omega_k^{\pm *}$ are already eigenvalues of $\mathcal{L}$, corresponding to one-excitation eigenmodes. Thus, *the smallest decay rates of the system belong to this sector*. This is a crucial observation, from which it follows that the relaxation dynamics before the final decay into the ground state (all spins down) is conveniently described in the one-excitation sector, considering the slowest modes that can be identified comparing their decay rates Γ_l (absolute value of the imaginary parts

[1]The adjective 'elementary' is motivated by the fact that the full spectrum of $\hat{K}$ is made of linear combinations of these basic eigenvalues, according to the 'populations' of each of the dissipative collective excitations.

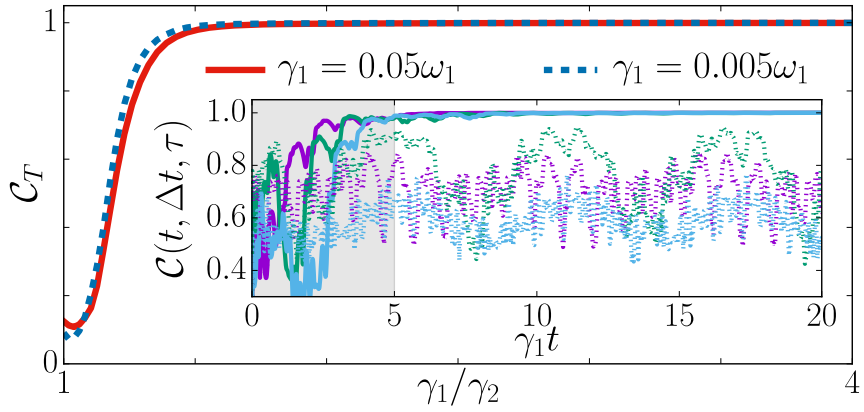

Figure 5.2: Emergent synchronization. Main panel: Global synchronization measure $\mathcal{C}_T(t, \Delta t, \tau)$ at time $t = 10/\gamma_1$ as a function of γ_1/γ_2 for two different rates γ_1. Inset: Evolution of $\mathcal{C}_{\langle\hat{\sigma}_j^x\rangle,\langle\hat{\sigma}_{j+1}^x\rangle}$ for $j = 1$ (purple line), $j = 2$ (in green), and $j = 3$ (in blue), with $\omega_1\Delta t = 3$. Here $\gamma_1/\omega_1 = 0.05$, solid lines correspond to $\gamma_1 = 4\gamma_2$ (staggered losses), dotted lines to $\gamma_1 = \gamma_2$ (homogeneous losses). Shadowed region displays the transient after which the staggered case displays synchronization. System of $N = 4$ spins, with $\delta = 0.75\omega_1$, $\lambda = 0.4\omega_1$, and initial state $|\Psi(t = 0)\rangle = |{+_1}\rangle \otimes |{+_2}\rangle \otimes |{+_3}\rangle \otimes |{+_4}\rangle$, where $|{+_j}\rangle = (|{\downarrow_j}\rangle + |{\uparrow_j}\rangle)/\sqrt{2}$.

of $\Omega_k^{\pm}$) and frequencies ν_l (real parts of $\Omega_k^{\pm}$) [2]. Therefore, we will be able to understand the synchronization dynamics by considering just these modes, which constitutes a huge simplification.

It is finally interesting to comment that this spin system does not display EPs as long as $\delta \neq 0$. Indeed, the square root in Eq. (5.9) cannot vanish when the spins are detuned. Hence, in spite of the similar dimeric structure as in the case of the harmonic oscillators of Sect. 4.2.1, in the present case the coherent and incoherent processes do not match in the right way to enable coalescence.

5.3.2 Staggered losses as a resource for transient synchronization

We now analyze the full system dynamics and quantify the emergence of spontaneous synchronization among atomic observables with no classical counterpart, as the spin coherences $\langle\hat{\sigma}_j^x\rangle$ [44]. Indeed, at any time during relaxation, coherences are present before reaching the equilibrium all spins down state. Their dynamical synchronization can be assessed using the Pearson factor, as introduced in Eq. (3.21). Here, we will generally encounter arbitrary locked phase differences, for which we consider its maximized version, i.e. the Pearson factor computed at different times, $x_1(t)$ and $x_2(t + \tau)$, and maximizing over τ (see appendix B). In Fig. 5.2 (inset) we show the maximized Pearson factor, i.e. $\mathcal{C}_{\langle\hat{\sigma}_j^x\rangle,\langle\hat{\sigma}_{j'}^x\rangle}(t, \Delta t, \tau)$, among nearest-neighbor spin pairs, ranging between 0 (no synchronization) and 1 (perfect synchronization): synchronization is found among all atoms in the presence of local staggered dissipation (solid lines), while it does not emerge for $\gamma_1 = \gamma_2$ (dotted lines). We also consider the global mutual synchronization indicator:

$$\mathcal{C}_T(t, \Delta t, \tau) = \prod_{i<j} \mathcal{C}_{\langle\hat{\sigma}_i^x\rangle,\langle\hat{\sigma}_j^x\rangle}(t, \Delta t, \tau), \tag{5.11}$$

(main panel of Fig. 5.2) reaching its maximum value 1 only if all atom coherences are synchronized. We see that mutual synchronization for a given detuning ($\delta = 0.75\omega_1$ in Fig. 5.2) is enabled by the presence of staggered dissipation rates, emerging for a wide range of γ_1/γ_2 values, while it disappears if losses become uniform ($\gamma_1/\gamma_2 \approx 1$).

[2] The eigenfrequencies (decay rates) given by (5.9), are denoted by ν_l (Γ_l) with $l \in [1, N]$. The first $N/2$ elements correspond to the band '−' with the $k \to l$, while the next $N/2$ to the band '+' with $k \to l - N/2$.

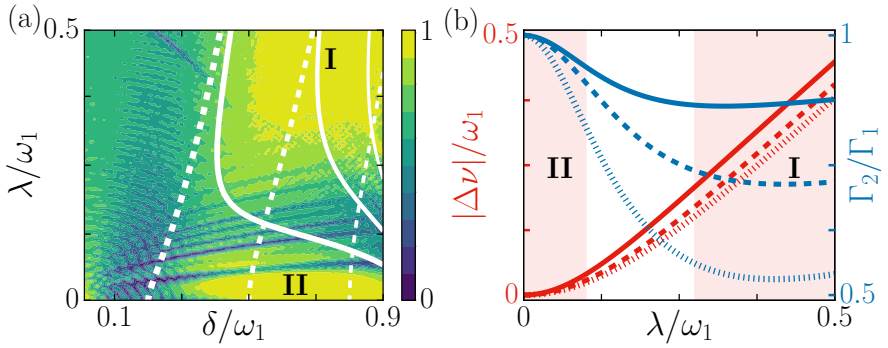

Figure 5.3: (a) Map of spontaneous synchronization among all spin pairs $\mathcal{C}_T(t, \Delta t, \tau)$ at $\gamma_1 t = 10$ and $\omega_1 \Delta t = 80$, varying detuning and coupling strength, with $|\Psi(t=0)\rangle = |\Downarrow\rangle/\sqrt{2} + (|\uparrow_2\rangle + |\uparrow_3\rangle)/2$, where $|\Downarrow\rangle$ is the vacuum state (in terms of collective modes) or all spins in the down state. Synchronization is found at the yellow (light color) regions I and II ($\mathcal{C}_T \geq 0.9$). White lines are contours of the ratio of the two smallest decay rates, Γ_2/Γ_1 (solid lines), and of the smallest decay rates of each band Γ_2/Γ_3 (dashed lines). Thicker lines for increasing ratio values, respectively $(0.9, 0.75, 0.6)$ and $(0.8, 0.5, 0.2)$. (b) In red, difference between the frequencies associated to the smallest decay rates: $|\Delta\nu| = |\nu_1 - \nu_2|$, varying λ. In blue, ratio between the smallest decay rates. Solid lines $\delta = 0.5\omega_1$, dashed lines $\delta = 0.75\omega_1$, dotted lines $\delta = 0.9\omega_1$. For both figures $\gamma_j = 0.05\omega_j$.

As we have discussed in the previous chapters and as reported for other models [45, 98, 89, 90], the emergence of synchronization is due the presence of multiple dissipative timescales. Normal modes can conjure to dissipate at widely different rates, Γ_l, so that the predominant contribution to the long-time dynamics is represented by the slowest decaying mode. Quantum synchronization then emerges as an ordered, spatially delocalized, monochromatic oscillation in the pre-asymptotic regime (transient synchronization). This is the case when considering our lattice with staggered dissipation, as revealed by inspection of the Liouvillian spectrum. On the other hand, if local dissipation is spatially homogeneous, the imaginary parts of the eigenvalues (5.9) coincide, there is no separation between decay rates, and in fact the system does not synchronize in spite of the presence of coherent coupling between spins (Fig. 5.2). Therefore, we can regard the staggered dissipation rates as a *resource for synchronization*. In the following subsection, we introduce two different forms of the enabled synchronization induced by staggered losses.

5.3.3 Inter-band and intra-band synchronization

Here, we proceed to analyze systematically the emergence of synchronization in the system, by calculating the global Pearson factor $\mathcal{C}_T$ [Eq. (5.11)] varying the detuning between the two sublattices δ and their coupling strength λ, for a short chain of four spins [Fig. 5.3 (a)]. The global Pearson factor is calculated after an initial transient, similarly to Fig. 5.2, such that we allow for the slowest modes (if present) to already dominate the dynamics and synchronize the system. This synchronization map shows a non-trivial scenario with two different and well separated regions that support synchronization, both occurring for strong detuning (yellow regions with $\mathcal{C}_T \geq 0.9$): region I characterized by strong coupling, and region II, by small coupling and a larger detuning window. The fact that here synchronization is found only for large detunings contrasts with the usual Arnold tongue behavior (as that of Fig. 3.4) in which synchronization is found when the system units have a similar frequency. Below, we will discuss the mechanism behind this peculiar behavior.

These mutual synchronization regimes can be understood analyzing the spectral content of the coherences' dynamics in the one-excitation sector. That is, we can use the

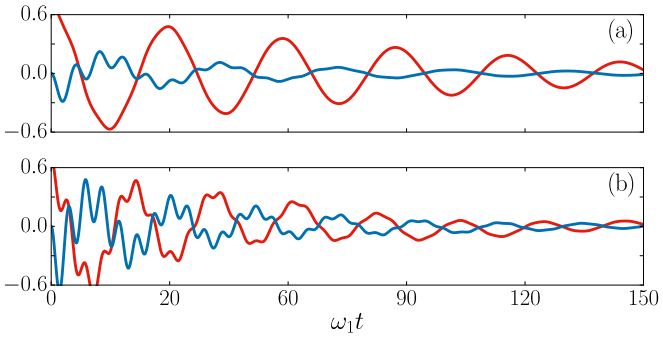

Figure 5.4: Synchronized trajectories for spins $\langle\sigma_2^x\rangle$ (red) and $\langle\sigma_3^x\rangle$ (blue), with initial condition $|\Psi(t=0)\rangle = |\Downarrow\rangle/\sqrt{2} + (|\uparrow_2\rangle + |\uparrow_4\rangle)/2$. In (a) we fix $\lambda = 0.1\omega_1$, $\delta = 0.75\omega_1$ (synchronization region II), while in (b) $\lambda = 0.475\omega_1$, $\delta = 0.85\omega_1$ (synchronization region I). In both cases we have $N = 4$ and $\gamma_j = 0.05\omega_j$.

analytical expression for the eigenvalues and eigenvectors of the Liouvillian in the one-excitation sector as based on Eqs. (5.9) and (5.10) (see Sect. G.2.1 in appendix G) to write down the dynamics of the observables, similarly to what we have done in the previous chapter. Hence, for the x-components of the spins we obtain:

$$\langle\hat{\sigma}_j^x(t)\rangle = 2Re\Big[\sum_{l=1}^{4} u_l(j)e^{-(i\nu_l+\Gamma_l)t}\Big], \tag{5.12}$$

with weights $u_l(j)$ depending on the site j, eigenmode l [3], and initial condition (see Eq. (G.17) in appendix G). In region II the frequencies are nearly degenerate in each ($\pm$) band, while N well separated frequencies are present in region I. To support this observation, we plot in Fig. 5.3 (b) the frequency difference between the two modes of the '-' band and the ratio between their decay rates (notice that the longest lived mode belongs to this band).

Inter-band synchronization. The "flat" and well separated two-band spectrum found in region II leads to what we term *inter-band synchronization*. In fact, in the limit of vanishing λ, the two frequency degenerate bands [Fig. 5.3 (b)] are separated by $\delta+i(\gamma_1-\gamma_2)$, as can be deduced from Eq. (5.9). For weak coupling λ, two manifolds emerge with very similar frequencies and damping rates. Each of the sublattices of the atomic dimer is strongly coupled to one of the manifolds and weakly coupled to the other one, leading to an effective two-body behavior. Inter-band synchronization is present as long as the difference in local losses $\gamma_{1,2}$ allows one to establish two well separated timescales [region highlighted by white dashed lines in Fig. 5.3 (a)]. Being the staggered damping rates related to the sublattices detuning (here we consider $\gamma_1/\omega_1 = \gamma_2/\omega_2$), mutual synchronization only emerges for detuning δ larger than a threshold value, at difference from the typical scenario of synchronization favored by small detuning [43] and similarly to synchronization blockade [95, 89], as we have anticipated. This region shrinks when decreasing dissipation strength γ_j, as shown in appendix G. This can be understood from the fact that in the presence of smaller dissipation rates, the spins are sensitive to smaller frequency differences, and thus they can resolve better the small differences within each of the quasi flat bands, hindering the emergence of mutual synchronization.

Intra-band synchronization. Increasing the coupling λ, the quality of synchronization deteriorates (Fig. 5.3 (a), $0.1 \lesssim \lambda/\omega_1 \lesssim 0.25$) as the two-body behavior of the spectrum disappears and several non-degenerate modes compete. Further increasing the coupling

[3] As for the frequencies and decay rates, the first $N/2$ elements correspond to the band '−' with the $k \to l$, i.e. to $|v_k\rangle$, while the next $N/2$ to the band '+' with $k \to l - N/2$, i.e. to $|u_k\rangle$.

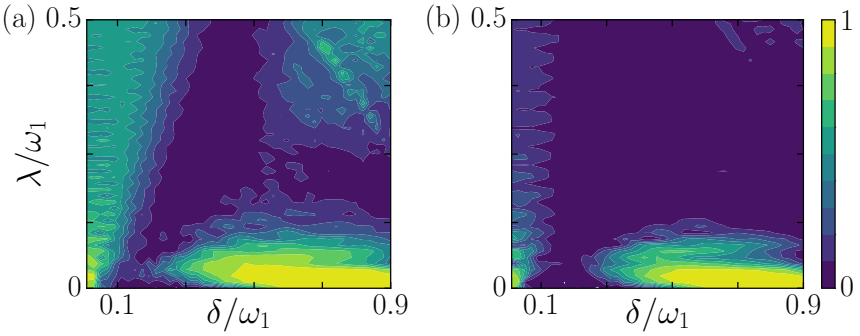

Figure 5.5: Synchronization map as product of Pearson correlation between spin pairs coherence operators $\mathcal{C}_T(t) = \prod_{i<j} \mathcal{C}_{\langle\hat{\sigma}_i^x\rangle,\langle\hat{\sigma}_j^x\rangle}(t)$ at $\gamma_1 t = 10$ and $\omega_1 \Delta t = 80$, varying detuning and coupling strength, and with $|\Psi(t=0)\rangle = |\Downarrow\rangle/\sqrt{2} + \sum_{j=1}^{N} |\uparrow_j\rangle/\sqrt{2N}$. Strong synchronization is found at the yellow regions ($\mathcal{C}_T \geq 0.9$). (a) For a chain of $N = 6$ spins. (b) For a chain of $N = 8$ spins. For both figures $\gamma_j = 0.05\omega_j$.

strength, synchronization is restored for coupling strengths such that there is a significant difference between the two slowest dissipation rates, now in the lower band, so that a leading mode governs the long-time dynamics. This is *intra-band synchronization* occurring in region I of Fig. 5.3 (a) and requiring significant deviations between the slowest dissipation rates [as highlighted by white solid lines in Fig. 5.3 (a)]. This picture is confirmed when looking at the two slowest modes in Fig. 5.3 (b), with frequencies and decay rates of the lower band (-) drifting apart as the coupling increases. In this figure, we can clearly appreciate how for small coupling strength the eigenvalues within the same band are almost degenerate, allowing inter-band synchronization, while when this is increased the spins can clearly resolve the different collective frequencies and only intra-band synchronization is possible, when one of them has a decay rate much smaller than the rest.

In Fig. 5.4 we show two examples of synchronized trajectories. In (a) we plot a case in region II, while in (b) a case in region I. We only show two spin's coherences, $\langle\sigma_2^x\rangle$ and $\langle\sigma_3^x\rangle$ for clarity, although all of them are synchronized. In both cases we can see that after a transient, the spins synchronize almost in anti-phase and at the slow frequency, corresponding to the eigenmode with the smallest decay rate. Notice how in the case of inter-band synchronization [panel (a)], one of the sublattices is more excited than the other; while for intra-band synchronization [panel (b)], both display a similar amount of excitation. This is because in region II, the collective modes of each of the bands (5.10) display a stronger localization in each of the sublattices, while in region I, they tend to be more evenly distributed between the two sublattices.

Synchronization in larger chains When considering longer chains, the two physical mechanisms I and II for SS imply different levels of robustness. In fact, inter-band synchronization II persists for long chains, as it mainly relies on the presence of the gap $\delta + i(\gamma_1 - \gamma_2)$. This is not the case of region I, where the relevant spectral gap is obtained taking the difference between the two values of Ω_k^- with the smallest imaginary parts, which goes to zero as N increases, Eq. (5.9). This is shown in Fig. 5.5, in which we present the synchronization maps for larger chains of $N = 6$ and $N = 8$, panel (a) and (b) respectively. We observe how synchronization in region I rapidly disappears as the size of the chain is increased. In contrast inter-band synchronization of region II is rather robust as it depends on the fixed gap δ.

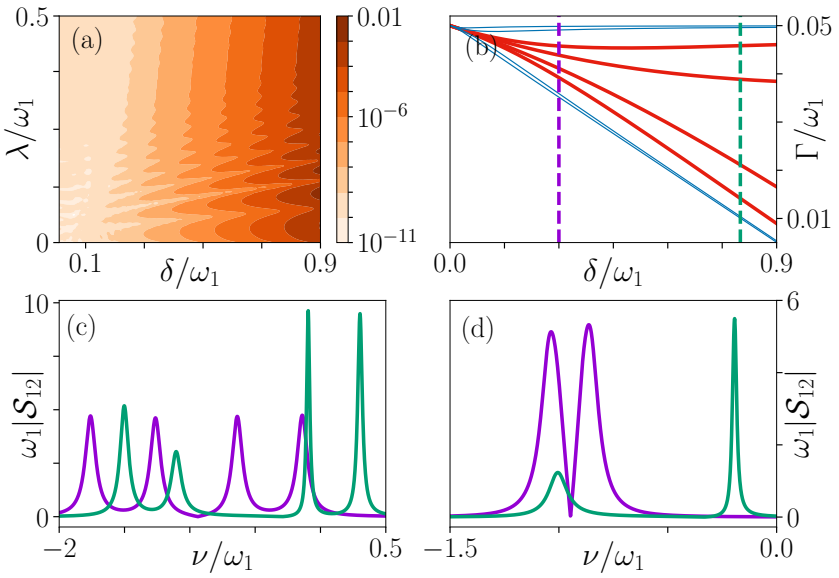

Figure 5.6: (a) In color $|Z(\bar{t})|$, with $\gamma_1\bar{t} = 10$, and for $|\Psi(t=0)\rangle = |\Downarrow\rangle/\sqrt{2} + \sum_{j=1}^{4} |\uparrow_j\rangle/\sqrt{8}$, and averaged over few oscillations. We plot the absolute value as the magnitude of the correlations is the relevant quantity. (b) Decay rates Γ_l as a function of the detuning, for $\lambda = 0.5\omega_1$ (red) and $\lambda = 0.05\omega_1$ (blue). (c) and (d) $\omega_1|\mathcal{S}_{12}(\nu/\omega_1)|$, with $\delta = 0.1\omega_1$ (purple) and $\delta = 0.8\omega_1$ (green). In (c) we fix $\lambda = 0.5\omega_1$ (synchronization region I), and in (d) $\lambda = 0.05\omega_1$ (synchronization region II). We plot the absolute values to ease peak comparison. In all plots $\gamma_j/\omega_j = 0.05$.

5.3.4 Transient synchronization and correlations

Often, two-body quantum correlation indicators are taken as *bona fide* synchronization measures [44], as they are able to reveal the presence of phase-locking. However, as already discussed in chapter 1, it is an important issue to determine in which cases they capture faithfully the emergence of synchronization. Here, we show that the presence of such correlations is necessary but not sufficient to predict the emergence of spontaneous synchronization in the present system. We study the one-time correlation $Z(t) \equiv \langle \hat{\sigma}_1^x(t)\hat{\sigma}_2^x(t)\rangle$ often considered in the context of superradiance [348], where t is set after the onset of synchronization. As shown in Fig. 5.6 (a), Z increases with detuning (analogous results are found for other pairs) but it displays a weak dependence on λ, being then unable to capture the transition from region I to region II. An explanation for this behavior can be given considering the one-excitation sector, where we can write this quantity in terms of the Liouvillian eigenmodes:

$$\begin{aligned} Z(t) &= 2\mathrm{Re}[\langle \hat{\sigma}_1^+(t)\hat{\sigma}_2^-(t)\rangle] \\ &= 2\mathrm{Re}[\sum_{l,m=1}^{4} w_{l,m}(1,2)e^{[-i(\nu_l-\nu_m)-\Gamma_m-\Gamma_l]t}], \end{aligned} \tag{5.13}$$

with weights $w_{l,m}(1,2)$ depending on the spins, eigenmodes l and m, and initial condition (see Eq. (G.20) in appendix G). The evolution of Z is governed by exponentials containing *combinations* of eigenvalues instead of single ones, depending then on slow and less slow rates. Therefore, differently from $\mathcal{C}$, it does not allow us to distinguish the slowest relaxation modes.

Two-time correlations. Different is the case for two-time correlation functions of the type $\langle \hat{\sigma}_l^-(t+\tau)\hat{\sigma}_m^+(t)\rangle$ in the stationary state, related to absorption spectra [349] (for emission of radiating dipoles see Refs.[46, 80]). Similarly to what we have found for the

case of the two spins of the previous chapter, this kind of correlations gives more insight on the temporal dynamics and capture the presence of mutual synchronization in both regimes I and II described above. In Fig. 5.6 (c), (d) we plot the Fourier transform of the two-time cross-correlations:

$$\mathcal{S}_{12}(\nu) = \mathrm{Re}\Big[\int_0^\infty d\tau e^{-i\nu\tau}\langle\hat{\sigma}_1^-(\tau)\hat{\sigma}_2^+(0)\rangle\Big] \tag{5.14}$$

in the (vacuum of collective modes or all spins down) stationary state of the system. Notice that, since the stationary state is the all spins down state, this kind of two-time correlations belong to the one-excitation sector (similarly to the case of the spins with zero pumping of the previous chapter), and hence they could be a good witness for the emergence of synchronization. In particular, using the one-excitation eigenvectors and eigenvalues of the Liouvillian we get:

$$\langle\hat{\sigma}_1^-(\tau)\hat{\sigma}_2^+(0)\rangle = \sum_{l=1}^{4} v_l(1,2)e^{-(i\nu_l+\Gamma_l)\tau}, \tag{5.15}$$

with weights $v_l(1,2)$ depending on the overlap of the eigenmode with the considered spin sites (see Eq. (G.22) in appendixG). We observe that the dynamics of these correlation functions is the same as the one for the spin coherences (with the initial condition $\hat{\sigma}_j^+|\Downarrow\rangle$). Thus the spectra $\mathcal{S}_{lm}(\nu)$ for each pair l,m display a set of at most N resonance peaks, localized at the eigenfrequencies of the one-excitation sector, with linewidths determined by the corresponding decay rates, and height depending on the weights $v_l(1,2)$. These spectra contain the information needed for the analysis of synchronization.

In Fig. 5.6 (c) we plot a synchronized (green line) and an unsynchronized (purple line) two-time correlation function for strong coupling, while in Fig. 5.6 (d) we do it for weak coupling. In the absence of synchronization, for small detuning and strong coupling [Fig. 5.6(c)], the spectrum displays multiple peaks, no one significantly sharper than the others. For both small detuning and coupling, we find two peaks with similar decay rates [Fig. 5.6 (d)], while in the no-synchronization region between region I and II of Fig. 5.3 (a) two of the four peaks (the ones of the same band) display similar width (see Fig. 5.7 and discussion below). Looking instead at synchronized parameter regions, the spectra are characterized by the presence of a peak with width significantly smaller than the rest. Intra-band synchronization (I) in Fig. 5.6 (c) displays a sharper third line among four, while in Fig. 5.6 (d), inter-band synchronization (II) clearly shows the effective two-body behavior of the system discussed above. This is also appreciated in Fig. 5.6 (b) where, for small coupling (blue lines), two pairs of nearly degenerate decay rates emerge as detuning is increased. In contrast, for strong coupling (red lines), the system displays four well-differentiated decay rates.

For both strong and weak coupling as detuning grows one of the peaks becomes significantly thinner, transiting from the purple spectra in Fig. 5.6 (c), (d) to the green ones, as we show in Fig. 5.7. In (a) we plot examples for weak coupling ($\lambda = 0.05\omega_1$), in (c) for strong coupling ($\lambda = 0.5\omega_1$) and in (b) for a coupling strength in which there is no synchronization ($\lambda = 0.2\omega_1$). Different colors correspond to three different detunings: $\delta = 0.3\omega_1$ (gold), $\delta = 0.5\omega_1$ (blue), $\delta = 0.8\omega_1$ (red). In Fig. 5.7 (a) there are effectively only two peaks, and we can appreciate how when increasing the detuning one of the peaks becomes significantly thinner, indicating mutual synchronization of region II. In contrast, if we increase the coupling to $\lambda = 0.2\omega_1$, four different peaks emerge [Fig. 5.7 (b)]. In this case there are two peaks which become thinner as detuning is increased; however, both of them display a similar width, hindering synchronization. In contrast, for stronger coupling [Fig. 5.7 (c)], these two peaks display clearly different widths. This asymmetry in the decay rates of the eigenmodes is what enables synchronization in region I.

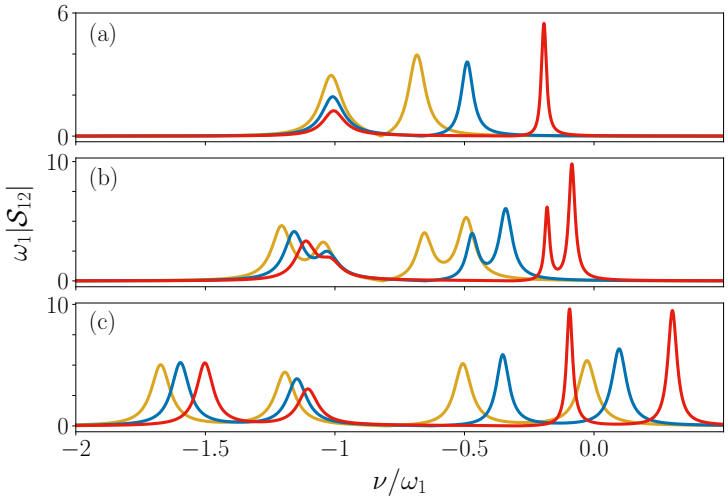

Figure 5.7: $\omega_1|\mathcal{S}_{12}(\nu/\omega_1)|$ for different couplings and detunings. In (a) $\lambda = 0.05\omega_1$, in (b) $\lambda = 0.2\omega_1$, and in (c) $\lambda = 0.5\omega_1$. Different line colors correspond to different detunings: gold $\delta = 0.3\omega_1$, blue $\delta = 0.5\omega_1$, red $\delta = 0.8\omega_1$. In all cases $N = 4$ and $\gamma_j = 0.05\omega_j$.

We further mention that the two-time autocorrelation functions behave analogously, and they are also good witnesses of synchronization (not shown). However, cross-correlation functions yield better results, as the peaks tend to display less disparity in their height, easing peak comparison, and hence making it easier to extract conclusions.

5.4 Concluding remarks

In this chapter, we have shown that synchronization can emerge in the dynamics of a one-dimensional atomic lattice that could pave the way for the experimental simulation of this phenomenon. In particular, we have considered the low-energy physics of atoms trapped in the two lowest motional levels of a dimeric optical potential in the Mott-insulator regime of one atom per site, as described by an effective one-dimensional spin-1/2 Hamiltonian. Laser cooling techniques enable tunable local dissipation, a key element for synchronization.

As a first important result, we have shown that synchronization is possible when we allow for staggered decay rates, i.e. the neighboring spins are not only detuned but also dissipate at different rates. Then, a monochromatic phase-locked oscillation emerges in the temporal evolution of the spins' coherences until the stationary state is reached. This means that, in a pre-equilibration regime, the atoms oscillate coherently in a synchronized fashion between the two lowest vibrational states of the optical trap. Furthermore, this *quantum* synchronization emerges in two flavors: inter-band synchronization, in which there are many long-lived quasi-degenerate collective modes synchronizing the system, and intra-band synchronization, in which there is a single long-lived collective mode synchronizing the system. Inter-band synchronization is indeed a novel form of transient synchronization, not reported before Ref. [3], while the results presented here further show that quantum synchronization is possible beyond collective dissipation, at difference with [45, 64, 65, 98, 101].

The synchronization dynamics that we have reported is accompanied by spin-spin correlations. This is because the same long-lived collective (delocalized) modes that synchronize the system also correlate them. However, when considering single-time correlations, we have found that they do not capture the fact that there is an unsynchronized parameter region between the regimes of intra- and inter-band synchronization. Hence, this

constitutes an example that not all correlated regions correspond to synchronized regions. On the other hand, and in agreement with the previous chapter, two-time correlations can be used to assess synchronization, as they capture the relevant dynamics of the spin's coherences: i.e. the long-time synchronized response towards the stationary state of the system

PART III

Emergent phenomena in the quantum van der Pol oscillator

CHAPTER 6

Metastable quantum entrainment

Are there connections between synchronization phenomena and other quantum non-equilibrium phenomena? This is the fundamental question on which we will focus in this chapter and the following one. We will do so by considering the particular but rich scenario of the quantum van der Pol oscillator (QvdP), a paradigmatic driven-dissipative system for classical and quantum synchronization. In this chapter, based on the work *Metastable quantum entrainment* [9], we will study the QvdP oscillator forced by a squeezed drive, a scenario in which the frequency of the oscillator adjusts to half of the forcing displaying multiple preferred phases. We will analyze the physical origin of this entrained response, establishing a connection with the phenomenon of metastability in open quantum systems. As we shall see, the entrained regime is indeed characterized by a huge separation of timescales and the long-time dynamics corresponds to an incoherent process between two metastable states. These states are the preferred phases of the synchronized oscillator and the fluctuations between them ultimately limit the temporal coherence of entrainment in the quantum regime.

6.1 Introduction

The non-equilibrium dynamics of a system can be characterized by the *emergence* of disparate timescales, resulting from the combined action of several of the underlying physical processes. An important example is *metastability* [88, 350, 351], in which a system settles into a long-lived state of apparent equilibrium, where it remains trapped until the action of fluctuations or perturbations drives it towards the true equilibrium state, on a longer timescale. Glassy systems constitute a timely example of classical metastable systems [352, 353], as they "freeze" into a long-lived disordered state before reaching the true thermodynamically stable state on a much longer timescale, as it can be a crystalline solid. Quite generically, metastability can be expected to occur in multistable dynamical systems in the presence of fluctuations: on a short timescale, the system might relax to an apparent stationary state in which it fluctuates around one of the (deterministic) attractors; however, on a longer timescale, rare "big" fluctuations make the system to jump between these different possible attractors, and the resulting true stationary state actually corresponds to a probabilistic mixture of them [88, 351].

Metastability in open quantum systems. Similarly, metastability can also occur in quantum non-equilibrium systems. In fact, the interplay between driving, dissipation and interactions in an open quantum system can make the dynamics to be dominated by a huge separation of timescales, a characteristic of this phenomenon [162]. Then, and analogously to the classical case, initially highly excited configurations quickly relax to a set of metastable states that act as attractors of the dynamics for a long intermediate timescale, until final relaxation to the true stationary state occurs. This multi-step dynamics might have different physical origins, as population trapping in a driven three-level system [162], the coexistence of different phases in an open Ising model [354] or in a non-linear oscillator [85]. Moreover, it has also been reported for a systen of Rydberg atoms in [189], in the long-time response of a driven-dissipative Rabi model [355], or in a chain of interacting fermions subject to a localized particle loss [356]. A general approach towards metastability in open quantum systems has been recently introduced in Ref. [162], in which some of its crucial signatures in the spectral properties of the Liouvillian have been identified.

The characteristic timescale separation of metastability has also been found in between different dynamical regimes of driven-dissipative systems [136, 357], or as a precursor of eventual spontaneous symmetry breaking in the thermodynamic or infinite-excitation limits of these systems [35]. Indeed, as explained in chapter 1, sudden changes can occur in the stationary state of these systems in these limits, which are known as dissipative phase transitions (DPTs) [34, 35]. These transitions are accompanied by the closure of the Liouvillian gap, which has profound consequences even far from the thermodynamic or classical limits, as it can lead to a very slow relaxation timescale and hence metastability in the quantum dynamics [162]. While for first order DPTs this usually occurs in a narrow region between the different regimes [135, 136], as experimentally observed in Refs. [165, 164], for symmetry-breaking DPTs this occurs in a whole parameter regime characterized by the emergence of metastable symmetry-broken states [35, 358, 359].

Driven-dissipative phenomena and synchronization. As we have already seen, synchronization is also a phenomenon that can emerge in driven-dissipative systems. We talk of entrainment when a system adjusts its frequency and phase to that of an external forcing or to a multiple/fraction of it (see chapter 1). The van der Pol oscillator (vdP) is a paradigmatic example while synchronization can be addressed both in the classical [42, 43] and quantum regimes [67, 68]. Indeed, both quantum entrainment by a harmonic drive and quantum spontaneous synchronization between coupled oscillators have been found (see also [69, 70]). Furthermore, this driven-dissipative system presents a rich phenomenology allowing us to explore the connection between quantum synchronization and other driven-dissipative phenomena. This is the question underlying the present and the following chapter and in particular, advancing the key results, we are going to show that entrainment in a type of QvdP oscillator is indeed intimately connected with the timely topics of metastability, DPTs, and time-crystals.

The squeezed QvdP oscillator. As reviewed in chapter 1, signatures of synchronization have been identified in phase-space representations of the stationary state as well as in the power spectrum of quantum systems. Indeed, for the *harmonically driven* QvdP oscillator, entrainment is signaled by the Wigner distribution (appendix A) displaying a localized lobe [67], while the dominant frequency of the power spectrum shifts towards that of the driving [68] (for a more detailed presentation of the harmonically driven QvdP oscillator see also appendix H). The more in the quantum regime the system operates, the harder it is to synchronize it due to the detrimental effect of quantum fluctuations [68]. As an alternative implementation strategy, a squeezed forcing has been reported to enhance entrainment in the quantum regime [166]: this is the *squeezed* QvdP oscillator. However,

very deep into the quantum regime, where the system behaves effectively as a few-level system, the enhancing effect of squeezing is limited [360].

The introduction of the squeezed forcing comes at the expense of changing qualitatively the dynamical scenario of entrainment [166, 361, 362]. This is an observation of utmost importance to understand the entrained quantum dynamics of this system, as we will show in this chapter. While in the classical harmonically driven vdP oscillator entrainment arises in correspondence of a fixed point attractor (in the rotating frame) [43, 363], for the squeezed vdP oscillator it corresponds to bistability (in the rotating frame) [166, 362], characterized by frequency locking to half of the frequency of the forcing and two possible locked-phases. As it turns out, the nature of the classical attractors has a deep influence in the quantum dynamics. In fact, for the driven QvdP oscillator, the entrained dynamics has been shown to be well described by a linearized model around the fixed point attractor [363] (see also appendix H). This approach sheds light on the synchronized dynamics of this system and on the reported behavior of the power spectrum, while it unveils new dynamical features as phase-coherent dynamics [363]. In contrast, we show that the squeezed QvdP oscillator displays a distinct dynamical scenario in which the main features of the entrained response cannot be captured by a linearized model, a fact rooted in the emergence of bistability in the classical limit.

In this chapter, we show that the squeezed vdP oscillator offers the opportunity to establish a connection between metastability and entrainment, that we argue to transcend this specific system and to be applicable to other synchronization scenarios in the presence of phase multistability. More specifically, we identify the huge timescale separation characteristic of a metastable dynamics as the distinctive feature of the entrained dynamics for this system. On the shortest timescale, any initial state rapidly relaxes to the manifold of states spanned by two metastable ones. These are the two preferred phases of the oscillator when it is well entrained by the forcing. On the longest timescale, the dynamics is dominated by a slow fluctuation mode connecting both phases, which eventually drives the state of the quantum system to an even incoherent mixture of both. In between, there is a long period of time in which the response of the system is a quasi-coherent subharmonic oscillation. This is precisely how subharmonic entrainment manifests in the quantum regime, and it dominates the behavior of the power spectrum.

6.2 The squeezed quantum van der Pol oscillator

In this section, we introduce the general master equation that models the QvdP oscillator, as well as the specific squeezed forcing. We will also mention some proposed schemes to implement this system experimentally and recall some basic results of the Liouvillian formalism (see chapter 2) of use along the chapter. We later present the mean-field equation that governs this system in the classical limit and which motivates the name van der Pol oscillator. We finally overview the classical entrainment regimes of the squeezed vdP oscillator.

6.2.1 The model

The QvdP oscillator. In the laboratory frame, the QvdP oscillator is described by a master equation for the state of a bosonic mode $\hat{\rho}_L$ [67, 68] ($\hbar = 1$):

$$\frac{d}{dt}\hat{\rho}_L = -i[\hat{H}, \hat{\rho}_L] + \gamma_1 \mathcal{D}[\hat{a}^\dagger]\hat{\rho}_L + \gamma_2 \mathcal{D}[\hat{a}^2]\hat{\rho}_L, \tag{6.1}$$

where for the bare QvdP oscillator (i.e. in the absence of coherent driving) the Hamiltonian term is the that of an harmonic oscillator:

$$\hat{H} = \omega_0 \hat{a}^\dagger \hat{a}. \tag{6.2}$$

Here, $\hat{a}(\hat{a}^\dagger)$ is the annihilation (creation) operator of the bosonic mode. The bare QvdP oscillator is characterized by the following processes: an intrinsic harmonic oscillation frequency ω_0; an incoherent energy gain term of strength γ_1; a non-linear, or two-boson, damping term with strength γ_2. These two incoherent processes are fundamental for the QvdP oscillator, as the interplay between energy gain and *non-linear* dissipation makes the stationary state to be a limit cycle with characteristic frequency ω_0 [67, 68, 82] (see also appendix H). Then, when coupling multiple QvdP oscillators [67, 69, 70], or when forcing this basic system with a time-dependent field [67, 68, 166, 363], this bare limit-cycle phase can evolve into a synchronized phase, in which there is a readjustment of the characteristic frequency of the system and there emerge preferred phases.

Squeezed forcing. In this chapter, we are going to consider the squeezed QvdP oscillator [166], in which the bare QvdP oscillator of Eq. (6.1) is supplemented by the squeezed (two-boson) drive, so the Hamiltonian part now reads [166]:

$$\hat{H}_L(t) = \omega_0 \hat{a}^\dagger \hat{a} + i\eta(\hat{a}^2 e^{i2\omega_s t} - \hat{a}^{\dagger 2} e^{-i2\omega_s t}), \tag{6.3}$$

where the squeezed forcing is characterized by its strength, η, and its frequency, $2\omega_s$. Importantly, the explicit time-dependence of this model enters only through the Hamiltonian term (6.3), which can be eliminated in a rotating frame corresponding to a standard time-dependent unitary transformation, $\hat{U}_t = \exp(-i\omega_s \hat{a}^\dagger \hat{a} t)$. This leads to a master equation with the same dissipative part but with a time-independent Hamiltonian[1]:

$$\hat{H} = \Delta \hat{a}^\dagger \hat{a} + i\eta(\hat{a}^2 - \hat{a}^{\dagger 2}), \tag{6.4}$$

with the detuning defined as $\Delta = \omega_0 - \omega_s$. Notice that we denote the state of the system in this frame as $\hat{\rho}$, without any subscript, while the laboratory frame is indicated by the subscript "L".

Proposals of implementation. Even in the absence of time-dependent forcing fields, the master equation (6.1) models a non-equilibrium bath, as the gain term is not accompanied by its conjugate process, i.e. the one-boson dissipation term, which should be there for a system in contact with a thermal environment (see chapter 2). In fact, the main proposals to implement such a dynamical system are based on adiabatic elimination of laser-driven degrees of freedom, a resource also used to implement the effective spin dynamics of chapter 5, and for which we have presented the basic ideas in chapter 2.

In particular, experimental implementations of the QvdP oscillator have been proposed for platforms of trapped ions [67] and optomechanical oscillators [68, 70]. In both cases, the QvdP oscillator corresponds to the properly engineered effective dynamics of a mechanical degree of freedom. Then, amplification and non-linear dissipation are implemented by driving the fast optical degrees of freedom with lasers resonant with one-phonon absorption and two-phonon emission processes. In both of these systems, it is also possible to implement the two-phonon driving term (6.3), as detailed in [166]: either by considering membrane-in-the-middle optomechanical systems [23], in which there is a quadratic photon-phonon interaction [152], or in trapped ions, by properly combining standing- and travelling-wave laser fields [364] or by a combination of two Raman beams detuned by $2\omega_s$ [365].

[1] The rotating frame and laboratory frame Hamiltonians are related by $\hat{H} = \hat{U}_t^\dagger \hat{H}_L(t) \hat{U}_t - i\hat{U}_t^\dagger \partial_t \hat{U}_t$, while the state of the system transforms as $\hat{\rho}(t) = \hat{U}_t^\dagger \hat{\rho}_L(t) \hat{U}_t$.

Liouvillian analysis. As in the rotating frame the Liouvillian superoperator, $\mathcal{L}$, is time-independent, the dynamics of the system can be analyzed considering its eigenspectrum, i.e. its eigenvalues λ_j, and the corresponding right and left eigenmatrices $\hat{\rho}_j$ and $\hat{\sigma}_j$, respectively (see chapter 2). We remind here the state decomposition in terms of the Liouvillian eigenmodes, first presented in Eq. (2.54), i.e.:

$$\hat{\rho}(t) = \hat{\rho}_{ss} + \sum_{j\geq 1} \mathrm{Tr}[\hat{\sigma}_j^\dagger \hat{\rho}(0)]\hat{\rho}_j e^{\lambda_j t}, \tag{6.5}$$

where the stationary state is $\hat{\rho}_{ss} = \hat{\rho}_0/\mathrm{Tr}[\hat{\rho}_0]$. The real part of these eigenvalues are non-positive, and we order them such that $\mathrm{Re}[\lambda_0] \geq \mathrm{Re}[\lambda_1] \geq \mathrm{Re}[\lambda_2] \geq \ldots$. In the following, we will refer to the decay rates and frequencies of the eigenmodes

$$\Gamma_j = |\mathrm{Re}[\lambda_j]| \quad \text{and} \quad \nu_j = \mathrm{Im}[\lambda_j], \tag{6.6}$$

respectively.

6.2.2 Classical subharmonic entrainment

While the formalism is fully quantum, we can identify the imbalance between nonlinear dissipation and linear amplification γ_2/γ_1 as the physical quantity controlling the excitation strength (i.e. boson number) in the family of QvdP oscillator systems [67, 68], and hence the classical versus quantum system operation. In the limit $\gamma_2/\gamma_1 \gg 1$ the QvdP oscillator is well approximated by a two-level system [68, 69, 360], while in the limit $\gamma_2/\gamma_1 \ll 1$ the typical number of excitations becomes macroscopic and a mean-field classical description applies (as we shall investigate in detail in the following chapter). Let us introduce the mean-field equation of motion that governs the classical limit, and to briefly discuss the classical entrainment regimes, as this will help us to understand better the quantum phenomena in which we are interested here.

In the classical (or infinite-excitation) limit, we define the complex amplitude $\alpha = \langle \hat{a} \rangle$, whose equation of motion is obtained from that of $\langle \hat{a} \rangle$ making the approximation of factorizing higher-order moments, i.e. $\langle \hat{a}^\dagger \hat{a}^2 \rangle \to \langle \hat{a}^\dagger \rangle \langle \hat{a} \rangle^2$, which leads to:

$$\frac{d}{dt}\alpha = -i\Delta\alpha + \frac{\gamma_1}{2}\alpha - \gamma_2|\alpha|^2\alpha - 2\eta\alpha^*. \tag{6.7}$$

Notice that Eq. (6.7) for $\eta = 0$ is known as the Stuart-Landau equation [362], which actually corresponds to the van der Pol oscillator only in the *weakly non-linear* regime [43, 82]. Nevertheless, calling Eq. (6.1) [and in consequence (6.7)] the (quantum) van der Pol oscillator is standard in the literature of quantum synchronization [67, 68, 69, 70, 166, 363], while some thoughts about this misnomer and "alternative" quantization of the vdP oscillator can be found in Ref. [82].

The system described by this mean-field equation displays two different dynamical regimes depending solely on the relation between squeezing and detuning, η and Δ. This follows from the fact that the phase dynamics is uncoupled from the amplitude dynamics. That is, defining $\alpha = Re^{i\phi}$ where R is the modulus of the amplitude and ϕ is the phase, Eq. (6.7) can be rewritten as:

$$\frac{d}{dt}R = \Big[\frac{\gamma_1}{2} - \gamma_2 R^2\Big]R - 2\eta R\cos 2\phi, \quad \frac{d}{dt}\phi = -\Delta + 2\eta\sin 2\phi. \tag{6.8}$$

Then, from the equation for the phase it follows that the bifurcation separating the two regimes occurs at the classical critical point:

$$\eta_c = \frac{|\Delta|}{2}. \tag{6.9}$$

For $\eta < \eta_c$, the stable attractor is a limit cycle of fundamental frequency:

$$\Omega = \Delta\sqrt{1-(2\eta/\Delta)^2}. \tag{6.10}$$

For $\eta = 0$, the limit cycle is perfectly harmonic, while as the bifurcation is approached, higher harmonics of this frequency are activated. Numerical analysis reveals that the squared amplitude averaged over a cycle is constant in this regime and reads:

$$|\alpha|^2 = \frac{\gamma_1}{2\gamma_2}, \tag{6.11}$$

as can be analytically checked for the limiting case of $\eta = 0$.

For $\eta > \eta_c$ the stable attractors are two bistable fixed points that only differ by a complex phase $e^{i\pi}$, whose amplitudes are given by $\alpha_\pm = \pm R_s e^{i\phi_s}$ with [166, 362]:

$$R_s = \sqrt{\frac{\gamma_1}{2\gamma_2} + \frac{1}{\gamma_2}\sqrt{4\eta^2-\Delta^2}}, \quad 2\phi_s = \pi - \sin^{-1}[|\Delta|/(2\eta)]. \tag{6.12}$$

The transition between these regimes corresponds to an infinite period bifurcation, as the period of the limit cycle increases with η and diverges as $\eta \to \eta_c$, as can be appreciated from the expression of Ω given in Eq. (6.10). At this point, the limit cycle disappears giving rise to two saddle-nodes [55] that later become the couple of stable fixed points for $\eta > \eta_c$ and two corresponding unstable fixed points [166, 362].

Back to the laboratory frame, the limit-cycle regime corresponds to the lack of entrainment since Ω and $2\omega_s$ are not generally commensurate. On the other hand, the bistable fixed points oscillate harmonically at half of the frequency of the forcing, i.e. $\alpha_\pm(t) = \pm R_s e^{i\phi_s - i\omega_s t}$, and thus this regime corresponds to subharmonic entrainment [42, 43]. Then, each of the fixed points corresponds to one of the possible bistable locked-phases, with a characteristic difference of phase of π. Indeed, in the following chapter we will analyze in detail how the classical attractors emerge in this model as $\gamma_2/\gamma_1 \to 0$. In the present chapter instead, we will focus on intermediate values of γ_2/γ_1 for which entrainment in the quantum regime has been reported [166].

6.3 Timescale separation and metastability

In this section we report on the signatures of metastability in the framework of the Liouvillian analysis: the presence of an eigenmode with a lifetime much longer than the rest, i.e. the opening of a spectral gap, and how this can be exploited to derive a simplified effective picture for the long-time dynamics of the system.

6.3.1 Opening of a spectral gap

The most important characteristic of the Liouvillan spectrum of the squeezed QvdP oscillator is the presence of a parameter region where the minimum (nonzero) decay rate Γ_1 can be orders of magnitude smaller than $\Gamma_{j\geq 2}$. The inverse of such a small decay rate determines the longest relaxation timescale of our system. In Fig. 6.1 we numerically show the formation of such a gap between the decay rates, while in the forthcoming sections we discuss its dynamical consequences and its relation to quantum entrainment.

The spectral gap is characterized through the ratio Γ_1/Γ_2 and can vary several orders of magnitude depending on the squeezing strength and the non-linear damping, Fig. 6.1 (a) and (b). As commented, we focus on parameter regimes for which the QvdP oscillator displays a moderate boson number, being neither strongly confined to the two lowest levels nor in the classical limit of a large population. As the excitation number grows not only

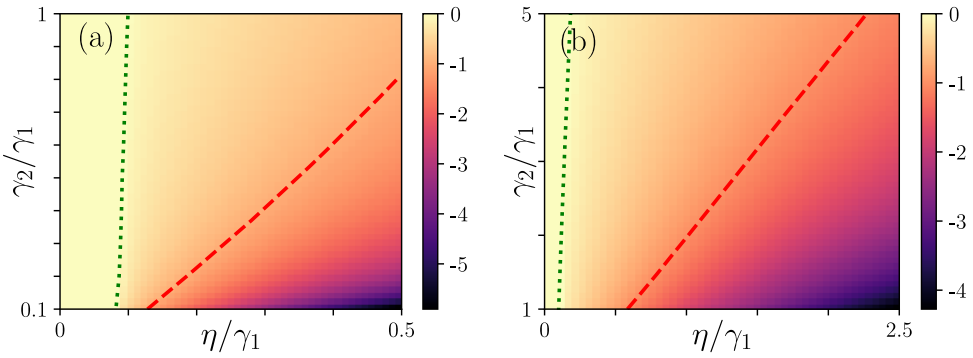

Figure 6.1: Colormaps: $\log_{10}(\Gamma_1/\Gamma_2)$ varying γ_2/γ_1 and η/γ_1. Panel (a) covers in detail the small values of γ_2/γ_1 and η/γ_1, while panel (b) displays a wider range of larger values. Green-dotted lines: contour limiting the region in which $\Gamma_1/\Gamma_2 = 1$. Red-dashed lines: contours indicating $\Gamma_1/\Gamma_2 = 0.1$. In all panels $\Delta/\gamma_1 = 0.1$. Notice that in all this chapter the numerical results are obtained after truncation of the Fock space to a large enough Fock state such that the convergence of the results with this truncation can be assured. The needed truncation size generally increases as γ_2/γ_1 is diminished and as η/γ_1 is increased, and for the parameter regimes explored in this chapter this is bounded to the first 50 levels.

with the linear amplification but also with the squeezing strength, this corresponds to intermediate values of γ_2/γ_1 and small squeezing η/γ_1 [Fig. 6.1 (a)] or to larger non-linear damping while increasing the squeezing [Fig. 6.1 (b)].

The ratio of decay rates displays the following characteristic dependence on the squeezing strength η: below a certain threshold value, this ratio remains constant and equal to one (bright region), while further increasing η the ratio diminishes steeply (dark region), as separated by a green-dotted line. This threshold value corresponds to an *exceptional point* of the Liouvillian, at which the eigenvalues $\lambda_{1,2}$ become the same [Fig. 6.2 (a)-(b)] while the corresponding eigenmatrices coalesce (not shown). Therefore, the green-dotted line in Fig. 6.1 (a-b) indicates the squeezing strength at which the EP occurs (η_{EP}) as γ_2/γ_1 is varied. For $\eta < \eta_{EP}$, $\lambda_{1,2}$ are complex conjugates, hence explaining the fact that $\Gamma_1/\Gamma_2 = 1$ for this region. While for $\eta > \eta_{EP}$, $\lambda_{1,2}$ become real valued and Γ_1 decreases when increasing the squeezing strength, while Γ_2 increases, as exemplified in Fig. 6.2 (b).

Although the behavior of Γ_1/Γ_2 is qualitatively the same for all the considered range of γ_2/γ_1, we find that there are important quantitative differences. In particular, the smaller is γ_2/γ_1 the wider is the gap for a given squeezing strength. This is intimately related to the behavior of Γ_1 as the classical limit is approached (i.e. $\gamma_2/\gamma_1 \to 0$). Indeed, anticipating the results of the following chapter, in this limit it is found that $\Gamma_1 \to 0$ for $\eta > \eta_c$ while Γ_2 saturates to a non-zero value. This means that the steady state becomes degenerate and the system undergoes a DPT [34, 35]. This is intimately related to the emergence of the classical bistable attractors, as we shall see in chapter 7. Notice that in this limit it is also found that $\eta_{EP} \to \eta_c$.

In broad terms, the spectral gap is enhanced in the presence of a large number of excitations: the larger is the non-linear damping, the more squeezing is needed. The dynamics of the system displays a significant timescale separation for rates Γ_1 and Γ_2 differing by an order of magnitude or more, as in the (right dark) regions delimited by a red-dashed line (where $\Gamma_1/\Gamma_2 \leq 0.1$) in Fig. 6.1 (a) and (b).

6.3.2 Effective long-time dynamics

The disparity between the weakest damping rate Γ_1 and the others allows us to capture the system dynamics after a transient considering only the disparate timescales $\tau_{1,2}^{-1} = \Gamma_{1,2}$.

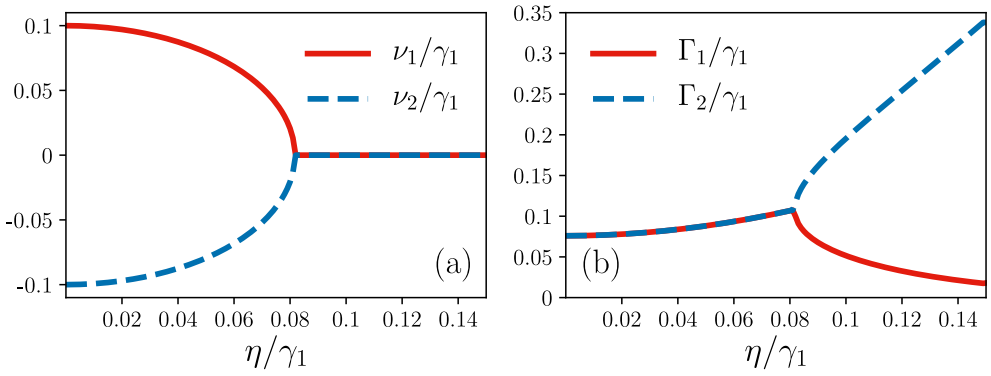

Figure 6.2: (a) and (b), eigenfrequencies and decay rates of the first two eigenmodes varying η/γ_1, respectively, and for $\gamma_2/\gamma_1 = 0.1$. In all panels $\Delta/\gamma_1 = 0.1$.

This large separation of timescales makes an initially excited state to rapidly decay ($\sim \tau_2$) to the manifold spanned by $\hat{\rho}_{ss}$ and the longest-lived eigenmode $\hat{\rho}_1$, where it displays a slow relaxation to $\hat{\rho}_{ss}$ at times of the order of τ_1 [162, 354]. Thus, there is a well-defined intermediate timescale, $\tau_2 \ll t \ll \tau_1$, in which the contribution of the higher modes is negligible while the decay of $\hat{\rho}_1$ is not yet appreciable, and thus the state of the system appears stationary in this time window. This is actually a signature of *metastability* [162], as we develop further here.

Approximation of the long-time transient. After times of the order of τ_2, the dynamics is well approximated just considering the contributions of the longest-lived eigenmode and of the stationary state. As we have shown in the previous section, the parameter regime in which $\Gamma_1/\Gamma_2 \ll 1$ corresponds to $\eta > \eta_{EP}$, and thus $\lambda_{1,2}$ are real valued and the corresponding right and left eigenmatrices are Hermitian [35, 268] (see also chapter 2). Then, the long-time dynamics can be approximated as

$$\hat{\rho}(t) \approx \hat{\rho}_{ss} + \mathrm{Tr}[\hat{\sigma}_1 \hat{\rho}(0)]\hat{\rho}_1 e^{-\Gamma_1 t}, \tag{6.13}$$

which follows from Eq. (6.5) neglecting the contributions for the modes with $j \geq 2$. By using the formalism introduced in Refs. [162, 354], the approximate long-time dynamics of Eq. (6.13) can be recast in terms of an effective stochastic process between two particular *metastable states*, which provides an insightful representation of this long-time response in a basis different from that provided by the stationary state and the longest-lived eigenmode $\hat{\rho}_1$, the latter not being a physical state since it is traceless [35]. In the following, we discuss the application of such formalism [162, 354] to our system (further details are in appendix I).

Metastable manifold. From the approximation of the long-time transient given in Eq. (6.13) it follows that the state of the system is restricted to the convex manifold of states spanned by the projection of the initial condition over the stationary state and the longest-lived eigenmode:

$$\mathcal{P}\hat{\rho} = \hat{\rho}_{ss} + \mathrm{Tr}[\hat{\sigma}_1 \hat{\rho}]\hat{\rho}_1. \tag{6.14}$$

We denote this manifold as the *metastable manifold*. In Refs. [162, 354], it is shown that the metastable manifold can be parametrized in terms of the two extreme metastable states (EMSs), defined as:

$$\hat{\mu}_1 = \hat{\rho}_{ss} + c_{max}\hat{\rho}_1, \quad \hat{\mu}_2 = \hat{\rho}_{ss} + c_{min}\hat{\rho}_1, \tag{6.15}$$

where c_{max} and c_{min} are the maximum and minimum eigenvalues of the Hermitian $\hat{\sigma}_1$. In our system, numerical analysis reveals that $c_{min} = -c_{max}$ for the considered regime, i.e. when $\Gamma_1/\Gamma_2 < 1$. Moreover, we find that for a significant spectral gap ($\Gamma_1/\Gamma_2 \ll 1$) these coefficients can be well approximated by $c_{max} = -c_{min} \approx 1$, which yields the simpler expressions for the EMSs: $\hat{\mu}_{1(2)} \approx \hat{\rho}_{ss} + (-)\hat{\rho}_1$ (see appendix I). The projection of the state of the system at a given time onto the metastable manifold can be written in terms of the EMSs as:

$$\mathcal{P}\hat{\rho}(t) = p_1(t)\hat{\mu}_1 + p_2(t)\hat{\mu}_2, \tag{6.16}$$

where the real coefficients $p_{1,2}(t)$ are defined in appendix I, while they are constraint to satisfy [162, 354]:

$$p_{1,2}(t) \geq 0, \quad p_1(t) + p_2(t) = 1. \tag{6.17}$$

Effective two-state incoherent process. By means of the EMSs the long-time dynamics can be parametrized in terms of two (in a good approximation) physical states[2], whose properties can be readily characterized. Crucially, the EMSs constitute the only basis for which $p_{1,2}(t)$ satisfy Eq. (6.17) in the whole metastable manifold. Therefore, in this case, $p_{1,2}(t)$ can be interpreted as *probabilities* and the dynamics within the metastable manifold is given by [162, 354]:

$$\dot{p}_1(t) = -\dot{p}_2(t) = -\frac{\Gamma_1}{2}\big[p_1(t) - p_2(t)\big], \tag{6.18}$$

whose solution makes Eq. (6.16) equivalent to Eq. (6.13). Thus, the approximate long-time dynamics for the state of the system has been recast in the form of a two-state stochastic process between the EMSs, with a switching rate $\Gamma_1/2$ [88]. This characterizes the long transient to which an initially excited state rapidly relaxes. From the solution of this dynamics (appendix I) we find that $p_1(t \to \infty) = p_2(t \to \infty) = 1/2$, which could be also deduced from the fact that $\hat{\rho}_{ss} = (\hat{\mu}_1 + \hat{\mu}_2)/2$. This illustrates the notion of metastability in our system: any initial unbalanced mixture of the EMSs decays on a very long timescale to the balanced one ($\hat{\rho}_{ss}$), remaining apparently stable for the long transient in the well-defined intermediate timescale $\tau_2 \ll t \ll \tau_1$. In the following section we explore in detail the physical meaning of this statement by characterizing the properties of $\hat{\mu}_{1,2}$, through a visual representation based on the Wigner function, and of this effective incoherent dynamics between these EMSs.

6.4 Metastable preferred phases

As we show here, the characterization of the EMSs $\hat{\mu}_{1,2}$ provides a first important insight on the relation between the metastable dynamics and entrainment. In fact, we can gain intuition from their visual rendering as provided by their Wigner representation (see appendix A). In Fig. 6.3 we plot the Wigner distribution for $\hat{\rho}_{ss}$, and $\hat{\mu}_{1,2}$. As illustrated in Fig. 6.3 (a) and (d) the Wigner distribution of the stationary state displays a manifest bimodal character. Here, we consider two disparate parameter values $\gamma_2/\gamma_1 = (0.1, 3)$ and $\eta/\gamma_1 = (0.2, 2)$, both satisfying $\Gamma_1/\Gamma_2 \ll 1$ (Fig. 6.1). In fact, we find this bimodality to be present in the whole metastable regime. This can be intuitively understood by considering the Wigner distribution of $\hat{\mu}_{1,2}$, as shown in panels (b), (c) and (e), (f). We can appreciate that each of the lobes corresponds indeed to one of the metastable states.

[2]Notice that $\hat{\mu}_{1,2}$ are Hermitian with trace one, but only approximately positive. The small corrections to positivity arise after neglecting the contribution of the higher modes in Eq. (6.13). Thus, the smaller is Γ_1/Γ_2, the better is the approximation to neglect them for $t \gg \tau_2$ and, accordingly, the smaller are these corrections [162].

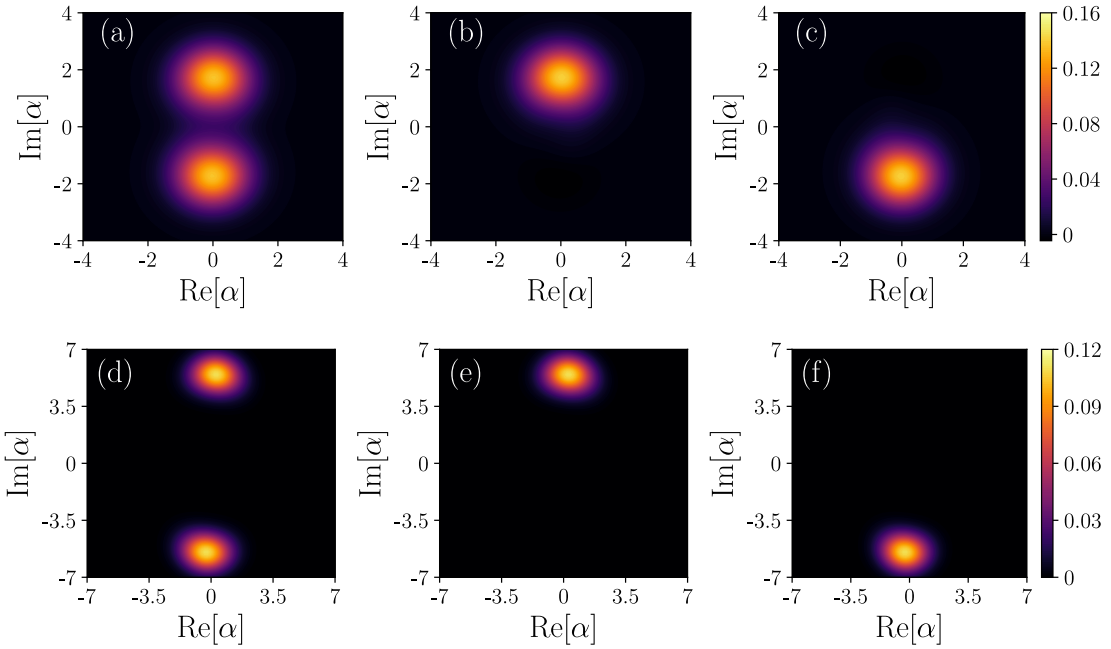

Figure 6.3: Colormaps: Wigner distribution $W(\alpha, \alpha^*)$, where α is the amplitude of a coherent state, in different cases: (a) of $\hat{\rho}_{ss}$, (b) of $\hat{\mu}_1/2$, (c) of $\hat{\mu}_2/2$, where the factor 1/2 is introduced for display purposes. Parameters: $\gamma_2/\gamma_1 = 3$, $\eta/\gamma_1 = 2$, $\Delta/\gamma_1 = 0.1$. In panels (d) to (f) we plot the same as in (a) to (c) but for $\gamma_2/\gamma_1 = 0.1$, $\eta/\gamma_1 = 0.2$ and $\Delta/\gamma_1 = 0.1$.

Metastable phase-locking. The bimodality of the stationary state is a reminiscence of classical bistability. However, in stark contrast to the classical case, according to the quantum formalism, these states are not stable but metastable, and the effective dynamics of Eq. (6.18) tells us that quantum fluctuations eventually drive the system to an even mixture of both. In fact, if we consider an initial condition consisting only of one lobe, i.e. $p_j(0) = 1$ and $p_k(0) = 0$ with $j \neq k$, we can see how on times of the order of τ_1 the population of both lobes becomes progressively the same, until the stationary state is finally reached. This follows from the fact that the long-time transient is well described by the dynamics on the metastable manifold, i.e. Eq. (6.16), with the formal solution given in Eq. (I.7).

As reviewed in chapter 1, the Wigner distribution of the stationary state is a well known indicator of the emergence of phase-locking between the oscillator and the external forcing [67, 68, 86, 166], or between coupled oscillators [66, 69, 70]. In the case of the squeezed QvdP oscillator, the emergence of phase preference is accompanied by the bimodality of the Wigner distribution [166] as displayed in Fig. 6.3. Therefore, each of the EMSs $\hat{\mu}_{1,2}$ can be interpreted as one of the two possible preferred phases to which the squeezed QvdP oscillator settles for large enough squeezing strength. It follows that the incoherent process between these two *metastable preferred phases* limits phase-locking in the long-time limit, as the stationary state that is reached is an even incoherent mixture of both. The manifestation of this incoherent process limiting phase-locking in different dynamical quantities is explored in more detail in the following section.

Symmetry-broken preferred phases. We will next show that the assessment of symmetries in the metastable states manifold discloses the mechanism of (anti-) synchronization in this regime. Let us start noticing that our master equation is invariant under the transformation $\hat{a} \to -\hat{a}$, $\hat{a}^\dagger \to -\hat{a}^\dagger$, i.e. it displays *parity-symmetry* [35, 268]. This means

that we can define the unitary transformation:

$$\mathcal{Z}_2\hat{\rho} = e^{i\pi\hat{a}^\dagger\hat{a}}\hat{\rho}e^{-i\pi\hat{a}^\dagger\hat{a}}, \tag{6.19}$$

whose action commutes with that of the Liouvillian (see chapter 2):

$$[\mathcal{Z}_2, \mathcal{L}]\hat{\rho} = 0. \tag{6.20}$$

Hence, the eigenmodes are either parity symmetric or parity antisymmetric, which means $\mathcal{Z}_2\hat{\rho}_j = z_j\hat{\rho}_j$ with $z_j = \pm 1$, respectively [35, 268]. An important observation is that the stationary state and the longest-lived eigenmode belong to different symmetry sectors:

$$\mathcal{Z}_2\hat{\rho}_{ss} = \hat{\rho}_{ss} \quad \mathcal{Z}_2\hat{\rho}_1 = -\hat{\rho}_1. \tag{6.21}$$

While the stationary state must be parity symmetric, as shown in Refs. [35, 268], the symmetry of $\hat{\rho}_1$ is assessed numerically by realizing that its contribution for parity symmetric observables vanishes identically, i.e. $\mathrm{Tr}[\hat{\rho}_1(\hat{a}^\dagger)^m\hat{a}^n] = 0$ for $m+n =$ even, while its contribution for parity antisymmetric ones is generally non-zero, i.e. $\mathrm{Tr}[\hat{\rho}_1(\hat{a}^\dagger)^m\hat{a}^n] \neq 0$ for $m+n =$ odd, where m and n are integers. As a consequence of this and of $c_{max} = -c_{min}$, it follows that the EMSs do not have a well-defined parity symmetry, and actually they are parity-broken states satisfying:

$$\mathcal{Z}_2\hat{\mu}_{1(2)} = \hat{\mu}_{2(1)}. \tag{6.22}$$

Thus, both EMSs yield the same value for the expected value of parity symmetric observables[3], while for parity antisymmetric ones their value solely differs by a phase $e^{i\pi}$. Then, parity-symmetric observables are insensitive to this metastable dynamics, as for any $\mathcal{P}\hat{\rho}(t)$ [Eq. (6.16)] both $\hat{\mu}_{1,2}$ contribute exactly the same, making irrelevant the particular evolution of $p_{1,2}(t)$ as their sum is one for all t. In contrast, notice the particular case of the amplitude in which since it is an antisymmetric observable we have $\langle\hat{a}\rangle_1 = -\langle\hat{a}\rangle_2$. This is precisely the same phase relation between the two possible classical amplitudes in the synchronized regime, as briefly commented in Sec. 6.2.2. In this sense, it turns out that, as the classical limit is approached, observables computed over the EMSs approach the corresponding classical values for each bistable fixed point (see next chapter). These observations together with the Wigner representations of Fig. 6.3, suggest an intimate connection between the emergence of preferred phases in the quantum regime, and thus synchronization, and metastability.

6.5 Metastable entrained dynamics

In this section we consider how the characteristic metastable response of the system manifests in the amplitude dynamics and two-time correlations used to characterize entertainment. We find that the metastable regime corresponds to the regime in which the system is entrained by the external forcing. Still, the temporal coherence of this entrained response is ultimately limited by the incoherent process between the two possible preferred phases. Finally, we find that while the long-time amplitude dynamics can be understood from a classical stochastic process, the quantum nature of the fluctuations becomes manifest in the two-time correlations.

[3] If $\hat{Z}_2\hat{O}_S = \hat{O}_S$, then $\langle\hat{O}_S\rangle_1 = \langle\hat{O}_S\rangle_2$, while there is "$-$" sign in the case of $\mathcal{Z}_2\hat{O}_A = -\hat{O}_A$. Where we have used the notation $\langle\hat{o}\rangle_{1(2)} = \mathrm{Tr}[\hat{o}\hat{\mu}_{1(2)}]$.

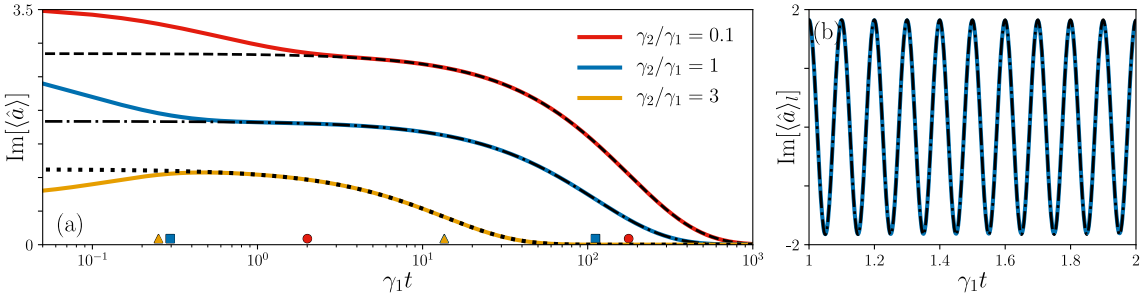

Figure 6.4: (a) Imaginary part of $\langle\hat{a}(t)\rangle$ in the rotating frame for different initial conditions and parameters. Red solid line: $\gamma_2/\gamma_1 = 0.1$, $\eta/\gamma_1 = 0.2$, $\hat{\rho}(0) = |1.2\alpha_+\rangle\langle 1.2\alpha_+|$, where $|x\alpha_+\rangle$ is a coherent state of amplitude x times the classical solution α_+ (6.2.2) corresponding to the considered parameters. Blue solid line: $\gamma_2/\gamma_1 = 1$, $\eta/\gamma_1 = 1.5$, $\hat{\rho}(0) = |1.5\alpha_+\rangle\langle 1.5\alpha_+|$. Yellow solid line: $\gamma_2/\gamma_1 = 3$, $\eta/\gamma_1 = 2.5$, $\hat{\rho}(0) = |0.5\alpha_+\rangle\langle 0.5\alpha_+|$. Broken black lines: results using the approximate dynamics of Eq. (6.23). The markers on the time axis indicate τ_1 (right) and τ_2 (left) for the different parameters: $\gamma_2/\gamma_1 = 0.1$ (red circles), $\gamma_2/\gamma_1 = 1$ (blue squares), $\gamma_2/\gamma_1 = 3$ (yellow triangles). (b) Zoom in of the $\gamma_2/\gamma_1 = 1$ case, in the laboratory frame, for $\omega_s/\gamma_1 = 20\pi$. In this case the black-broken line corresponds to Eq. (6.25). In all cases $\Delta/\gamma_1 = 0.1$.

6.5.1 Amplitude dynamics

According to the theoretical analysis of the previous sections, after a short transient of the order of τ_2, the amplitude dynamics for an arbitrary initial state is restricted to the metastable manifold and it is well approximated by

$$\langle\hat{a}(t)\rangle \approx \langle\hat{a}\rangle_1 p_1(t) + \langle\hat{a}\rangle_2 p_2(t) \propto p_1(t) - p_2(t), \tag{6.23}$$

where $p_{1,2}(t)$ are the solutions of Eq. (6.18). This is numerically confirmed in Fig. 6.4 (a) for three different values of γ_2/γ_1. In this panel we plot in logarithmic scale the imaginary part of $\langle\hat{a}(t)\rangle$ (the real part would be similar) comparing the exact results of the full model (color solid lines) with the ones following the reduced EMSs effective long-time dynamics (black broken lines). We see that the initial excited (coherent) state rapidly relaxes to the metastable manifold which is accurately described by Eq. (6.23). Notice that Eq. (6.23) is the same we would obtain from the two-state stochastic process using the rules of classical stochastics [88], which state that the average dynamics of a first moment is the sum of the contributions of each state weighted by $p_{1,2}(t)$ (see also appendix I).

Plateaus of perfect entrainment. The behavior observed in Fig. 6.4 (a) can be fully understood recalling the Liouvillan analysis of Sec. 6.3, where we found that whenever $\Gamma_1/\Gamma_2 \ll 1$, there is a well-defined intermediate timescale $\tau_2 \ll t \ll \tau_1$ in which the dynamics is apparently stable, as the contributions of the modes with $j \geq 2$ have already decayed out while the final decay is not yet appreciable since $\Gamma_1 t \ll 1$. Thus,

$$\langle\hat{a}(t)\rangle \approx \langle\hat{a}\rangle_1 p_1(0) + \langle\hat{a}\rangle_2 p_2(0) \tag{6.24}$$

on this long transient. This corresponds to the *plateaus* displayed for intermediate times in Fig. 6.4 (a), in between the corresponding markers in the time axis (indicating $\tau_{1,2}$), and which we now show to be intimately related to entrainment.

The tight connection between metastability and entrainment can be made explicit going back to the laboratory frame[4], where for this intermediate timescale we find the approximate solution

$$\langle\hat{a}(t)\rangle_L \approx \langle\hat{a}\rangle_1 e^{-i\omega_s t}(p_1(0) - p_2(0)), \tag{6.25}$$

[4]We use the notation $\langle\hat{O}(t)\rangle_L$ to designate observables in the laboratory frame. Recall that $\hat{\rho}_L(t) = \hat{U}_t\hat{\rho}(t)\hat{U}_t^\dagger$, from which temporal oscillations at ω_s or multiples of it can be easily recovered.

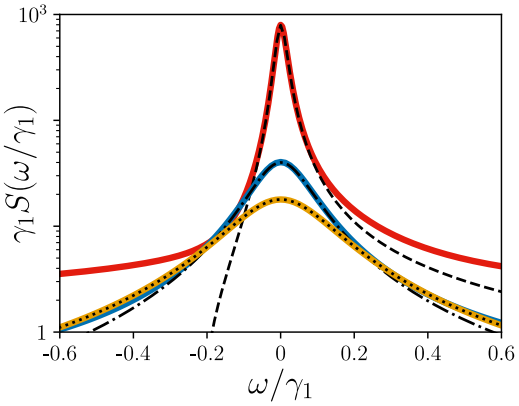

Figure 6.5: Emission spectrum considering the exact dynamics (color solid) and the approximate ones (black-broken) for $\gamma_2/\gamma_1 = (0.1, 1, 3)$ and $\eta/\gamma_1 = (0.15, 0.75, 1.875)$ such that $\Gamma_1/\Gamma_2 \approx 0.05$, with the following color code: in red $\gamma_2/\gamma_1 = 0.1$, in blue $\gamma_2/\gamma_1 = 1$, in yellow $\gamma_2/\gamma_1 = 3$. In all cases $\Delta/\gamma_1 = 0.1$.

According to this, the QvdP oscillator displays an "apparently" stable and perfectly entrained subharmonic response. Provided that $\omega_s \gg \gamma_1$, the system will oscillate coherently for many cycles at exactly half of the frequency of the forcing until the effects of the incoherent process described by Eqs. (6.18) and (6.23) start to be evident at times of the order of τ_1. This is exemplified in panel (b), in which we compare the approximate non-decaying subharmonic response of Eq. (6.25) (black-broken line) with the exact result (color solid line) and for intermediate times inside the plateau, finding a very good agreement.

While in a long transient entrainment is then achieved in the presence of metastability, Eq. (6.23) also illustrates precisely how the incoherent process between the two metastable phases eventually hinders the entrained response in the long-time limit. In particular, as the stationary state is a symmetric mixture of both phases, and since they differ by a π-phase, the expected value of the amplitude eventually decays out on the long timescale given by τ_1 following the dynamics given by Eqs. (6.18), as illustrated in Fig. 6.4 (a). Again, this is to be contrasted with the classical deterministic case, in which the system settles in one of the bistable locked-phases oscillating subharmonically forever, due to the absence of fluctuations connecting both phases.

6.5.2 Two-time correlations and observed frequency

We now consider the dynamics of the amplitude two-time correlation in the stationary state, as from this two-time correlation a well known indicator of frequency entrainment can be computed. This is the observed frequency [68, 70, 166, 361], ω_{obs}, defined as the maximum of the emission or power spectrum[5]:

$$\omega_{obs} = \text{argmax}[S(\omega)] \tag{6.26}$$

with

$$S(\omega) = \int_{-\infty}^{\infty} d\tau e^{-i\omega\tau} \langle \hat{a}^\dagger(\tau)\hat{a}(0)\rangle_{ss}] = 2\text{Re}\Big[\int_0^{\infty} d\tau e^{-i\omega\tau} \langle \hat{a}^\dagger(\tau)\hat{a}(0)\rangle_{ss}\Big] \tag{6.27}$$

where the subscript "ss" denote that this correlation is calculated in the stationary state in which two-time correlations only depend on the difference between the time arguments,

[5]For models displaying parity symmetry, as in our case, we have that $\langle \hat{a}\rangle_{ss} = 0$ and thus the emission spectrum as defined in Eq. (6.27) coincides with the fluctuation spectrum or power spectrum as defined by [361] $S_{inc}(\omega) = \int_{-\infty}^{\infty} d\tau e^{-i\omega\tau}[\langle \hat{a}^\dagger(\tau)\hat{a}(0)\rangle_{ss} - \langle \hat{a}^\dagger(\tau)\rangle_{ss}\langle \hat{a}\rangle_{ss}]$ (see also appendix I). Notice that in some contexts $S_{inc}(\omega)$ is known as the incoherent part of the emission spectrum [59].

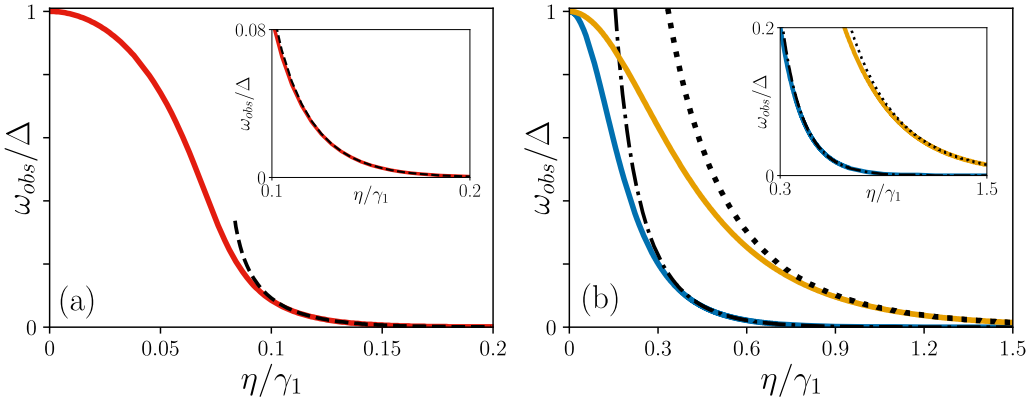

Figure 6.6: (a),(b) Ratio of the observed frequency and the detuning ω_{obs}/Δ, considering the exact results (color solid) lines and the approximate ones (black-broken). The lines correspond to $\gamma_2/\gamma_1 = (0.1, 1, 3)$, with the following color code: in red $\gamma_2/\gamma_1 = 0.1$, in blue $\gamma_2/\gamma_1 = 1$, in yellow $\gamma_2/\gamma_1 = 3$. The insets show a zoom in of the well-entrained region. In all cases $\Delta/\gamma_1 = 0.1$.

i.e. $\langle\hat{a}^\dagger(-\tau)\hat{a}(0)\rangle_{ss} = \langle\hat{a}^\dagger(0)\hat{a}(\tau)\rangle_{ss}$, while we have also used the fact that $\langle\hat{a}^\dagger(0)\hat{a}(\tau)\rangle_{ss} = [\langle\hat{a}^\dagger(\tau)\hat{a}(0)\rangle_{ss}]^*$. Perfect (subharmonic) entrainment arises when the system oscillates at (a fraction of) the driving frequency. As Eq. (6.27) is in the rotating frame, the observed frequency will be zero when the system is well entrained, and close to the intrinsic detuning, Δ, when there is no synchronization [68, 166].

Dominant fluctuation mode. In the metastable regime, the emission spectrum is dominated by the contribution of the longest-lived eigenmode. Since in this regime we have that $\Gamma_1/\Gamma_{j\geq 2} \ll 1$, the resonance associated with this mode should stand out in the spectrum. Indeed, we show in Fig. 6.5 how the contribution of this mode fits accurately the main peak of the spectrum in this regime. Furthermore, this panel also illustrates how Γ_1 diminishes when decreasing γ_2/γ_1: in the three cases amplification/damping rates and squeezing are varied but maintaining $\Gamma_1/\Gamma_2 \approx 0.05$, and we can see how diminishing γ_2/γ_1 the resonances become significantly sharper, a signature of the vanishing of Γ_1 in the classical limit (see next chapter). In fact, the decay rate of the dominant mode takes the values $\Gamma_1/\gamma_1 \approx (0.017, 0.087, 0.152)$ for the cases $\gamma_2/\gamma_1 = (0.1, 1, 3)$, respectively.

We recall that, while the large-τ dynamics of two-time correlations can be written in terms of Eq. (6.18) [162, 354], we find that it is more illustrative to write it in terms of the (fully equivalent) Eq. (6.13). In particular from Eqs. (I.2) and (6.13) it follows that for $\Gamma_1/\Gamma_2 \ll 1$:

$$\langle\hat{a}^\dagger(\tau)\hat{a}(0)\rangle_{ss} \approx \mathrm{Tr}[\hat{\sigma}_1\hat{a}\hat{\rho}_{ss}]\mathrm{Tr}[\hat{a}^\dagger\hat{\rho}_1]e^{-\Gamma_1\tau}. \tag{6.28}$$

We highlight the factor $\mathrm{Tr}[\hat{\sigma}_1\hat{a}\hat{\rho}_{ss}]$ in this equation stemming from the quantumness of the model. Indeed, the two-time correlation (and thus the emission spectrum) follows from an initial perturbation of the stationary state (here $\hat{a}\hat{\rho}_{ss}$) [59], and can be interpreted as the unavoidable disturbance of a measurement process. Generally, this factor makes this two-time correlation different from the corresponding one of a classical two-state stochastic process [88], which is found to be $C(\tau) = |\langle\hat{a}\rangle_1|^2 e^{-\Gamma_1\tau}$ (see appendix I). Since generally $\mathrm{Tr}[\hat{\sigma}_1\hat{a}\hat{\rho}_{ss}] \neq \langle\hat{a}\rangle_1$, we find that $\langle\hat{a}^\dagger(\tau)\hat{a}(0)\rangle_{ss} \neq C(\tau)$. This manifests in the fact that the Fourier transform of $C(\tau)$ is centered at the origin for $\eta \geq \eta_{EP}$ while this is not the case for the quantum case, as we shall see in Fig. 6.6. Thus, in contrast to the case of the long-time amplitude dynamics Eq. (6.23), multi-time correlations do not follow straightforwardly from the corresponding classical law of a two-state stochastic process. In these two-time correlations, the quantum nature of the fluctuations and of the degrees of freedom becomes manifest.

Metastable entrained regime. We now proceed to analyze the behavior of the observed frequency. In Figs. 6.6 (a) and (b) we exemplify for different parameter values how as the squeezing strength η increases the system becomes entrained, i.e. ω_{obs}/Δ goes from one to zero. Notice how the transition to entrainment is sharper the smaller is γ_2/γ_1 (large number of excitations). For $\eta > \eta_{EP}$ we have plotted in black-broken lines the observed frequency calculated from the effective long-time dynamics, i.e. Eq. (6.28). Here, we can observe that the asymptotic decay of ω_{obs} towards zero is very well captured by this approximate calculation. This can be further appreciated in the insets of these two panels, in which the well-entrained region, that of ω_{obs} close to zero, is shown in more detail. Hence, as the entrained dynamics is well characterized by the metastable response of the state of the system, the signatures of entrainment in the power spectrum are captured by the effective long-time dynamics between the metastable phases that follows from the opening of a spectral gap.

6.6 Discussion and concluding remarks

In this chapter we have established the connection between the quantum entrainment in the squeezed QvdP oscillator and quantum metastability. We have reported that squeezing enables the opening of a spectral gap in the Liouvillian, which leads to a huge separation of timescales in the dynamics: after a short transient of time the system settles into the so-called metastable manifold in a mixture of two metastable states that depends on the initial condition. It then follows an incoherent process between the two parity-broken metastable preferred phases of the entrained oscillator. Indeed, the oscillation frequency settles to the value of half of the forcing. Still, quantum entrainment is ultimately limited by this incoherent process, as for the stationary state the temporal coherence of the subharmonic response eventually decays out.

Entrainment and fluctuations dynamics. The distinctive features of the analyzed quantum entrained dynamics stem from the distinct classical attractors introduced by the squeezed forcing. Hence, classical phase bistability becomes phase metastability in the presence of quantum fluctuations, as reflected by the dominant fluctuation mode in the system. This scenario is to be contrasted with quantum entrainment in the driven QvdP oscillator (in the absence of squeezing) [67, 68, 363], where the dominant fluctuation modes describe the dynamics around the unique fixed point attractor of the entrained regime [363]. This qualitative difference is behind the reported specific features of the power spectrum presented in Refs. [166, 363]. In fact, in Ref. [363] (see also appendix H) this fluctuations dynamics is analyzed in detail as well as its signatures in the power spectrum (or incoherent part of the emission spectrum). Fluctuations are shown to display an overdamped regime and an underdamped one, which translate in the power spectrum displaying either a broad peak centered at the driving frequency or displaying sidebands around this frequency, respectively [363]. Moreover, in the overdamped regime the width of the peak is reported to increase with the driving strength [166], which can be interpreted as the suppression (or faster decay) of the fluctuations around the coherent dynamics of the unique fixed point attractor of the entrained regime (appendix H). This is to be contrasted with the squeezed QvdP oscillator, in which the width of the main Lorentzian peak decreases significantly as the squeezing strength is increased (as reported here, see Fig 6.2 (b), or in [166]). As our analysis reveals, this contrasting behavior is due to the completely different physical origin of this peak, rooted in the fluctuation dynamics *between* two fixed point attractors of the entrained regime. Thus, the decreasing of this linewidth is to be interpreted as the jumps between the two preferred-phases becoming

suppressed (or less frequent), which leads to an enhanced temporal coherence for the entrained subharmonic response. Therefore, we conclude that a careful assessment of the fluctuation dynamics is crucial to understand the synchronized response of quantum systems and its key signatures in the power spectrum.

Precisely, the characteristic fluctuation dynamics reported here transcends the particular context of the squeezed QvdP oscillator. As discussed, metastability appears in many different driven-dissipative quantum systems [162]. A particularly relevant example for us is the case of DPTs with spontaneous parity-symmetry breaking [35]. This is indeed what happens in this system in the infinite-excitation limit where the classical attractors emerge, and the parity-broken metastable preferred phases acquire a divergent lifetime (see next chapter). Other examples of metastable dynamics associated with parity-breaking transitions have been reported in Refs. [35, 358, 359]. Moreover, such long timescales associated with fluctuations between multiple possible phases have also been reported for quantum systems of parametric oscillators [196], period-tripling oscillators [366], and optomechanical oscillators [87]. Thus, slow-relaxation timescales seem a characteristic feature of multistable dynamical systems in the quantum regime, and a seemingly metastable manifold and dynamics could be expected for these examples as well as in further synchronization scenarios with multiple preferred phases. In this sense, it would also be interesting to investigate whether the metastable entrained dynamics reported here can be seen as a form of quantum activation process [367, 368] emerging in a far-from-equilibrium scenario, in which *non-linear* dissipation plays a fundamental role in shaping the properties of the metastable states.

Temporal coherence of quantum synchronization. Finally, two aspects of the results presented here might have caught the attention of the reader in relation to the results of the previous chapters: the occurrence of *coalescence* as the entrained regime is approached and the fact that the entrained oscillation is *transient*, i.e. it emerges after an initial fast decay and eventually fades out. The EP reported here plays the same role as in chapter 4, i.e. it lies in between different dynamical regimes, and thus, it signals the reorganization of the (fluctuation) modes governing the dynamics of the system. This will be further investigated in the following chapter, in which the relation between the EP and the classical bifurcation point will be addressed. With regard to the transient character of entrainment, it connects nicely with transient synchronization, something which was unnoticed in the literature. Hence, for both phenomena, we find that the emergence of synchronization is associated with a significant timescale separation in the dynamics, i.e. the opening of a spectral gap, that leads to a long-lived synchronized response practically independent of the initial conditions (see previous chapters or Refs. [5, 44, 65]). In a bigger picture, this illustrates the more general fact that, while synchronization in quantum systems is possible, the temporal coherence of such a dynamical response is often limited by the presence of quantum fluctuations inherent in open quantum systems, generally leading to a finite time-window for the observation of the synchronized dynamics, in stark contrast to the case of classical noiseless dynamical systems [42, 43].

CHAPTER 7

Dissipative phase transition, time-crystals and entrainment

In this chapter, we follow our quest on the study of synchronization within the more general context of driven-dissipative phenomena, such as DPTs and time-crystals. Here, we will meet again the squeezed QvdP oscillator, but focusing on the physics emerging as the infinite-excitation limit is approached (classical limit). As we shall see, the system displays two regimes in which different symmetries are spontaneously broken and which correspond to the emergent mean-field bifurcation diagram. In the first regime, time-translation symmetry is broken continuously, and the system displays a set of coherences whose lifetime diverges as this limit is approached. In the second regime, the Liouvillian gap closes, and the system breaks simultaneously parity symmetry and discrete time-translation symmetry. Hence, the system displays a peculiar transition from a continuous to a discrete dissipative time-crystal. This transition is actually a DPT and corresponds to the entrainment transition. Thus, we find that the presence or the absence of synchronization is here related to different types of time-crystalline order. Furthermore, we will show that the bifurcation point manifests in the Liouvillian as an EP. The results of this chapter correspond to a work in preparation [10].

7.1 Introduction

Can we understand the transition to synchronization as a dissipative phase transition? Is the emergence of synchronization accompanied by time-crystalline order? These are two fundamental questions that we have first introduced in chapter 1 and which motivate the research presented in this chapter.

DPTs and synchronization. As explained in section 1.2, DPTs occur in the thermodynamic and infinite-excitation limits in which system observables display a non-analytical behavior in between different phases or regimes. Furthermore, this can be accompanied by the closure of the Liouvillian gap and the spontaneous breakdown of underlying system symmetries. When considering classical driven-dissipative systems, the transition

to synchronization often corresponds to a bifurcation to a dynamical regime characterized by phase- and frequency-locking, with non-analytical behavior of the system observables as a control parameter is varied [42, 43]. In such cases and when considering their quantum counterpart, does this transition translate to a DPT with the corresponding Liouvillian gap closure? This question, despite being fundamental, remains unexplored. Interesting candidates to analyze it are arrays of QvdP oscillators [67, 69, 70] and optomechanical oscillators [66] or other non-linear oscillators, as the "321-oscillator" [85], as they display mutual synchronization and they can be studied approaching the thermodynamic or infinite-excitation limits. A single QvdP oscillator forced by an external field is also a promising candidate to address this question. Indeed, in the previous chapter we have shown that entrainment in the squeezed QvdP oscillator is intimately related to a metastable response. This immediately points out the possibility of a DPT occurring in the infinite-excitation limit, as metastability is a known precursor of such transitions [35, 162]. Moreover, since it is made of a single bosonic mode (and not many), numerical exploration of the full quantum model is not so forbidding, which constitutes an important advantage. In this chapter, we will show that the transition to entrainment corresponds to a DPT with parity symmetry breaking, in which an EP plays the role of the bifurcation point. In appendix H, we also discuss this possibility for the driven QvdP oscillator.

Time-crystals and synchronization. The question on the relation between synchronization and time-crystals (see Sect. 1.2 for an overview of time-crystals) was already raised in some of the seminal works on dissipative time-crystals [38, 193]. In fact, some examples in which such phenomena go hand-in-hand have been reported. In particular, in Ref. [193] a driven-dissipative atomic system of the family of "superradiant lasers" in which atomic synchronization is known to occur [46, 80] is considered, and the synchronized phase is shown to correspond to a continuous time-crystal. As for the side of discrete time-crystals in open quantum systems, measures of quantum synchronization have been used to detect this form of time-crystalline order in Ref. [39]. In a different work, the different units of a driven-dissipative Hubbard model have been reported to be synchronized in the time-crystalline phase [369]. On the other hand, in Refs. [370, 371] classical systems of parametric oscillators are shown to display a discrete time-crystalline phase, and the connection with classical subharmonic entrainment is pointed out.

In this regard, here we contribute on this connection from the side of quantum synchronization, i.e. we consider a system known to display synchronization both in the quantum and classical regimes and we investigate the connection with time-crystals. Again, the squeezed QvdP oscillators provide a rich and convenient playground in which to address this program. As we show, the squeezed QvdP oscillator is an emergent semiclassical time-crystal (i.e. the time-crystalline phase is well described by mean-field [199]). Furthermore, this time-crystal is interesting by itself as it has the peculiarity to display two regimes that can be accessed by simply tuning the parameters of the system: a regime in which time-translation symmetry is broken continuously, and a regime in which it is broken in a discrete fashion. In fact, the emergence of the continuous time-crystal indicates the lack of entrainment, while the emergence of the discrete one indicates perfect entrainment with the forcing. We argue that continuous time-translation symmetry breaking might be a generic feature of the lack of entrainment as (at the classical level) other systems also display a limit-cycle attractor in the unentrained regime [42, 43] (e.g. the driven vdP oscillator, see appendix H). Instead, the regime in which time-translation symmetry is broken discretely is accompanied by parity symmetry breaking and occurs after the DPT. Interestingly, the simultaneous breakdown of these two symmetries had been reported also for dissipative Dicke models [39] and in systems of non-linear oscillators [196, 370].

7.2 Infinite-excitation limit

In this chapter, we consider again the squeezed QvdP oscillator as described by Eqs. (6.1) and (6.3), and we focus on the physics that emerges as the number of excitations becomes macroscopic. This limit is well described by the classical mean-field equation of motion (6.7), as the role of quantum fluctuations and correlations is no longer important. As commented in chapter 6, γ_2/γ_1 controls the number of excitations of the system. In fact, a convenient way to reach this *infinite-excitation limit* consists in decreasing the non-linear dissipation rate with respect to the linear amplification, i.e. setting $\gamma_2/\gamma_1 \to 0$. Two important observations of the mean-field solutions described in Sect. 6.2.2 are: (i) the bifurcation diagram is independent of γ_2/γ_1 as it just depends on the relation between squeezing strength and detuning, i.e. on η vs. Δ; (ii) in both regimes the squared modulus of the amplitude is inversely proportional to γ_2, see Eqs. (6.11) and (6.12), which suggests that as the regime of validity of the mean-field equation is approached, the boson number becomes inversely proportional to γ_2.

The small non-linearity per boson limit. These considerations suggest the following recipe to study the limit of macroscopic occupation. (i) Rescale all parameters by γ_1, and keep this one fixed. (ii) Define the dimensionless control parameter

$$N = \frac{1}{\gamma_2/\gamma_1}. \tag{7.1}$$

(iii) Take the limit $N \to \infty$ while keeping all the other parameters fixed, which leads to $\langle \hat{a}^\dagger \hat{a} \rangle \to \infty$. Physically, this means that the non-linearity *per boson* becomes vanishingly small such that a *macroscopic number of bosons* is necessary to saturate the eventual instabilities of the system, settling the oscillator in an attractor with macroscopic occupation number[1]. Importantly, this kind of limit has been discussed in zero-dimensional systems (i.e. few mode systems) both in the contexts of dissipative phase transitions [35, 122, 136, 158] and dissipative time-crystals [40, 168, 197, 199, 200]. Interestingly, in some of these systems an analogy can be established between this infinite-excitation limit and the usual thermodynamic limit, as N can be made to represent the actual size or number of sites of a (ficticious) lattice system, while the (actual) zero-dimensional system is found to approximately correspond to the fundamental Fourier mode of this lattice (i.e. the one with zero wavevector)[136, 168].

This way of performing the infinite-excitation limit has the advantage that the population number is increased independently of Δ and η, and hence, these parameters are reserved to access the different regimes of the bifurcation diagram. In fact, following this approach, by simply rescaling the creation and annihilation inside the expectation values following the rule:

$$\hat{a}(\hat{a}^\dagger) \to \hat{a}(\hat{a}^\dagger)/\sqrt{N}, \tag{7.2}$$

in the limit $N \to \infty$, they will tend to the results of the rescaled classical equation:

$$\frac{d}{d(\gamma_1 t)}\tilde{\alpha} = -i(\Delta/\gamma_1)\tilde{\alpha} + \frac{1}{2}\tilde{\alpha} - |\tilde{\alpha}|^2\tilde{\alpha} - 2(\eta/\gamma_1)\tilde{\alpha}^*. \tag{7.3}$$

where we have defined the scaled amplitude $\tilde{\alpha} = \alpha/\sqrt{N}$ with $\alpha = \langle \hat{a} \rangle$, and which only depends on the detuning and squeezing strength.

[1] Therefore, this limit consists in decreasing progressively the non-linearity per boson, which should not be confused with simply dropping the term $\gamma_2 \mathcal{D}[\hat{a}^2]\hat{\rho}$ from Eq. (6.1). Simply killing a term does not define any limiting procedure, while progressively making it small means that one progressively explores increasing boson numbers.

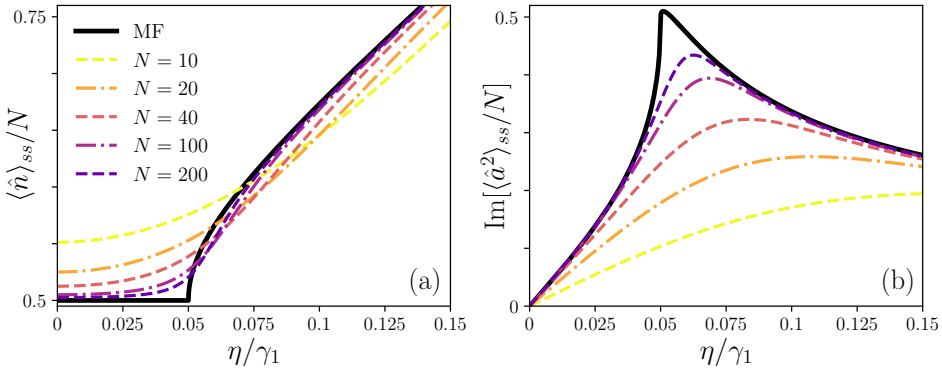

Figure 7.1: (a) Color dashed and dashed-dotted lines correspond to the quantities computed using the stationary state of the master equation for the different values of N as indicated in the legend. Solid black lines correspond to the mean-field calculation as detailed in the text. (a) $\langle \hat{n} \rangle_{ss}/N$. (b) $\mathrm{Im}[\langle \hat{a}^2 \rangle_{ss}/N]$. In both cases $\Delta/\gamma_1 = 0.1$

Non-commutative limits. When studying the infinite-excitation limit, we are interested in comparing the outcomes of the quantum master equation with the ones of the classical mean-field equation. More in particular, we want to understand whether and how the stable attractors of the mean-field dynamical system emerge from the master equation. Hence, we aim to assess both asymptotic time and high-excitation limits. In a first approach, we might be tempted to directly analyze how expectation values computed in the stationary state, i.e. $\langle \hat{O} \rangle_{ss} = \mathrm{Tr}[\hat{O}\hat{\rho}_{ss}]$, behave when increasing N. However, we must recognize that when doing so, a subtle effect needs to be accounted for. When studying the asymptotic behavior of $\langle \hat{O} \rangle_{ss}$ with N, we are actually performing two limits in the following order:

$$\lim_{N\to\infty} \langle \hat{O} \rangle_{ss} = \lim_{N\to\infty} \lim_{t\to\infty} \mathrm{Tr}[\hat{O}\hat{\rho}(t)], \tag{7.4}$$

which need not to be equivalent to the limits taken in the opposite order:

$$\lim_{t\to\infty} \lim_{N\to\infty} \langle \hat{O}(t) \rangle = \lim_{t\to\infty} \lim_{N\to\infty} \mathrm{Tr}[\hat{O}\hat{\rho}(t)]. \tag{7.5}$$

In the presence of stable limit cycles or multistability, these limits do not generally commute, i.e. $\lim_{N\to\infty} \langle \hat{O} \rangle_{ss} \neq \lim_{t\to\infty} \lim_{N\to\infty} \langle \hat{O}(t) \rangle$. The reason is that the stationary state of the master equation, $\hat{\rho}_{ss}$, usually contains a probabilistic mixture of the different possible attractors[2], even if the strength of the fluctuations is vanishingly small (but non-zero), as it is the case when the infinite-excitation limit is approached (for different examples see Refs. [35, 82, 136]).

In our particular system, we find that these two limits do not commute, as we shall see in the following. Indeed, in the limit-cycle regime, the limit (7.4) is found to approach the solutions of Eq. (7.3) time-averaged over a period, similar to what has been reported for other systems [200]. On the other hand, in the bistable regime, this limit [Eq. (7.4)] tends to the mean-field results averaged over the two stable solutions. This is shown numerically in Fig. 7.1, in which we compare the results obtained using the stationary state increasing N (color broken lines), with those obtained averaging (over a period or over the two solutions) the mean-field solutions of Eq. (7.3) (black solid lines). In panel (a) we compare $|\tilde{\alpha}|^2$ calculated using these rules with $\langle \hat{n} \rangle_{ss}/N$, while in (b) we compare the imaginary part

[2]If the attractor is a limit cycle with a free phase, this means that the stationary state is a mixture of all the possible phases. This is the case of the undriven QvdP oscillator in which the phase space representation of the stationary state displays a ring-like shape. This is similar to what also occurs for classical stochastic systems [59, 88, 351].

of $\tilde{\alpha}^2$ with $\mathrm{Im}[\langle\hat{a}^2\rangle_{ss}/N]$. We can see how as N increases, the quantum results converge towards the averaged mean-field results. Notice that the largest differences are found near the bifurcation, where the quantum results feature a crossover that becomes sharper with larger N. On the other hand, it is the subject of the following sections to address the other limit, i.e. Eq. (7.5), which might reveal the emergence of the features missed when considering only $\hat{\rho}_{ss}$, as persistent oscillations or other symmetry broken solutions [38]. As we shall see, a way to analyze this limit systematically consists in performing a finite-size analysis of the Liouvillian spectrum and of the long-time dynamics of some relevant observables.

7.3 Spontaneous symmetry breaking

7.3.1 Symmetries of the Liouvillian

In order to address the presence of spontaneous symmetry breaking, we recall the symmetries that our system displays and some important features that follow from them.

Discrete time-translation symmetry. In the laboratory frame, the master equation (6.1) is time-periodic with period $T_s = 2\pi/(2\omega_s)$, as $\hat{H}(t+T_s) = \hat{H}(t)$, Eq. (6.3), and thus displays a discrete time-translation symmetry. In terms of the laboratory frame Liouvillian, i.e. $\mathcal{L}_L(t)$, this means that:

$$\mathcal{L}_L(t+nT_s) = \mathcal{L}_L(t), \tag{7.6}$$

where n is any integer. Notice that this symmetry is not apparent in the rotating frame, in which the explicit time-dependence of the master equation is eliminated.

Parity symmetry. For $\eta \neq 0$ the model is parity symmetric, as we have already seen in the previous chapter, i.e. the master equation is invariant under the transformation $\hat{a} \to -\hat{a}$, $\hat{a}^\dagger \to -\hat{a}^\dagger$, being this true in both the laboratory and the rotating frames. In the rotating frame, this symmetry translates in the eigenmodes of $\mathcal{L}$ displaying certain properties, from which we highlight the following: (i) all eigenmodes are parity symmetric or parity antisymmetric, $\mathcal{Z}_2\hat{\rho}_j = z_j\hat{\rho}_j$ with $\mathcal{Z}_2$ defined in Eq. (6.19) and $z_j = \pm 1$; (ii) the stationary state is parity symmetric $\mathcal{Z}_2\hat{\rho}_{ss} = \hat{\rho}_{ss}$; (iii) all parity antisymmetric observables are zero in the stationary state $\mathrm{Tr}[\hat{\rho}_{ss}(\hat{a}^\dagger)^m\hat{a}^n] = 0$ for $m+n =$ odd.

Furthermore, in the absence of squeezing, $\eta = 0$, the Liouvillian becomes invariant under the transformation $\hat{a} \to \hat{a}e^{-i\phi}$, $\hat{a}^\dagger \to \hat{a}^\dagger e^{i\phi}$ with ϕ *any* real number, i.e. parity symmetry is promoted to $U(1)$ symmetry. This symmetry has been already presented in chapter 2, and it can be formally written as $\mathcal{U}_\phi\hat{\rho} = e^{-i\phi\hat{a}^\dagger\hat{a}}\hat{\rho}e^{i\phi\hat{a}^\dagger\hat{a}}$, where $[\mathcal{U}_\phi, \mathcal{L}]\hat{\rho} = 0$. Furthermore, in this case, since there is no time-dependent driving field, the master equation displays a continuous time-translation symmetry, i.e. it is the same at all times t.

7.3.2 Infinite-excitation limit and spontaneous symmetry breaking

For finite N, the stationary state of the system satisfies the symmetries of the Liouvillian [35, 268] (see also chapter 1.2). In particular, in our case, this means that the stationary state in the rotating frame is unique and parity symmetric. This implies that back to the laboratory frame this state displays a period T_s (see Eq. (7.13) below). In stark contrast, when considering the infinite-excitation limit, spontaneous symmetry breaking can occur. In the case of parity symmetry this requires the Liouvillian gap to close, such

that stationary states mixing different symmetry sectors can emerge [35]. On the other hand, in the case of continuous time-translation symmetry breaking, this requires a set of eigenvalues to display a vanishing decay rate while a non-zero imaginary part [38]. In such cases, in the long-time limit, the state of the system might not respect some of the symmetries of the underlying Liouvillian. We now discuss how this can be assessed considering the appropriate "order parameters".

Continuous time-translation symmetry breaking. As we have already seen, in the rotating frame, the master equation is time independent. Then, one talks of continuous time-symmetry breaking when there are observables for which there emerge non-decaying persistent oscillations, i.e. they evolve in time according to [38, 199]:

$$f(\tau) = \lim_{t\to\infty}\lim_{N\to\infty} \mathrm{Tr}[\hat{O}\hat{\rho}(t+\tau)], \tag{7.7}$$

where $f(\tau)$ is a periodic function whose period varies continuously with the system parameters, hence the adjective *continuous*. This has been recently studied in the context of dissipative (or boundary) time-crystals [38, 197, 199, 200]. While we study this phenomenon in the rotating frame, it can be equivalently defined in the laboratory frame, in which the system breaks *continuously* the discrete time-translation symmetry of the Liouvillian. That is, there are observables that display non-decaying time-dependent trajectories incommensurate with an oscillation of period T_s.

Discrete time-translation symmetry breaking. In the laboratory frame, discrete time-translation symmetry is signaled by observables that display non-decaying oscillations whose period is a *multiple* of T_s:

$$f_L(\tau) = \lim_{t\to\infty}\lim_{N\to\infty} \mathrm{Tr}[\hat{O}\hat{\rho}_L(t+\tau)], \tag{7.8}$$

with

$$f_L(\tau + nT_s) = f_L(\tau), \quad n > 1. \tag{7.9}$$

and thus they break the time-periodicity of $\mathcal{L}_L(t)$ *discretely*. This type of time-translation symmetry breaking has been discussed extensively in the context of discrete time crystals [39, 40, 183].

Parity symmetry breaking. In this case, it is enough to consider as an order parameter any operator that is parity antisymmetric. Then, the spontaneous breakdown of this symmetry will be signaled by:

$$C = \lim_{t\to\infty}\lim_{N\to\infty} \mathrm{Tr}[(\hat{a}^\dagger)^m \hat{a}^n \hat{\rho}(t)] \neq 0, \quad \text{with} \quad m+n = \text{odd}, \tag{7.10}$$

where C is a constant. Parity symmetry breaking has been reported recently in relation with dissipative phase transitions [35], in which the closure of the Liouvillian gap is shown to give rise to a second stationary state that breaks this symmetry.

It is interesting to recall that in our system parity symmetry and discrete time-translation symmetry are interrelated [3]. This can be seen from the stationary state rotated back to the laboratory frame:

$$\hat{\rho}_L(t) = \hat{U}_t \hat{\rho}_{ss} \hat{U}_t^\dagger, \tag{7.11}$$

[3] This does not mean that parity symmetry is equivalent to discrete time-translation symmetry. For instance, notice that a term of the type $H_d(t) = F(\hat{a}e^{-i2\omega_s t} + \hat{a}^\dagger e^{i2\omega_s t})$ breaks explicitly parity symmetry but not discrete time-translation symmetry.

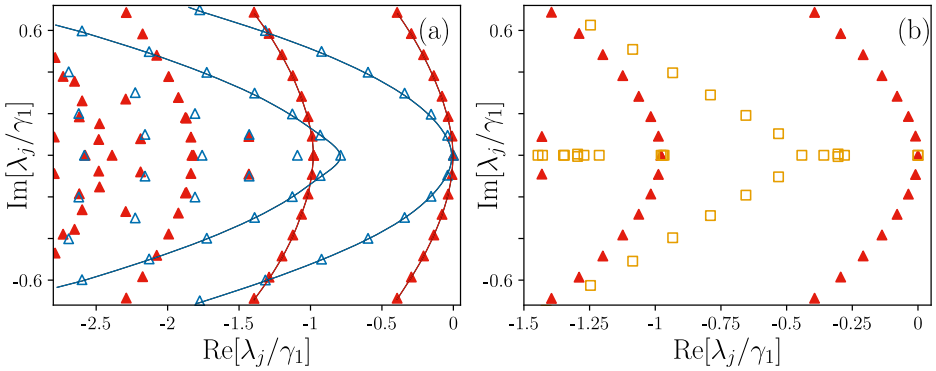

Figure 7.2: (a) Leading eigenvalues for $\eta/\gamma_1 = 0.02$, $\Delta/\gamma_1 = 0.1$ and $N = 20$ (blue empty triangles) or $N = 100$ (red triangles). Here, $\eta_c/\gamma_1 = 0.05$. For each case and for the two lowest bands, we use lines to join the modes of the same band. Hence, the blue lines evolve towards the red lines as N is increased. (b) Leading eigenvalues for $N = 100$ and $\eta/\gamma_1 = 0.02$ (red triangles) and $\eta/\gamma_1 = 0.1$ (golden empty squares) with $\Delta/\gamma_1 = 0.1$, that is below and above η_c/γ_1 respectively.

where we recall that $\hat{U}_t = \exp(-i\omega_s \hat{a}^\dagger \hat{a} t)$. Then, the following identity holds:

$$\hat{U}_{t+T_s} = \exp(-i\omega_s \hat{a}^\dagger \hat{a} t)\exp(-i\pi \hat{a}^\dagger \hat{a}), \tag{7.12}$$

which leads to

$$\hat{\rho}_L(t+T_s) = \hat{U}_t\big(\mathcal{Z}_2\hat{\rho}_{ss}\big)\hat{U}_t^\dagger = \hat{\rho}_L(t), \tag{7.13}$$

since the stationary state is parity-symmetric. Thus, the parity symmetry of the stationary state in the rotating frame ensures that the steady state in the laboratory frame is invariant under a time-translation T_s. This observation already points out that our system might break these two symmetries simultaneously: what in the rotating frame appears as a parity-breaking DPT, back in the laboratory frame it appears as the breakdown of discrete time-translation symmetry.

7.4 Continuous time-translation symmetry breaking ($\eta < \eta_c$)

In this section we show how the system breaks time-translation symmetry *continuously* in the infinite-excitation limit and for $\eta < \eta_c = |\Delta|/2$, which corresponds to the regime in which the mean-field system displays a limit cycle as the stable attractor.

In the rotating frame, we can study systematically the limit given in (7.5) analyzing how the Liouvillian eigenspectrum behaves with N. In particular, from the state eigendecomposition of Eq. (6.5) it becomes clear that in order for the non-decaying oscillations of Eq. (7.7) to emerge, a set of eigenmodes must display non-zero eigenfrequencies, while their decay rates must tend to zero in the infinite-excitation limit [38, 197, 199]:

$$\lim_{N\to\infty} \nu_j = \mathrm{Im}[\lambda_j] \neq 0, \qquad \lim_{N\to\infty} \Gamma_j = |\mathrm{Re}[\lambda_j]| \to 0, \tag{7.14}$$

where we recall that we order the eigenvalues such that $\mathrm{Re}[\lambda_0] \geq \mathrm{Re}[\lambda_1] \geq \mathrm{Re}[\lambda_2] \geq \ldots$.

Bands of eigenmodes. In Figure 7.2 we begin our analysis of the eigenspectrum for $\eta < \eta_c$. In panel (a) we show the leading eigenvalues for $\eta/\gamma_1 = 0.02$, $\Delta/\gamma_1 = 0.1$ and two "system sizes" $N = 20$ (blue empty triangles) and $N = 100$ (red triangles). Recall that the critical squeezing strength is $\eta_c/\gamma_1 = 0.05$ for the given parameters, that is we are considering $\eta < \eta_c$. For both N's, we can appreciate how for approximately the same frequency there appear many eigenvalues with different decay rate. We refer to

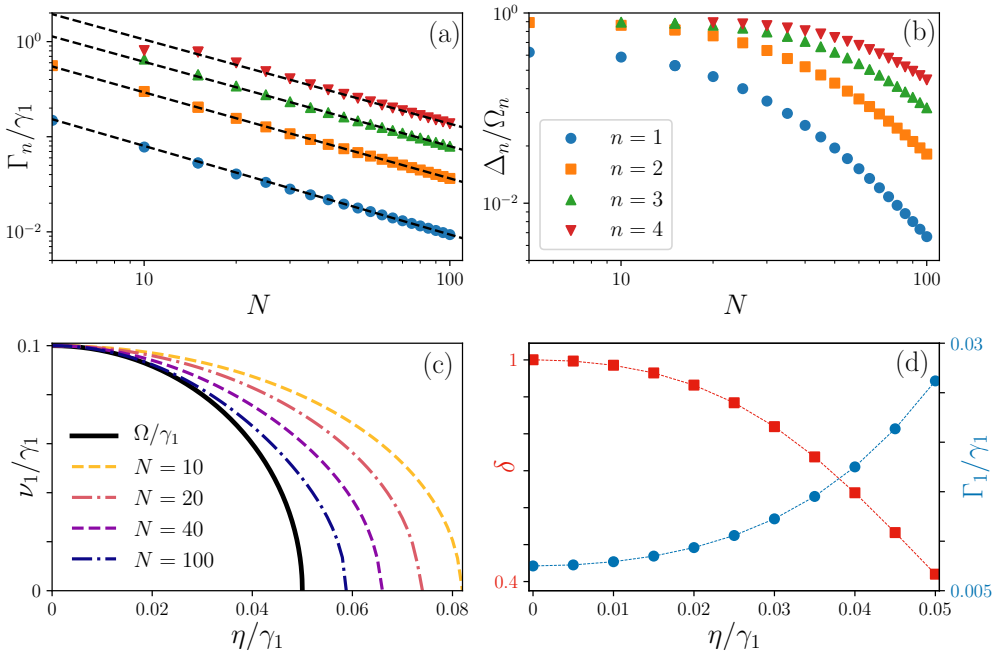

Figure 7.3: (a) First four fundamental decay rates Γ_n/γ_1. Black-dashed lines correspond to a fit given in Eq. (7.15) for the ten points with the largest N of the data set. The coefficients read $\chi = (0.68, 2.35, 4.74, 8.09)$ and $\delta = (0.93, 0.91, 0.89, 0.89)$ for $n = (1, 2, 3, 4)$, respectively. (b) $\Delta_n = \nu_n - \Omega_n$ with $\Omega_n = n\Omega$ varying N for the first four frequencies. Panels (a) and (b) share the same legend and $\eta/\gamma_1 = 0.02$. Both axes of both panels are in logscale. (c) Frequency of the leading eigenmode varying N and η compared to the fundamental frequency of the classical limit cycle, Ω. (d) Left scale and in red-squares: exponent δ that fits $\Gamma_1/\gamma_1 \propto N^{-\delta}$ varying the squeezing strength and below the bifurcation point $\eta_c/\gamma_1 = 0.05$. Right scale and in blue circles: decay rate of the leading eigenvalue for $N = 100$. In all panels $\Delta/\gamma_1 = 0.1$.

the ones with the smallest decay rate for each frequency as *the fundamental band* of modes, while those with approximately the same frequency and larger decay rates form the subsequent *higher-order bands* of modes. In order to visualize the two lowest bands we join the respective modes with two lines. Comparing the results for small and large N we can appreciate the following crucial difference: the real part of the eigenvalues of the fundamental band diminishes with N, while the one of the rest of the bands displays a different behavior. In fact, as we shall see, for $N \to \infty$ and $\eta < \eta_c$, the decay rates of the fundamental band vanish, while the rest saturate to finite values, where a gap of the order or $\sim \gamma_1$ is formed between the different bands. As we shall see, the fundamental band is behind the emergence of persistent oscillations.

Importantly, this behavior only occurs for $\eta < \eta_c$, as we illustrate in panel (b), where we compare the typical spectrum for $\eta < \eta_c$ and $\eta > \eta_c$ for the large value $N = 100$. We anticipate that the break of symmetry occurs at η_c for $N \to \infty$ while at finite N qualitative changes in the spectrum are occurring at η_{EP} where we find the EP reported in Fig. 6.2. Notice that η_{EP} is slightly larger than η_c for finite N, while as we approach the infinite-excitation limit the differences between both vanish, i.e. $\eta_{EP} \to \eta_c$ (see next section). For $\eta > \eta_c$, the characteristic band structure of the leading eigenvalues disappears (golden empty squares) and the spectrum looks and behaves differently: now the leading eigenvalues have collapsed to the real axes. In fact, and as we discuss extensively in the following section, the leading eigenvalue vanishes $\lambda_1 \to 0$ while λ_2 saturates to a finite value, resulting in a gaped spectrum in which $\lambda_j \ \forall j \geq 2$ are separated from the two zero eigenvalues.

Asymptotic behavior of the fundamental band. In Fig. 7.3 (a) we show how the four smallest decay rates change with N. We display only the four smallest ones as their asymptotic behavior is more evident for finite N than that of larger frequencies, as we comment below. A numerical analysis shows that these decay rates follow a power law scaling with N:

$$\Gamma_n/\gamma_1 = \chi N^{-\delta}, \tag{7.15}$$

with $\delta > 0$, which indicates that they vanish at the infinite-excitation limit, and thus, points out continuous time-translation symmetry breaking. In panel (b) we analyze the behavior of the frequency of these eigenvalues finding that they approach the corresponding harmonic of the mean-field frequency Ω. Notice that they do so at a different rhythm, so that finite-excitation effects are larger for higher frequencies. Moreover, we show in panel (c) the comparison of the fundamental classical frequency Ω [Eq. (6.10)] with ν_1, varying N and the forcing strength. We can appreciate that for a given N, the closer the system is to the bifurcation, the larger are the deviations between both. Interestingly, the squeezing strength to which ν_1 vanishes is shifted towards larger values than η_c for finite N. We discuss this effect in more detail in the following section. Furthermore, recall that, since it is only the real part of the fundamental eigenvalues that vanishes, while their imaginary part remains finite, the parity symmetry of these eigenmodes remains well defined and this symmetry is not broken in this regime. This is in stark contrast with the case $\eta = 0$, in which continuous time-translation symmetry breaking is found to correspond to the spontaneous breaking of the underlying $U(1)$ symmetry [168], since a rotating frame can be found in which the infinite fundamental eigenmodes become degenerate and true stationary states, and thus they can be recombined to yield symmetry broken states [35, 168].

The dependence of the exponents "δ" on the squeezing strength is shown in more detail in Fig. 7.3 (d). At $\eta = 0$ the scaling is linear while as $\eta \neq 0$ it becomes sublinear, displaying exponents around $\delta \sim 0.9$ for the case $\eta/\gamma_1 = 0.02$. The fact that δ diminishes with the squeezing strength indicates that the closer we are to the bifurcation, the smaller is the rhythm at which these decay rates vanish, similarly to what we have just commented for the fundamental quantum frequency (ν_1) and the classical one (Ω). In this panel, we also show in blue points the smallest decay rate obtained by direct diagonalization and varying the squeezing strength. We find this quantity to increase as we get closer to the bifurcation, as it could be expected from the behavior of δ. These observations suggest that the emergence of the classical dynamics needs larger Ns to reveal itself the closer the system is to the bifurcation.

Signatures of continuous time-translation symmetry breaking in expectation values. The progressive emergence of the limit-cycle solution can be appreciated in, e.g., the dynamics of the amplitude, as shown in Fig. 7.4. Here, we consider:

$$f(t) = \mathrm{Im}[\langle \hat{a}(t) \rangle / N] \tag{7.16}$$

by increasing N and taking as initial condition a coherent state of amplitude $\sqrt{\gamma_1/(2\gamma_2)}$, i.e. that of the classical limit cycle [see Eq. (6.11)]. The study of expectation values allows us to explore larger "system sizes" (N) than those of Fig. 7.5, as we do not need to diagonalize the Liouvillian[4], an operation that is numerically more expensive than

[4]Results relying on the diagonalization of the Liouvillian are obtained for up to $N \sim 100$ for $\eta < \eta_c$, while for $\eta > \eta_c$ direct diagonalization is more limited due to an increasing excitation number. For stationary state results and dynamics we can generally go beyond this number as shown in the plots. Notice that all numerical results for the quantum master equation are obtained truncating the Hilbert space to a large enough Fock state such that convergence is assured.

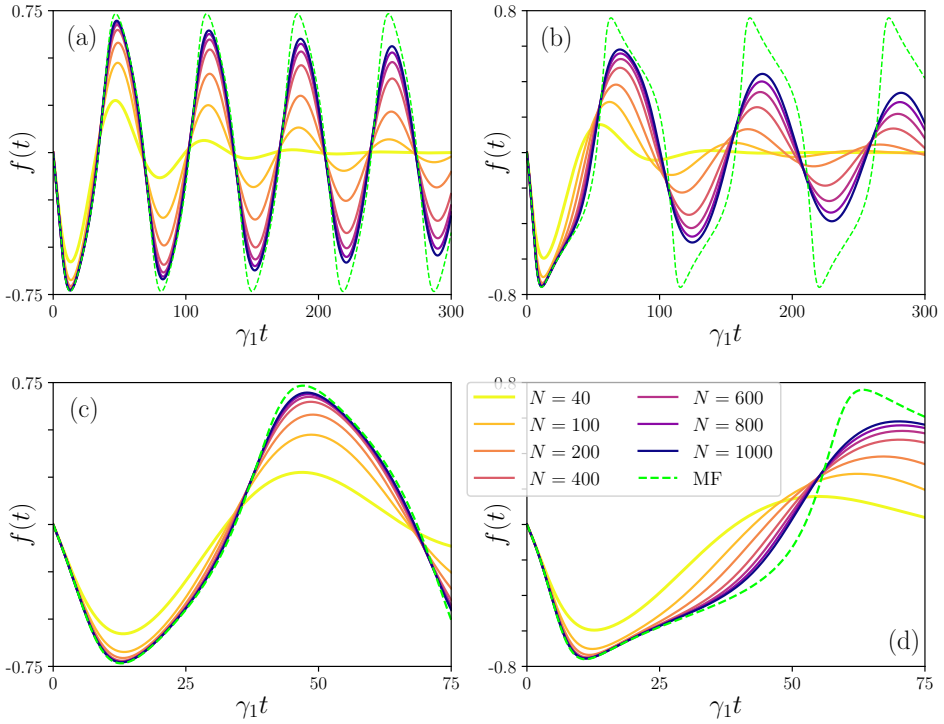

Figure 7.4: Imaginary part of the rescaled amplitude $f(t) = \mathrm{Im}[\langle \hat{a}(t) \rangle / N]$ for different values of N as indicated in the legend and for $\eta/\gamma_1 = 0.02$ (a), and $\eta/\gamma_1 = 0.04$ (b). As an initial state we consider a coherent state of amplitude $\sqrt{\gamma_1/(2\gamma_2)}$ as in the classical limit cycle [see Eq. (6.11)]. In green dashed line, the mean-field trajectory as given by Eq. (7.3) with the same initial amplitude and phase. (c) and (d), zoom in of (a) and (b) for early times, respectively. All panels share the same legend.

integrating the master equation, as one needs to double the dimension of the Hilbert space (see Sect. 2.5.2). In Figs. 7.4 we also show the mean-field self-sustained oscillation (green-dashed line) for $\eta/\gamma_1 = 0.02$ (a), and $\eta/\gamma_1 = 0.04$ (b). As the squeezing strength is increased, more harmonics are involved in this oscillation, and very close to the bifurcation the classical self-sustained oscillation resembles a square wave. Moreover, in this figure we can clearly appreciate how the lifetime of the oscillations increases with N, for both squeezing strengths, and in agreement with the previous results. Notice that the closer the bifurcation, the stronger are finite-N effects, and the oscillations decay faster in the large squeezing case, also in agreement with our previous findings.

In this figure, we also plot the mean-field self-sustained oscillations governed by Eq. (7.3), for the same initial (dimensionless) amplitude and phase (green dashed lines). Notice how the period of the classical oscillation diminishes with the squeezing strength, see Eq. (6.10), while it is also apparent that higher harmonics play a more relevant role as the bifurcation is approached. Comparing the mean-field and the quantum results, we can see how the quantum oscillations progressively approach the mean-field ones as N is increased. In fact, we find that they are already in good agreement for early times, as shown in more detail in panels (c) and (d), in which the large-N results almost overlap with the mean-field ones. Indeed, the effects of higher harmonics are also evident in the quantum case, especially for large squeezing. However, from panels (a) and (b), we also observe that, at later times, the quantum oscillations become harmonic (with just one frequency), departing progressively from their classical counterparts. This is a clear manifestation of a feature already unveiled in our spectral analysis [see Fig. 7.3 (a)], which is the fact that, for finite N, higher harmonics are more damped, and thus they decay out earlier than the fundamental one, resulting in the observed change in the form of the oscillations. Again,

this is more evident for large squeezing, in which this finite-N effect is more visible due to the more relevant role played by higher harmonics, and also due to the larger decay rates displayed near the bifurcation [see Fig. 7.3 (d)].

Semiclassical approach. The limiting case of $\eta/\gamma_1 = 0$ can be accurately understood by means of a semiclassical approach essentially based on the analysis of the mean-field model supplemented by Gaussian fluctuations. Such a classical stochastic model can be obtained from the Wigner representation of the full quantum model dropping third-order partial derivatives [67], while subsequent approximations are used to obtain the main results (see appendix J). While analytical results are only obtained for $\eta/\gamma_1 = 0$, this approach still provides valuable insights for small squeezing strength (see appendix J). For this reason, we overview the main results here.

In particular, for large N the dynamics of amplitude and phase fluctuations can be approximately decoupled. This is a crucial approximation that enables us to obtain the following expression for the decay rates within the different bands (see appendix J):

$$\Gamma_{k,n}/\gamma_1 = 3k^2/(4N) + n, \tag{7.17}$$

where $n = 0, 1, 2, \ldots$ is the band index and $k = 0, \pm 1, \pm 2, \ldots$ indicates the position within the band, i.e. that the corresponding frequency is $k\omega_0$ (or $k\Omega$ for $\eta/\gamma_1 \neq 0$). We find that for large N and $\eta = 0$, the bands $n = 0, 1$ are accurately described by this expression (see appendix J). Therefore, this approach predicts the asymptotic $(1/N)$-scaling of the fundamental decay rates found for $\eta = 0$ [see Fig. 7.2 (d)], as well as the fact that the different bands of eigenmodes are separated by a gap that tends to γ_1. Furthermore, this approach also provides insights about the physical interpretation of the different bands of eigenmodes: while the fundamental one is only associated with the fluctuation dynamics of the phase of the emerging limit cycle, higher-order bands also describe the amplitude fluctuation dynamics. Since for the emerging limit cycle the phase is marginally stable, the associated fluctuation modes display a diverging lifetime when the intensity of the fluctuations vanishes for $N \to \infty$, i.e. the decay rates of the fundamental band tend to zero. On the other hand, the amplitude of the cycle is dynamically stable, and thus the decay rates of the higher-order bands saturate to a finite value.

Departing progressively from the zero squeezing case, the decay rates progressively depart from the analytical prediction of Eq. (7.17) (see appendix J). However, for small squeezing and detuning as compared to γ_1 and N (i.e. the situation considered here), the crucial approximation of decoupling amplitude and phase fluctuation dynamics still seems reasonable. While in this case this is not enough to obtain an analytical expression for the decay rates, it still provides qualitative understanding. Specifically, the intensity of the fluctuations in the phase dynamics is found to vanish in the limit $N \to \infty$, while amplitude fluctuations follow approximately the same process as in the zero squeezing case. This might explain why we still observe a gap of the order $\sim \gamma_1$ between the different bands, and why the decay rates of the fundamental band tend to zero, as we discuss in more detail in appendix J. In this sense, further work could focus on the numerical study of the eigenspectrum of the modified phase equation [i.e. Eq. (J.19)], and analyze whether this approach enables to extend the present results to larger N.

7.5 Parity and discrete time-translation symmetry breaking ($\eta > \eta_c$)

As we have briefly commented, the structure of the Liouvillian spectrum qualitatively changes increasing the squeezing strength for $\eta > \eta_c$ as N is increased [see Fig. 7.2 (b)].

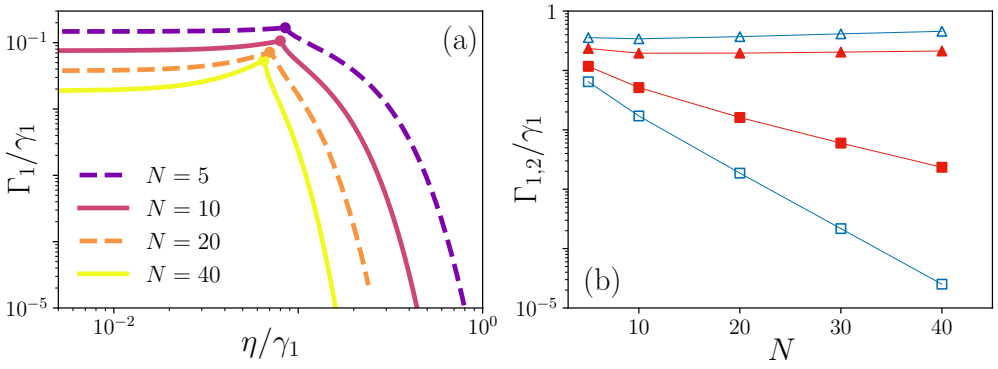

Figure 7.5: (a) Γ_1/γ_1 varying η and for different N. Both axes are in logscale. The corresponding EPs are indicated by circles of the same color as each line. (b) Γ_1/γ_1 varying N for $\eta/\gamma_1 = 0.1$ (filled red squares) and $\eta/\gamma_1 = 0.15$ (empty blue squares). Γ_2/γ_1 varying N for $\eta/\gamma_1 = 0.1$ (filled red triangles) and $\eta/\gamma_1 = 0.15$ (empty blue triangles). Lines are drawn as guide to the eye. Vertical axes is in logscale. In both panels $\Delta/\gamma_1 = 0.1$, which corresponds to $\eta_c/\gamma_1 = 0.05$.

Now, the leading eigenvalues become real valued and the characteristic band structure reported in the previous section disappears. In fact, as the number of excitations increases, there opens a gap between λ_j for $j \geq 2$ and $\lambda_{0,1}$, while simultaneously $\lambda_1 \to 0$. The consequences of the gap opening between $\lambda_{0,1}$ and $\lambda_{j\geq 2}$ have been studied in the previous chapter, in which we have characterized in detail the resulting effective metastable dynamics and its relation with entrainment. Here instead, we will focus on how, as $N \to \infty$ and for $\eta > \eta_c$, the Liouvillian gap closes[5], i.e. $\lambda_1 \to 0$, and thus, a second stationary state emerges resulting in the occurrence of a DPT in which parity and discrete time-translation symmetry are spontaneously broken.

Liouvillian gap closure and EP. The behavior of $\Gamma_1 = |\mathrm{Re}[\lambda_1]|$ varying the squeezing strength and for different N is shown in Fig. 7.5 (a) in a log-log scale. From this panel, we can see that close to η_c there is a turning point (indicated by a colored dot) in which the behavior of Γ_1 changes abruptly, and it tends steeply to zero with increasing squeezing strength. This point corresponds to the EP we have reported in Fig. 6.2 of the previous chapter, in which at η_{EP} the eigenmodes corresponding to $\lambda_{1,2}$ coalesce, and their eigenvalues become real. The larger is N, the faster λ_1 vanishes after the EP. In fact, in panel (b), we plot λ_1 varying N for two squeezing strengths above the critical one (filled and empty squares). Notice that the gap seems to close exponentially with the "system size" N, in contrast with the fundamental decay rates for $\eta < \eta_c$ that vanish following a power of N as we have reported. On the other hand, λ_2 follows the opposite trend when increasing N (filled and empty triangles) and it is found to saturate to a finite value.

Interestingly, we observe that $\eta_{EP} > \eta_c$ for finite N, while in the infinite-excitation limit their difference vanishes [as anticipated when discussing Fig. 7.3 (c)]. This points to an intimate connection between this EP and the mean-field bifurcation point. In Fig. 7.6 (a) we numerically analyze this, considering three different values of the detuning and plotting their distance:

$$\Delta\eta_c = \eta_{EP} - \eta_c \tag{7.18}$$

for increasing values of N. In all cases the scaling law:

$$\Delta\eta_c/\gamma_1 \propto N^{-\beta} \tag{7.19}$$

[5]Notice that we denote as the "Liouvillian gap" the real part of λ_1, following the standard notation [35], while we use the bare term "spectral gap" to denote any other gap in the spectrum, as for instance that involving λ_1 and $\lambda_{j\geq 2}$.

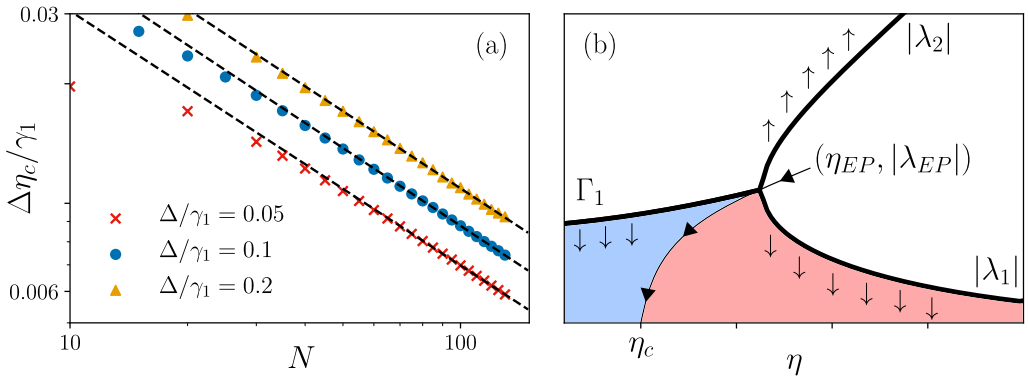

Figure 7.6: (a) $\Delta\eta_c = (\eta_{EP} - \eta_c)$ varying N and for different values of Δ/γ_1. Black-dashed lines correspond to a fit of the type $\Delta\eta_c/\gamma_1 \propto N^{-\beta}$ for the ten points with largest N of the data set. The exponents read $\beta = (0.641, 0.651, 0.645)$ for $\Delta/\gamma_1 = (0.05, 0.1, 0.2)$ respectively. Both axes are in logscale. (b) Cartoon of the emerging bifurcation diagram and the behavior of the leading eigenvalues of the Liouvillian varying the squeezing strength. For finite N there is an EP at η_{EP} at which the two leading eigenvalues become real-valued: $\lambda_{1,2} = \lambda_c$. As N increases the EP progressively approaches the bifurcation point, $\eta_{EP} \to \eta_c$, as indicated by the black line with arrows labeled by $(\eta_{EP}, |\lambda_{EP}|)$. Above the EP, $|\lambda_1|$ decreases with N, while $|\lambda_2|$ increases, as indicated by the black arrows. Below the EP, only the real part of the eigenvalues Γ_n diminishes with N, as also indicated by black arrows. The colored red region indicates the region in which the Liouvillian tends to close eventually leading to a DPT. The colored blue region indicates the region in which the decay rates of the fundamental band of modes tend to vanish as the excitation of the system is increased. For finite N both regions are separated by η_{EP}, which for $N \to \infty$ tends to η_c, as indicated.

is numerically found to fit with accuracy the points with largest N, with a similar $\beta > 0$ (~ 0.65) for three different values of the detunings. Therefore, from figures 7.5 and 7.6 (b) we conclude that as $N \to \infty$, and $\eta > \eta_c$, the Liouvillian gap closes $\lambda_1 \to 0$, while the turning point (EP) observed for finite N approaches the mean-field bifurcation point following a power law in N.

Emergent eigenvalue/bifurcation diagram. In Fig. 7.6 (b) we show a cartoon that illustrates the behavior of the leading eigenvalues of the Liouvillian for the two considered regimes and summarizes the results we have reported. For finite N, the point in which the eigenspectrum changes qualitatively is η_{EP}, at which $\lambda_{1,2}$ become real and equal to λ_{EP}. Above the EP, $\lambda_1 \to 0$ as $N \to \infty$ while λ_2 saturates to a finite value, as indicated by the arrows in this figure. Below the EP, it is only the real part of the fundamental band of eigenmodes that vanishes as $N \to \infty$, i.e. Γ_n. Simultaneously, the squeezing strength at which the EP occurs approaches the classical bifurcation point as $N \to \infty$, as indicated by the arrows on top of the black line labeled $(\eta_{EP}, |\lambda_{EP}|)$. Therefore, as the infinite-excitation limit is approached two different regimes progressively emerge: the one in which the Liouvillian gap tends to vanish ($\eta > \eta_{EP}$, red colored region), and the one in which only the fundamental decay rates tend vanish ($\eta < \eta_{EP}$, blue colored region). In the limit $N \to \infty$ these regimes become sharply defined and they are separated by the classical bifurcation point η_c.

Second stationary state and parity symmetry breaking. Recalling the results of chapter 6, we can see that as a direct consequence of the Liouvillian gap closure, the extreme metastable states defined in Eq. (6.15) become truly stationary states, and hence, since they do not have a well defined parity symmetry [Eq. (6.22)], this results in a DPT in which parity is spontaneously broken. Alternatively, the emergence of these two parity-breaking states can be shown by analyzing the properties of the eigenmode with vanishing lifetime [35], i.e. $\hat{\rho}_1$, and without the need of invoking the metastability formalism used

in the previous chapter. In particular, as λ_1 is real for $\eta \geq \eta_{EP}$, we can decompose $\hat{\rho}_1$ in two density matrices obtained from the projectors of the Hermitian $\hat{\rho}_1$ with positive and negative eigenvalues[6] (as explained in appendix K):

$$\hat{\rho}_1 = \frac{1}{2}(\hat{\rho}_1^+ - \hat{\rho}_1^-), \tag{7.20}$$

which reminds us the decomposition of $\hat{\rho}_1$ in terms of the EMSs [see Eq. (6.15)]. In fact, while the EMSs are especially suited for the study of the dynamics for finite N, as they provide the unique basis in which it makes sense to define an effective stochastic process, they display small positivity corrections for finite N (see Sect. 6.3.2). On the other hand, $\hat{\rho}_1^\pm$ are perfectly defined density matrices for any N, and for this reason they are more appealing to study the emergence of a second stationary state. For this reason, here we will consider $\hat{\rho}_1^\pm$ instead of $\hat{\mu}_{1,2}$. However, as we shall discuss below, the difference between them vanishes when $N \to \infty$.

As commented in the previous chapter, numerical analysis reveals that $\mathcal{Z}_2\hat{\rho}_1 = -\hat{\rho}_1$. In the limit in which $\lambda_1 \to 0$, $\hat{\rho}_1$ and $\hat{\rho}_0$ become degenerate, and we might be able to write down ρ_{ss} also in terms of $\hat{\rho}_1^\pm$. Indeed, we make the following ansatz to be checked numerically:

$$\hat{\xi} = \frac{1}{2}(\hat{\rho}_1^+ + \hat{\rho}_1^-), \quad \lim_{N\to\infty} \hat{\rho}_{ss} \to \hat{\xi}. \tag{7.21}$$

This is an appealing hypothesis, as together with the different symmetry of $\hat{\rho}_{ss}$ and $\hat{\rho}_1$ it automatically follows that $\hat{\rho}_1^\pm$ are symmetry broken states:

$$\mathcal{Z}_2\hat{\rho}_1^\pm = \hat{\rho}_1^\mp, \tag{7.22}$$

while together with $\lambda_0 = 0$ it follows that they are both stationary states:

$$\mathcal{L}\hat{\rho}_1^\pm = 0, \tag{7.23}$$

which (if confirmed) would provide a very clear picture of the spontaneous break of parity symmetry.

In Fig. 7.7 (a) we numerically check the hypothesis of Eq. (7.21), by plotting the trace distance between $\hat{\rho}_{ss}$ and $\hat{\xi}$, i.e.:

$$D(\hat{\rho}_{ss}, \hat{\xi}) = \frac{1}{2}\mathrm{Tr}\Big[\sqrt{(\hat{\rho}_{ss} - \hat{\xi})^\dagger(\hat{\rho}_{ss} - \hat{\xi})}\Big], \tag{7.24}$$

for $\eta \geq \eta_{EP}$ and various values of N. We can clearly appreciate how this distance vanishes as the Liouvillian gap closes, numerically confirming Eq. (7.21). Therefore, the fact that an eigenmode of a different symmetry sector (than the stationary state) displays a vanishing eigenvalue for $\eta > \eta_c$ and $N \to \infty$ results in the emergence of two stationary states, i.e. $\hat{\rho}_1^\pm$, that break parity symmetry in this regime.

This is intimately related to the presence of bistability at the mean-field level. In fact, we can check that observables calculated over these states tend to the mean-field results for each fixed point. This is illustrated in Fig. 7.7 (b), in which we numerically show that:

$$C = \frac{1}{\sqrt{N}}\langle \hat{a} \rangle_+ = \frac{1}{\sqrt{N}}\mathrm{Tr}[\hat{a}\hat{\rho}_1^+], \quad \lim_{N\to\infty} C \to \tilde{\alpha}_+, \tag{7.25}$$

[6] Essentially one diagonalizes $\hat{\rho}_1$. Then, the eigenvectors (pure states) with positive eigenvalue are combined in a weighted (by the eigenvalue) sum to build $\hat{\rho}_1^+$. The same is done for the eigenvectors with negative eigenvalue to obtain $\hat{\rho}_1^-$. Notice that the sum of all eigenvaules must be zero as $\hat{\rho}_1$ is traceless.

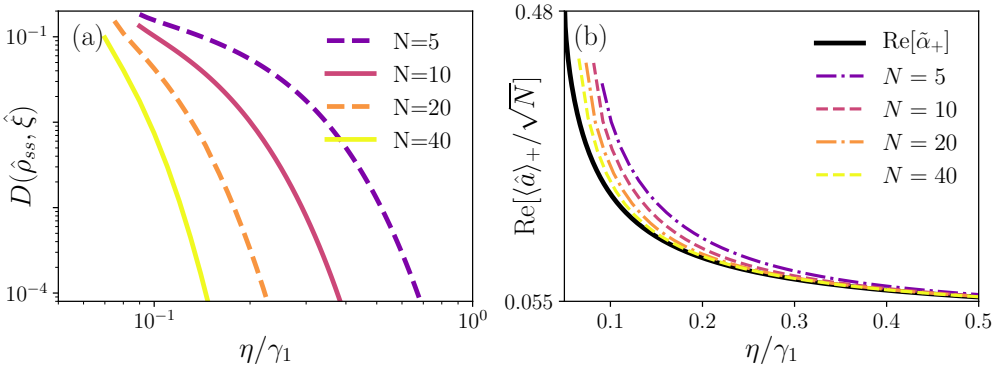

Figure 7.7: (a) Trace distance between the exact stationary state and $\hat{\xi}$. This figure of merit is plotted only for $\eta \geq \eta_{EP}$ as it is where it is valid to decompose $\hat{\rho}_1$ in terms of the density matrices $\hat{\rho}_1^{\pm}$. Both axes are in logscale. (b) Comparison of the real part of $\langle\hat{a}\rangle_+$ with the mean-field solution $\tilde{\alpha}_+$. In both panels $\Delta/\gamma_1 = 0.1$

for $\eta \geq \eta_{EP}$[7], and where $\tilde{\alpha}_+$ is one of the mean-field fixed points [see Eq. (6.12)]. As the lifetime of these states diverges in this limit, $\langle\hat{a}\rangle_\pm \neq 0$ can be regarded as an order parameter for parity symmetry breaking of the type given in Eq. (7.10).

Finally, it is important to recall that as N is increased the EMSs of Eq. (6.15) can be approximated as $\hat{\mu}_{1(2)} \approx (\hat{\rho}_{ss} + (-)\hat{\rho}_1)/2$ with increasing accuracy (see chapter 6 and appendix I). Therefore, as the infinite-excitation limit is approached, it becomes essentially equivalent to study either $\hat{\mu}_{1,2}$ or $\hat{\rho}_1^{\pm}$. Hence, from the results reported here and in the previous chapter, we get a clear picture of how the mean-field bistable regime emerges from the quantum model, as we summarize now: (i) the EP occurs at $\eta_{EP} \to \eta_c$, which can be seen as the bifurcation point as it leads to the qualitatively different behavior of λ_1; (ii) the Liouvillian gap vanishes in the whole regime, implying that the metastable states of the previous chapter display a diverging lifetime and thus they act as stable attractors; (iii) these states correspond to the mean-field fixed points, as observables computed over them tend to the classical ones. Then, it is clear that the limits defined in Eqs. (7.4) and (7.5) neither commute in this regime, since $\mathrm{Tr}[\hat{a}\hat{\rho}_{ss}] = 0$ no matter N, while $\lim_{t\to\infty}\lim_{N\to\infty}\langle\hat{a}(t)\rangle = p_1(0)\langle\hat{a}\rangle_1 + p_2(0)\langle\hat{a}\rangle_2$ which is not necessarily zero (as follows from the results of Sect. 6.3.2 for $\lambda_1 = 0$).

Discrete time-translation symmetry breaking. The parity breaking DPT that we have analyzed in the rotating frame also leads to discrete time-translation symmetry breaking in the laboratory frame. An elegant way to demonstrate this consists in writing down the dynamics of the state in the laboratory frame and at stroboscopic times, i.e. $\hat{\rho}_L(t = nT_s)$ with n a positive integer. Recalling the identity presented in Eq. (7.12), we find that the unitary transform connecting both frames at $t = nT_s$ is equivalent to n parity transforms, which leads to:

$$\hat{\rho}_L(nT_s) = \hat{\rho}_{ss} + \sum_{j\geq 1}(z_j)^n \,\mathrm{Tr}[\hat{\sigma}_j^\dagger\hat{\rho}(0)]\hat{\rho}_j e^{\lambda_j nT_s}. \tag{7.26}$$

Hence, depending on the parity of the eigenmodes ($z_j = \pm 1$) they can display the additional oscillating phase $(-1)^n$. Then, as the Liouvillian gap closes in the infinite-excitation limit and $\hat{\rho}_1$ is antisymmetric, for $nT_s \gg \Gamma_2^{-1}$ the state of the system reads

$$\hat{\rho}_L(nT_s) \approx \hat{\rho}_{ss} + (-1)^n \,\mathrm{Tr}[\hat{\sigma}_1\hat{\rho}(0)]\hat{\rho}_1 \tag{7.27}$$

[7]Notice that we plot these figures of merit for $\eta \geq \eta_{EP}$, and not $\eta \geq \eta_c$, as for finite N it is only in the former case where decomposition (7.20) is possible. Of course this range tends to $\eta \geq \eta_c$ when $N \to \infty$.

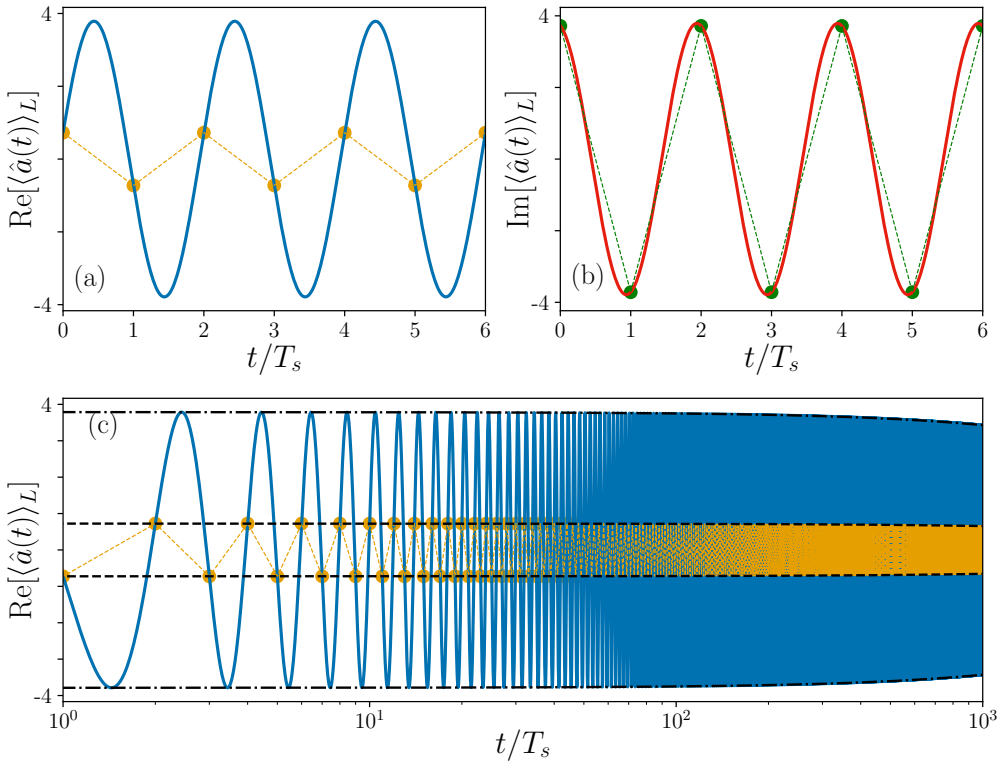

Figure 7.8: Amplitude dynamics in the laboratory frame and for the initial condition $\hat{\rho}(0) = \hat{\rho}_1^+$, $N = 20$, $\eta/\gamma_1 = 0.15$, $\omega_s/\gamma_1 = 20\pi$ and $\Delta/\gamma_1 = 0.1$. The timescale is given in units of the Hamiltonian period T_s. In (a) we plot the real part of the amplitude dynamics, while in (b) the imaginary part. Blue and red solid lines corresponds to the exact solution integrating the explicit time-dependent master equation. The yellow and green points depict the stroboscopic amplitude $\langle\hat{a}(nT_s)\rangle_L$ dynamics, where the different points have been joined by a dashed line for display purposes. In (c) the long-time behavior of panel (a) is shown, from which it can be appreciated that for finite N the period-doubled response eventually decays out. In particular, the black-broken lines correspond to the envelopes $\pm|\langle\hat{a}\rangle|_+ e^{-\Gamma_1 t}$ (dashed-dotted lines) and $\pm\mathrm{Re}[\langle\hat{a}\rangle_+]e^{-\Gamma_1 t}$ (dashed line).

where in the infinite-excitation limit the approximation sign accounts for having neglected the rest of modes ($j > 1$) at large times. Eq. (7.27) clearly signals the breakdown of discrete time-translation symmetry, as the state of the system displays a non-decaying period-doubled dynamics. Moreover, any parity antisymmetric observable is able to resolve this period doubling, and thus, it can be used as an order parameter of the type given in Eq. (7.8). This is illustrated in Fig. 7.8, in which we plot $\langle\hat{a}(t)\rangle_L$ solving the master equation in the laboratory frame and for $\hat{\rho}(0) = \hat{\rho}_1^+$, both at stroboscopic times (yellow and green filled circles) and continuous time (blue and red lines). We can see that the stroboscopic dynamics alternate between two values that depend on the initial condition, while the full time evolution depicts the complete harmonic oscillation of frequency ω_s. Since the considered N is finite, the symmetry broken state displays a finite lifetime and thus this period-doubled dynamics eventually decays out on a timescale Γ_1^{-1}, as essentially follows from the metastable dynamics we have studied in detail in the previous chapter. This is shown in panel (c) of this figure, in which the black-broken lines correspond to the envelopes $\pm|\langle\hat{a}\rangle|_+ e^{-\Gamma_1 t}$ (dashed-dotted lines) and $\pm\mathrm{Re}[\langle\hat{a}\rangle_+]e^{-\Gamma_1 t}$ (dashed line).

7.6 Discussion and concluding remarks

In this chapter, we have analyzed the physics emerging in the squeezed QvdP oscillator as the excitation number becomes macroscopic. As we have seen, this system displays two different regimes in which different symmetries are spontaneously broken. Moreover, these are intimately connected with the mean-field bifurcation diagram and thus with the presence or the absence of subharmonic entrainment. In both regimes, the system breaks time-translation symmetry yet in different ways: when the squeezing strength is smaller than the critical one, this symmetry is broken *continuously*, while when it is larger, it is broken *discretely*. The time-translation symmetry breaking phenomena discussed here belong to the context of *emergent semiclassical time-crystals* [199], in which zero-dimensional systems and many-body systems with all-to-all interactions have been found to break this symmetry both in a continuous fashion [38, 168, 195, 197, 199, 200] as well as discretely [39, 40], in the limit in which the emergent physics is well described by mean-field semiclassical equations of motion. Interestingly, our system displays the distinctive feature not observed before of being able to go from a continuous time-crystal to a discrete one by varying the parameter values.

As we have seen, the presence or the absence of entrainment is linked with the time-crystalline order of the system; when it behaves as a continuous time-crystal there is no entrainment, while when it does as a discrete one there is entrainment. Physically, this correspondence has a clear explanation: in an entrained regime, a system (by definition) oscillates at the *same* or at a *multiple/fraction* of the frequency of a forcing, which means that it does either *respect* the time-translation symmetry imposed by the forcing (as in the driven QvdP oscillator, see appendix H), or it does *break* it discretely, as in the present case. On the other hand, in the absence of entrainment, the system oscillates at its own intrinsic frequency or at a frequency incommensurate with that of the forcing [42, 43], and hence, the discrete time-translation symmetry imposed by the forcing is broken *continuously*, as we have shown to happen in the present case and as it would be interesting to asses for the harmonically driven QvdP oscillator too. Finally notice that the connection between entrainment and time-crystalline order unveiled here differs from that of other synchronization phenomena reported in the literature, as in Ref. [193] in which the regime of *mutual* synchronization corresponds indeed to a continuous time-crystal. However, this is naturally rooted in the different considered synchronization scenario; in entrainment, an external frequency is imposed while, in mutual synchronization, a common frequency emerges.

As a second important result, we have shown that the transition to entrainment corresponds to a dissipative phase transition. Hence, the transition from one regime to the other implies the closure of the Liouvillian gap in the whole entrained regime. Moreover, we have shown an EP to be intimately related to the classical bifurcation point, separating two regimes in which the eigenspectrum displays a qualitatively different behavior, and indeed, approaching the classical bifurcation point as the infinite-excitation limit is approached. The eventual emergence of this gap closure is behind the connection between entrainment and metastability in the quantum regime that we have discussed in the previous chapter. Moreover, it seems that a gap closure, and thus a DPT, also takes place in the driven QvdP oscillator (see appendix H), further strengthening the connection between such driven-dissipative phenomena. In the case of the squeezed QvdP oscillator the DPT leads to parity symmetry breaking. Therefore, parity and discrete time-translation symmetry are broken simultaneously, which becomes evident when moving from the rotating frame to the laboratory frame. Interestingly, this parallels the results recently reported in Ref. [168], in which a DPT with $U(1)$ symmetry breaking in a rotating frame corresponds to continuous time-translation symmetry breaking in the laboratory frame.

PART IV

Final remarks

CHAPTER 8

Summary, conclusions and outlook

Specific conclusions related to the topics discussed in this thesis are included in the corresponding chapters. Here we shall summarize the main contributions and conclusions following a more unifying perspective. Some of the open questions identified along the thesis will be recalled, providing an outlook for future research work.

8.1 Summary

Quantum synchronization has been the unifying topic treated in all works presented in this thesis, in which we have established links with other intriguing phenomena as coalescence, metastability, DPTs, or time-crystals. Here we summarize our main contributions about these topics.

i) *Transient synchronization is a widespread phenomenon.* This follows from the fact that it has been observed in many different systems [5] (some of which have been discussed in detail in this thesis in chapters 3, 4 and 5), and for different dissipation scenarios. Moreover, in chapter 3 we have shown that transient synchronization occurs frequently under collective dissipation even in the presence of complex topologies and inhomogeneities in the parameters, that is, far from highly symmetrical or fine tuned scenarios.

ii) *Synchronization can be enabled by coalescence.* In coupled dissipative systems it can happen that several collective modes display the same frequency after an EP, and as we have shown in chapter 4 this also leads to a form of transient synchronization. The peculiarity of this scenario is that even if all the relevant modes have the same frequency, the different oscillating coherences can experiment a sort of dephasing due to the presence of multiple degenerate collective modes, and *phase-locking* generally emerges after a transient in which only the longest-lived mode survives. When considering the power/emission spectrum we have shown that this effect manifests in interference features such as asymmetric shapes or transparency windows.

iii) *Quantum synchronization can be engineered in atomic lattices with local dissipation.* As we have shown in chapter 5, the low-energy physics of a one-dimensional system of atoms trapped in an optical potential, as described by a dimeric dissipative spin chain, can display transient synchronization. Moreover, we have reported on the novel *inter-band* synchronization, in which a whole band of quasi-degenerate extended modes synchronizes the system. These results pave the way for the study of quantum synchronization in this important class of quantum simulators.

iv) *Synchronization is not generally isolated from other non-equilibrium phenomena like DPTs and time-crystals.* Prior to the results obtained in this thesis, it was already known that quantum synchronization was related in some systems to subradiance and long-lived correlations [65, 90], to superradiance [46, 80], or to time-crystals [193]. In this thesis we have contributed to establish connections between quantum synchronization and other non-equilibrium phenomena, for instance by showing that quantum entrainment in the squeezed QvdP oscillator is intimately related to quantum metastability. Moreover, we have found that in this system the transition to entrainment corresponds to a DPT, and that the presence/absence of entrainment corresponds to a different type of time-crystalline order.

v) *EPs can separate different dynamical regimes.* Looking at the non-Hermitian matrices describing the dynamics of a dissipative quantum system (see chapters 4, 6 and 7), we have found that EPs separate different dynamical regimes. Furthermore, in the squeezed QvdP oscillator, the classical bifurcation point seems to manifest as an EP involving the two leading excitations of the Liouvillian (see chapters 6 and 7). This follows from our observations that the EP separates the two regimes in which the leading eigenvalues display a qualitatively different behavior, as well as the fact that the critical squeezing strength at which the EP occurs approaches the one of the classical bifurcation in the infinite-excitation limit.

vi) *From continuous to discrete time-translation symmetry breaking.* Besides the interesting relation between time-crystals and synchronization that we have reported, the squeezed QvdP oscillator also displays a peculiar transition from continuous to discrete time-translation symmetry breaking that is interesting by itself, and which up to our knowledge constitutes a novel contribution of this thesis. As discussed in chapter 7, this essentially stems from the peculiar infinite-period bifurcation occurring in the infinite-excitation limit, in which a limit cycle leads to bistability.

8.2 Concluding remarks

Beyond this spectrum of results, it would be valuable to devote a few lines to reflect on the question "what is quantum synchronization?" and to comment on what this thesis can say about it. From the overview of the literature presented in chapter 1 one already gets the idea that this is a very diverse phenomenon: quantum synchronization does not always manifest in the same way, nor are the mechanisms behind it universal. In this regard, one might try to give a minimal definition of quantum synchronization: Quantum synchronization should encompass dynamical phenomena occurring in quantum systems

that are characterized by a strong correlation or similitude among the temporal evolution of interacting systems (spontaneous synchronization) or of a system and an external driving (entrainment). An important key aspect about synchronization phenomena is that it has to do with correlation in the temporal evolution, which is the feature that distinguishes it from other types of correlations [44]. Indeed, we have found that this basic notion of quantum synchronization enables to extend and identify this phenomenon beyond the standard paradigm of self-sustained oscillators, also considering dissipative systems of spins and harmonic oscillators, in which both transient and non-decaying synchronous oscillations can emerge. Moreover, by summarizing some of the main shared/different aspects of the quantum synchronization scenarios reported here, we can further illustrate this basic notion of quantum synchronization and also already appreciate the diversity surrounding this phenomenon:

i) *Static vs. dynamic signatures of synchronization.* While in some cases the transition to synchronization does manifest in static quantities, as the transition from a ring-like shape to a localized pattern of the stationary Wigner distribution of the QvdP oscillator, in this thesis we have found that what is common in *all* the considered scenarios is the fact that synchronization implies some changes in the characteristics of the dynamical excitations of the system. These can consist in, for instance, the emergence of long-lived modes that dominate the long-time dynamics of the system, or the occurrence of coalescence of the dominant excitation modes which leads to a qualitative change in their behavior. In fact, for some of the considered systems (see chapters 3, 4 and 5), the stationary state is the same whether there is synchronization or not, and does indeed correspond to the thermal or vacuum state. In contrast, these changes in the excitation spectrum can be appreciated in the study of dynamical quantities as e.g. the emission/absorption spectrum or correlations computed over a whole time window as the Pearson factor, as we have shown extensively along the thesis. Therefore, our conclusion in the matter of static vs. dynamic approaches to quantum synchronization (i.e. indicators at a single time vs. on a whole time window, see discussion in chapter 1) is that the dynamical ones are those that work in the general case as, essentially, the phenomenon of synchronization implies some modification of the temporal evolution of the system. In this sense, it remains to be analyzed how synchronization scenarios reported deep in the quantum regime by means of just static quantities, as e.g. in Refs. [69, 91, 92, 96], do actually translate in the characteristics of the dynamical excitations of these systems or which signatures display when considering such dynamical quantities.

ii) *Lifetime of the synchronized response.* As a further shared feature of the considered scenarios, we have found that the temporal coherence of the synchronized response is often limited, i.e. although the synchronized response can be long-lived it eventually decays out. While the case of "stationary synchronization" is a notable exception, both for transient synchronization and for the squeezed QvdP oscillator the synchronized oscillation does not display an infinite lifetime. This finite lifetime can have a different specific origin, as the atoms decaying to the motional ground state in the atomic lattice (see chapter 5), or the fluctuations driving jumps between two metastable preferred phases (see chapter 6). However, the common underlying driving force of these incoherent processes is the presence of fluctuations and dissipation that generally characterizes the dynamics of open quantum systems. This seems to be a common feature in quantum synchronization scenarios and it is in stark contrast to classical noiseless dynamical scenarios in which synchronization is usually addressed.

iii) *Diverse scenarios of synchronization.* Finally, even when considering similar synchronization phenomena, we have found rich dynamical scenarios moving from case to case. For instance, in the case of transient synchronization we have reported this phenomenon to occur in the presence of a single long-lived mode, in the presence of many modes with the same frequency (coalescence) or quasi-degenerate ones (interband synchronization), each scenario displaying its own peculiarities, despite the overall phenomenon is the same. On the other hand, for the case of entrainment, even considering the same oscillator but different external drivings (i.e. squeezed or harmonic driving), we have seen that the dynamical landscape changes significantly and the entrainment dynamics shows in each case its own specific features. Quantum synchronization, as other dynamical phenomena in complex systems, is thus characterized by a rich phenomenology and connections might be drawn between scenarios that seem, at first, independent of each other.

8.3 Outlook

Building upon the results and open questions we have identified along the text, we now propose an outlook for the topics discussed in this thesis.

i) *Synchronization in hybrid systems and beyond Markovian dissipation.* Hybrid quantum systems made of several types of degrees of freedom, as few level systems coupled to bosonic modes, and dissipative systems going beyond Markovian dissipation constitute interesting scenarios with an increased level of complexity in which to address the study of quantum synchronization (for some first works going beyond Markovian systems see [97, 372]). An interesting question would be whether new quantum synchronization phenomena can emerge due to these new ingredients. Moreover, it would be especially interesting to consider models motivated by the field of quantum biology [294, 298], as light-harvesting complexes, which can indeed be complex quantum systems containing a combination of different types of degrees of freedom, an intricate dissipation landscape with Markovian and non-Markovian channels, and also complex topologies with non-uniform parameters. Indeed, a first work on this subject in which a small dimer system is studied was recently reported in Ref. [99]. The fundamental question to address is whether there are any synchronization phenomena in these systems, and whether does it play any functional role. In fact, in classical biological systems synchronization is known to occur, e.g.: as in neural processes, or to ensure the correct functioning of our heart [42, 43]. These questions are as interesting and fundamental, as challenging to address: the study of these many-body open quantum systems often requires advanced numerical techniques [298, 373]. Moreover, in this context, it would also be interesting to analyze the signatures of synchronization phenomena in two-dimensional spectroscopy: this is a kind of nonlinear spectroscopy technique used in the study of light-harvesting complexes (see e.g. [374, 375]) which can provide information about the dynamics beyond that of the emission/absorption spectrum [376].

ii) *Spectral theory of bifurcations in quantum systems.* A single nonlinear dynamical system can be a complex system by itself. The popular saying "easy to write, difficult to understand" summarizes accurately this fact. Driven-dissipative quantum nonlinear systems have been considered for a long time, as for instance in quantum optics [59, 377]. The richness of the displayed phenomena, and the growing body of engineerable driven-dissipative nonlinear quantum systems keep pushing interest on this subject (see chapter 1). In particular, recent efforts have focused on DPTs and the associated closure of the

Liouvillian gap [34, 35]. In this sense, it would be timely and interesting to analyze in general how bifurcations translate into the spectral properties of the Liouvillian. In fact, from the work done in this thesis several relevant questions can be already identified. In particular, which bifurcations involve the closure of the Liouvillian gap? In which cases does a bifurcation manifest as an EP? Are there some universal quantum properties associated with a particular bifurcation? A first step could be achieved comparing in more detail the squeezed and the harmonically driven QvdP oscillator, as in both cases the bifurcation corresponds to a SNIC bifurcation, and moreover, in the driven QvdP an EP also seems to play an important role (see appendix H). Furthermore, the type of bifurcation occurring in the driven vdP varies depending on the parameter values, which could further help to find a correspondence between a particular bifurcation and some particular spectral features of the Liouvillian.

iii) *Experiments and applications for quantum synchronization.* Here we can identify several fronts on which to work. On the side of small quantum systems, recent experiments with cold atoms [120] and the IBM quantum computer [121] have studied synchronization in the spin-1 system. Moreover, in this kind of few level systems connections have been established between synchronization and thermodynamic performance [94]. An interesting direction to follow would be to analyze whether with the IBM quantum computer small arrays of driven-dissipative spins can be simulated, or even QvdP oscillators in the few excitation regime. Moreover, it seems promising to try to establish further links between the quantum synchronization phenomena occurring in these small systems and quantum thermodynamics. In particular, in this thesis we have found that synchronization is usually associated with an enhancement of the temporal coherence of the dynamical response, even for small systems (see chapters 4 and 5) or far from the infinite-excitation limit (see chapter 6). Can this be used, for instance, as a resource for small and efficient time-keeping machines [378]? On the side of many-body quantum systems, a recent work [379] has studied the driven-dissipative dynamics of a lattice Bose-Hubbard model and it has been shown that some of the identified non-equilibrium phases can be understood as quantum synchronization in QvdP oscillators arrays. This model is motivated in part by recent experiments with cold atoms in which nonlinear dissipation has been implemented [380]. This is the key ingredient for implementing QvdP oscillators. While for the study of small arrays of QvdP oscillators simulators based on trapped ions and optomechanical platforms have been proposed [67, 68, 70, 166], these large atomic platforms could pave the way to simulate larger arrays of QvdP experimentally, allowing to circumvent the current numerical limitations to address such many-body scenarios. Hence, another promising research line could address how to implement the missing ingredients, i.e. linear amplification and some forms of coherent driving, in this kind of systems.

PART V

Appendices

APPENDIX A

Phase-space representations: the Wigner distribution

In this appendix we provide a brief presentation of phase-space methods as based on phase-space representations of the density matrix of the system. In a phase-space representation one essentially maps the state of the system to a function or distribution of complex numbers, known as quasiprobability distribution, while the operator master equation is replaced by a partial differential equation for this distribution. The term quasiprobability distribution is motivated by the fact that these distributions play an analogous role as classical probability distributions, and in many instances expectation values and multi-time correlations can be calculated in analogous form as in classical statistics [59]. However, notice that these phase-space representations need not to satisfy the properties of a probability distribution, as positive-definiteness, and subtleties related to operator ordering can further limit this useful analogy [59].

Phase-space representations provide an important alternative route for the analysis of the dynamics of quantum systems which is formally closer to that of classical physics and classical statistics, as one deals with distributions over a complex number space and with differential operators. Therefore, these methods provide a particularly convenient way to bridge the gap between the quantum and classical regime of dissipative systems, and they are often the basis of semiclassical approximate schemes. In fact, in some cases the obtained partial differential equation is a Fokker-Planck equation [59, 88, 381], a well known equation in classical statistics, and which enables the application of powerful classical methods developed for this important class of fluctuating classical systems [88, 381, 382] to the quantum realm, providing significant physical insights about the effects of quantum fluctuations [59].

Phase-space methods have been developed mainly in the field of quantum optics in which they have enjoyed widespread application. Some paradigmatic examples of their usage can be found in the study of dispersive optical bistability [155, 357, 383], the single-mode laser [59, 381], or the degenerate parametric oscillator [377]. Moreover, these methods have also been applied in the study of driven-dissipative quantum many-body systems, in which they provide a convenient starting point for semiclassical treatments [13, 66, 384]. In this thesis we make a rather restricted use of phase representations as we only consider them for visualization of the state of the system and as a convenient starting point for

semiclassical approximations, while we do not consider them for the calculation of expectation values and multi-time correlations. Hence, in the following we introduce them with these goals in mind.

The basic idea of phase-space representations is to write the density matrix of the system in terms of coherent states, as defined by $\hat{a}|\alpha\rangle = \alpha|\alpha\rangle$ for bosonic systems[1]. For a review of the main properties of this overcomplete basis of states we refer the reader to [59, 60]. Precisely because of this overcompleteness, one can define many possible phase-space representations of the density matrix and of the Lindblad master equation, and the choice of a particular one usually depends both on the goal or focus of the study as well as on the peculiarities of the considered system. For completeness, here we present the three main phase-space representations used in the literature: the Glauber-Sudarshan P-representation, the Husimi Q-representation and the Wigner representation[59, 60]. The P-representation is defined as:

$$P(\alpha,\alpha^*) = \frac{1}{\pi^2}\int d^2z\,\mathrm{Tr}[\hat{\rho}e^{iz^*\hat{a}^\dagger}e^{iz\hat{a}}]e^{-i(z\alpha+z^*\alpha^*)}. \tag{A.1}$$

It is illustrative to write the inverse of this definition:

$$\hat{\rho} = \int d^2\alpha\,|\alpha\rangle\langle\alpha|P(\alpha,\alpha^*). \tag{A.2}$$

as it reminds a classical probability distribution and thus further motivates the use of the term quasiprobability. Indeed, in this representation normal-ordered expectation values and multi-time correlations can be calculated in a completely analogous way as in classical statistics [59, 60]. Hence, the P-representation is especially suited for quantum optics as it is the most convenient one to study normal-ordered expectation values and multi-time correlations, which are prevalent in the theory of photodetection [59]. The Husimi Q-representation enjoys a very simple definition:

$$Q(\alpha,\alpha^*) = \frac{1}{\pi}\langle\alpha|\hat{\rho}|\alpha\rangle, \tag{A.3}$$

and moreover is especially suited for anti-normal ordered expectation values and multi-time correlations. Finally, the well known Wigner representation can be defined as:

$$W(\alpha,\alpha^*) = \frac{1}{\pi^2}\int d^2z\,\mathrm{Tr}[\hat{\rho}e^{i(z\hat{a}+z^*\hat{a}^\dagger)}]e^{-i(z\alpha+z^*\alpha^*)}, \tag{A.4}$$

and it is especially suited to compute expectation values and multi-time correlations in symmetric or Weyl order. Notice that one can move from one representation to the others by means of integral transforms [59, 60]. Furthermore, it is important to comment that while the Q and Wigner representations of a density matrix are always well-behaved functions, the P-representation for a density matrix might be a generalized function or distribution, as it is the case of Fock states, whose corresponding P-representation contains Dirac deltas and their derivatives [59, 60]. For this reason the Q- and the Wigner quasiprobability distributions can be more convenient when trying to gain visual intuition about the state of the system. In this thesis we will consider only the Wigner distribution, as besides it is a well-behaved function, it is the usual choice in the study of quantum synchronization and dissipative phase transitions [67, 68, 136].

Finally, we describe how to transform the master equation for the density matrix into an equation for a quasiprobability distribution. We focus on the case of the Wigner distribution as it is the one that we will work with. In order to do so we make use of the

[1] In this thesis we only consider phase-space representations of bosonic systems, and hence we only cover this case in this brief introduction. For generalization to spin systems the reader is referred to [59, 384].

following correspondence between the action of operators on the density matrix and the action of partial derivatives on the Wigner distribution [60]:

$$\begin{aligned} \hat{a}\hat{\rho} &\leftrightarrow \big(\alpha + \frac{1}{2}\partial_{\alpha^*}\big)W(\alpha,\alpha^*), \quad \hat{\rho}\hat{a} \leftrightarrow \big(\alpha - \frac{1}{2}\partial_{\alpha^*}\big)W(\alpha,\alpha^*), \\ \hat{a}^\dagger\hat{\rho} &\leftrightarrow \big(\alpha^* - \frac{1}{2}\partial_{\alpha}\big)W(\alpha,\alpha^*), \quad \hat{\rho}\hat{a}^\dagger \leftrightarrow \big(\alpha^* + \frac{1}{2}\partial_{\alpha}\big)W(\alpha,\alpha^*). \end{aligned} \tag{A.5}$$

We exemplify the use of this correspondence by considering the case of an harmonic oscillator coupled to a thermal bath. Then making use of Eq. (A.5) we can transform the operator Lindblad master equation (2.31) to a partial differential equation for the Wigner distribution:

$$\begin{aligned} \frac{d}{dt}W(\alpha,\alpha^*,t) = \big[\big(\frac{\gamma}{2} + i\omega_0\big)\partial_\alpha\alpha + \big(\frac{\gamma}{2} - i\omega_0\big)\partial_{\alpha^*}\alpha^* \\ + \gamma(\bar{n}+1)\partial_\alpha\partial_{\alpha^*}\big]W(\alpha,\alpha^*,t), \end{aligned} \tag{A.6}$$

where again we have reabsorbed the Lamb-shift into the definition of the frequency. This partial differential equation is a particular case of a Fokker-Planck equation [59, 88, 381, 382] with linear drift and with a constant diffusion term. This means that the terms containing one partial derivative are are linear in the complex amplitudes while the terms containing two partial derivatives display constant coefficients, respectively.

Fokker-Planck equations are well known in the theory of stochastic processes and classical statistics in general, and a number of methods of analysis can be directly imported from there [88, 381, 382]. In particular, a very convenient method is the derivation of Langevin equations, which enable the use of powerful 'Monte-Carlo' numerical methods [382]. Moreover, notice that the mathematical properties of some particular Fokker-Planck equations are also well known. For instance, equations of the type of (A.6), i.e. with linear coefficients and constant diffusion, are known to preserve Gaussian states, i.e. to map Gaussian distributions to Gaussian distributions [59]. This is rooted to what we have commented previously at the operator level, that the master equation (2.31) is quadratic or bilinear in the creation and annihilation operators and thus preserves Gaussian states [266, 267].

As an example we consider an initial coherent state of amplitude α_0, which is represented by the Gaussian distribution centered at α_0 [59, 88]:

$$W(\alpha,\alpha^*,0) = \frac{2}{\pi}e^{-2|\alpha-\alpha_0|^2}. \tag{A.7}$$

Then the solution of Eq. (A.6) with this initial condition is [59]:

$$W(\alpha,\alpha^*,t) = \frac{1}{\pi\big[\frac{1}{2} + \bar{n}(1-e^{-\gamma t})\big]}\exp\left[-\frac{|\alpha - \alpha_0 e^{-(\gamma/2)t - i\omega_0 t}|^2}{\frac{1}{2} + \bar{n}(1-e^{-\gamma t})}\right], \tag{A.8}$$

which features a Gaussian distribution of growing variance. Moreover, this time-evolving distribution tends to a Gaussian distribution centered at the origin which corresponds to a thermal state [59, 60]:

$$W_{ss}(\alpha,\alpha^*) = \frac{2}{\pi(2\bar{n}+1)}e^{-2|\alpha|^2/(2\bar{n}+1)}, \tag{A.9}$$

where $W_{ss}(\alpha,\alpha^*) = \lim_{t\to\infty} W(\alpha,\alpha^*,t)$.

Finally, it is important to comment that not all operator master equations map to a Fokker-Planck equation for a quasiprobability distribution. In fact, for more involved examples containing non-linear processes this is usually not the case, and one might be

faced with a general partial differential equation which might be as challenging as the original operator master equation. However, it is sometimes possible to approximate the dynamics of the system in the semiclassical limit by a Fokker-Planck equation, by means of approximation schemes as the system-size expansion or the truncation of higher-order derivatives, and which can make the usage of phase-space methods advantageous [13, 59, 60].

APPENDIX B

The Pearson factor

In this appentix we introduce the Pearson factor, a measure that we use to assess the presence of synchronization, which consists in a correlation function that quantifies the degree of similitude between two temporal trajectories [5, 44]. In particular, these trajectories correspond to local observables of each system, as for instance the x-component of spins $A_1(t) = \langle \hat{\sigma}_1^x(t) \rangle$ and $A_2(t) = \langle \hat{\sigma}_2^x(t) \rangle$, for some particular parameter choice and initial condition. The corresponding correlator is the Pearson factor defined as:

$$\mathcal{C}_{A_1(t),A_2(t)}(t|\Delta t) = \frac{\int_t^{t+\Delta t} ds[A_1(s) - \bar{A}_1][A_2(s) - \bar{A}_2]}{\sqrt{\prod_{j=1}^{2} \int_t^{t+\Delta t} ds[A_j(s) - \bar{A}_j]^2}}, \tag{B.1}$$

with $\bar{A}_j = \frac{1}{\Delta t} \int_t^{t+\Delta t} ds A_j(s)$. Then $\mathcal{C}_{A_1(t),A_2(t)}(t|\Delta t) \in [-1, 1]$ by definition. This correlator is a function of time with a time window Δt, which for perfect synchronization or anti-phase synchronization is known to take the values 1 or -1, respectively. However, an important drawback is that it is not sensitive to synchronization at other phase-differences. For this reason, and in order to assess the emergence of synchronization with arbitrary *locked* phase differences, we can also consider the time delayed maximized Pearson factor [90]. This is defined as $\mathcal{C}_{\max}(t) = \max\left[\mathcal{C}_{A_1(t),A_2(t+\tau)}(t|\Delta t)\right]_{\tau\in[0,\delta t]}$, or in words: it is the maximum value that the Pearson factor takes considering two time delayed trajectories with a delay time in the range 0 to δt. This measure takes the value 1 for perfect synchronization. Notice that in this case, from the optimal τ we can obtain the locked phase difference between the synchronized trajectories. At this point, we should remark that there are not universal prescribed values for δt and Δt, rather there is a qualitative recipe for them to be meaningful: δt should be of the order of a period of the synchronous oscillation, and Δt should be of the order of few periods of the synchronous oscillation.

APPENDIX C

Master equation for two harmonic oscillators

Here we write down the master equation for two oscillators (3.11) in the basis of the oscillators, and we analyze the differences between the CB and SB cases, supplementing the discussion presented in chapter 3. Moreover, we show how these differences translate in the equations of motion for the first and second moments.

C.1 Master equation in the oscillator basis

In order to obtain the master equation in the oscillator basis, we just need to use the canonical transformation (3.2) and express the normal mode variables in terms of the oscillator ones. Regrouping the equivalent terms, we obtain:

$$\begin{aligned}\frac{d}{dt}\hat{\rho} = -i[\hat{H}_S,\hat{\rho}] + \frac{1}{2}\sum_{j=1,2}\Big[&\tilde{D}_j^{(x)}\mathcal{D}[\hat{x}_j]\hat{\rho} + \tilde{D}_j^{(p)}\mathcal{D}[\hat{p}_j]\hat{\rho} \\ &- i\tilde{\Gamma}_j\big(\hat{x}_j\hat{\rho}\hat{p}_j - \frac{1}{2}\{\hat{p}_j\hat{x}_j,\hat{\rho}\}\big) + i\tilde{\Gamma}_j\big(\hat{p}_j\hat{\rho}\hat{x}_j - \frac{1}{2}\{\hat{x}_j\hat{p}_j,\hat{\rho}\}\big) \\ &+ \tilde{D}_c^{(x)}\big(\hat{x}_j\hat{\rho}\hat{x}_{k\neq j} - \frac{1}{2}\{\hat{x}_{k\neq j}\hat{x}_j,\hat{\rho}\}\big) + \tilde{D}_c^{(p)}\big(\hat{p}_j\hat{\rho}\hat{p}_{k\neq j} - \frac{1}{2}\{\hat{p}_{k\neq j}\hat{p}_j,\hat{\rho}\}\big) \\ &- i\tilde{\Gamma}_c\big(\hat{x}_j\hat{\rho}\hat{p}_{k\neq j} - \frac{1}{2}\{\hat{p}_{k\neq j}\hat{x}_j,\hat{\rho}\}\big) + i\tilde{\Gamma}_c\big(\hat{p}_j\hat{\rho}\hat{x}_{k\neq j} - \frac{1}{2}\{\hat{x}_{k\neq j}\hat{p}_j,\hat{\rho}\}\big)\Big],\end{aligned} \tag{C.1}$$

where the cross-diffusion and cross-damping terms correspond to the last two lines, respectively. The diffusion coefficients are defined as follows:

$$\begin{aligned}\tilde{D}_{1(2)}^{(x)} &= D_{+(-)}\sin^2\theta + D_{-(+)}\cos^2\theta, \quad \tilde{D}_{1(2)}^{(p)} = \frac{D_{+(-)}}{\Omega_{+(-)}^2}\sin^2\theta + \frac{D_{-(+)}}{\Omega_{+(-)}^2}\cos^2\theta, \\ \tilde{D}_c^{(x)} &= (D_+ - D_-)\cos\theta\sin\theta, \quad \tilde{D}_c^{(p)} = (D_+/\Omega_+^2 - D_-/\Omega_-^2)\cos\theta\sin\theta,\end{aligned} \tag{C.2}$$

while the damping rates read:

$$\tilde{\Gamma}_{1(2)} = \Gamma_{+(-)}\sin^2\theta + \Gamma_{-(+)}\cos^2\theta, \quad \tilde{\Gamma}_c = (\Gamma_+ - \Gamma_-)\cos\theta\sin\theta. \tag{C.3}$$

The difference between the CB case and the SB one resides again in the definition of $D_\pm$ and $\Gamma_\pm$. Notice that, while in both scenarios the cross-diffusion terms are generally non-zero, the cross-damping term are only non-zero in the CB case, as for a SB $\Gamma_+ = \Gamma_-$ and thus $\tilde{\Gamma}_c = 0$. This crucial difference results in the fact that only in the CB case there is dissipative coupling between the oscillators, as we can see writing down the equations of motion for the expectation values.

C.2 Equations of motion for the first and second moments

The equations of motion for the first moments read:

$$\frac{d}{dt}\langle \hat{x}_j \rangle = \langle \hat{p}_j \rangle - \frac{\tilde{\Gamma}_j}{2}\langle \hat{x}_j \rangle - \frac{\tilde{\Gamma}_c}{2}\langle \hat{x}_{k\neq j} \rangle, \tag{C.4}$$

$$\frac{d}{dt}\langle \hat{p}_j \rangle = -\omega_j^2 \langle \hat{x}_j \rangle - \lambda \langle \hat{x}_{k\neq j} \rangle - \frac{\tilde{\Gamma}_j}{2}\langle \hat{p}_j \rangle - \frac{\tilde{\Gamma}_c}{2}\langle \hat{p}_{k\neq j} \rangle, \tag{C.5}$$

while for the second moments we have:

$$\begin{aligned}\frac{d}{dt}\langle \hat{x}_j \hat{x}_k \rangle =& \frac{1}{2}\langle \{\hat{p}_j, \hat{x}_k\} + \{\hat{p}_j, \hat{x}_k\} \rangle - \frac{\tilde{\Gamma}_c}{2}\langle \hat{x}_j \hat{x}_j + \hat{x}_k \hat{x}_k \rangle (1-\delta_{jk}) \\ &- \frac{(\tilde{\Gamma}_j + \tilde{\Gamma}_k)}{2}\langle \hat{x}_j \hat{x}_k \rangle - \tilde{\Gamma}_c \langle \hat{x}_j \hat{x}_{l\neq j} \rangle \delta_{jk} + \frac{\tilde{D}_j^{(p)}}{2}\delta_{jk} + \frac{\tilde{D}_c^{(p)}}{2}(1-\delta_{jk}),\end{aligned} \tag{C.6}$$

$$\begin{aligned}\frac{d}{dt}\langle \hat{p}_j \hat{p}_k \rangle =& -\frac{\omega_j^2}{2}\langle \{\hat{p}_k, \hat{x}_j\} \rangle - \frac{\omega_k^2}{2}\langle \{\hat{p}_j, \hat{x}_k\} \rangle - \lambda \langle \{\hat{p}_j, \hat{x}_{l\neq j}\} \rangle \delta_{jk} \\ &- \lambda \langle \hat{x}_j \hat{p}_j + \hat{x}_k \hat{p}_k \rangle (1-\delta_{jk}) - \frac{\tilde{\Gamma}_c}{2}\langle \hat{p}_j \hat{p}_j + \hat{p}_k \hat{p}_k \rangle (1-\delta_{jk}) \\ &- \frac{(\tilde{\Gamma}_j + \tilde{\Gamma}_k)}{2}\langle \hat{p}_j \hat{p}_k \rangle - \tilde{\Gamma}_c \langle \hat{p}_j \hat{p}_{l\neq j} \rangle \delta_{jk} + \frac{\tilde{D}_j^{(x)}}{2}\delta_{jk} + \frac{\tilde{D}_c^{(x)}}{2}(1-\delta_{jk}),\end{aligned} \tag{C.7}$$

$$\begin{aligned}\frac{d}{dt}\langle \{\hat{x}_j, \hat{p}_k\} \rangle =& \langle \hat{p}_j \hat{p}_k \rangle - 2\omega_k^2 \langle \hat{x}_j \hat{x}_k \rangle - 2\lambda \langle \hat{x}_j \hat{x}_k \rangle \\ &- \frac{(\tilde{\Gamma}_j + \tilde{\Gamma}_k)}{2}\langle \{\hat{x}_j, \hat{p}_k\} \rangle - \frac{\tilde{\Gamma}_c}{2}\langle \{\hat{x}_j, \hat{p}_{l\neq j}\} + \{\hat{p}_j, \hat{x}_{l\neq j}\} \rangle \delta_{jk} \\ &- \frac{\tilde{\Gamma}_c}{2}\langle \{\hat{x}_j, \hat{p}_j\} + \{\hat{p}_k, \hat{x}_k\} \rangle (1-\delta_{jk}).\end{aligned} \tag{C.8}$$

Therefore, as anticipated, cross-diffusion terms do not lead to dissipative coupling of the oscillator. Then, only if $\tilde{\Gamma}_c \neq 0$, i.e. only for the CB scenario, we have dissipative coupling between the oscillators, which is the hallmark of collective dissipation. Moreover, from this set of equations it is readily apparent that the dynamics is easier to understand in the normal mode basis.

APPENDIX D

Noiseless modes in small-world networks and other models

This appendix contains additional details and results supplementing what is presented in chapter 3. In particular, we consider different Hamiltonians and even a different type of complex networks: that of Small-world networks. We also present additional results for Erdős-Rényi networks.

D.1 Noiseless modes for other Hamiltonians

In this section[1] we consider two possible variations of the Hamiltonian presented in Eq. (3.23), analyzing differences that might arise in the results of abundance of NSs discussed in chapter 3.

D.1.1 Spring-like coupling

The system Hamiltonian considering spring-like couplings:

$$\hat{H}_S = \frac{1}{2}\sum_{i=1}^{N}\left(\hat{p}_i^2 + \omega_0^2\hat{q}_i^2\right) + \sum_{i=1}^{N}\sum_{j=1}^{N}\lambda_{ij}(\hat{q}_i - \hat{q}_j)^2, \tag{D.1}$$

can be written as the sum of the following matrices:

$$\hat{H}_{ij}^d = \frac{1}{2}\left(\hat{p}_i^2 + \omega_0^2\hat{q}_i^2\right)\delta_{ij}, \tag{D.2}$$

$$\hat{H}_{ij}^c = \left[\alpha_i\delta_{ij} - \lambda_{ij}(1-\delta_{ij})\right]\hat{q}_i\hat{q}_j. \tag{D.3}$$

where $\alpha_i = \sum_j \lambda_{ij}$. When studying ER random networks described by spring-like couplings, the only part of the Hamiltonian that changes among different realizations is (D.3). Moreover as $\hat{H}^d$ is proportional to the identity, it is not involved in shaping the normal modes of the system. Then, with respect to the eigenvectors, we only need to diagonalize matrix

[1] The following three sections have been adapted from the supplementary material of Ref. [2].

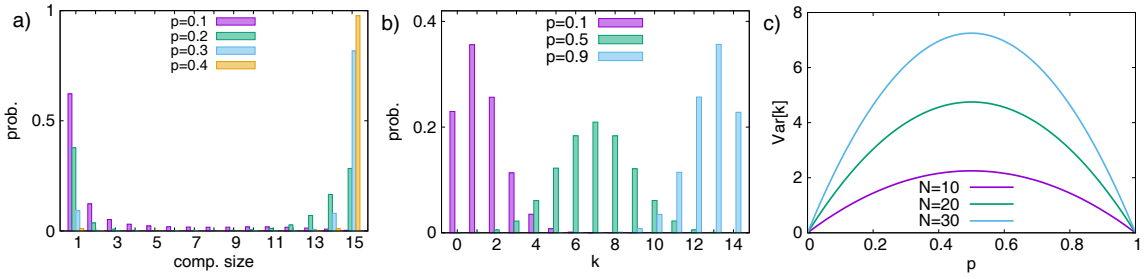

Figure D.1: a) Probability distribution of component sizes for ER networks with $N = 15$ and different values of p. b) Degree distribution for $N = 15$ and different values of p. c) Variance of the degree distribution varying p and for different network sizes.

(D.3). Notice that this matrix has always the property that the sum of the elements of each row or each column takes the same constant value (zero in this case), and thus it is a Laplacian matrix. For this type of matrix, the center of mass mode is always an eigenvector and thus the rest of them are perpendicular to it and decoherence free. It then follows the remarkable fact that systems described by Hamiltonian (D.1) have always $N-1$ NSs whatever is the underlying topology.

D.1.2 Tight-binding model

The tight-binding model describes a different class of systems to those of Eq. (3.23) of the main text, or of Eq. (D.1), in which the oscillators interact only by exchanging excitations. In the case of *uniform* parameters the system is described by the following Hamiltonian ($\hbar = 1$):

$$\hat{\mathcal{H}}_{TB} = \sum_{i=1}^{N}(\tilde{\omega}_0 + k_m)\hat{a}_i^\dagger \hat{a}_i - \sum_{i=1}^{N}\sum_{j=1}^{N}\tilde{\lambda}_{ij}(1-\delta_{ij})(\hat{a}_i^\dagger \hat{a}_j + \hat{a}_j^\dagger \hat{a}_i), \tag{D.4}$$

where $\hat{a}_j^\dagger(\hat{a}_j)$ are the creation (annihilation) operators of oscillator j and $\tilde{\lambda}_{ij} = \tilde{\lambda}$ or 0. In this case, we have also introduced the parameter k_m to ensure positive eigenvalues, where k_m is defined as the maximum degree of the network (for a given realization) times $\tilde{\lambda}$. Then we can see that despite the parameters and the type of interaction between the nodes is different from Eq. (3.23) and (3.32), the adjacency matrix is the same for both models, if the underlying networks are the same. This implies that both models have the same eigenvectors and the results about the NSs for uniform parameters of chapter 3 apply to both of them. On the other hand, for inhomogeneous problems in which there are *nonuniform* frequencies and couplings, this does not hold and some quantitative difference might arise even if the same main qualitative results are expected.

D.2 Topology of Erdős-Rényi random networks

In this section we consider in more detail two aspects of the topology of ER networks: the component size distribution and the degree distribution, which complement the discussions presented in chapter 3.

D.2.1 Component size distribution

When p increases, networks move from a topological regime in which they are composed of many small components to a connected regime in which there is a single component. In Figure 3.7 (a) it can be observed that the $\tilde{p}_c$ for which $P_{conn}(p, N) = 1/2$, diminishes with the size of the network. In particular for $N = 15$ we have $\tilde{p}_c \approx 0.23$. In Figure D.1 we plot

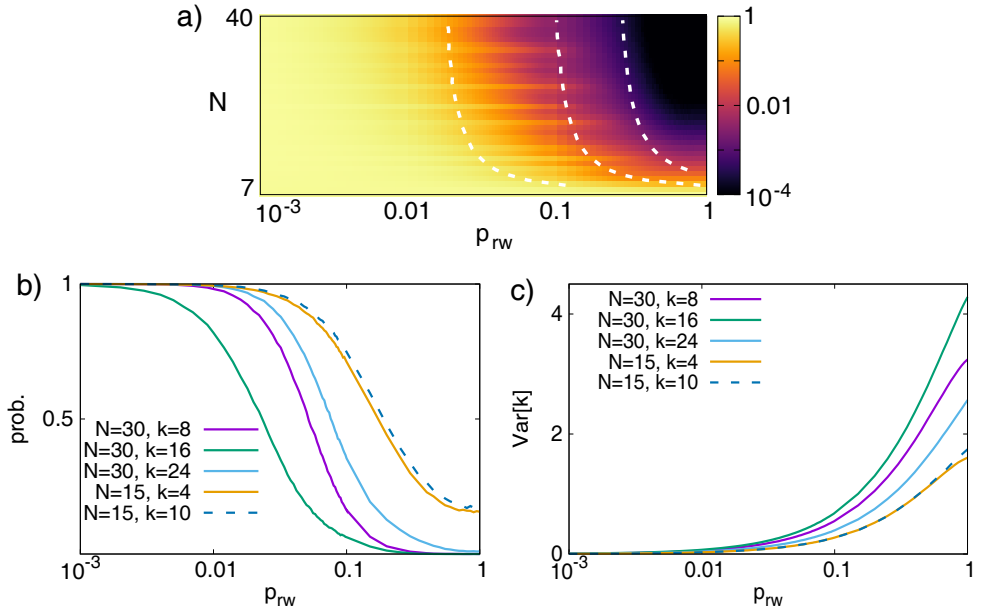

Figure D.2: a) Fraction of noiseless modes out of the total varying the size N and rewiring probability p_{rw}, with $k = 6$. White dashed lines correspond to constant contours of the variance of the degree distribution, where the variance increases from the leftmost to the rightmost contour. Probability to find at least a noiseless normal mode for Small-world networks (b) and variance of the degree distribution (c), varying the rewiring probability, p_{rw}, and for different network sizes, N, and degrees, k, of the initial ring network.

some examples of the component size distribution for $N = 15$ and p below and above the threshold one, $\tilde{p}_c$, in order to illustrate how the network connectedness evolves. From this figure it can be appreciated that for small p, networks are composed mainly by uncoupled oscillators, while as p increases, the probability to find one big component spanning all the network increases progressively.

D.2.2 Degree distribution

The degree distribution for an ER network is known to follow a binomial distribution [272], that is the probability of an oscillator to be coupled to k other oscillators is:

$$P_k = \binom{N-1}{k} p^k (1-p)^{N-1-k}, \tag{D.5}$$

and thus the variance of such distribution is given by:

$$\mathrm{Var}[k] = (N-1)\, p(1-p). \tag{D.6}$$

In Fig. D.2 we have plotted these two quantities: in D.1 (b) the degree distribution for $N = 15$ and different p's, while in D.1 (c) the variance for different network sizes. From these figures we can observe that the width of the degree distribution increases as p approaches $p = 0.5$, and also as the size of the network increases.

D.3 Noiseless modes in Small-world random networks

In this section we consider the model of small-world (SW) networks by Watts and Strogatz [273]. The starting point of this model is a degree regular ring network in which each node is coupled to its k nearest neighbors, together with the definition of a stochastic rewiring process. In the first step of this process, nodes are considered successively in a clockwise

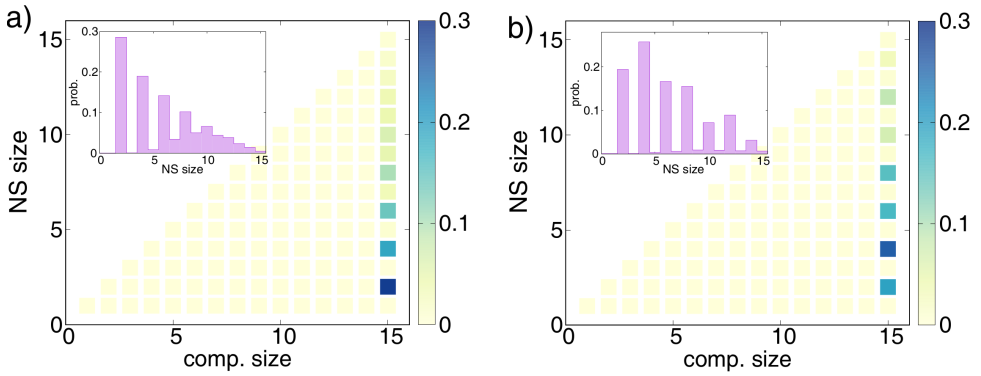

Figure D.3: In color: probability that a NS of a given size (vertical axis) is located in a component of a particular size (horizontal axis). Inset: noiseless mode size distribution. a) Parameter values: $N = 15$, $p_{rw} = 0.5$, $k = 4$. b) Parameter values: $N = 15$, $p_{rw} = 0.5$, $k = 12$.

sense and with probability p_{rw} the connection with its clockwise nearest neighbor is rewired to a randomly chosen node (from a uniform distribution). Whenever the new connection coincides with an already existing one no change is made and the original link remains. After all nearest neighbor connections have been considered, the process is repeated for next to nearest connections. In the same fashion, the remaining longer range connections are successively addressed until all links of the original ring network have been considered in a rewiring step once. Thus as p_{rw} increases, the initial regular lattice is progressively disordered, and in the limit of $p_{rw} = 1$ all couplings of the network are randomly rewired.

D.3.1 Noiseless mode abundance and structure

The fact that in this model we can progressively disorder a regular network (which is in a shifted Laplacian form and thus always has $N-1$ noiseless modes[2] facilitates the analysis of how topological disorder affects the abundance of noiseless modes. As discussed in the main text, it seems that for increasing disorder in network topology the abundance of normal modes diminishes. In figure D.2 (a) we plot the fraction of noiseless modes out of the total varying the rewiring probability and the size of the networks. The initial degree of the ring network is fixed to $k = 6$. In this colormap, contour lines with constant variance of the degree distribution are also plotted (white dashed lines, inner contours correspond to higher variances). In figure D.2 (b) we plot the probability to find at least a noiseless mode when varying the rewiring probability p_{rw}, and for different network parameters N and k. In Fig. D.2 (c) we plot the variance of the degree distribution for the same parameters as in Fig.D.2 (b), and varying again the rewiring probability.

From these plots we see that the probability to find noiseless modes diminishes when randomizing the network by rewiring. The observed abundance of noiseless modes in small-word networks is in agreement with our results in ER networks: the presence of noiseless modes is degraded when departing from topologically ordered configurations, and in small networks there is a finite probability to observe them for all values of p_{rw}. We observe that the results depend also on the initial degree, although the behaviour is qualitatively the same [Fig. D.2 (b)].

Finally we also analyze the structure of the noiseless modes present in this network model. In Fig. D.3 we consider SW networks with $N = 15$, $p_{rw} = 0.5$, $k = 4$ (a), and $k = 12$ (b). Here, we observe again that noiseless modes spanning over an odd number

[2]This follows from Hamiltonian (3.23) and parameters (3.32); since in the initial regular lattice (for $p_{rw} = 0$), every node has the same degree k_m and hence the Hamiltonian matrix can be split in a diagonal matrix and a Laplacian matrix, similarly to Hamiltonian (D.1) in which (D.3) is of the Laplacian form.

of oscillators are strongly suppressed. Moreover, we see that in the case of $k = 12$ this asymmetry is present also for big noiseless modes. Finally, in the case of Small-world networks and for these parameter values, we see that they are composed by a single component.

D.4 Noiseless eigenvectors in the connected regime.

In this section, we write down a general condition by which the noiseless eigenvectors of a motif (like those of Fig. 3.6 (b) or Fig. D.4) can become noiseless eigenvectors of the whole network in which the motif is embedded. This enables us to gain insight on why the NS size distributions in the poorly connected regime and in the very connected one are so similar (Fig. 3.8). Importantly, in all the section we assume uniform frequencies so that this constant diagonal term does not influence the shape of the eigenvectors and it can be factorized out.

General condition. Suppose we have a network whose edges are encoded in the adjacency matrix A, and we divide the set of nodes in two subsets: the motif M, and the rest of the network R. Define also the adjacency matrix describing the internal structure of the motif as A_M (i.e. edges amongst the nodes of M). Assume $\vec{u}$ is a noiseless eigenvector of the motif; i.e. $A_M\vec{u} = \alpha\vec{u}$ where $\sum_{j\in M} u_j = 0$, and u_j are the vector entries. Now, we define the vector $\vec{v}$ as $v_j = u_j \ \forall j \in M$, and $v_j = 0 \ \forall j \in R$, and we establish the conditions under which $\vec{v}$ is a noiseless eigenvector of the whole network adjacency matrix A with the same eigenvalue α. First, we divide M in n subsets m_k (each node being only in one subset), such that we can rewrite $\sum_{j\in M} u_j = \sum_{k=1}^{n}\sum_{j\in m_k} u_j$. These subsets are chosen so that $\vec{u}$ is noiseless within each subset, i.e. $\sum_{j\in m_k} u_j = 0 \ \forall m_k$. Then, if the connections between any node in R with the nodes of M only depend on the subset m_k and not on the particular node j, i.e. $\lambda_{ij} = \lambda_i^{(m_k)} \ \forall i \in R$ and $\forall j \in m_k$, $\vec{v}$ is a noiseless eigenvector of A with eigenvalue α.

Proof. We first prove that $\vec{v}$ is noiseless: $\sum_j v_j = \sum_{j\in M} v_j + \sum_{j\in R} v_j = \sum_{j\in M} u_j + 0 = \sum_{k=1}^{n}\sum_{j\in m_k} u_j = 0$. Now we prove it is an eigenvector. Without loss in generality we can write $A\vec{v} = \vec{w}$ with $\sum_j \lambda_{ij}v_j = w_i$, and we want to show that $w_i = \alpha v_i$. First assume $i \in R$, then $\sum_j \lambda_{ij}v_j = \sum_{j\in M} \lambda_{ij}u_j$ since $v_j = 0 \ \forall j \in R$ and $v_j = u_j \ \forall j \in M$. Then, we can factorize this sum in terms of the subsets, i.e. $\sum_{j\in M} \lambda_{ij}u_j = \sum_{k=1}^{n}\sum_{j\in m_k} \lambda_{ij}u_j$. Finally, apply the property of identical coupling between a subset and the nodes out of the motif: $\sum_{k=1}^{n}\sum_{j\in m_k} \lambda_{ij}u_j = \sum_{k=1}^{n} \lambda_i^{(m_k)} \sum_{j\in m_k} u_j = 0$, where we have also used the subset noiseless condition, i.e. $\sum_{j\in m_k} u_j = 0 \ \forall m_k$. Hence, $w_i = \alpha v_i = 0 \ \forall i \in R$. Now assume $i \in M$, using $v_j = 0 \ \forall j \in R$ and $v_j = u_j \ \forall j \in M$, we obtain $\sum_j \lambda_{ij}v_j = \sum_{j\in M} \lambda_{ij}u_j$ which is just row i of the matrix product $A_M\vec{u}$, and thus, using the definition of $\vec{u}$, we have $\sum_{j\in M} \lambda_{ij}u_j = \alpha u_i$. Therefore, we have proved that $w_i = \alpha v_i \ \forall i$, i.e. that $\vec{v}$ is a noiseless eigenvector of the whole network with eigenvalue α. ■

Symmetric case. It is insightful to consider the very symmetric case in which $n = 1$. Then, the edges of nodes of R with nodes of M are the same for all nodes of the motif, i.e. $\lambda_{ij} = \lambda_i \ \forall i \in R$ and $\forall j \in M$, and we see that for each noiseless eigenvector of A_M we can construct the corresponding noiseless eigenvector of A.

The results written above rely on a subset of nodes having the same connections with another subset of nodes, which intuitively seems more plausible when networks tend to be more homogeneous (small variance of the degree distribution). In table D.1 we have written down all noiseless eigenvectors of size 4, which are not degenerate, and that can be found in motifs of size 4 and 5 (the corresponding ones shown in Fig. 3.6 (b) and Fig. D.4). It is illustrative to observe that some of the motifs of 5 oscillators can be seen as motifs of size 4 properly connected (as dictated by the above conditions) to an extra node, and

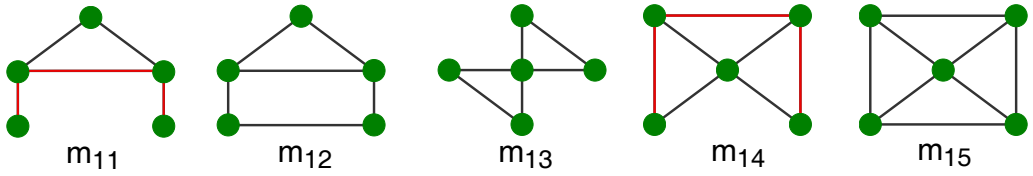

Figure D.4: Motifs of 5 oscillators that contribute with non-degenerate noiseless eigenvectors of size 4. Motif m_8 also contributes but is already included in figure 3.6 (b) of the main text. The nodes are labeled as 1, 2, 3, 4 and 5 from left to right and from top to bottom. As illustrative examples, motifs m_{11} and m_{14} can be considered as motif m_4 (in red) connected to an extra node in such a way that they satisfy the general condition (m_{11}) and also the symmetric case (m_{14}).

thus the same noiseless eigenvector and eigenvalue is found (see caption of figure D.4 and table D.1). In fact, we have checked the consistency of these theoretical predictions with the results of numerical simulations. In table D.1 we have listed all motifs of size ≤ 5 that contribute with non-degenerate noiseless eigenvectors of size 4, and their corresponding eigenvalues (assuming $\lambda = -1$ and zero frequencies). Then, we have analyzed numerically the eigenvalues associated to the noiseless eigenvectors of size 4, for ER networks (we have generated a set of 10^5 networks) of size $N = 15$ and for various choices p (not shown here), finding the eigenvalues to correspond exclusively to the ones listed in table D.1. The same has been done for $NS = 2$, for which the predicted eigenvalues (by looking to motifs of size up to ≤ 5) are $\alpha = 0$ and $\alpha = 1$, also finding numerical agreement. In the case of $NS = 3$, both numerics and theory predict that there are no non-degenerate noiseless eigenvectors. The analysis of larger NSs becomes complicated as the number of possible motifs of bigger size increases significantly. The observed consistency between theory and numerics suggests that NSs in very connected networks come from the NSs of the small motifs properly embedded within the rest of the network.

Motif	Noiseless eigenvectors	Eigenvalues
m_4	$\vec{v}_1 = (-1, 1.62, -1.62, 1)$ $\vec{v}_2 = (-1, -0.62, 0.62, 1)$	$\alpha_1 = 1.62$ $\alpha_2 = -0.62$
m_6	$\vec{v}_1 = (1, -1, 1, -1)$	$\alpha_1 = 2$
m_8	$\vec{v}_1 = (-1, 1, 0, -1, 1)$ $\vec{v}_2 = (-1, -1, 0, 1, 1)$	$\alpha_1 = 1$ $\alpha_2 = -1$
m_{11}	$\vec{v}_1 = (0, 1.62, -1.62, -1, 1)$ $\vec{v}_2 = (0 - 0.62, 0.62, -1, 1)$	$\alpha_1 = 1.62$ $\alpha_2 = -0.62$
m_{12}	$\vec{v}_1 = (0, -1, 1, -1, 1)$ $\vec{v}_2 = (0, -1, -1, 1, 1)$	$\alpha_1 = 2$ $\alpha_2 = 0$
m_{13}	$\vec{v}_1 = (-1, 1, 0, -1, 1)$	$\alpha_1 = -1$
m_{14}	$\vec{v}_1 = (1.62, -1.62, 0, -1, 1)$ $\vec{v}_2 = (-0.62, 0.62, 0, -1, 1)$	$\alpha_1 = 1.62$ $\alpha_2 = -0.62$
m_{15}	$\vec{v}_1 = (-1, 1, 0, -1, 1)$	$\alpha_1 = 2$

Table D.1: Noiseless eigenvectors of size 4 that are not degenerate and that come from motifs of size 4 and 5. The entries of the vectors are ordered according to how nodes have been ordered in figures 3.6(b) and D.4. The associated eigenvalues are displayed in the third column, where we have assumed zero frequencies and $\lambda = -1$. Following the illustrative example of Fig. D.4, we see that the noiseless eigenvectors of m_4 appear again in m_{11} and m_{14}, being localized in the red part of the motif, and with the same eigenvalue, according to what is predicted by the general condition derived in the text.

APPENDIX E

Dynamics of harmonic oscillators and spins in the presence of coalescence

In this appendix we present some additional details and results corresponding to chapter 4. The following sections have been mainly adapted from the appendices and supplemental material of Refs. [3, 7].

E.1 Additional details for the array of harmonic oscillators

In the following, we present the details on how to solve the equations of motion with a general nonzero driving term, as well as on how to solve the equations for the amplitude two-time correlations.

E.1.1 Solution for the first moments with general driving

The starting point are the equations for the first moments with nonzero driving in the site basis:

$$\frac{d}{dt}\langle\hat{a}_n\rangle = -\gamma_a\langle\hat{a}_n\rangle - i\lambda\big(\langle\hat{b}_{n-1}\rangle(1-\delta_{n,1}) + \langle\hat{b}_n\rangle\big) + \alpha_n(t), \tag{E.1}$$

$$\frac{d}{dt}\langle\hat{b}_n\rangle = -\gamma_b\langle\hat{b}_n\rangle - i\lambda\big(\langle\hat{a}_n\rangle + \langle\hat{a}_{n+1}\rangle(1-\delta_{n,N})\big) + \beta_n(t), \tag{E.2}$$

with $n \in [1, N]$. Using the same orthogonal transformation defined in the main text, we can block-diagonalize this system of equations. In particular, the driving in the k-basis is defined as $\vec{\tilde{F}} = \mathsf{P}^T\vec{F}$, with the k-driving terms $\alpha_{k_l}(t)$ and $\beta_{k_l}(t)$ related to their direct-space amplitudes $\alpha_n(t)$ and $\beta_n(t)$ analogously to the k-modes of Eq. (4.6) of the main text. Then Eqs. (E.1) and (E.2) transform to:

$$\frac{d}{dt}\langle\hat{a}_{k_l}\rangle = -\gamma_a\langle\hat{a}_{k_l}\rangle - i\lambda_{k_l}\langle\hat{b}_{k_l}\rangle + \alpha_k(t), \tag{E.3}$$

$$\frac{d}{dt}\langle\hat{b}_{k_l}\rangle = -\gamma_b\langle\hat{b}_{k_l}\rangle - i\lambda_{k_l}\langle\hat{a}_{k_l}\rangle + \beta_k(t). \tag{E.4}$$

Assuming that the Laplace transform of these general driving terms exists, the general solution in the s-domain is given by:

$$\langle \hat{a}_{k_l}(s)\rangle = \frac{(s+\gamma_b)[\langle \hat{a}_{k_l}\rangle_0 + \alpha_{k_l}(s)] - i\lambda_{k_l}[\langle \hat{b}_{k_l}\rangle_0 + \beta_{k_l}(s)]}{(s+\Omega^+_{k_l})(s+\Omega^-_{k_l})}, \tag{E.5}$$

$$\langle \hat{b}_{k_l}(s)\rangle = \frac{(s+\gamma_a)[\langle \hat{b}_{k_l}\rangle_0 + \beta_{k_l}(s)] - i\lambda_{k_l}[\langle \hat{a}_{k_l}\rangle_0 + \alpha_{k_l}(s)]}{(s+\Omega^+_{k_l})(s+\Omega^-_{k_l})}, \tag{E.6}$$

which display the same dynamical regimes as the homogeneous case determined by $\Omega^{\pm}_{k_l}$. From these general solutions we can obtain the particular case of periodic driving presented in the main text in Eqs. (4.21) and (4.22).

E.1.2 General solution for the two-time correlation functions

In this section we study the two-time correlation functions of the type $\langle \hat{c}^\dagger_n(t)\hat{a}_{n'}(t+\tau)\rangle$ and $\langle \hat{c}^\dagger_n(t)\hat{b}_{n'}(t+\tau)\rangle$, where $\hat{c}^\dagger_n$ can be either $\hat{a}^\dagger_n$ or $\hat{b}^\dagger_n$. The quantum regression theorem states that the time evolution in τ of these correlations is given by the same matrix M introduced in the main text (see chapter 2 or [59]), i.e. $\partial_\tau \vec{v}_n(t,\tau) = \mathsf{M}\vec{v}_n(t,\tau)$ for any fixed n, with:

$$\vec{v}_n(t,\tau) = \begin{pmatrix} \langle \hat{c}^\dagger_n(t)\hat{a}_1(t+\tau)\rangle \\ \langle \hat{c}^\dagger_n(t)\hat{b}_1(t+\tau)\rangle \\ \vdots \\ \langle \hat{c}^\dagger_n(t)\hat{a}_N(t+\tau)\rangle \\ \langle \hat{c}^\dagger_n(t)\hat{b}_N(t+\tau)\rangle \end{pmatrix}. \tag{E.7}$$

Hence, the time evolution of these correlations can be obtained from that of the first moments with the second moments $\langle \hat{c}^\dagger_n(t)\hat{a}_{n'}(t)\rangle$ and $\langle \hat{c}^\dagger_n(t)\hat{b}_{n'}(t)\rangle$ as initial condition. Proceeding as before, we write this system of equations in a block-diagonal form as $\partial_\tau \vec{\tilde{v}}_n(t,\tau) = \mathsf{P}^T\mathsf{M}\mathsf{P}\vec{\tilde{v}}_n(t,\tau)$ with $\vec{\tilde{v}}_n(t,\tau) = \mathsf{P}^T\vec{v}_n(t,\tau)$:

$$\vec{\tilde{v}}_n(t,\tau) = \begin{pmatrix} \langle \hat{c}^\dagger_n(t)\hat{a}_{k_1}(t+\tau)\rangle \\ \langle \hat{c}^\dagger_n(t)\hat{b}_{k_1}(t+\tau)\rangle \\ \vdots \\ \langle \hat{c}^\dagger_n(t)\hat{a}_{k_N}(t+\tau)\rangle \\ \langle \hat{c}^\dagger_n(t)\hat{b}_{k_N}(t+\tau)\rangle \end{pmatrix}. \tag{E.8}$$

Thus, the system of equations in the k-basis is given by:

$$\partial_\tau\langle \hat{c}^\dagger_n(t)\hat{a}_{k_l}(t+\tau)\rangle = -\gamma_a\langle \hat{c}^\dagger_n(t)\hat{a}_{k_l}(t+\tau)\rangle - i\lambda_{k_l}\langle \hat{c}^\dagger_n(t)\hat{b}_{k_l}(t+\tau)\rangle, \tag{E.9}$$

$$\partial_\tau\langle \hat{c}^\dagger_n(t)\hat{b}_{k_l}(t+\tau)\rangle = -\gamma_b\langle \hat{c}^\dagger_n(t)\hat{b}_{k_l}(t+\tau)\rangle - i\lambda_{k_l}\langle \hat{c}^\dagger_n(t)\hat{a}_{k_l}(t+\tau)\rangle, \tag{E.10}$$

which is the same, up to the involved expected values, as the one for the first moments given in Eqs. (4.11) and (4.12) of the main text. In consequence, the solutions are given by Eqs. (4.16)-(4.18) of the main text replacing $\langle \hat{a}_{k_l}\rangle$ by $\langle \hat{c}^\dagger_n(t)\hat{a}_{k_l}(t+\tau)\rangle$, $\langle \hat{b}_{k_l}\rangle$ by $\langle \hat{c}^\dagger_n(t)\hat{b}_{k_l}(t+\tau)\rangle$, changing t by τ in the right hand side of the equations, and taking the second moments $\tilde{v}_n(t,0)$ as initial condition.

Despite our approach is general, we now focus on these correlation functions evaluated in the stationary state, which yield the (asymptotic) emission spectrum of the system. We now define the spectrum of correlations $\vec{v}_n(\Delta) = \lim_{t\to\infty}\int_0^\infty d\tau \vec{v}_n(t,\tau)e^{i\Delta\tau}$ with $\Delta = \omega - \omega_0$. This spectrum is obtained recombining the expressions in the k-basis as $\langle \hat{c}^\dagger_n(t)\hat{a}_{n'}(t+\tau)\rangle = \sum_{l=1}^N \mathcal{S}^{(a)}_{n',k_l}\langle \hat{c}^\dagger_n(t)\hat{a}_{k_l}(t+\tau)\rangle$ and $\langle \hat{c}^\dagger_n(t)\hat{b}_{n'}(t+\tau)\rangle = \sum_{l=1}^N \mathcal{S}^{(b)}_{n',k_l}\langle \hat{c}^\dagger_n(t)\hat{b}_{k_l}(t+\tau)\rangle$. In the

following, we write down the general solutions in the k-basis Fourier transformed and for each dynamical regime from which the particular case of the main text can be obtained. In the single-frequency regime we have:

$$\begin{aligned}\langle \hat{c}_n^\dagger \hat{a}_{k_l}(\Delta)\rangle = \frac{\langle \hat{c}_n^\dagger \hat{a}_{k_l}\rangle_{ss}}{(\gamma_{k_l}^+ - \gamma_{k_l}^-)}\left[\frac{(\gamma_{k_l}^+ - \gamma_b)(\gamma_{k_l}^+ + i\Delta)}{\Delta^2 + \gamma_{k_l}^{+2}} - \frac{(\gamma_{k_l}^- - \gamma_b)(\gamma_{k_l}^- + i\Delta)}{\Delta^2 + \gamma_{k_l}^{-2}}\right] \\ + i\frac{\lambda_{k_l}\langle \hat{c}_n^\dagger \hat{b}_{k_l}\rangle_{ss}}{(\gamma_{k_l}^+ - \gamma_{k_l}^-)}\left[\frac{\gamma_{k_l}^+ + i\Delta}{\Delta^2 + \gamma_{k_l}^{+2}} - \frac{\gamma_{k_l}^- + i\Delta}{\Delta^2 + \gamma_{k_l}^{-2}}\right].\end{aligned} \tag{E.11}$$

At the EP:

$$\langle \hat{c}_n^\dagger \hat{a}_{k_l}(\Delta)\rangle = \langle \hat{c}_n^\dagger \hat{a}_{k_l}\rangle_{ss}\left[\frac{\frac{\bar{\gamma}}{2} + i\Delta}{\Delta^2 + \frac{\bar{\gamma}^2}{4}} + \frac{\gamma_b - \gamma_a}{2}\frac{\frac{\bar{\gamma}^2}{4} - \Delta^2 + i\Delta\bar{\gamma}}{(\Delta^2 + \frac{\bar{\gamma}^2}{4})^2}\right] - i\lambda_{k_l}\langle \hat{c}_n^\dagger \hat{b}_{k_l}\rangle_{ss}\left[\frac{\frac{\bar{\gamma}^2}{4} - \Delta^2 + i\Delta\bar{\gamma}}{(\Delta^2 + \frac{\bar{\gamma}^2}{4})^2}\right], \tag{E.12}$$

While in the two-frequency regime:

$$\begin{aligned}\langle \hat{c}_n^\dagger \hat{a}_{k_l}(\Delta)\rangle = \frac{\langle \hat{c}_n^\dagger \hat{a}_{k_l}\rangle_{ss}}{2i\nu_{k_l}}\left[\frac{(\frac{\gamma_b - \gamma_a}{2} + i\nu_{k_l})(\frac{\bar{\gamma}}{2} + i(\Delta + \nu_{k_l}))}{\frac{\bar{\gamma}^2}{4} + (\Delta + \nu_{k_l})^2} - \frac{(\frac{\gamma_b - \gamma_a}{2} - i\nu_{k_l})(\frac{\bar{\gamma}}{2} + i(\Delta - \nu_{k_l}))}{\frac{\bar{\gamma}^2}{4} + (\Delta - \nu_{k_l})^2}\right] \\ - \frac{\lambda_{k_l}\langle \hat{c}_n^\dagger \hat{b}_{k_l}\rangle_{ss}}{2\nu_{k_l}}\left[\frac{\frac{\bar{\gamma}}{2} + i(\Delta + \nu_{k_l})}{\frac{\bar{\gamma}^2}{4} + (\Delta + \nu_{k_l})^2} - \frac{\frac{\bar{\gamma}}{2} + i(\Delta - \nu_{k_l})}{\frac{\bar{\gamma}^2}{4} + (\Delta - \nu_{k_l})^2}\right].\end{aligned} \tag{E.13}$$

Notice that the expressions for $\langle \hat{c}_n^\dagger \hat{b}_{k_l}(\Delta)\rangle$ can be obtained from Eqs. (E.11) to (E.13) exchanging the labels $a \leftrightarrow b$ and the stationary second moments $\langle \hat{c}_n^\dagger \hat{a}_{k_l}\rangle_{ss} \leftrightarrow \langle \hat{c}_n^\dagger \hat{b}_{k_l}\rangle_{ss}$. Moreover, these stationary second moments can be obtained from Eqs. (4.41)-(4.43) of the main text as $\langle \hat{c}_n^\dagger \hat{a}_{k_l}\rangle_{ss} = \sum_{m=1}^N \mathcal{S}^{(a)}_{m,k_l}\langle \hat{c}_n^\dagger \hat{a}_m\rangle_{ss}$ and $\langle \hat{c}_n^\dagger \hat{b}_{k_l}\rangle_{ss} = \sum_{m=1}^N \mathcal{S}^{(b)}_{m,k_l}\langle \hat{c}_n^\dagger \hat{b}_m\rangle_{ss}$.

E.2 Additional details for the spin system

In this section, we present the matrix representation of the Liouvillian together with some analytical expressions for the eigenvalues in some limiting cases. We also show an example of EPs in the Liouvillian block $\mathcal{L}_a$. Later, we derive the general expression for $\langle \hat{\sigma}^x_{1,2}(t)\rangle$, and the absorption spectrum in the absence of pumping.

E.2.1 Liouville representation of the master equation

The master equation (4.48) describing the evolution of $\hat{\rho}$ can be written in terms of the Liouvillian superoperator, $\mathcal{L}$. In the Liouville representation, the state of the system is represented by a vector of the Hilbert-Schmidt space $\mathcal{H} = \mathbb{C}^{16}$, and the Liouvillian is a non-Hermitian matrix $\bar{\bar{\mathcal{L}}}$ (see chapter 2 or Refs. [90, 269]). Then, the matrix representation of $\mathcal{L}$ is given by

$$\begin{aligned}\bar{\bar{\mathcal{L}}} = -i(\hat{H}\otimes\mathbb{1} - \mathbb{1}\otimes\hat{H}^\top) + \sum_{i,j=1}^{2}\gamma\big[\hat{\sigma}_i^-\otimes(\hat{\sigma}_j^+)^\top - (\hat{\sigma}_j^+\hat{\sigma}_i^-)\otimes\frac{\mathbb{1}}{2} - \frac{\mathbb{1}}{2}\otimes(\hat{\sigma}_j^+\hat{\sigma}_i^-)^\top\big] \\ + \sum_{i=1}^{2} w\big[\hat{\sigma}_i^+\otimes(\hat{\sigma}_i^-)^\top - (\hat{\sigma}_i^-\hat{\sigma}_i^+)\otimes\frac{\mathbb{1}}{2} - \frac{\mathbb{1}}{2}\otimes(\hat{\sigma}_i^-\hat{\sigma}_i^+)^\top\big].\end{aligned} \tag{E.14}$$

An important feature for this kind of system is that the Liouvillian matrix takes a block-diagonal form [90, 269]: $\bar{\bar{\mathcal{L}}} = \bigoplus_\mu \bar{\bar{\mathcal{L}}}_\mu$, with $\mu \in \{a, b, c, d, e\}$. Analogously, the Hilbert-Schmidt space $\mathcal{H}$ can be decomposed in these same blocks or subspaces $\mathcal{H} = \bigoplus_\mu \mathcal{H}_\mu$, each of which is spanned by the following basis elements: subspace $\mathcal{H}_a$ is spanned by $|eeee\rangle\!\rangle$, $|egeg\rangle\!\rangle$, $|egge\rangle\!\rangle$, $|geeg\rangle\!\rangle$, $|gege\rangle\!\rangle$, and $|gggg\rangle\!\rangle$; $\mathcal{H}_b$ by $|eeeg\rangle\!\rangle$, $|eege\rangle\!\rangle$, $|eggg\rangle\!\rangle$, and $|gegg\rangle\!\rangle$; $\mathcal{H}_c$ by

$|egee\rangle\!\rangle$, $|geee\rangle\!\rangle$, $|ggeg\rangle\!\rangle$, and $|ggge\rangle\!\rangle$; $\mathcal{H}_d$ by $|eegg\rangle\!\rangle$; and $\mathcal{H}_e$ by $|ggee\rangle\!\rangle$. Then, the different Liouvillian blocks read as

$$\bar{\bar{\mathcal{L}}}_a = \begin{pmatrix} -2\gamma & w & 0 & 0 & w & 0 \\ \gamma & -(\gamma+w) & -\frac{\gamma}{2}+is_{12} & -\frac{\gamma}{2}-is_{12} & 0 & w \\ \gamma & -\frac{\gamma}{2}+is_{12} & -(\gamma+w)-i\delta & 0 & -\frac{\gamma}{2}-is_{12} & 0 \\ \gamma & -\frac{\gamma}{2}-is_{12} & 0 & -(\gamma+w)+i\delta & -\frac{\gamma}{2}+is_{12} & 0 \\ \gamma & 0 & -\frac{\gamma}{2}-is_{12} & -\frac{\gamma}{2}+is_{12} & -(\gamma+w) & w \\ 0 & \gamma & \gamma & \gamma & \gamma & -2w \end{pmatrix}, \tag{E.15}$$

$$\bar{\bar{\mathcal{L}}}_b = \begin{pmatrix} -\frac{\Gamma_1}{2}-i\omega_2 & -\frac{\gamma}{2}+is_{12} & 0 & w \\ -\frac{\gamma}{2}+is_{12} & -\frac{\Gamma_1}{2}-i\omega_1 & w & 0 \\ \gamma & \gamma & -\frac{\Gamma_2}{2}-i\omega_2 & -\frac{\gamma}{2}-is_{12} \\ \gamma & \gamma & -\frac{\gamma}{2}-is_{12} & -\frac{\Gamma_2}{2}-i\omega_1 \end{pmatrix}, \tag{E.16}$$

where $\Gamma_1 = 3\gamma + w$ and $\Gamma_2 = \gamma + 3w$. $\bar{\bar{\mathcal{L}}}_c$ is the complex conjugate of $\bar{\bar{\mathcal{L}}}_b$, $\bar{\bar{\mathcal{L}}}_d = -(\gamma+w) - 2i\omega_0$, and $\bar{\bar{\mathcal{L}}}_e = (\bar{\bar{\mathcal{L}}}_d)^*$.

Analytical expressions for the eigenvalues. Generally the analytical expression for the eigenvalues is too cumbersome to be insightful; however, in some particular cases, simple analytical expressions can be found. In fact for $w/\gamma = 0$ the full eigenspectrum can be obtained [90]. The eigenvalues of $\bar{\bar{\mathcal{L}}}_b$, which are the relevant ones for our synchronization analysis, are:

$$\begin{aligned} \lambda_1^b &= -\frac{1}{2}[3\gamma + V^*] - i\omega_0, \quad \lambda_2^b = -\frac{1}{2}[3\gamma - V^*] - i\omega_0, \\ \lambda_3^b &= -\frac{1}{2}[\gamma + V] - i\omega_0, \quad \lambda_4^b = -\frac{1}{2}[\gamma - V] - i\omega_0, \end{aligned} \tag{E.17}$$

ordered with increasing real part and $V = \sqrt{(\gamma + 2is_{12})^2 - \delta^2}$. Notice that for $\delta = 0$ the real part of λ_4^b is zero. The appearance of purely imaginary eigenvalues corresponds to the existence of decoherence-free subspaces which enable the possibility of stationary synchronization [2, 93, 101]. It is also useful (and possible) to write down the eigenvalues for the case with $\delta/\gamma = 0$ and nonvanishing pumping, in which we have:

$$\begin{aligned} \lambda_1^b &= -\frac{1}{2}[3\gamma + 2w + \tilde{V}] - i\omega_0, \quad \lambda_2^b = -\frac{1}{2}[3\gamma + 2w - \tilde{V}] - i\omega_0, \\ \lambda_3^b &= -\gamma - \frac{w}{2} - i(\omega_0 + s_{12}), \quad \lambda_4^b = -\frac{3}{2}w - i(\omega_0 - s_{12}), \end{aligned} \tag{E.18}$$

with $\tilde{V} = \sqrt{(w^2 + \gamma^2 + 6w\gamma - 4s_{12}^2) + i4s_{12}(w-\gamma)}$.

E.2.2 EPs in $\bar{\bar{\mathcal{L}}}_a$

In this section we show an example of EP in $\bar{\bar{\mathcal{L}}}_a$. In this sector, and for the case $w \neq 0$, $s_{12} = 0$ and $\delta = 0$, there are three eigenvalues with simple expressions:

$$\lambda_1^a = 0, \quad \lambda_2^a = -(w+\gamma), \quad \lambda_3^a = -(w+\gamma), \tag{E.19}$$

while the remaining three are roots of the third order equation:

$$\lambda^3 + 4\lambda^2(w+\gamma) + \lambda(5w^2 + 10w\gamma + 4\gamma^2) + 2w^3 + 6w^2\gamma + 8w\gamma^2 = 0. \tag{E.20}$$

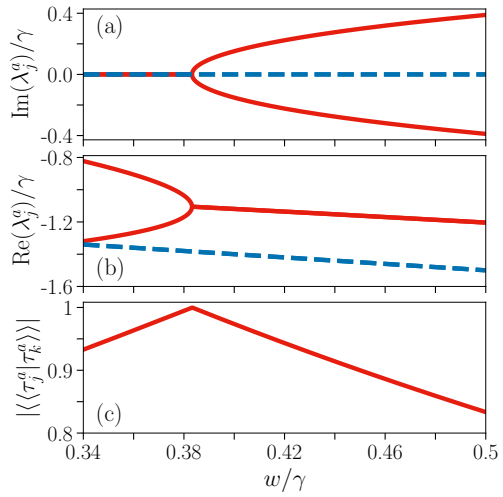

Figure E.1: (a) Imaginary part of the eigenvalues (eigenfrequencies) of $\bar{\bar{\mathcal{L}}}_a$, varying w/γ, for $\delta/\gamma = 0$, and $\omega_0/\gamma = 20$. In solid red the pair of eigenvalues that coalesce, in blue dashed lines the rest of eigenvalues. (b) The real part of the corresponding eigenvalues (decay rates). (c) Product of the corresponding pair of eigenvectors that coalesce. Notice that not all eigenvalues are visible, as we have adjusted the range of the plots to display clearly the EP.

Notice that here the eigenvalues are not ordered. Without the need of finding the solutions of Eq. (E.20), we can readily obtain important information. First notice that for $w = 0$ there is a second eigenvalue together with λ_1^a which is zero, and thus the stationary state is not unique. In fact, for $\delta = w = 0$, we have shown that there are pure imaginary eigenvalues in $\bar{\bar{\mathcal{L}}}_{b(c)}$, which represent the non-decaying oscillating coherences between the two steady states, which attain the possibility of stationary synchronization [2, 93, 90, 101]. Second, notice that as a third order equation can have either three real roots or one real root and two complex conjugate ones, the corresponding branching of eigenvalues resembles what has been discussed for $\bar{\bar{\mathcal{L}}}_{b(c)}$ and thus there could be an EP at the branching point. This turns out to be the case, as we show in Fig. E.1 in which at the point in which two roots become complex, the corresponding eigenvectors become parallel.

E.2.3 Dynamics of $\langle\hat{\sigma}_j^x(t)\rangle$

Here, we write down the formal solution for the dynamics of $\langle\hat{\sigma}_j^x(t)\rangle$ in terms of coefficients that depend on the eigenvalues and eigenvectors of $\bar{\bar{\mathcal{L}}}_{b(c)}$. Notice that as it depends on the diagonalization of $\bar{\bar{\mathcal{L}}}$, it is not valid at an EP. Considering the general state decomposition of Eq. (4.50) and from the definition of expected value we obtain

$$\langle\hat{\sigma}_j^x(t)\rangle = \mathrm{Tr}(\hat{\sigma}_j^x\hat{\rho}(t)) = \sum_\mu \sum_k p_{0k}^\mu \langle\tau_k^\mu\rangle_{xj} e^{\lambda_k^\mu t}, \tag{E.21}$$

with $\langle\tau_k^\mu\rangle_{xj} = \langle\langle\sigma_j^x|\tau_k^\mu\rangle\rangle$ and, invoking the block structure of the Liouvillian, we find that $\langle\tau_k^\mu\rangle_{xj}$ are nonzero only for $\mu = b, c$. Finally, as $\bar{\bar{\mathcal{L}}}_c = \bar{\bar{\mathcal{L}}}_b^*$, then $\lambda_k^c = \lambda_k^{b*}$, $\langle\tau_k^c\rangle_{xj} = \langle\tau_k^b\rangle_{xj}^*$ and $p_{0k}^c = p_{0k}^{b*}$. Thus, the formal solution can be written just in terms of $\mu = b$ as

$$\langle\hat{\sigma}_j^x(t)\rangle = \sum_{k=1}^{4} 2|p_{0k}^b\langle\tau_k^b\rangle_{xj}|e^{\mathrm{Re}(\lambda_k^b)t}\cos[\mathrm{Im}(\lambda_k^b)t + \psi_{k,xj}^b], \tag{E.22}$$

with $\psi_{k,xj}^b = \arg(p_{0k}^b\langle\tau_k^b\rangle_{xj})$.

E.2.4 Correlation spectrum for $w/\gamma = 0$

In this section, we outline the main steps involved in computing two-time correlations of the type $\langle\hat{\sigma}_j^-(t+\tau)\hat{\sigma}_k^+(t)\rangle$ in the stationary state of the system, that is $\langle\hat{\sigma}_j^-(\tau)\hat{\sigma}_k^+(0)\rangle_{ss} = \lim_{t\to\infty}\langle\hat{\sigma}_j^-(t+\tau)\hat{\sigma}_k^+(t)\rangle$. In the absence of pumping the stationary state of the system is the vacuum, $\rho_{ss} = |gg\rangle\langle gg|$. Then, the definition of these two-time correlations is given by [59]

$$\langle\hat{\sigma}_j^-(\tau)\hat{\sigma}_k^+(0)\rangle_{ss} = \mathrm{Tr}\big(\hat{\sigma}_j^- e^{\mathcal{L}\tau}(\hat{\sigma}_k^+|gg\rangle\langle gg|)\big) = \mathrm{Tr}\big(\hat{\sigma}_j^- e^{\mathcal{L}_b\tau}(\hat{\sigma}_k^+|gg\rangle\langle gg|)\big), \tag{E.23}$$

for $\tau \geq 0$. In the second equality we have used the fact that $\hat{\sigma}_k^+|gg\rangle\langle gg|$ yields either $|eg\rangle\langle gg|$ or $|ge\rangle\langle gg|$ whose dynamics is ruled by $\bar{\bar{\mathcal{L}}}_b$. Moreover, as $w/\gamma = 0$, and as this type of initial condition belongs to the one excitation sector, the dynamics of these correlations can be obtained just considering the one excitation sector. Thus, considering a more general initial condition of this type, we have that $e^{\mathcal{L}_b\tau}(\rho_{eggg}(0)|eg\rangle\langle gg| + \rho_{gegg}(0)|ge\rangle\langle gg|) = \rho_{eggg}(\tau)|eg\rangle\langle gg| + \rho_{gegg}(\tau)|ge\rangle\langle gg|$, where these amplitudes follow a system of equations given by $\bar{\bar{\mathcal{L}}}_b$ that reads as

$$\begin{aligned}
\frac{d}{d\tau}\rho_{eggg}(\tau) &= -\Big[\frac{\gamma}{2} + i(\omega_0 + \frac{\delta}{2})\Big]\rho_{eggg}(\tau) - (\frac{\gamma}{2} + is_{12})\rho_{gegg}(\tau),\\
\frac{d}{d\tau}\rho_{gegg}(\tau) &= -\Big[\frac{\gamma}{2} + i(\omega_0 - \frac{\delta}{2})\Big]\rho_{gegg}(\tau) - (\frac{\gamma}{2} + is_{12})\rho_{eggg}(\tau).
\end{aligned} \tag{E.24}$$

The solution in the Laplace domain, $\rho_{xxgg}(s) = \int_0^\infty \rho_{xxgg}(\tau)e^{-s\tau}d\tau$, is readily obtained

$$\begin{aligned}
\rho_{eggg}(s) &= \frac{[s+\gamma/2+i(\omega_0-\delta/2)]\rho_{eggg}(0) - (\gamma/2+is_{12})\rho_{gegg}(0)}{(s-\lambda_3^b)(s-\lambda_4^b)},\\
\rho_{gegg}(s) &= \frac{[s+\gamma/2+i(\omega_0+\delta/2)]\rho_{gegg}(0) - (\gamma/2+is_{12})\rho_{eggg}(0)}{(s-\lambda_3^b)(s-\lambda_4^b)},
\end{aligned} \tag{E.25}$$

where the poles correspond to two of the eigenvalues given in Eq. (E.17). Notice that for $s_{12} = 0$ there is an EP at $\delta = \gamma$ but, in contrast to Eq. (E.22), this solution is correct at the EP as it is not written in terms of the eigenvectors of $\bar{\bar{\mathcal{L}}}_b$. In the main text, we consider both collective and local correlations, each case corresponding to different linear combinations of the above general results. For instance, for the collective correlation function associated to $\hat{L} = (\hat{\sigma}_1^- + \hat{\sigma}_2^-)/\sqrt{2}$, we have $\langle\hat{L}(\tau)\hat{L}^\dagger(0)\rangle_{ss} = (\rho_{eggg}(\tau) + \rho_{gegg}(\tau))/\sqrt{2}$ with the initial condition $\rho_{eggg}(0) = 1/\sqrt{2}$ and $\rho_{gegg}(0) = 1/\sqrt{2}$. Otherwise, considering only the initial excitation of one of the qubits, we have $\langle\hat{\sigma}_1^-(\tau)\hat{\sigma}_1^+(0)\rangle_{ss} = \rho_{eggg}(\tau)$ and $\langle\hat{\sigma}_2^-(\tau)\hat{\sigma}_2^+(0)\rangle_{ss} = \rho_{gegg}(\tau)$ for either $\rho_{eggg}(0) = 1$ and $\rho_{gegg}(0) = 0$ or the other way around.

In general, we will be interested in the Fourier transform or spectrum of these correlations, i.e.

$$\begin{aligned}
\mathcal{S}_{\hat{o}\hat{o}^\dagger}(\omega) &= \int_{-\infty}^{\infty} d\tau\, e^{-i\omega\tau}\langle\hat{o}(\tau)\hat{o}^\dagger\rangle_{ss}\\
&= 2\mathrm{Re}\Big\{\int_0^\infty d\tau\, e^{-i\omega\tau}\langle\hat{o}(\tau)\hat{o}^\dagger)\rangle_{ss}\Big\},
\end{aligned} \tag{E.26}$$

where $\hat{o}$ stands either for $\hat{\sigma}_j^-$ or $\hat{L}$. The second equality in (E.26) follows from the fact that in the stationary state $\langle\hat{o}(-\tau)\hat{o}^\dagger\rangle_{ss} = \langle\hat{o}\hat{o}^\dagger(\tau)\rangle_{ss}$, and moreover, for these correlations $\langle\hat{o}\hat{o}^\dagger(\tau)\rangle_{ss} = \langle\hat{o}(\tau)\hat{o}^\dagger\rangle_{ss}^*$. Finally notice that these Fourier transformed correlations can be written in terms of the solutions in the Laplace domain as combinations of the terms $2\mathrm{Re}[\rho_{eggg}(s = i\omega)]$ and $2\mathrm{Re}[\rho_{gegg}(s = i\omega)]$.

APPENDIX F

Implementation of the dissipative spin chain

In chapter 5 we have presented a dissipative spin model and we have provided a bird-eye picture of what is needed to implement it in a platform of cold atoms. Here, we will proceed to discuss the main details of this proposal. In Section F.1 we present the Hamiltonian that models the atomic lattice. We follow in Sect. F.2 explaining how from this atomic lattice one can realize effective spin Hamiltonians. In Sect. F.3 we comment on the proposed dissipation scheme of Ref. [265], while we end in Sect. F.4 discussing briefly typical numerical values for the parameters of the atomic system.

F.1 Two band Bose-Hubbard model

We consider a system of bosonic atoms in the Mott-insulator regime (MI), trapped in the two lowest energy bands of a bichromatic optical lattice. The optical lattice is assumed to be strongly anharmonic, such that higher vibrational levels are not populated. The system is described by the following two-band Bose-Hubbard Hamiltonian:

$$\hat{H}_{BH} = \hat{H}_0 + \hat{H}_1 + \hat{H}_t. \tag{F.1}$$

The different contributions to this Hamiltonian are the following. $\hat{H}_0$ describes the atom-atom repulsive interactions and the unperturbed optical potential [265]:

$$\begin{aligned}\hat{H}_0 = \sum_{j=1}^{N} \Bigg\{ & \frac{\omega_0}{2}(\hat{d}_j^\dagger \hat{d}_j - \hat{c}_j^\dagger \hat{c}_j) + U_{01}\hat{c}_j^\dagger \hat{c}_j \hat{d}_j^\dagger \hat{d}_j \\ & + \frac{U_{00}}{2}\hat{c}_j^\dagger \hat{c}_j(\hat{c}_j^\dagger \hat{c}_j - 1) + \frac{U_{11}}{2}\hat{d}_j^\dagger \hat{d}_j(\hat{d}_j^\dagger \hat{d}_j - 1)\Bigg\},\end{aligned} \tag{F.2}$$

$\hat{H}_1$ contains the small modulations to the optical potential:

$$\hat{H}_1 = \sum_{j\in\text{odd}} \frac{\omega_1}{2}(\hat{d}_j^\dagger \hat{d}_j - \hat{c}_j^\dagger \hat{c}_j) + \sum_{j\in\text{even}} \frac{\omega_2}{2}(\hat{d}_j^\dagger \hat{d}_j - \hat{c}_j^\dagger \hat{c}_j), \tag{F.3}$$

and $\hat{H}_t$ the perturbative tunneling processes between neighboring sites:

$$\hat{H}_t = \sum_{j=1}^{N-1} (t_0 \hat{c}_j^\dagger \hat{c}_{j+1} + t_1 \hat{d}_j^\dagger \hat{d}_{j+1} + H.c.). \tag{F.4}$$

The bosonic operators $\hat{c}_j^\dagger$ and $\hat{c}_j$ ($\hat{d}_j^\dagger$ and $\hat{d}_j$) create and annihilate an atom in the lowest (second lowest) motional state of site j of the optical lattice. As in [265] the only atom-atom interactions are given by the same site and same motional state repulsion energies U_{00} and U_{11}, and the same site different motional state repulsion U_{01}. Tunneling between neighboring sites without exchange of the motional state is permitted, with rates t_0 and t_1 [265]. The motional states are separated by a large energy ω_0 with small dimeric modulations ω_1 and ω_2, where it is convenient to define two possible energy separations $\tilde{\omega}_{1,2} = \omega_0 + \omega_{1,2}$. These processes are schematically illustrated in Fig. 5.1. We consider the system to be in a regime in which there is one atom per site. We recall the usual hierarchy of parameter values that ensures the validity of the model [265, 340, 341]:

$$\omega_0 \gg U_{00}, U_{11}, U_{01} \gg t_0, t_1. \tag{F.5}$$

Notice that as we consider small frequency modulations of the optical potential, we must also require that:

$$\omega_0 \gg \omega_1, \omega_2, \quad U_{00}, U_{11}, U_{01} \gg \delta, \tag{F.6}$$

with $\delta = \omega_1 - \omega_2$. The first condition is necessary to be able to treat the modulations of the potential as a perturbation to the monochromatic Hamiltonian (F.2). The second additional condition is instead necessary to obtain the desired effective spin Hamiltonian (see next section).

F.2 Effective spin Hamiltonian

An important observation is that $\hat{H}_{BH}$, besides conserving the total number of atoms n, also conserves the total number of atoms in each motional state n_0 and n_1. Hence, the eigenstates of $\hat{H}_0 + \hat{H}_1$ are given by the possible ways to distribute n atoms in the two motional states of the optical lattice. Here, we are interested in the low-energy sector of the case $n = N$ in which there is one atom per site. In fact, for prescribed values of n_0 and n_1, the lowest energy eigenstates, i.e. the ones with an atom per site, form a manifold of states with intra-energy separation of the order of δ. In turn, all possible configurations in which there is one site with two atoms form also a manifold with intra-energy separation again of order δ. Importantly, both manifolds are separated by an energy gap of the order of the repulsive interactions, i.e. $\sim U_{00}, U_{11}, U_{01}$, and hence much larger than the intra-manifold energy scales [Eq. (F.6)]. As we shall see, for small tunneling rates, one can take advantage of this manifold structure of the energy spectrum to engineer an effective spin Hamiltonian that captures the low-energy physics of the system [221].

In these conditions, when considering $\hat{H}_t$, only matrix elements between unperturbed states of different manifold are non-zero. Then, if one is interested in the low-energy physics of the system, one can use perturbation theory to obtain an effective Hamiltonian for the lowest energy manifold, and further neglect all states with more than one atom per site [221]. In this Schrieffer-Wolff kind of approach [221, 265, 334, 335, 336], second-order tunneling processes couple the lowest energy states by means of virtual transitions to states with two atoms per site, which are energetically unfavorable due to the large repulsive interactions. The matrix elements characterizing the strength of this kind of second-order processes can be computed with the following formula [221, 265]:

$$\langle x_j, y_{j+1} | \hat{H}_{\text{eff}} | x'_j, y'_{j+1} \rangle = \frac{1}{2} \sum_{\psi} \langle x_j, y_{j+1} | \hat{H}_t | \psi \rangle \frac{1}{E'} \langle \psi | \hat{H}_t | x'_j, y'_{j+1} \rangle, \tag{F.7}$$

where $\hat{H}_t$ is the tunneling Hamiltonian given in (F.4), $|\psi\rangle$ are the states with more than one particle per site, and the E' the energies of the unperturbed Hamiltonian, i.e. of $\hat{H}_0 + \hat{H}_1$:

$$\frac{1}{E'} = \frac{1}{E_{xy} - E_\psi} + \frac{1}{E_{x'y'} - E_\psi}. \tag{F.8}$$

In this appendix, the states $|x_j, y_{j+1}\rangle$ correspond to the eigenstates of $\hat{H}_0 + \hat{H}_1$ in the manifold of one atom per site. Then, x_j and y_{j+1} denote the motional state of the atoms at site j and $j+1$, e.g. $x_j = 0$ if at site j the atom is in the ground state and $x_j = 1$ if it is in the first excited state. Notice that as the tunneling Hamiltonian only couples nearest neighbors, it is enough to apply the perturbative formula (F.7) to the neighboring sites j and $j+1$ in order to obtain the effective Hamiltonian for all the chain. This is done by computing the matrix elements for all the possible combinations of $|x_j, y_{j+1}\rangle$ and $|x'_j, y'_{j+1}\rangle$ where x_j, x'_j, y_{j+1} and y'_{j+1} can take the values 0 and 1.

Then, after laborious but straightforward algebra, one obtains the second-order effective Hamiltonian governing the manifold of states with one atom per site:

$$\begin{aligned}
\hat{H}_{\text{eff}} = &\sum_{j=1}^{N-1} \left\{ C_1\, \hat{c}_j^\dagger \hat{c}_j \hat{c}_{j+1}^\dagger \hat{c}_{j+1} + C_2\, \hat{d}_j^\dagger \hat{d}_j \hat{d}_{j+1}^\dagger \hat{d}_{j+1} + C_3 \left(\hat{c}_j^\dagger \hat{c}_{j+1} \hat{d}_{j+1}^\dagger \hat{d}_j + \hat{d}_j^\dagger \hat{d}_{j+1} \hat{c}_{j+1}^\dagger \hat{c}_j \right) \right\} \\
&+ \sum_{j \in \text{odd}} \left\{ \frac{\tilde{\omega}_1}{2} (\hat{d}_j^\dagger \hat{d}_j - \hat{c}_j^\dagger \hat{c}_j) + \left(C_4^+\, \hat{c}_j^\dagger \hat{c}_j \hat{d}_{j+1}^\dagger \hat{d}_{j+1} + C_5^+\, \hat{d}_j^\dagger \hat{d}_j \hat{c}_{j+1}^\dagger \hat{c}_{j+1} \right) (1 - \delta_{j,N}) \right\} \\
&+ \sum_{j \in \text{even}} \left\{ \frac{\tilde{\omega}_2}{2} (\hat{d}_j^\dagger \hat{d}_j - \hat{c}_j^\dagger \hat{c}_j) + \left(C_4^-\, \hat{c}_j^\dagger \hat{c}_j \hat{d}_{j+1}^\dagger \hat{d}_{j+1} + C_5^-\, \hat{d}_j^\dagger \hat{d}_j \hat{c}_{j+1}^\dagger \hat{c}_{j+1} \right) (1 - \delta_{j,N}) \right\},
\end{aligned} \tag{F.9}$$

with the coefficients taking the following values[1]:

$$\begin{aligned}
&C_1 = -\frac{t_0^2}{U_{00} - \delta/2} - \frac{t_0^2}{U_{00} + \delta/2} \approx -\frac{2t_0^2}{U_{00}}, \quad C_2 = -\frac{t_1^2}{U_{11} - \delta/2} - \frac{t_1^2}{U_{11} + \delta/2} \approx -\frac{2t_1^2}{U_{11}}, \\
&C_3 = -\frac{t_0 t_1}{U_{01} - \delta/2} - \frac{t_0 t_1}{U_{01} + \delta/2} \approx -\frac{2t_0 t_1}{U_{01}}, \\
&C_4^\pm = -\frac{t_0^2 + t_1^2}{U_{01} \mp \delta/2}, \quad C_5^\pm = -\frac{t_1^2 + t_0^2}{U_{01} \pm \delta/2}, \quad C_4^\pm \approx C_5^\pm \approx -\frac{t_0^2 + t_1^2}{U_{01}}.
\end{aligned} \tag{F.10}$$

Notice that in (F.10) we make use of the condition (F.6) to further approximate the expression of the coefficients.

We can now define the pseudospin states $|0_j\rangle = |\downarrow_j\rangle$ and $|1_j\rangle = |\uparrow_j\rangle$, together with the proper pseudospin operators:

$$\begin{aligned}
&\hat{\sigma}_j^+ = \hat{d}_j^\dagger \hat{c}_j, \quad \hat{\sigma}_j^- = \hat{c}_j^\dagger \hat{d}_j, \quad \hat{\sigma}_j^z = \hat{d}_j^\dagger \hat{d}_j - \hat{c}_j^\dagger \hat{c}_j, \\
&\mathbb{1}_{2\times 2} = \hat{d}_j^\dagger \hat{d}_j + \hat{c}_j^\dagger \hat{c}_j,
\end{aligned} \tag{F.11}$$

thus obtaining the following effective spin Hamiltonian:

$$\begin{aligned}
\hat{H}_{\text{spin}} = &\sum_{j=1}^{N-1} \left\{ \lambda (\hat{\sigma}_j^+ \hat{\sigma}_{j+1}^- + \hat{\sigma}_{j+1}^+ \hat{\sigma}_j^-) + \lambda_z \hat{\sigma}_j^z \hat{\sigma}_{j+1}^z \right\} \\
&+ \sum_{j \in \text{odd}} \left(\frac{\omega_0 + \omega_1}{2} + h_z \right) \hat{\sigma}_j^z + \sum_{j \in \text{even}} \left(\frac{\omega_0 + \omega_2}{2} + h_z \right) \hat{\sigma}_j^z.
\end{aligned} \tag{F.12}$$

[1] The coefficients correspond to $C_1 = \langle 0_j, 0_{j+1} | \hat{H}_{\text{eff}} | 0_j, 0_{j+1} \rangle$, $C_2 = \langle 1_j, 1_{j+1} | \hat{H}_{\text{eff}} | 1_j, 1_{j+1} \rangle$, $C_3 = \langle 0_j, 1_{j+1} | \hat{H}_{\text{eff}} | 1_j, 0_{j+1} \rangle = \langle 1_j, 0_{j+1} | \hat{H}_{\text{eff}} | 0_j, 1_{j+1} \rangle$, $C_4^\pm = \langle 0_j, 1_{j+1} | \hat{H}_{\text{eff}} | 0_j, 1_{j+1} \rangle$ and $C_5^\pm = \langle 1_j, 0_{j+1} | \hat{H}_{\text{eff}} | 1_j, 0_{j+1} \rangle$, where the '+' corresponds to the case where j is odd, while the '−' to the case in which it is even. Notice that the missing combinations, such as $\langle 0_j, 0_{j+1} | \hat{H}_{\text{eff}} | 1_j, 1_{j+1} \rangle$, are zero; second-order tunneling process of the type described by Eq. (F.7) with Eq. (F.4) cannot couple these states.

with the parameters defined as:

$$\lambda \approx -\frac{2t_0 t_1}{U_{01}}, \quad h_z \approx \frac{1}{2}\left(\frac{t_0^2}{U_{00}} - \frac{t_1^2}{U_{11}}\right), \quad \lambda_z \approx -\frac{1}{2}\left(\frac{t_0^2}{U_{00}} + \frac{t_1^2}{U_{11}} - \frac{t_0^2 + t_1^2}{U_{01}}\right). \tag{F.13}$$

Finally, the Hamiltonian given in Eq. (5.4) corresponds to the parameters of the optical lattice such that $\lambda_z = 0$. Then, $\hat{H}$ is $\hat{H}_{\text{spin}}$ in a frame rotating with $\frac{\omega_0}{2} + h_z$.

F.3 Engineered dissipation

A detailed derivation of the dissipation scheme used in this chapter is found in Ref. [265] and here we review the main conditions to implement it. The basic idea is to use laser cooling techniques to engineer a tunable decay process from the first motional excited state $|1\rangle$ to the motional ground state $|0\rangle$. Laser cooling is essentially based on coupling some relevant internal electronic transitions of the atoms with their motional degrees of freedom. Then, under the appropriate resonance conditions, motional excitations are converted to excitations of the electronic level structure that spontaneously decay to the ground state emitting a photon into the electromagnetic environment in a short time scale, as compared with the one characterizing the motional-electronic coupling [248]. Thus, in simple terms, one can see it as a clever way to couple the hot motional degrees of freedom of the atoms to the cold electromagnetic environment.

Engineered two-level system. An important technique to enhance the performance and tunability of laser cooling is to couple the motional degrees of freedom to a dipole forbidden transition between two ground states [255]. Precisely, this is an important ingredient of the proposal of Ref. [265]. Hence, we consider that the relevant atoms transitions form a 'Λ' three level system, in which there are two ground states, $|g\rangle$ and $|r\rangle$, and an excited state $|e\rangle$ [255, 265]. Then, by means of weak off-resonant Raman transitions, the excited state is adiabatically eliminated, leading to an effective two level system with tunable decay rates composed by $|g\rangle$ and $|r\rangle$ [255, 265, 385]. This effective two-level system is characterized by an effective Rabi frequency Ω_{eff}, an effective detuning δ_r, an effective decay rate Γ, and an effective dephasing rate γ, where the expression for these parameters can be found in several references [255, 265, 385]. Using this engineered two-level system, one is able to tune the relevant effective decay rate, Γ, and make it much smaller than the characteristic frequency of the atomic motion, here ω_0, enabling the efficient suppression of unwanted heating processes [255], and thus enhancing laser cooling.

Laser cooling in the Lamb-Dicke regime. A crucial assumption of Ref. [265] is that the system works in the so-called Lamb-Dicke regime [248]. This is the regime in which the motion of the atoms is well confined in a region small compared to the wavelength of the cooling laser. This can be characterized by the dimensionless (if restoring $\hbar$) Lamb-Dicke parameter:

$$\eta_j = \frac{\hbar k_l}{\sqrt{2M\tilde{\omega}_j}} \tag{F.14}$$

which takes small values in this regime $\eta_j \ll 1$, where k_l is the wavelength of the cooling laser and M is the atomic mass. This condition ensures that the laser-mediated interaction between the internal atomic transitions and the motion of the atoms is well described by a first order series expansion in the Lamb-Dicke parameter of the full interaction term. Physically, this means that multiphonon processes are strongly suppressed. Hence, the

resulting effective interaction between atomic motion at site j and the engineered two-level system at site j reads (in the appropriate rotating frame) [265]:

$$\hat{V}_j = \Omega_{\text{eff}}\eta_j(\hat{\sigma}_j^+ + \hat{\sigma}_j^-)(|r_j\rangle\langle g_j| + |g_j\rangle\langle r_j|), \tag{F.15}$$

and the same for the other atoms in the chain. Notice that we are already incorporating the fact that we have one atom per site and that the atoms are restricted to the ground and first motional states, and thus we can model them through the pseudo-spin operators defined in Eq. (F.11).

The parameters are then adjusted so that the two-level system resolves the motional degrees of freedom, i.e. $\Gamma+\gamma \ll \tilde{\omega}_j$ [255, 265, 385]. Then, in the parameter regime in which [265]:

$$\eta_j|\Omega_{\text{eff}}| \ll \Gamma, \gamma, |\delta_r|, \tilde{\omega}_j \tag{F.16}$$

the internal and motional degrees of freedom are weakly coupled, while the dissipative time-scale of the internal dynamics is much shorter than that induced by the weak coupling of the interaction term Eq. (F.15). Therefore, one can adiabatically eliminate the internal degrees of freedom obtaining an effective master equation just for the motional degrees of freedom [248]. Notice that this type of derivation follows from similar approximations as those used to derive a Born-Markov master equation, although the starting point is a non-equilibrium system, as we have already commented in chapter 2. Then, proceeding in this way for all the chain [265] we obtain the master equation:

$$\frac{d}{dt}\hat{\rho} = -i[\hat{H}, \hat{\rho}] + \sum_j \left(2\gamma_j^- \mathcal{D}[\hat{\sigma}_j^-] + 2\gamma_j^+ \mathcal{D}[\hat{\sigma}_j^+]\right), \tag{F.17}$$

where the motional decay and absorption rates are given by:

$$\gamma_j^{\pm} = \eta_j^2\Omega_{\text{eff}}^2 \frac{\Gamma+\gamma}{(\Gamma+\gamma)^2 + (\delta_r \pm \tilde{\omega}_j)^2}. \tag{F.18}$$

Notice that, in order to suppress heating, the effective detuning should be tuned close to the large mechanical energy, i.e. $\delta_r \sim \omega_0$, such that $\gamma_j^+ \ll \gamma_j^-$ and the master equation given in Eq. (5.5) can be recovered with $\gamma_j = \gamma_j^-$ [265]. Further notice that we have neglected the perturbative coherent renormalization of $\tilde{\omega}_j$ induced by the elimination of the internal degrees of freedom, as they scale with $\Omega_{\text{eff}}^2\eta_j^2$, which in virtue of the hierarchy (F.16), are small compared to the bare frequencies.

In these conditions, the dependence of the decay rate on the lattice site comes mainly from the resonant frequency window of the Lorentzian, as differences between η_1^2 and η_2^2 are of the order of $\omega_j/\omega_0 \ll 1$. Defining $\epsilon = \delta_r - \omega_0 \sim |\omega_j|$ (which can be positive or negative), and by properly adjusting it, the decay rates can in general take staggered values. Furthermore, besides implementing staggered decay rates by means of the effective detuning (as described here), different approaches are also proposed in [265], as for example by tuning the phase difference between two cooling lasers.

F.4 Brief survey of parameter values

We follow references [340, 341] to illustrate the values that the parameters of this system can take. For sodium atoms in a blue detuned optical trap of wavelength $\lambda_T = 514$nm, the recoil energy is $E_R = 2\pi \times 33$kHz. Tuning the light intensity, the energy separation between the two lowest energy motional states of the lattice can be fixed to $\omega_0 \sim 1$MHz, which leads to $U_{lm} \sim 40$kHz and $t_l \sim 4$kHz $(l, m = 0, 1)$. In these conditions, the atomic chain is in the MI regime with one atom per site. Moreover, according to Eq. (F.13), $\lambda \sim 0.8$kHz which

sets the order of magnitude of the small modulations ω_j, as we take $\omega_j \sim \lambda$ in all chapter 5. Notice that this is consistent with the assumed hierarchy of parameters given in Eqs. (F.5) and (F.6).

Considering possible uncontrolled sources of dissipation, we notice that in the MI regime with one atom per site atom-atom collisions are strongly suppressed [340]. In addition, for these parameter values, the rate of dissipation due to the optical potential can be estimated to be of the order of 10^{-2}Hz [341], and we neglect it. This last approximation is consistent with the much larger values that we consider for the engineered decay rates, γ_j, which accordingly, can be estimated to be in the range $\sim 1 - 40$Hz.

APPENDIX G

Dynamics of the dissipative spin chain

In this appendix we discuss how to diagonalize the spin Hamiltonian of chapter 5, as well as how to obtain the eigenspectrum of the Liouvillian in the one excitation sector. We also derive analytical expressions for the dynamics of different observables in this sector, and we present some additional results supplementing the discussion presented in chapter 5.

G.1 Liouvillian spectrum

As it is shown in Ref. [346], the eigenvalues of the type of Liouvillian $\mathcal{L}$ considered here, are prescribed linear combinations of those of the non-Hermitian Hamiltonian $\hat{K} = \hat{H} - i\sum_j^N \gamma_j \hat{\sigma}_j^+ \hat{\sigma}_j^-$. In fact, as commented in the main text, the eigenvalues with the smallest decay rates coincide with eigenvalues of $\hat{K}$ and their complex conjugates. Thus in order to characterize the long-time relaxation dynamics we need to diagonalize $\hat{K}$. To do so we use the Jordan-Wigner transformation to work with fermions instead of spins [347]:

$$\hat{\sigma}_j^z = 2\hat{f}_j^\dagger \hat{f}_j - 1, \quad \hat{\sigma}_j^+ = \hat{f}_j^\dagger e^{i\hat{\phi}_j}, \quad \hat{\sigma}_j^- = \hat{f}_j e^{-i\hat{\phi}_j}, \quad \hat{\phi}_j = \pi \sum_{l<j} \hat{n}_l, \tag{G.1}$$

where $\hat{f}_j^\dagger(\hat{f}_j)$, $\hat{n}_j = \hat{f}_j^\dagger \hat{f}_j$, are the creation (annihilation) and number fermionic operators of site j. Then defining $\Omega_{1(2)} = \omega_{1(2)} - i\gamma_{1(2)}$, and using a notation that displays explicitly the dimeric character of the chain, we obtain the *fermionic* non-Hermitian Hamiltonian:

$$\begin{aligned} \hat{K}_F = &\sum_{j=1}^{N/2} \Omega_1 \hat{a}_j^\dagger \hat{a}_j + \sum_{j=1}^{N/2} \Omega_2 \hat{b}_j^\dagger \hat{b}_j \\ &+ \sum_{j=2}^{N/2} \lambda(\hat{a}_j^\dagger \hat{b}_{j-1} + H.c) + \sum_{j=1}^{N/2} \lambda(\hat{a}_j^\dagger \hat{b}_j + H.c.), \end{aligned} \tag{G.2}$$

where now $\hat{a}_j^\dagger(\hat{a}_j)$ and $\hat{b}_j^\dagger(\hat{b}_j)$ are fermionic creation (annihilation) operators of site j and its basis, respectively. The diagonalization of $\hat{K}_F$ is accomplished in two steps: first we

diagonalize the system assuming periodic boundary conditions, and later we combine the obtained eigenstates to find the ones of the open boundary case. In the following we write down the main results of each step.

G.1.1 Periodic boundary conditions

In this case the summation in the third term of Eq. (G.2) starts from $j = 1$, and the boundary conditions imply that $\hat{a}_0 = \hat{a}_{N/2}$ and $\hat{b}_0 = \hat{b}_{N/2}$. We define $M = N/2$ and relabel the index j to run from $j = 0$ to $M-1$. Then exploiting translational invariance we define the Fourier modes (denoted by k index):

$$\hat{a}_j = \frac{1}{\sqrt{M}} \sum_k \hat{a}_k e^{-i\frac{k}{2}} e^{ikj}, \quad \hat{b}_j = \frac{1}{\sqrt{M}} \sum_k \hat{b}_k e^{ikj}, \tag{G.3}$$

with $k = 2\pi l/M$ and $l = 0, 1, \ldots, M-1$. Notice that we have anticipated the need of a complex phase $-k/2$ in the expression for the $\hat{a}_j$'s. These modes leave $\hat{K}_F$ in a block-diagonal form $\hat{K}_F = \bigoplus_k \hat{K}_F(k)$ in which each block is given by:

$$\hat{K}_F(k) = (\hat{a}_k^\dagger \;\; \hat{b}_k^\dagger) \begin{pmatrix} \Omega_1 & 2\lambda \cos\frac{k}{2} \\ 2\lambda \cos\frac{k}{2} & \Omega_2 \end{pmatrix} \begin{pmatrix} \hat{a}_k \\ \hat{b}_k \end{pmatrix}. \tag{G.4}$$

A sufficient but not necessary condition for this non-Hermitian matrix to be diagonalizable is that it is not degenerate. Note that this is always fulfilled in the parameter region $\omega_1 \neq \omega_2$ and $\omega_{1(2)} > \gamma_{1(2)}$. Then, the diagonalization is accomplished by means of an orthogonal transformation defined as:

$$\begin{aligned} \hat{\alpha}_k(\hat{\alpha}_k') &= \hat{a}_k(\hat{a}_k^\dagger)\cos\theta_k - \hat{b}_k(\hat{b}_k^\dagger)\sin\theta_k, \\ \hat{\beta}_k(\hat{\beta}_k') &= \hat{a}_k(\hat{a}_k^\dagger)\sin\theta_k + \hat{b}_k(\hat{b}_k^\dagger)\cos\theta_k, \end{aligned} \tag{G.5}$$

with

$$\tan 2\theta_k = -\frac{4\lambda\cos\frac{k}{2}}{\Omega_1 - \Omega_2}. \tag{G.6}$$

Importantly as θ_k is complex, this orthogonal transformation is not unitary and hence $\hat{\alpha}_k'(\hat{\beta}_k') \neq \hat{\alpha}_k^\dagger(\hat{\beta}_k^\dagger)$. Only in the case $\gamma_1 = \gamma_2 = 0$, θ_k becomes real and we recover the standard operators. The eigenvalues of (G.4) are given by:

$$\Omega_k^\pm = \frac{\Omega_1 + \Omega_2}{2} \pm \frac{1}{2}\sqrt{(\Omega_1 - \Omega_2)^2 + 16\lambda^2\cos^2\frac{k}{2}}, \tag{G.7}$$

with the k's as above prescribed, and the correspondence of band '+(−)' to operator $\hat{\alpha}_k(\hat{\beta}_k)$. An important characteristic of this spectrum is that under the transformation $l \to M-l$ yields $\Omega_{k_l}^\pm = \Omega_{k_{M-l}}^\pm$ and $\theta_{k_l} = -\theta_{k_{M-l}}$. Indeed, part of the Fourier modes appear in pairs of degenerate eigenvalues, here corresponding to the pairs with the k's associated to $\{l, M-l\}$. Besides the degenerate eigenmodes, there is the mode $k = 0$, and when M is even there is also $k = \pi$. Notice that, although the spectrum is partially degenerate, the Fourier modes for different k are linearly independent and hence the set of eigenvectors too, as it is required for a matrix to be diagonalizable. Finally we write down the expression of $\hat{\alpha}_k$ and $\hat{\beta}_k$ in the site basis:

$$\begin{aligned} \hat{\alpha}_k &= \frac{1}{\sqrt{M}} \sum_{j=0}^{M-1} \left(\hat{a}_j \cos\theta_k e^{i\frac{k}{2}} - \hat{b}_j \sin\theta_k\right) e^{-ikj}, \\ \hat{\beta}_k &= \frac{1}{\sqrt{M}} \sum_{j=0}^{M-1} \left(\hat{a}_j \sin\theta_k e^{i\frac{k}{2}} + \hat{b}_j \cos\theta_k\right) e^{-ikj}. \end{aligned} \tag{G.8}$$

G.1.2 Open boundary conditions

In this case, we first consider a larger system of $M' = 2M + 1$ cells with periodic boundary conditions and we take linear combinations of its degenerate eigenmodes, i.e. $\hat{u}_{k_l} = x_1\hat{\alpha}_{k_l} + x_2\hat{\alpha}_{k_{M'-l}}$ and $\hat{v}_{k_l} = y_1\hat{\beta}_{k_l} + y_2\hat{\beta}_{k_{M'-l}}$, with $l = 1, 2, ..., M$. By requiring $\hat{u}_{k_l}(\hat{v}_{k_l})$ to be zero at sites b_0 and a_{M+1}, we can obtain the eigenmodes of the open boundary case with M cells. In particular the first condition is satisfied for any k if we take $x_1 = x_2$ and $y_1 = -y_2$, i.e. we replace as usual the exponentials by sines. Then, we see that the sine modes have a vanishing amplitude on a_{M+1} too, as it follows from the definition of the allowed k's:

$$k = \frac{2\pi l}{N+1} \implies \sin[k(M+\frac{1}{2})] = 0, \tag{G.9}$$

with $N = 2M$. Hence the normalized eigenmodes read as:

$$\begin{aligned}
\hat{u}_k &= \sqrt{\frac{4}{N+1}} \sum_{j=1}^{M} \big(\hat{a}_j \cos\theta_k \sin[k(j-\frac{1}{2})] - \hat{b}_j \sin\theta_k \sin[kj]\big), \\
\hat{v}_k &= \sqrt{\frac{4}{N+1}} \sum_{j=1}^{M} \big(\hat{a}_j \sin\theta_k \sin[k(j-\frac{1}{2})] + \hat{b}_j \cos\theta_k \sin[kj]\big),
\end{aligned} \tag{G.10}$$

where the eigenvalues of $\hat{u}_k(\hat{v}_k)$'s belong to the '+(−)' band. We can obtain $\hat{u}'_k(\hat{v}'_k)$ by replacing the operators $\hat{a}_j(\hat{b}_j)$ by $\hat{a}^\dagger_j(\hat{b}^\dagger_j)$. Again, $\hat{u}'_k(\hat{v}'_k) \neq \hat{u}^\dagger_k(\hat{v}^\dagger_k)$, except for the case $\gamma_{1(2)} = 0$, for the same reasons as before. Notice that this set of eigenvectors forms a complete orthogonal basis, both for θ_k real and complex. Moreover, notice that, besides the different notation (here N is the number of sites), the kind of Fourier transformation that block-diagonalizes the open boundary case is the same as that discussed for the array of harmonic oscillators in chapter 4, as both systems share a dimeric structure, i.e. unit cells of two sites.

G.2 Dynamics in the one-excitation sector

In the one excitation sector, the phase $\hat{\phi}_j$ of the Jordan-Wigner transformation (G.1) is zero. Then, fermionic and spin operators are equivalent, and the master equation in the fermionic picture takes the same form as the spin one. $\hat{f}_j(\hat{f}^\dagger_j)$ denote the fermionic annihilation (creation) operators, which in the one excitation sector are equivalent to the spin coherences. Moreover, it is useful to use the following notation. In the site basis we define $\hat{f}^\dagger_j|0\rangle = |F_j\rangle$, and $\langle 0|\hat{f}_j = \langle F_j|$, while we use Eqs. (G.10) to define $\hat{u}'_k(\hat{v}'_k)|0\rangle = |K_l\rangle$, and $\langle 0|\hat{u}_k(\hat{v}_k) = \langle K^*_l|$, with l running from 1 to N and the first half belonging to the energy band '−', while the other to the '+' band (as in chapter 5). $|K_l\rangle$, $\langle K^*_l|$ correspond to the right and left eigenvectors of $\hat{K}_F$ respectively. Notice that, as $\hat{K}_F$ is represented by a non-Hermitian symmetric matrix, the left eigenvectors are just the transpose of the right ones, as the '*' indicates in the Bra-Ket notation. Moreover, $\langle K^*_l|K_{l'}\rangle = \delta_{l,l'}$.

G.2.1 Exact time evolution

We now rewrite the master equation in the fermionic basis as $\partial_t\hat{\rho} = -i(\hat{K}_F\hat{\rho} - \hat{\rho}\hat{K}^\dagger_F) + 2\sum_j \gamma_j \hat{f}_j\hat{\rho}\hat{f}^\dagger_j$. Notice that in the one-excitation sector only density matrix terms of the type $|F_j\rangle\langle F_{j'}|$, $|F_j\rangle\langle 0|$ and $|0\rangle\langle F_j|$ contribute to the expectation values we are interested in. Moreover, in the one excitation sector, the jump part of the master equation does not contribute to the time evolution of these quantities. Thus, we only need to consider $\partial_t\hat{\rho} = \hat{\mathcal{K}}\hat{\rho}$, with $\hat{\mathcal{K}}\hat{\rho} = -i(\hat{K}_F\hat{\rho} - \hat{\rho}\hat{K}^\dagger_F)$. As $\hat{K}^\dagger_F$ is $\hat{K}_F$ with $\Omega^*_{1(2)}$, its eigenvalues and

eigenstates are obtained from Eq. (G.7) and (G.10) making the same replacement. Thus the right and left eigenvectors of $\hat{K}_F^\dagger$ are $|K_l^*\rangle$ and $\langle K_l|$ respectively. Taking all these into account, we can write:

$$\begin{aligned}\hat{\mathcal{K}}|K_l\rangle\langle K_m| &= [-i(\nu_l-\nu_m)-\Gamma_l-\Gamma_m]|K_l\rangle\langle K_m|,\\ \hat{\mathcal{K}}|K_l\rangle\langle 0| &= -(i\nu_l+\Gamma_l)|K_l\rangle\langle 0|,\\ \hat{\mathcal{K}}|0\rangle\langle K_m| &= (i\nu_m-\Gamma_m)|0\rangle\langle K_m|.\end{aligned} \tag{G.11}$$

Defining the following projectors:

$$\begin{aligned}\mathcal{P}_{l,m}\hat{\rho}(t) &= (\langle K_l^*|\hat{\rho}(t)|K_m^*\rangle)|K_l\rangle\langle K_m|,\\ \mathcal{P}_{l,0}\hat{\rho}(t) &= (\langle K_l^*|\hat{\rho}(t)|0\rangle)|K_l\rangle\langle 0|,\\ \mathcal{P}_{0,m}\hat{\rho}(t) &= (\langle 0|\hat{\rho}(t)|K_m^*\rangle)|0\rangle\langle K_m|,\end{aligned} \tag{G.12}$$

we can write the time evolution of these density matrix projections as:

$$\begin{aligned}\mathcal{P}_{l,m}\hat{\rho}(t) &= \mathcal{P}_{l,m}\hat{\rho}(0)e^{[-i(\nu_l-\nu_m)-\Gamma_l-\Gamma_m]t},\\ \mathcal{P}_{l,0}\hat{\rho}(t) &= \mathcal{P}_{l,0}\hat{\rho}(0)e^{-(i\nu_l+\Gamma_l)t},\\ \mathcal{P}_{0,m}\hat{\rho}(t) &= \mathcal{P}_{0,m}\hat{\rho}(0)e^{(i\nu_m-\Gamma_m)t}.\end{aligned} \tag{G.13}$$

Finally notice that the explicit form of the Liouvillian eigenmodes can be found generalizing the two-spin results of Ref. [90] to k-dependent couplings.

G.2.2 Main results

We first write down the fermionic operators in the following way:

$$\hat{f}_j = |0\rangle\langle F_j|, \quad \hat{f}_j^\dagger = |F_j\rangle\langle 0|, \quad f_j^\dagger f_{j'} = |F_j\rangle\langle F_{j'}|. \tag{G.14}$$

Then using these definitions and Eqs. (G.12) and (G.13), we can obtain the expressions for the time evolution of the expected values presented in chapter 5. First we consider $\langle\hat{\sigma}_j^x(t)\rangle$, with an initial condition $\hat{\rho}(0) = |\Psi_0\rangle\langle\Psi_0|$. Hence:

$$\begin{aligned}\langle\hat{\sigma}_j^x(t)\rangle &= 2\mathrm{Re}\big(\mathrm{Tr}[\hat{f}_j\hat{\rho}(t)]\big)\\ &= 2\mathrm{Re}\big(\mathrm{Tr}[\hat{f}_j\sum_l\mathcal{P}_{l,0}\hat{\rho}(t)]\big),\end{aligned} \tag{G.15}$$

which yields:

$$\langle\hat{\sigma}_j^x(t)\rangle = 2\mathrm{Re}\big(\sum_l u_l(j)e^{-(i\nu_l+\Gamma_l)t}\big), \tag{G.16}$$

with

$$u_l(j) = \langle K_l^*|\Psi_0\rangle\langle\Psi_0|0\rangle\langle F_j|K_l\rangle. \tag{G.17}$$

Next we consider the correlation $\langle\hat{\sigma}_j^x(t)\hat{\sigma}_{j'}^x(t)\rangle$, which in the one excitation sector is given by $2\mathrm{Re}[\langle\hat{f}_j^\dagger(t)\hat{f}_{j'}(t)\rangle]$. Proceeding analogously, we find that:

$$\mathrm{Tr}[\hat{f}_j^\dagger\hat{f}_{j'}\hat{\rho}(t)] = \mathrm{Tr}[\hat{f}_j^\dagger\hat{f}_{j'}\sum_{l,m}\mathcal{P}_{l,m}\hat{\rho}(t)], \tag{G.18}$$

and hence:

$$\langle\hat{\sigma}_j^x(t)\hat{\sigma}_{j'}^x(t)\rangle = 2\mathrm{Re}\big(\sum_{l,m}w_{l,m}(j,j')e^{[-i(\nu_l-\nu_m)-\Gamma_l-\Gamma_m]t}\big), \tag{G.19}$$

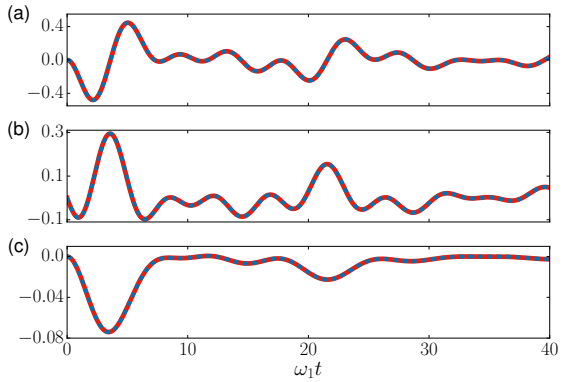

Figure G.1: In all cases the parameters are fixed to $N = 4$, $\delta = 0.25\omega_1$, $\lambda = 0.3\omega_1$ and $\gamma_j/\omega_j = 0.05$. Red solid lines correspond to exact numerical results, blue dashed lines to the analytical expressions derived in this section. (a) $\langle\hat{\sigma}_1^x(t)\rangle$, considering the initial condition $|\Psi_0\rangle = (|0\rangle + |F_2\rangle)/\sqrt{2}$. (b) Imaginary part of $\langle\hat{\sigma}_1^-(t)\hat{\sigma}_2^+(0)\rangle$. Notice that the real part of this quantity is the same as (a). (c) $\langle\hat{\sigma}_1^x(t)\hat{\sigma}_2^x(t)\rangle$, considering the initial condition $|\Psi_0\rangle = (|0\rangle + |F_2\rangle)/\sqrt{2}$.

with:

$$w_{l,m}(j,j') = \langle K_l^*|\Psi_0\rangle\langle\Psi_0|K_m^*\rangle\langle K_m|F_j\rangle\langle F_{j'}|K_l\rangle. \tag{G.20}$$

Finally we consider the two time correlation function $\langle\hat{\sigma}_j^-(\tau)\hat{\sigma}_{j'}^+(0)\rangle$ where 0 denotes an arbitrary time origin in the stationary state (the vacuum). Using the formulas introduced in chapter 2 (see also [59]), we know that this is equivalent to compute the time evolution of $\langle\hat{\sigma}_j^-(\tau)\rangle$ with the initial condition $\hat{\sigma}_{j'}^+|0\rangle\langle 0|$. Thus proceeding analogously as for (G.15), we obtain:

$$\langle\hat{\sigma}_j^-(\tau)\hat{\sigma}_{j'}^+(0)\rangle = \sum_l v_l(j,j')e^{-(i\nu_l+\Gamma_l)\tau}, \tag{G.21}$$

with

$$v_l(j,j') = \langle K_l^*|F_{j'}\rangle\langle F_j|K_l\rangle. \tag{G.22}$$

We also write down the Fourier transform of this correlation $\mathcal{S}_{jj'}(\nu)$ studied in the main text:

$$\begin{aligned}\mathcal{S}_{jj'}(\nu) &= \mathrm{Re}\Big[\int_0^\infty d\tau e^{-i\nu\tau}\langle\hat{\sigma}_j^-(\tau)\hat{\sigma}_{j'}^+(0)\rangle\Big] \\ &= \sum_l \frac{\Gamma_l \mathrm{Re}[v_l(j,j')] + (\nu+\nu_l)\mathrm{Im}[v_l(j,j')]}{\Gamma_l^2 + (\nu+\nu_l)^2}.\end{aligned} \tag{G.23}$$

These equations are the results we use in the main text to compare and analyze different synchronization measures. In Fig. G.1 we plot an example for each of these quantities, comparing numerical trajectories with the analytical results as a consistency check, finding that they agree.

G.3 Synchronization maps for various dissipation strengths

In this section we analyze the effects of varying γ_j/ω_j over the emergence of spontaneous synchronization for all the considered parameter region [Fig. 5.3(a)]. In Fig. G.2 we plot the synchronization map for increasing values of the ratio γ_j/ω_j, (a)-(d), from 0.005 to 0.05 respectively. Comparing these plots, we observe that the main difference is the change in size of region II of synchronization (small λ and large δ), which diminishes with the ratio γ_j/ω_j. Indeed, the value of λ above which synchronization II is no longer found diminishes strongly, while the range of δ for which there is synchronization does not change significantly. Conversely, the other regions of the map do not change significantly

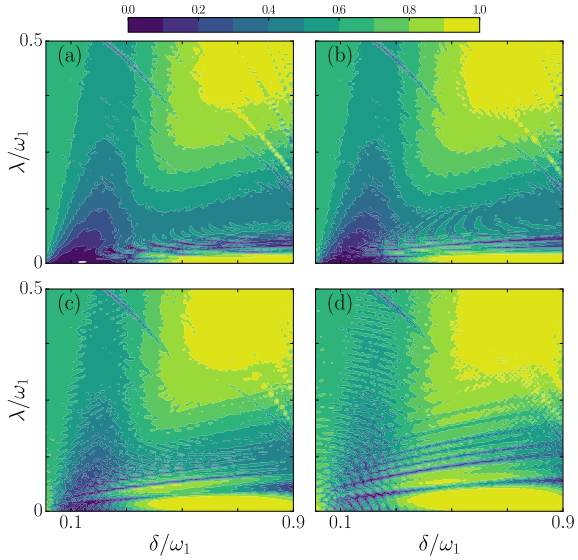

Figure G.2: Map of mutual synchronization among all spin pairs $\mathcal{C}_T(t) = \prod_{i<j} \mathcal{C}_{\langle\hat{\sigma}_i^x\rangle,\langle\hat{\sigma}_j^x\rangle}(t)$ at $\gamma_1 t = 10$ and $\omega_1 \Delta t = 80$, varying detuning and coupling strength, and with $|\Psi(t=0)\rangle = |\Downarrow\rangle/\sqrt{2} + (|\uparrow_2\rangle + |\uparrow_3\rangle)/2$. Strong synchronization is found at the yellow (light color) regions I (*intra-band* synchronization) II (*inter-band* synchronization) ($\mathcal{C}_T \geq 0.9$). For all figures $\omega_1 = 1$, while in (a) $\gamma_j/\omega_j = 0.005$, in (b) $\gamma_j/\omega_j = 0.01$, in (c) $\gamma_j/\omega_j = 0.025$ and in (d) $\gamma_j/\omega_j = 0.05$. (d) corresponds to Fig. 2(a) of the main text, and we have included it to ease comparison.

when varying the dissipation strength. The decreasing size of region II is explained by recalling the mechanism behind synchronization in this region. As we explain in the main text, synchronization in region II emerges because the small difference between the eigenfrequencies (ν_l's) of the same band is blurred by the decay rates (Γ_l's), resulting in an effective two body behavior [Fig. 5.6 (d)]. When decreasing γ_j/ω_j, the Γ_l's become smaller relative to the ν_l's, and the dynamics of the system resolves better small frequency differences. This implies that the effective two-body behavior will be lost for smaller values of λ, hence hindering synchronization.

APPENDIX H

The harmonically driven quantum van der Pol oscillator

In this appendix we introduce the physics of the driven QvdP oscillator. The analysis of quantum entrainment phenomena in this system has been addressed mainly in Refs. [67, 68, 363], while a discussion of its classical counterpart can be found in Refs. [42, 43]. Here, we will present and discuss some of the main results regarding the emergence of entrainment in this system, complementing chapters 6 and 7. Moreover, we will follow the same spirit of these chapters, i.e. that of trying to connect quantum synchronization phenomena with other driven-dissipative phenomena, identifying some key questions and results to be further investigated.

H.1 The model

The QvdP oscillator forced by a harmonic driving is modeled by the master equation (6.1) with the following Hamiltonian:

$$\hat{H}(t) = \omega_0 \hat{a}^\dagger \hat{a} + iF(\hat{a}e^{i\omega_d t} - \hat{a}^\dagger e^{-i\omega_d t}), \tag{H.1}$$

where F is the strength of the forcing, and ω_d its frequency. As for the squeezed QvdP oscillator, we can eliminate the explicit time-dependence of the model by moving to a rotating frame defined by the time-dependent unitary transform: $\hat{U}_t = \exp(-i\omega_d \hat{a}^\dagger \hat{a} t)$. In this frame the Hamiltonian reads:

$$\hat{H} = \Delta_d \hat{a}^\dagger \hat{a} + iF(\hat{a} - \hat{a}^\dagger), \tag{H.2}$$

where $\Delta_d = \omega_0 - \omega_d$, while the rest of the terms of the master equation (6.1) are the same in both frames. From Eq. (H.2) we observe that the driving term breaks explicitly the $U(1)$ symmetry of the bare QvdP oscillator, and also the parity symmetry of the squeezed one. In this case the model only displays a discrete time-translation symmetry of period $T_d = 2\pi/\omega_d$ [see Eq. (H.1)] in the laboratory frame, which is not apparent when we move to the rotating frame.

H.2 Classical entrainment

The mean-field equation governing the classical dynamics can be obtained proceeding as in Sect. 6.2.2. Hence, defining $\alpha = \langle \hat{a} \rangle$ and factorizing higher-order moments from its equation of motion, we obtain:

$$\frac{d}{dt}\alpha = -i\Delta_d \alpha + \frac{\gamma_1}{2}\alpha - \gamma_2 |\alpha|^2 \alpha - F. \tag{H.3}$$

The bifurcation diagram given by the solution of Eq. (H.3) displays a richer phenomenology than that of the squeezed vdP oscillator. A clear and concise introduction to its main features can be found in Ref. [43]. It is convenient to define the amplitude R and phase ϕ, such that $\alpha = Re^{i\phi}$, which allow us to rewrite Eq. (H.3) as:

$$\begin{aligned} \frac{d}{dt}R &= \Big[\frac{\gamma_1}{2} - \gamma_2 R^2\Big]R - F\cos\phi, \\ \frac{d}{dt}\phi &= -\Delta_d + \frac{F}{R}\sin\phi, \end{aligned} \tag{H.4}$$

It is insightful to compare Eq. (H.4) with the corresponding equations for the squeezed case, i.e. Eq. (6.8). In the driven case, amplitude and phase are mutually coupled, which is the source of the increased complexity of the bifurcation diagram that we have commented. Nevertheless, we can still distinguish between two regimes: one in which the stable attractor is a fixed point, and another in which is a limit cycle. The type of bifurcation between the two regimes changes depending on the value of the detuning and forcing in relation to the amplitude of the limit cycle. For small detunings we find an infinite-period bifurcation, while for large detunings a Hopf bifurcation [43]. Hence, in contrast to the squeezed case, the bifurcation diagram also depends on the ratio γ_2/γ_1[1].

The small detuning regime. In the small detuning and forcing scenario, we can make the approximation that the amplitude of the limit cycle is constant during all the cycle and equal to that of the bare vdP oscillator:

$$R(t) \approx \bar{R} = \sqrt{\frac{\gamma_1}{2\gamma_2}}. \tag{H.5}$$

This allows us to make the phase dynamics independent of the amplitude dynamics, i.e.:

$$\frac{d}{dt}\phi \approx -\Delta_d + \frac{F}{\bar{R}}\sin\phi. \tag{H.6}$$

As it can be checked numerically, this is a reasonable approximation in the considered regime, i.e. for

$$F/\gamma_1, |\Delta_d|/\gamma_1 \ll \bar{R}. \tag{H.7}$$

Then, as in the squeezed case, this simplified dynamics for the phase enables us to obtain approximate expressions for the small detuning and small forcing region of the bifurcation diagram. In particular, the critical point is given by:

$$F_c \approx |\Delta_d|\bar{R}. \tag{H.8}$$

For $F < F_c$, the stable attractor is a limit cycle whose approximate fundamental frequency can be obtained from Eq. (H.6):

$$\Omega_d \approx \Delta_d \sqrt{1 - (F/F_c)^2}, \tag{H.9}$$

[1]Notice that in this appendix, we will provide all parameters in terms of γ_1, as we have done for the squeezed case.

and with an amplitude given approximately by Eq. (H.5). On the other hand, for $F > F_c$ the stable attractor is a fixed point whose amplitude and phase are more conveniently determined numerically.

Let us now take another look to Eq. (H.8): we can see that as long as the detuning is small, the limit-cycle regime will exist only for small forcing strengths as compared to $\bar{R}$ since $F < |\Delta_d|\bar{R}$, which is automatically consistent with the approximation of not taking into account the effects of the driving on the amplitude of the limit cycle, i.e. Eq. (H.5). Therefore, we can call this regime *the small detuning regime* without the need to explicitly assume small values of F, as the limit cycle turns out to be present only for the small ones.

The expression for Ω_d [Eq. (H.9)] indicates that the bifurcation between these regimes (for small detunings) corresponds to an infinite-period bifurcation, as in the squeezed case. In fact, this feature is confirmed when numerically analyzing the exact equations, i.e. Eq. (H.3) or (H.4), in which it is found that at the critical forcing strength the limit cycle suddenly disappears giving birth to a pair of fixed points (one stable and one unstable) through a saddle-node bifurcation [43]. This kind of bifurcation is also known as SNIC, or saddle-node on the invariant circle, which also occurs in the squeezed case (with the birth of two saddle-nodes), and which is dramatically different from the familiar supercritical Hopf bifurcation route towards a limit cycle: in the latter a focus loses its stability (but it does not disappear) and the amplitude of the limit cycle grows smoothly from zero [55]; while in the SNIC bifurcation the limit cycle is born with a non-zero amplitude and at least a pair of fixed points disappears through a saddle-node.

Entrained regime. As in the case of the squeezed vdP oscillator, the fixed point regime corresponds to the driven vdP oscillator being perfectly entrained by the forcing, while the limit-cycle regime to the case in which there is no synchronization. Again, this can be understood going back to the laboratory frame in which the fixed point oscillates harmonically at a frequency ω_d, while the limit cycle becomes a quasiperiodic trajectory as Ω_d and ω_d are in general not commensurate. This mean-field diagram indicates that in the entrained regime there is no discrete time-translation symmetry breaking, as the system respects the periodicity of the driving. On the other hand, in the unentrained regime this symmetry is broken continuously, at least at the mean-field level. This is discussed in more general terms in the concluding remarks of chapter 7.

H.3 Signatures of quantum entrainment

Here we present the main signatures of entrainment in the quantum regime. The emergence of entrainment is manifested in the Wigner distribution of the stationary state as well as in the emission and power spectra, as first reported in Refs. [67, 68].

Signatures of entrainment in the Wigner distribution. In Fig. H.1 we plot the Wigner representation of the stationary state of the driven QvdP oscillator for three different values of the forcing strength. Panel (a) corresponds to the bare QvdP oscillator with $F/\gamma_1 = 0$, in which the stationary state displays a symmetric ring-like shape. This is the signature of a limit-cycle regime in which all (oscillation) phases are equivalent. If the forcing strength is increased a bit, one still finds a ring-like shape [see panel (b)]; however, due to the non-zero forcing the system starts to display some phase-preference. Finally, further increasing the forcing strength, the Wigner distribution begins to display a localized lobe, as shown in panel (c), indicating the emergence of a preferred phase. In

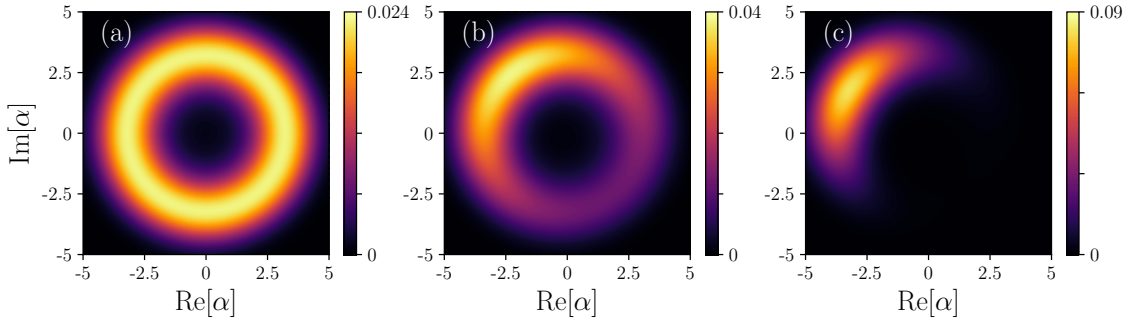

Figure H.1: In color: Wigner representation of the stationary state, $W_{ss}(\alpha, \alpha^*)$ (see appendix A), for (a) $F/\gamma_1 = 0$, (b) $F/\gamma_1 = 0.15$, (c) $F/\gamma_1 = 0.5$. In all cases $\Delta_d/\gamma_1 = 0.1$ and $\gamma_2/\gamma_1 = 0.1$.

contrast to the squeezed QvdP oscillator (see chapter 6) there is no phase multistability, and thus, the Wigner distribution just displays a single localized lobe.

Signatures of entrainment in the emission/power spectrum. As we have seen, the stationary Wigner distribution provides us with hints on the nature of the stable attractor: i.e. whether it is a limit cycle [e.g. Fig. H.1 (a)], a single fixed point [e.g. Fig. H.1 (b)], or bistable fixed points (e.g. Fig. 6.3). However, this is essentially a *static* (time-independent) quantity, and thus, we cannot use it to characterize important dynamical aspects of the system, as which is the dominant frequency. This is a limitation for the study of quantum synchronization, and for this reason in Ref. [68] it was proposed to complement the study of the Wigner distribution with other dynamical quantities such as the emission and power spectra, which allow one to analyze how the dominant frequency in the system changes as this becomes entrained by the external forcing.

In Fig. H.2 (a) we plot the emission spectrum for fixed forcing strength and for three different detunings. This quantity is defined as:

$$S(\omega) = \int_{-\infty}^{\infty} d\tau e^{-i\omega\tau} \langle \hat{a}^\dagger(\tau)\hat{a}(0)\rangle_{ss}. \tag{H.10}$$

Importantly, a non-zero forcing strength breaks the $U(1)$ symmetry of this model, which makes the system display a non-zero stationary amplitude $\langle \hat{a}\rangle_{ss} \neq 0$. This contrasts with the squeezed QvdP oscillator case (see chapter 6), in which parity symmetry implies that $\langle \hat{a}\rangle_{ss} = 0$. This explains why in Fig. H.2 (a) there are delta peaks at the frequency of the driving ($\omega/\gamma_1 = 0$ in the rotating frame), while in the squeezed case there are not (see Fig. 6.5), as it can be understood from the eigendecomposition of the relevant two-time correlations [see Eq. (2.57)]:

$$\langle \hat{a}^\dagger(\tau)\hat{a}(0)\rangle_{ss} = |\langle \hat{a}\rangle_{ss}|^2 + \sum_{j\geq 1} \mathrm{Tr}[\hat{\sigma}_j^\dagger(\hat{a}\hat{\rho}_{ss})]\mathrm{Tr}[\hat{a}^\dagger\hat{\rho}_j]e^{\lambda_j\tau}, \tag{H.11}$$

where the first term gives a delta peak when Fourier transformed. These delta peaks are in in some contexts known as the coherent part of the emission spectrum [59]. While its incoherent part or power spectrum is defined as[2]:

$$S_{inc}(\omega) = \int_{-\infty}^{\infty} d\tau e^{-i\omega\tau} [\langle \hat{a}^\dagger(\tau)\hat{a}(0)\rangle_{ss} - \langle \hat{a}^\dagger(\tau)\rangle_{ss}\langle \hat{a}\rangle_{ss}], \tag{H.12}$$

which is made up of the contribution of all modes with $\mathrm{Re}[\lambda]_j \neq 0$ and corresponds to the spectra in Fig. H.2 (a) besides the delta peaks. Notice that in some of the references

[2] As commented in chapter 6 for the squeezed QvdP oscillator both spectra are equivalent.

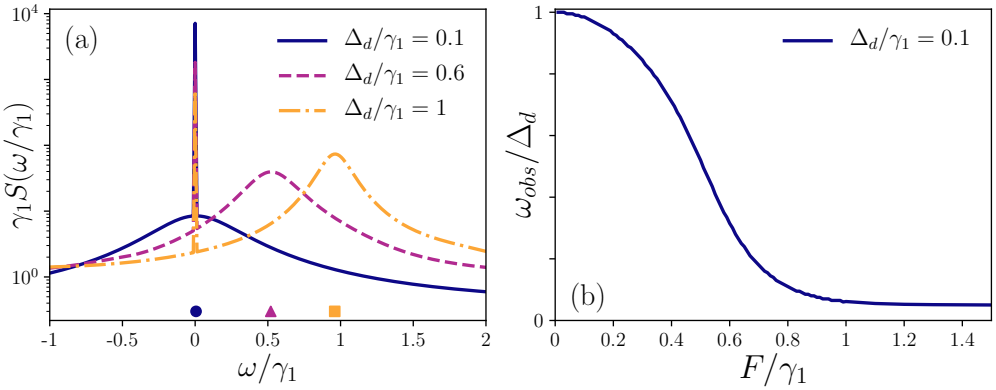

Figure H.2: (a) Emission spectrum for $\gamma_2/\gamma_1 = 0.1$, $F/\gamma_1 = 1$. Colored markers correspond to $\omega_{obs}/\Delta_d = (0.062, 0.867, 0.96)$ for the three considered detunings $\Delta_d/\gamma_1 = (0.1, 0.6, 1)$, following the same color code indicated in the legend. (b) Observed frequency (i.e. frequency of the maximum of the incoherent spectrum) for $\gamma_2/\gamma_1 = 0.1$ and $\Delta_d/\gamma_1 = 0.1$.

about the driven QvdP oscillator [68, 166] the incoherent spectrum is plotted directly, without a detailed discussion of the possible appearance of delta peaks when considering the coherent spectrum and their interpretation.

As explained in chapters 1 and 6, the observed frequency, defined as

$$\omega_{obs} = \text{argmax}[S_{inc}(\omega)], \tag{H.13}$$

constitutes a useful indicator to assess the emergence of entrainment [68, 361]. In fact, from Fig. H.2 (a) we observe that when decreasing the detuning for a fixed forcing strength, the ratio of the observed frequency over the detuning decreases, i.e. $\omega_{obs}/\Delta_d = (0.062, 0.867, 0.96)$ for $\Delta_d/\gamma_1 = (0.1, 0.6, 1)$ and $F/\gamma_1 = 1$, indicating that the system becomes entrained. Conversely, if we fix the detuning while increasing the forcing strength [see H.2 (b)], ω_{obs}/Δ_d goes from one to a value close to zero, also indicating the emergence of entrainment. This is analogous to what we have observed in the squeezed QvdP oscillator case when it becomes entrained (see Fig. 6.6).

Now that we have reported the emergence of entrainment, it is interesting to briefly comment on some particular aspects of the emission spectra of Fig. H.2 (a) and the observed frequency of panel (b), whose explanation will be discussed in Sec. H.5 in which the fluctuation dynamics in the entrained regime is studied in terms of a linearized master equation. In particular, from panel (a) we observe that as the system becomes entrained, the width of the Lorentzian-like lineshape increases, while its height diminishes. On the other hand, the height of the delta peak displays the opposite trend and increases as the detuning is diminished. For the observed frequency [Fig. H.2 (b)], we find that for large forcing strengths it diminishes very slowly. Both of these are in contrast with the case of the squeezed QvdP oscillator in which the linewidth of the main resonance of the emission spectrum diminishes as the system becomes entrainment, while the observed frequency tends faster to zero than for the driven case (see Figs. 6.5 and 6.6). The origin of these differences will be discussed in more detail in Sect. H.5 and H.6.

H.4 Infinite-excitation limit

We now discuss the infinite-excitation limit of this model. The way to perform this limit for the driven QvdP oscillator is similar to that for the squeezed case. As explained in Sect. 7.2, this essentially consists in a small non-linearity per boson limit in which

$N = (\gamma_2/\gamma_1)^{-1} \to \infty$. However, as we shall see, for the driven QvdP oscillator an additional step needs to be taken into account in other to perform this limit correctly. This can be understood analyzing the equation of motion for $\langle \hat{a} \rangle$ under the scaling transformation:

$$\hat{\tilde{a}} = \hat{a}/\sqrt{N}, \quad \hat{\tilde{a}}^\dagger = \hat{a}^\dagger/\sqrt{N}, \tag{H.14}$$

and rewriting in dimensionless parameters in terms of γ_1 for convenience:

$$\frac{d}{d(\gamma_1 t)}\langle \hat{\tilde{a}} \rangle = -i(\Delta_d/\gamma_1)\langle \hat{\tilde{a}} \rangle + \frac{1}{2}\langle \hat{\tilde{a}} \rangle - \langle \hat{\tilde{a}}^\dagger \hat{\tilde{a}}^2 \rangle - \frac{(F/\gamma_1)}{\sqrt{N}}. \tag{H.15}$$

Hence, from Eq. (H.15) we find that if the infinite-excitation limit just consists in taking the limit $N \to \infty$, then the driving term will be 'scaled out' of the model (i.e. vanish), and we will recover the physics of the *bare* van der Pol oscillator. This is clearly an unwanted side effect, which suggests that besides the limit $(\gamma_2/\gamma_1) \to 0$, we need to perform an additional step.

The small non-linearity per boson limit with constant amplitude/driving ratio. Our problem is solved by rescaling the driving strength in the following way:

$$F = \sqrt{N}\tilde{F}. \tag{H.16}$$

Therefore, the infinite-excitation limit corresponds to a limit in which the non-linearity per boson becomes vanishingly small while the *ratio of driving strength and amplitude* remains constant. As we will see, the results obtained with the master equation in this limit tend to the results of the rescaled mean-field equation:

$$\frac{d}{d(\gamma_1)}\tilde{\alpha} = -i(\Delta_d/\gamma_1)\tilde{\alpha} + \frac{1}{2}\tilde{\alpha} - |\tilde{\alpha}|^2\tilde{\alpha} - (\tilde{F}/\gamma_1), \tag{H.17}$$

obtained by replacing $\langle \hat{\tilde{a}} \rangle$ for $\tilde{\alpha}$ and factorizing higher-order moments. At this point, it can be insightful to compare Eq. (H.17) with the corresponding one for the squeezed case, i.e. Eq. (7.3): In the squeezed case there is no need to rescale η with $\sqrt{N}$ since the forcing term is parametric, i.e. it is paired with an amplitude term, $(\eta/\gamma_1)\alpha^*$, which ensures that as $N \to \infty$ it is not 'scaled out' of the model.

Numerical results. We now compare the results obtained from the master equation as the infinite-excitation limit is approached with the results obtained from the mean-field equation (H.17). Let us recall how this limit is implemented in practice: i) express all the parameters in terms of γ_1 and keep this one fixed; ii) implement the master equation with the properly scaled parameters, i.e. replace (γ_2/γ_1) by $1/N$, and (F/γ_1) by $\sqrt{N}(\tilde{F}/\gamma_1)$; iii) analyze the results for increasing values of N.

In Fig. H.3 we compare the results computed from the *stationary state* of the master equation for increasing N with the results obtained from the (properly averaged) mean-field equation (H.17). Actually, as we are considering two limits in the following order:

$$\lim_{N\to\infty} \langle \hat{O} \rangle_{ss} = \lim_{N\to\infty} \lim_{t\to\infty} \mathrm{Tr}[\hat{O}\hat{\rho}(t)], \tag{H.18}$$

the quantum results tend to the properly averaged mean-field results, as in the squeezed case (see Sect. 7.2). That is, in the limit-cycle phase the quantum results tend to the mean-field ones averaged over a period. While in the fixed point phase, as there is no bistability, there is no need to average over multiple mean-field solutions, and the quantum results tend to the bare mean-field ones. From Fig. (H.3) we can clearly see how the quantum results approach the mean-field physics as N is increased. As in the squeezed case (see Fig. 7.1), the larger discrepancies are found near the bifurcation in which the mean-field non-analytic behavior is smoothed out by finite-excitation effects.

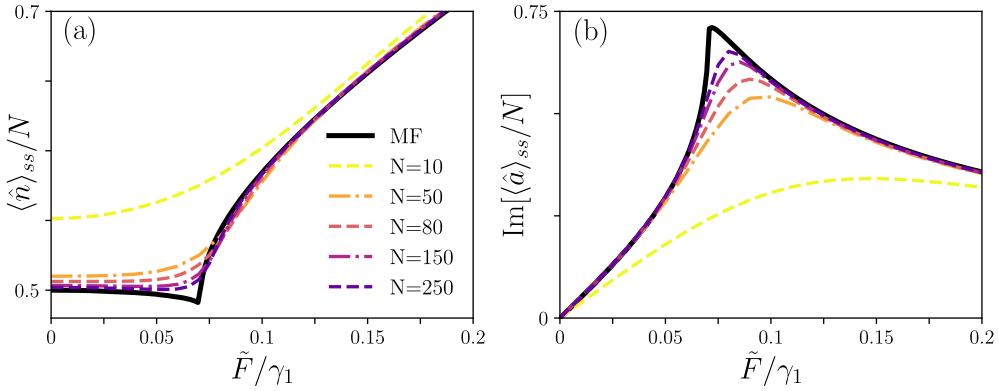

Figure H.3: (a) Solid line $|\tilde{\alpha}|^2$, points $\langle\hat{a}^\dagger\hat{a}\rangle_{ss}/N$. (b) Imaginary part of $\tilde{\alpha}$, and $\langle\hat{a}\rangle_{ss}/\sqrt{N}$. In both panels $\Delta_d/\gamma_1 = 0.1$. As N increases the points approach the mean-field solution, although the sharpest aspects of the transition are smoothed out. Notice that the mean-field results in the limit-cycle phase have been averaged over a period.

The small detuning regime. As we have seen in Sect. H.2, in the region of small detunings strength some approximate analytical results can be obtained. More importantly, in this parameter region the bifurcation between the entrained and unentrained regimes corresponds to an infinite-period bifurcation of the same type as that of the squeezed vdP oscillator. This allows us to explore the emergence of the same type of bifurcation from two different quantum systems. For the dimensionless and rescaled mean-field equation (H.17), the condition of validity for the crucial approximation of making the phase dynamics amplitude-independent [i.e. Eqs. (H.6) and (H.7)] becomes:

$$\tilde{F}/\gamma_1, \Delta_d/\gamma_1 \ll \sqrt{\frac{1}{2}}, \tag{H.19}$$

since $\bar{R} = \sqrt{1/2}$. Moreover, the bifurcation point is now located at:

$$\tilde{F}_c \approx |\Delta_d|\sqrt{\frac{1}{2}}, \tag{H.20}$$

while the fundamental frequency of the limit cycle reads:

$$(\Omega_d/\gamma_1) \approx (\Delta_d/\gamma_1)\sqrt{1-(\tilde{F}/\tilde{F}_c)^2}. \tag{H.21}$$

In this sense, the results of Fig. H.3 are computed for $\Delta_d/\gamma_1 = 0.1$, and hence they might still be accurately captured by these expressions. In particular, a first observation from panel (a) is that the averaged squared amplitude is approximately ≈ 0.5, as expected. However, as the bifurcation is approached the amplitude displays a small modulation with $\tilde{F}$, which indicates that the approximation of assuming a constant average amplitude is not perfect. On the other hand, the bifurcation is numerically found [e.g. as indicated by the cusp in Fig. H.3 (a)] to occur at $\tilde{F}_c/\gamma_1 = 0.0704$, which is very close to the predicted value given by Eq. (H.20), i.e. $\tilde{F}_c/\gamma_1 \approx 0.0707$.

H.5 Fluctuation dynamics in the entrained regime

In the driven vdP oscillator, the entrained regime corresponds to a unique fixed point attractor in the rotating frame. As we shall see, this allows us to understand the fluctuation dynamics in this regime (and for large N) in terms of the linearized dynamics around this

attractor [363]. This is a huge advantage in comparison with the cases in which the stable attractor is a limit cycle (e.g. appendix J) or multistable fixed points (e.g. chapter 6), in which such a linearization procedure finds difficulties: in the limit-cycle case one has to deal with the free phase, i.e. a degree of freedom which is neither stable nor unstable; while in the multistability case one has to deal with fluctuations that make the system jump from one attractor to the another (as in the squeezed case), an effect completely missed if one linearizes the dynamics around each of the fixed points. The advantage of this linearization procedure is that it yields a quadratic master equation for the dynamics of the fluctuations, which is easier to handle than the full non-linear model, and from which we can obtain closed expressions for many important quantities. As we shall see, the accuracy of the linearized model increases with N. Hence, as the infinite-excitation limit is approached, the dynamics of the full quantum model is well understood by the mean-field dynamics supplemented by the fluctuations governed by a quadratic master equation.

Derivation of the linear fluctuation master equation. The main assumption of this approach is that, for $F > F_c$, the amplitude of the system can be decomposed into a large coherent mean-field component plus a small fluctuation term, i.e.:

$$\hat{a} = \alpha_{ss} + \hat{d} \tag{H.22}$$

where the complex amplitude corresponds to that of the stable fixed point of Eq. (H.3) and thus satisfies:

$$0 = -i\Delta\alpha_{ss} + \frac{\gamma_1}{2}\alpha_{ss} - \gamma_2|\alpha_{ss}|^2\alpha_{ss} - F \tag{H.23}$$

as well as the stability condition, i.e. $\lim_{t\to\infty}\alpha(t) = \alpha_{ss}$. Instead, the fluctuation operator $\hat{d}$ corresponds to a bosonic mode obeying the linearized master equation. This is obtained inserting the definition (H.22) into the full master equation of the system, i.e. Eq. (6.1) with Hamiltonian (H.2), and neglecting all terms with more than two fluctuation operators, while making use of the fact that α_{ss} satisfies Eq. (H.23). Then, we arrive at:

$$\frac{d}{dt}\hat{\rho}_d = -i[\hat{H}_d, \hat{\rho}_d] + \gamma_1\mathcal{D}[\hat{d}^\dagger]\hat{\rho}_d + \gamma_\downarrow\mathcal{D}[\hat{d}]\hat{\rho}_d, \tag{H.24}$$

with

$$\hat{H}_d = \Delta_d\hat{d}^\dagger\hat{d} + i(\eta_d^*\hat{d}^2 - \eta_d\hat{d}^{\dagger 2}) \tag{H.25}$$

as first obtained in Ref. [363]. Notice that there are no terms linear in $\hat{d}$ as these can be grouped in a term proportional to the right-hand side of Eq. (H.23), and thus vanish. The new parameters are defined as:

$$\gamma_\downarrow = 4\gamma_2|\alpha_{ss}|^2 = 4\gamma_1|\tilde{\alpha}_{ss}|^2, \quad \eta_d = \frac{\gamma_2}{2}\alpha_{ss}^2 = \frac{\gamma_1}{2}\tilde{\alpha}_{ss}^2, \tag{H.26}$$

where $\tilde{\alpha}_{ss}$ is the amplitude of the stable fixed point of Eq. (H.17). We have rewritten the parameters in terms of this scaled amplitude to highlight the fact that the dynamics of $\hat{d}$ *is independent of* $N = (\gamma_2/\gamma_1)^{-1}$. In this sense, we can also rewrite Eq. (H.22) as:

$$\hat{a} = \sqrt{N}\tilde{\alpha}_{ss} + \hat{d}, \tag{H.27}$$

which illustrates that, in the linearization approach, the noiseless mean-field contribution is of order $\sim O(\sqrt{N})$, and thus much larger than that of the fluctuation term, presumably of order $\sim O(1)$ (as its dynamics is independent of N). This provides a nice perspective on why the 'mean-field law' emerges from the quantum model as $N \to \infty$. Moreover, this $\sqrt{N}$ enhancement of the mean-field contribution over the contribution of the fluctuations is also found in other quantum-optical systems[3] after a system-size expansion [59].

[3] In these other systems the particular expression of N might be different, however, the infinite-excitation limit also involves $N \to \infty$.

Fluctuation dynamics and power spectrum. As anticipated, the linearized model given by Eqs. (H.24) and (H.25) is bilinear in the fluctuation operators. Moreover, it is parity symmetric. From these two observations we deduce that the stationary state of the fluctuation master equation obey Gaussian statistics with zero mean, i.e. $\langle \hat{d} \rangle_{ss} = 0$. Therefore, in the linearization approach, the incoherent part of the emission spectrum, or power spectrum, is only determined by the fluctuation dynamics:

$$\begin{aligned} S_{inc}(\omega) &= \int_{-\infty}^{\infty} d\tau e^{-i\omega\tau} [\langle \hat{a}^\dagger(\tau)\hat{a}(0)\rangle_{ss} - \langle \hat{a}^\dagger(\tau)\rangle_{ss}\langle \hat{a}\rangle_{ss}] \\ &= \int_{-\infty}^{\infty} d\tau e^{-i\omega\tau} \langle \hat{d}^\dagger(\tau)\hat{d}(0)\rangle_{ss}, \end{aligned} \tag{H.28}$$

where the second equality follows from inserting the definition (H.22) and $\langle \hat{d} \rangle_{ss} = 0$. Notice that the contribution of the coherent noiseless amplitude α_{ss} in $\hat{a}$ is behind the delta peaks of the emission spectrum, reported in Fig. H.2 (a), and which we have removed by considering the incoherent spectrum. From the quantum regression theorem (see chapter 2) it follows that the fluctuation two-time correlations are described by:

$$\begin{aligned} \frac{d}{d\tau}\langle \hat{d}^\dagger(\tau)\hat{d}(0)\rangle_{ss} &= \Big[i\Delta_d - \frac{(\gamma_\downarrow - \gamma_1)}{2} \Big] \langle \hat{d}^\dagger(\tau)\hat{d}(0)\rangle_{ss} - 2\eta_d^* \langle \hat{d}(\tau)\hat{d}(0)\rangle_{ss}, \\ \frac{d}{d\tau}\langle \hat{d}(\tau)\hat{d}(0)\rangle_{ss} &= -\Big[i\Delta_d + \frac{(\gamma_\downarrow - \gamma_1)}{2} \Big] \langle \hat{d}(\tau)\hat{d}(0)\rangle_{ss} - 2\eta_d \langle \hat{d}^\dagger(\tau)\hat{d}(0)\rangle_{ss}, \end{aligned} \tag{H.29}$$

where the initial conditions are $\langle \hat{d}^\dagger \hat{d} \rangle_{ss}$ and $\langle \hat{d}^2 \rangle_{ss}$. While the system of equations (H.29) can be analytically solved, the resulting expressions are too cumbersome to provide insight and we will not report them here. On the other hand, it is enough to state the general form of the relevant two-time correlation:

$$\langle \hat{d}^\dagger(\tau)\hat{d}(0)\rangle_{ss} = c_+ e^{-\lambda_+ \tau} + c_- e^{-\lambda_- \tau}, \tag{H.30}$$

where the coefficients $c_\pm$ depend on the parameters of the system, and the eigenvalues read:

$$\lambda_\pm/\gamma_1 = \frac{1}{2} - 2|\tilde{\alpha}_{ss}|^2 \pm \sqrt{|\tilde{\alpha}|_{ss}^4 - (\Delta_d/\gamma_1)^2}. \tag{H.31}$$

For small detunings, the term inside the square root is always positive, as the squared amplitude typically grows with $\tilde{F}$ and thus it takes larger values than those for the limit cycle [see Fig. H.3 (a)], while Δ_d is assumed to be much smaller than the amplitude of the cycle [see Eq. (H.19)]. Hence, in the small detuning regime, $\lambda_\pm$ are always real and the dynamics of the fluctuations is overdamped. On the other hand, for large detunings and near the bifurcation (where $|\tilde{\alpha}_{ss}|^2$ takes the smallest values), the eigenvalues can become complex-valued, and the fluctuation dynamics become underdamped [363]. This is the regime in which Ref. [363] focused, and it is a precursor of the eventual Hopf bifurcation through which the fixed point attractor losses its stability for large detunings, as we have anticipated before.

Universal asymptotic behavior of the observed frequency. In Fig. H.4 we compare the observed frequency computed with the full quantum model (color-broken lines) and that computed with the linearized model (black-solid line). The results for the linearized model are shown for $\tilde{F} > \tilde{F}_c$. We observe that the linearized model captures accurately the behavior of the observed frequency in the entrained regime. Indeed, increasing N, the results of the full quantum model converge to those of the linearized model for smaller $\tilde{F}$. We recall that the results of the linearized model are independent of N. Hence, the asymptotic behavior of the observed frequency is universal, in the sense that the curves for different N eventually converge to the N-independent results. This

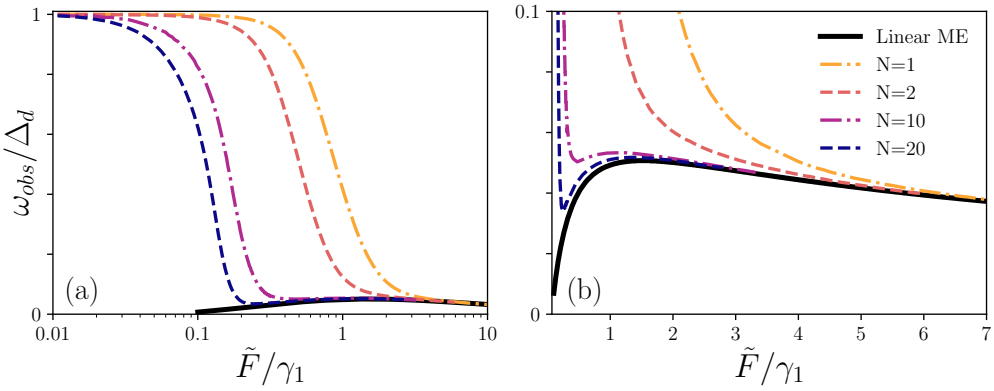

Figure H.4: (a) Color-broken lines: ratio of the observed frequency and the detuning $\omega_{\rm obs}/\Delta_d$ computed from the full quantum model [Eq. (6.1) and (H.2)] for different values of N and varying $\tilde{F}$. Black-solid line: observed frequency computed from the linear master equation [Eq. (H.24) and (H.25)] above the critical point $\tilde{F}_c$. (b) Region of panel (a) of small observed frequency and in linear scale. The legend is shared by the two panels, and in both cases $\Delta_d/\gamma_1 = 0.1$.

essentially means that for large enough $\tilde{F}$, the number of excitations in the driven QvdP oscillator becomes sufficiently large so that the description in terms of a mean-field amplitude plus a fluctuation term [i.e. Eq. (H.22)] captures accurately the physics of the system.

At this point, it is worth commenting that for the detuning considered in Fig. H.4, the eigenvalues $\lambda_\pm$ are real-valued. Then, the following question arises: if the power spectrum corresponds to the Fourier transform of a function made of two exponential decays (i.e. Eq. (H.30) with real $\lambda_\pm$), why is the observed frequency shifted from zero? Mathematically, the answer is rooted in the fact that the coefficients $c_\pm$ are complex valued[4], while the following identity holds:

$$\begin{aligned} S_{inc}(\omega) &= \int_{-\infty}^{\infty} d\tau e^{-i\omega\tau}\langle\hat{d}^\dagger(\tau)\hat{d}(0)\rangle_{ss} \\ &= 2\mathrm{Re}\Big[\int_0^{\infty} d\tau e^{-i\omega\tau}\langle\hat{d}^\dagger(\tau)\hat{d}(0)\rangle_{ss}\Big], \end{aligned} \tag{H.32}$$

which follows from the fact that two-time correlations in the stationary state only depend on the difference of time arguments, τ, and on the operator ordering (i.e. if $\langle\hat{d}^\dagger(t_1)\hat{d}(t_2)\rangle_{ss}$, on whether $t_1 > t_2$ or $t_2 > t_1$ with $\tau = |t_1 - t_2|$, see chapter 2 or [59]), and thus: $\langle\hat{d}^\dagger(-\tau)\hat{d}(0)\rangle_{ss} = \langle\hat{d}^\dagger(0)\hat{d}(\tau)\rangle_{ss} = \big(\langle\hat{d}^\dagger(\tau)\hat{d}(0)\rangle_{ss}\big)^*$[5]. Physically, this is the same kind of interference effect found in chapters 4 and 5, in which the presence of multiple 'eigendecay channels' leads to an asymmetric lineshape, or even to transparency windows.

Behavior of the Liouvillian gap. In Fig. H.5 we compare the real part of the leading eigenvalue for the full quantum model (color points), i.e. $\mathrm{Re}[\lambda_1]$, with the corresponding one for the linearized model (solid lines), which is $\mathrm{Re}[\lambda_+]$ given in Eq. (H.31). For the small values of the detuning considered in Fig. H.5, λ_+ is real-valued. In panel (a) we can see that, for a fixed detuning ($\Delta_d/\gamma_1 = 0.1$), the results for the full quantum model converge progressively to those of the linearized model as N and $\tilde{F}/\gamma_1$ increase. In panel

[4]Notice that $c_\pm$ can be complex-valued; however, their sum is constraint to be real-valued and to satisfy $c_+ + c_- = \langle\hat{d}^\dagger\hat{d}\rangle_{ss}$, since the solution of the system of equations (H.29) is constraint to satisfy the initial condition $\langle\hat{d}^\dagger(\tau=0)\hat{d}\rangle_{ss} = \langle\hat{d}^\dagger\hat{d}\rangle_{ss}$.

[5]Therefore, the formal expression for the incoherent spectrum is: $S_{inc}(\omega) = 2\big[(R_+|\lambda_+| + I_+\omega)/(\omega^2+\lambda_+^2) + (R_-|\lambda_-| + I_-\omega)/(\omega^2+\lambda_-^2)\big]$, with $R_\pm = \mathrm{Re}[c_\pm]$ and $I_\pm = \mathrm{Im}[c_\pm]$. This expression is not generally peaked at $\omega = 0$, as in the case $I_\pm = 0$.

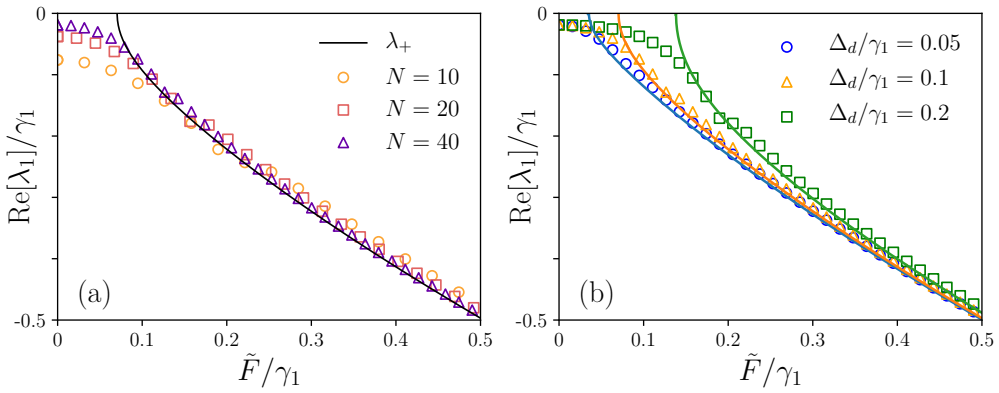

Figure H.5: (a) Color points: $\mathrm{Re}[\lambda_1/\gamma_1]$ computed from the full quantum model for various N and for $\Delta_d/\gamma_1 = 0.1$. Black-solid line: λ_+ as given in Eq. (H.31) for the same detuning. (b) Color points $\mathrm{Re}[\lambda_1/\gamma_1]$ computed from the full quantum model for various detunings Δ_d/γ_1 and $N = 40$. In color-solid lines we have plotted the corresponding λ_+ for each of the detunings (with the same color code as for the points).

(b) we fix $N = 40$ and we plot three different detunings, for which we observe the same agreement with the linear results as the forcing strength increases. Importantly, we find that for small detunings, $\lambda_+ = 0$ at the classical bifurcation point, i.e. the linearized model (H.24) displays a *Liouvillian gap closure* at $\tilde{F}_c$. In contrast, for large detunings, λ_+ becomes complex-valued near the bifurcation, and only $\mathrm{Re}[\lambda_+] = 0$ at the classical bifurcation point, while $\mathrm{Im}[\lambda_+] \neq 0$ [363].

Interestingly, the behavior of λ_1 as computed from the full quantum model displays a crossover between two regimes as the forcing strength is progressively increased: at first, it displays the typical behavior of the limit-cycle regime, i.e. it does not vary significantly with $\tilde{F}$ while it diminishes with N (see panel (a) and compare with the results of chapter 7 and appendix J); instead, as the forcing strength is increased, it progressively turns to the behavior of the fixed point regime, as captured by λ_+. Notice that the full quantum model displays an EP at $\tilde{F}_{EP} > \tilde{F}_c$, in which λ_1 become complex-valued for $\tilde{F} < \tilde{F}_{EP}$ (for the cases considered in Fig. H.5 the EP lies in the range $0.2 > \tilde{F}_{EP}/\gamma_1 > \tilde{F}_c/\gamma_1$). Moreover, it turns out that $\tilde{F}_{EP}$ approaches $\tilde{F}_c$ as N is increased (not shown), which rises the question on whether the EP and the classical bifurcation point are also intimately related in the case of the driven QvdP oscillator (as for the squeezed QvdP oscillator, see chapter 7).

Finally, it is also interesting to comment that the leading decay rate, $\Gamma_1 = |\mathrm{Re}[\lambda_1]|$, increases with $\tilde{F}$, i.e. as the system becomes more entrained the decay rates of the fluctuations become larger. This also manifests as the fact that for a fixed $\tilde{F} > \tilde{F}_c$, decreasing the detuning results in larger $|\lambda_+|$ [see Fig H.5 panel (b)]. Indeed, this explains what we have observed in Fig. H.2 (a), i.e. that as the system becomes entrained the width of the incoherent lineshape becomes larger while its height diminishes.

H.6 Discussion and outlook: DPT and time-crystals?

In this appendix, we have analyzed the entrainment dynamics of the driven QvdP oscillator and we have reviewed the main signatures of this phenomenon in the quantum regime. An important result is that the entrained regime corresponds to a single fixed point attractor in the rotating frame. As a consequence, and as the infinite-excitation limit is approached, the entrainment dynamics becomes accurately described by the mean-field model supplemented by fluctuations that follow a linearized quadratic master equation, i.e. Gaussian fluctuations.

Entrainment and fluctuations, driven vs squeezed QvdP oscillator. For small detunings, the fluctuations in the driven QvdP oscillator follow an overdamped dynamics in which the characteristic decay rates increase as the system deepens into the entrained regime (i.e. when decreasing the detuning with a fixed forcing, or when increasing the forcing with a fixed detuning). Physically, this can be interpreted as *the fixed point attractor becoming more stable*, i.e. the fluctuations around the mean-field noiseless amplitude decay faster. Moreover, this manifests in the emission spectra in which we find that the Lorentzian-lineshape associated to the fluctuations becomes wider and shorter, while the delta peak associated to the coherent amplitude increases its height. The increasing linewidth of the *incoherent spectrum* has been reported previously [166], and as commented in chapter 6, it contrasts with what happens in the squeezed QvdP oscillator, in which as the system becomes entrained the linewidth diminishes. As discussed in chapter 6, this is rooted in the different physical origin of the dominant fluctuation mode in the two cases: here, this describes the fluctuations around a single fixed point attractor, which decay faster as the system becomes entrained; while in the squeezed QvdP oscillator, this describes the jumps between the two possible phases, which become less frequent as the system becomes entrained. Therefore, despite these particular differences in the underlying fluctuation dynamics (and their manifestation in the emission spectra), we find that *in both cases* the emergence of entrainment has the same general implication: the importance of the coherent response of the system is enhanced, while the effects of the (different) incoherent process caused by fluctuations become suppressed.

Outlook. Finally, we identify some questions that remain open and that would be interesting to address in future work, in order to further explore the relation between synchronization and driven-dissipative phenomena:

i) Which is the role of the EP involving $\lambda_{1,2}$ in this system? We have briefly commented that the full quantum model displays an EP, and that $\tilde{F}_{EP}$ seems to approach $\tilde{F}_c$ when increasing N. For small detunings, this seems to be in agreement with the case of the squeezed QvdP oscillator (see chapter 7), which might indicate that this is the Liouvillian spectral signature of a SNIC bifurcation. However, for large detunings, the driven QvdP oscillator displays a different kind of bifurcation (a Hopf bifurcation). Then, what happens to this EP and how can this be interpreted?

ii) The closure of the Liouvillian gap for small detunings in the linearized model seems to indicate that the system displays a DPT at the synchronization transition (at least for small detunings). However, in stark contrast to the squeezed QvdP oscillator case, this gap closure seems to occur just at the critical point and not in a whole region, which can make it more difficult to observe in the full model. Can we confirm this gap closure studying the Liouvillian gap for the full model?

iii) Does the limit-cycle regime of this model correspond to a continuous time-crystal? The mean-field seems to indicate so, while in appendix J we find that the case for $F = 0$ is a continuous time-crystal. Moreover, the results of Fig. H.5 (a) for different N and small F seem to support the affirmative answer. Can we confirm this with a detailed finite-size analysis?

iv) Are there some universal critical behavior associated to the SNIC bifurcation that can be unveiled studying the driven and the squeezed QvdP oscillator? This could

be a common set of exponents characterizing how the EP approaches the bifurcation point, or how the fundamental decay rates in the limit-cycle phase vanish. Moreover, this would build up with recent work, as Ref. [136], in which the critical properties of DPTs are studied in search for genuine non-equilibrium universality classes.

APPENDIX I

Metastable dynamics

In this appendix we present some technical discussions and details supplementing chapter 6. We first write down the expression for one-time and two-time expectations using the Liouvillian formalism for the case of the squeezed QvdP oscillator. We later present some additional details in the formalism of quantum metastability [162, 354]. We end up discussing the classical stochastic dynamics of a two state process.

I.1 Expectation values in the Liouvillian formalism

Here, we recall some results of the eigenmode decomposition of the dynamics (see chapter 2). Notice that except for spectral singularities [209], the Liouvillian eigenmatrices form a biorthogonal basis that can be normalized by means of the Hilbert-Schmidt product: $\mathrm{Tr}[\hat{\sigma}_j^\dagger \hat{\rho}_k] = \delta_{jk}$. Moreover, in case the real part of the eigenvalues is negative, the corresponding eigenmodes are traceless, and hence they are not physical states [35]. In this case we can choose whether to rescale $\hat{\sigma}_j^\dagger$ or $\hat{\rho}_j$ freely, as long as they satisfy the normalization condition.

Then, away from EPs, we can use Eq. (6.5) to decompose the state of the system at any time. Recall that by taking the trace over a given operator we can obtain the dynamics of its expected values (see chapter 2). In particular for the amplitude dynamics we obtain:

$$\langle \hat{a}(t) \rangle = \sum_{j \geq 1} \mathrm{Tr}[\hat{\sigma}_j^\dagger \hat{\rho}(0)] \mathrm{Tr}[\hat{a}\hat{\rho}_j] e^{\lambda_j t}. \tag{I.1}$$

Here, we have used the fact that the Liouvillian displays a parity symmetry, and thus the eigenmodes are either parity symmetric or parity antisymmetric, and the stationary state is parity symmetric. In fact, it follows that for operators with a given symmetry, only eigenmodes with the same symmetry contribute to their dynamics. For the particular case of the amplitude only parity antisymmetric eigenmodes contribute to the sum, as $\mathrm{Tr}[\hat{a}\hat{\rho}_j] = 0$ is identically zero if $\mathcal{Z}_2\hat{\rho}_j = \hat{\rho}_j$, which implies $\langle \hat{a} \rangle_{ss} = 0$. Notice that this is also the case for the amplitude two-time correlations calculated in the stationary state:

$$\langle \hat{a}^\dagger(\tau)\hat{a}(0) \rangle_{ss} = \sum_{j \geq 1} \mathrm{Tr}[\hat{\sigma}_j^\dagger \hat{a}\hat{\rho}_{ss}] \mathrm{Tr}[\hat{a}^\dagger \hat{\rho}_j] e^{\lambda_j \tau}, \tag{I.2}$$

which follows from $\langle \hat{a}^\dagger(\tau)\hat{a}(0)\rangle_{ss} = \mathrm{Tr}\big[\hat{a}^\dagger e^{\mathcal{L}\tau}(\hat{a}\hat{\rho}_{ss})\big]$ for $\tau \geq 0$ [59] (see also chapter 2), and $t = 0$ denotes an arbitrary time-origin in the stationary state. Notice that in the absence of parity symmetry there can be a non-zero contribution from $j = 0$ in Eq. (I.2), i.e. an additional term that reads $\langle \hat{a}^\dagger\rangle_{ss}\langle \hat{a}\rangle_{ss} \neq 0$. Since $\lambda_0 = 0$, this term is time-independent and yields a Dirac delta when Fourier transformed. This contribution is known in some contexts as the coherent part of the emission spectrum [59].

I.2 Metastable dynamics

I.2.1 Additional definitions and formal solution

As we have explained in the main text, the long-time dynamics of the system is restricted to the so-called metastable manifold [162, 354]. Notice that since in the whole region in which $\Gamma_1/\Gamma_2 \neq 1$, λ_1 is real, we find that $\hat{\sigma}_1$ and $\hat{\rho}_1$ are Hermitian. This property enables to parametrize the metastable manifold in terms of the extreme metastable states (EMSs) defined in Eq. (6.15), as well as the projectors on these states, defined by:

$$\hat{P}_1 = \frac{1}{\Delta c}(\hat{\sigma}_1 - c_{min}\mathbb{1}), \quad \hat{P}_2 = \frac{1}{\Delta c}(-\hat{\sigma}_1 + c_{max}\mathbb{1}), \tag{I.3}$$

with $\Delta c = c_{max} - c_{min}$, while c_{max} and c_{min} are the maximum and minimum eigenvalues of $\hat{\sigma}_1$[1]. As commented, numerical analysis reveals that $c_{min} = -c_{max}$ for the considered regime, i.e. when $\Gamma_1/\Gamma_2 < 1$.

The projection of the initial state onto the metastable manifold can be decomposed as the projection onto the EMSs:

$$\mathcal{P}\hat{\rho}(0) = \mathrm{Tr}[\hat{P}_1\hat{\rho}(0)]\hat{\mu}_1 + \mathrm{Tr}[\hat{P}_2\hat{\rho}(0)]\hat{\mu}_2. \tag{I.4}$$

Importantly, we have that by construction:

$$\hat{P}_{1,2} \geq 0, \quad \hat{P}_1 + \hat{P}_2 = \mathbb{1} \quad \mathrm{Tr}[\hat{P}_i\hat{\mu}_j] = \delta_{ij}. \tag{I.5}$$

Moreover, we can define the expectation values:

$$p_{1(2)}(t) = \mathrm{Tr}[\hat{P}_{1(2)}\hat{\rho}(t)] \tag{I.6}$$

It follows that $p_{1,2}(t)$ are positive and they sum to one, as stated in chapter 6. Hence, $p_{1,2}(t)$ can be interpreted as probabilities as stated in the main text. Notice that this is only the case for the EMSs, as they form the only basis in which $\hat{P}_{1,2}$ are positive in all the metastable manifold [162]. The long-time dynamics can be recasted in this basis leading to Eq. (6.18), which in virtue of the properties of $p_{1,2}(t)$ can be interpreted as a stochastic process [162]. Then the solution to this equation is:

$$p_{1(2)}(t) = \frac{p^0_{1(2)}}{2}(1 + e^{-\Gamma_1 t}) + \frac{p^0_{2(1)}}{2}(1 - e^{-\Gamma_1 t}), \tag{I.7}$$

where the initial conditions are given by the projection of the initial state onto the metastable manifold in terms of the EMSs: $p^0_{1(2)} = \mathrm{Tr}[\hat{P}_{1(2)}\hat{\rho}(0)]$.

[1]Notice that from orthogonality $\mathrm{Tr}[\hat{\sigma}_1\hat{\rho}_{ss}] = 0$ it follows that $c_{min} \leq 0$, while since $\hat{\sigma}_1$ is Hermitian, it follows that all its eigenvalues are real.

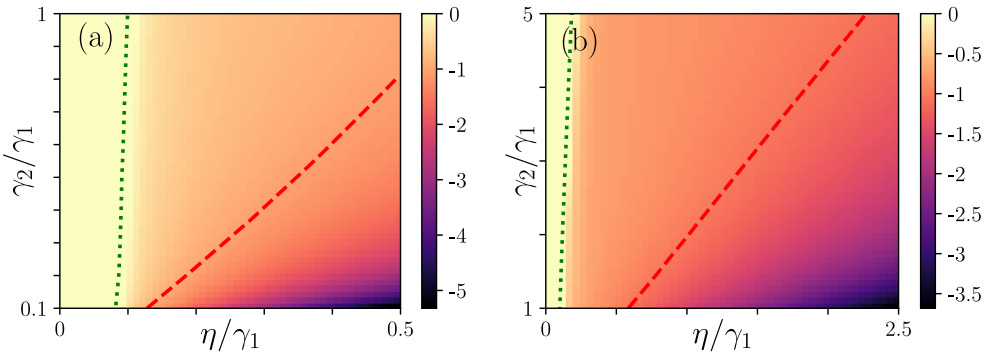

Figure I.1: Colormaps: $\log_{10}[D(\hat{\mu}_1, \hat{\mu}_1')]$ varying γ_2/γ_1 and η/γ_1. Panel (a) covers in detail the small values of γ_2/γ_1 and η/γ_1, while panel (b) displays a wider range of larger values. The regions in which $\Gamma_1 = \Gamma_2$, i.e. for $\eta \leq \eta_{EP}$ have been colored in pale yellow. Green-dotted lines: contour indicating the EP for different values of γ_2/γ_1. Red-dashed lines: contours indicating $\Gamma_1/\Gamma_2 = 0.1$.

I.2.2 Approximate metastable states

Finally, we compare the exact expressions for the EMSs, i.e. $\hat{\mu}_1 = \hat{\rho}_{ss} + c_{max}\hat{\rho}_1$ with the approximate ones, that we distinguish in this appendix with a prime, i.e.:

$$\hat{\mu}_1' = \hat{\rho}_{ss} + \hat{\rho}_1, \quad \hat{\mu}_2' = \hat{\rho}_{ss} - \hat{\rho}_1. \tag{I.8}$$

We do so by computing the trace distance between both, defined as

$$D(\hat{\mu}_1, \hat{\mu}_1') = \frac{1}{2}\mathrm{Tr}[\sqrt{(\hat{\mu}_1 - \hat{\mu}_1')^\dagger(\hat{\mu}_1 - \hat{\mu}_1')}], \tag{I.9}$$

which we plot in Fig. I.1. Notice that in this figure we have assigned the value one to the region below the EP in which $\Gamma_1 = \Gamma_2$, which we have delimited by a green-dotted line in order to highlight that it is not part of the analysis. Moreover, we have used a red-dashed line to indicate the contour $\Gamma_1/\Gamma_2 = 0.1$. Comparing Fig. I.1 (a), (b) with Fig. I.1 (a), (b), we can see how the trace distance becomes vanishingly small as Γ_1/Γ_2 becomes small. Indeed both quantities seem to be very well correlated, as can be checked from these figures. This means that in the regions in which there is a huge separation of time-scales, and hence it is meaningful to define the effective dynamics (6.18), we have that $\hat{\mu}_1 \approx \hat{\mu}_1'$ to a very good approximation. The same result is found for $\hat{\mu}_2$ and $\hat{\mu}_2'$ (not shown). Then, as commented in the main text, in the metastable regime we can use the more convenient expressions for the EMSs and also for the projectors: i.e. $\hat{\mu}_{1,2} \approx \hat{\mu}_{1,2}'$ and $\hat{P}_{1,2} \approx \hat{P}_{1,2}'$, with

$$\hat{P}_1' = \frac{1}{2}(\mathbb{1} + \hat{\sigma}_1), \quad \hat{P}_2' = \frac{1}{2}(\mathbb{1} - \hat{\sigma}_1). \tag{I.10}$$

I.3 Classical two-state stochastic process

In this appendix we consider Eq. (6.18) as a fully classical two-state stochastic process and we compute the amplitude dynamics and two-time correlations according to the classical rules [88]. In particular, we consider that state 1 is characterized by the complex amplitude $\alpha_1 = \langle \hat{a} \rangle_1$, while state 2 by the complex amplitude $\alpha_2 = -\langle \hat{a} \rangle_1$. The solution for the classical two-state process is again given by Eq. (I.7), while the difference with the effective long-time quantum dynamics resides, in principle, in the recipe to compute statistical quantities.

Firstly, we have that the classical averaged amplitude is given by [88]:

$$\overline{\alpha(t)} = \sum_{j=1}^{2} \alpha_j p_j(t), \tag{I.11}$$

where the overbar indicates a classical average over the stochastic process. As commented in the main text this expression coincides with Eq. (6.23). Notice that the stationary value for the amplitude is zero, i.e. $\overline{\alpha_{ss}} = 0$, as expected. Secondly, the classical recipe for the two-time amplitude correlations in the stationary state is given by [88]:

$$C(\tau) = \lim_{t\to\infty} \overline{\alpha^*(t+\tau)\alpha(t)} = \sum_{i=1}^{2}\sum_{j=1}^{2} \alpha_i^* \alpha_j \tilde{p}_{ij}(\tau) p_j(t\to\infty), \tag{I.12}$$

where we have defined the tilded probabilities $\tilde{p}_{ij}(\tau)$ as the solutions $p_i(\tau)$ given in Eq. (I.7) with the special initial condition $p_j^{(0)} = 1$. From this expression we recover the result quoted in the main text, that is $C(\tau) = |\alpha_1|^2 e^{-\Gamma_1 \tau}$.

APPENDIX J

Semiclassical approach for the squeezed QvdP oscillator

In this appendix we present the details of the semiclassical approach discussed in chapter 7. Specifically, we present a semiclassical approximation of the dynamics of the squeezed QvdP oscillator in which the classical equations of motion are supplemented by Gaussian fluctuations and which parallels previous studies of the single-mode laser [351, 386]. Both cases of vanishing squeezing strength and finite one are addressed.

J.1 Results in the absence of squeezing

U(1) symmetry. We start introducing some useful expressions that we will be of later use and following from the $U(1)$-symmetry for the case $\eta = 0$. As shown in Ref. [168] the eigenmodes in the Fock basis have the following general form:

$$\hat{\rho}_j = \sum_n C_n^{(j)} |n\rangle\langle n-k|, \tag{J.1}$$

where k is an integer and $C_n^{(j)}$ are complex coefficients and $n-k$ is constraint to be positive. Notice that the particular value of k determines the symmetry sector to which the eigenmode belongs, as $\mathcal{U}_\phi \hat{\rho}_j = e^{-i\phi k}\hat{\rho}_j$. Moreover, since the stationary state must have a unit trace and must be $U(1)$-symmetric [35, 268], it belongs to the $k = 0$ sector.

Similarly to what happens with parity-symmetry, the contribution to the dynamics of an observable from eigenmodes that belong to a different symmetry eigensector vanish identically. This means that as

$$\mathcal{U}_\phi (\hat{a}^\dagger)^l \hat{a}^m = e^{i\phi(m-l)} (\hat{a}^\dagger)^l \hat{a}^m, \tag{J.2}$$

only eigenmodes of the sector $k = m-l$ contribute to the dynamics of this observable. This can also be deduced using the general form (J.1) from which it is clear that a necessary condition for $\mathrm{Tr}[(\hat{a}^\dagger)^l \hat{a}^m \hat{\rho}_j] \neq 0$ is that $k = m - l$. Formally, we can write

$$\langle (\hat{a}^\dagger)^l \hat{a}^m(t)\rangle = \sum_{j\in u_k} \mathrm{Tr}[\hat{\sigma}_j^\dagger \hat{\rho}(0)]\mathrm{Tr}[(\hat{a}^\dagger)^l \hat{a}^m \hat{\rho}_j] e^{\lambda_j t}, \tag{J.3}$$

where $j \in u_k$ means that the sum is restricted to the eigenmodes of the symmetry sector $k = m - l$. Furthermore, the different symmetry sectors can be identified by the imaginary parts of the eigenvalues in the Laboratory frame. This follows from the fact that in the rotating frame with ω_0, the spectrum of the Liouvillian is found to be real, while the eigenvalues in this frame and in the laboratory frame are related by [168]

$$\lambda_j = \lambda_j^R - ik\omega_0, \tag{J.4}$$

where k is the symmetry sector and we have punctually used the superscript 'R' to denote the eigenvalues in the frame rotating with ω_0. Thus, the different multiples of ω_0 belong to the different symmetry sectors. This correspondence between the symmetry eigensector of the observable and that of the contributing eigenmodes is the basis of an important ansatz that we use below to connect the semiclassical results with the Liouvillian spectrum.

Phase space representation and semiclassical approximation. We now write the master equation in terms of the Wigner distribution [59, 67] (see also appendix A):

$$\begin{aligned}\partial_t W(\alpha,\alpha^*,t) = \Big\{ &(\partial_\alpha \alpha + \partial_{\alpha^*}\alpha^*)\Big[\gamma_2(|\alpha|^2-1) - \frac{\gamma_1}{2}\Big] \\ &+ \partial_\alpha\partial_{\alpha^*}\big[\frac{\gamma_1}{2} + \gamma_2(2|\alpha|^2-1)\big] + \frac{\gamma_2}{4}(\partial_\alpha^2\partial_{\alpha^*}\alpha + \partial_{\alpha^*}^2\partial_\alpha\alpha^*)\Big\} W(\alpha,\alpha^*,t).\end{aligned} \tag{J.5}$$

Recall that in this appendix we work in a frame rotating at ω_0 instead of ω_s, as $\eta = 0$ and hence ω_s does not play any role. The semiclassical approximation consists in neglecting third order partial derivatives while approximating the diffusion coefficient by the mean-field amplitude for $\eta = 0$ [67], i.e. $|\alpha|^2 \approx \gamma_1/(2\gamma_2)$ [see Eq. (6.11)]. This approximation becomes better and better as we approach the limit $N \to \infty$ ($\gamma_2/\gamma_1 \to 0$) [67]. Then the *semiclassical* equation for the Wigner distribution reads

$$\partial_t W(\alpha,\alpha^*,t) = \Big\{(\partial_\alpha\alpha + \partial_{\alpha^*}\alpha^*)\Big[\gamma_2|\alpha|^2 - \frac{\gamma_1}{2}\Big] + \frac{3\gamma_1}{2}\partial_\alpha\partial_{\alpha^*}\Big\} W(\alpha,\alpha^*,t). \tag{J.6}$$

Essentially, we have replaced the original quantum dynamics as described by the general partial differential equation (J.5), by a Fokker-Planck equation for the Wigner distribution [59]. Notice that from now on we will use $W(\alpha,\alpha^*,t)$ as a classical probability distribution and α (α^*) as classical variables, and hence to analyze Eq. (J.6) using the classical stochastics methods [88, 351].

Amplitude and phase decoupling. The classical stochastic process described by Eq. (J.6) has been studied in [351] or [386] for instance. Following [351] we define the change of variables $\alpha = \sqrt{r}e^{i\phi}$ and we rewrite Eq. (J.6) as

$$\partial_t P(r,\phi,t) = \Big\{ -2\partial_r\big[\frac{\gamma_1}{2} - \gamma_2 r\big]r + \frac{3\gamma_1}{2}\partial_r r\partial_r + \frac{3\gamma_1}{8r}\partial_\phi^2\Big\} P(r,\phi,t), \tag{J.7}$$

where $P(r,\phi,t)$ is the probability distribution in the new polar variables. This manifests that intensity (squared amplitude) and phase are only coupled through the phase-diffusion term. In the regime we are considering, i.e. $N \gg 1$, amplitude fluctuations decay much faster than phase fluctuations [351]. This can be appreciated in some of the numerical results presented recently in Ref. [82]. An approximation that exploits this separation of time-scales consists in linearizing Eq. (J.7) around the classical noiseless intensity, that is defining the small fluctuations

$$r_\delta = r - \bar{r} \quad \text{with} \quad \bar{r} = \gamma_1/(2\gamma_2), \tag{J.8}$$

and neglecting all the terms nonlinear in r_δ [351]. This approximation leads to

$$\partial_t P(r_\delta,\phi,t) = [\gamma_1 \partial_{r_\delta} r_\delta + \frac{3\gamma_1^2}{4\gamma_2}\partial^2_{r_\delta}]P(r_\delta,\phi,t) + \frac{3\gamma_2}{4}\partial^2_\phi P(r_\delta,\phi,t). \tag{J.9}$$

We have splitted the right hand side in two terms in order to highlight that we have two different independent processes: an Ornstein–Uhlenbeck process for r_δ, and a Wiener process for the phase ϕ [88, 351]. Thus, in this approximation r_δ and ϕ are Gaussian random variables characterized by their first two moments. In particular [88]:

$$\begin{aligned} \langle\phi(t)\rangle_c = \phi_0, \quad \langle\phi^2(t)\rangle_c = \frac{3\gamma_2}{2}t + \phi_0^2, \quad \langle r_\delta(t)\rangle_c = r_{\delta,0}e^{-\gamma_1 t}, \\ \langle r_\delta^2(t)\rangle_c = r_{\delta,0}^2 e^{-2\gamma_1 t} + \frac{3\gamma_1}{2\gamma_2}(1-e^{-2\gamma_1 t}), \end{aligned} \tag{J.10}$$

where $\phi_0 = \phi(t=0)$, $r_{\delta,0} = r_\delta(t=0)$, and $\langle\dots\rangle_c$ is to be interpreted as a classical average. Moreover, since $\phi(t)$ is a Gaussian variable, we can use the relation between its moment- and cumulant generating functions to obtain the important result:

$$\langle e^{im\phi(t)}\rangle_c = e^{im\phi_0 - m^2\frac{3\gamma_2}{4}t}, \tag{J.11}$$

where m is an integer. Hence from the fact that r_δ and ϕ follow independent stochastic processes, it follows that

$$\langle(\alpha^*)^l\alpha^m(t)\rangle_c = \langle(\bar r + r_\delta)^{\frac{l+m}{2}}(t)\rangle_c e^{i(l-m)\phi_0 - (l-m)^2\frac{3\gamma_2}{4}t}. \tag{J.12}$$

Analytical expression for the decay rates. In order to obtain an expression for the decay rates, we need to write Eq. (J.12) in a more explicit form. This is done by expanding $\langle(\bar r + r_\delta)^{\frac{l+m}{2}}\rangle_c$ in powers of the small quantity $r_\delta/\bar r$, obtaining an infinite series containing moments of r_δ of all orders, which can be written in terms of Eq. (J.10). In particular, we can use the Gaussian character of r_δ and Eq. (J.10) to rearrange this series in terms of the different possible decay rates:

$$\langle(\alpha^*)^l\alpha^m(t)\rangle_c = \Big[(\bar r^{\frac{l+m}{2}} + c_0) + \sum_{n\geq 1} c_n e^{-n\gamma_1 t}\Big] e^{i(l-m)\phi_0 - (l-m)^2\frac{3\gamma_2}{4}t}, \tag{J.13}$$

where we do not need to explicitly calculate the coefficients c_n for our purposes. Thus, this expansion enables to write $\langle(\alpha^*)^l\alpha^m(t)\rangle_c$ as an infinite series in which each term depends on time only through an exponential, sharing the formal structure with that of the expansion of Eq. (J.3) in terms of the Liouvillian eigenmodes. Moreover, notice the clear separation of time scales between amplitude fluctuations, with a short decay time-scale $\sim\gamma_1^{-1}$, and phase-fluctuations, with a long decay time-scale $\sim\gamma_2^{-1}$.

Importantly, our ansatz consists in considering the decay rates appearing in Eq. (J.13) as the large-N approximation of the corresponding Liouvillian decay rates for the symmetry sector $k = m - l$. That is, we postulate the general expression

$$\Gamma_{k,n} = \frac{3k^2\gamma_2}{4} + n\gamma_1 \tag{J.14}$$

for the n decay rates of each k symmetry sector. Of course we must proceed with care and assess numerically the validity of such statement, as we have obtained this expression after several approximations and guesswork. This is what we do in Fig. J.1. As we can see, Eq. (J.14) is a very good approximation for the fundamental decay rates $n = 0$ [Fig J.1 (a)] and also for $n = 1$ [Fig J.1 (b)]. For $n > 1$, Eq. (J.14) generally overestimates the decay rates and the agreement is lost (not shown), although importantly, it still predicts

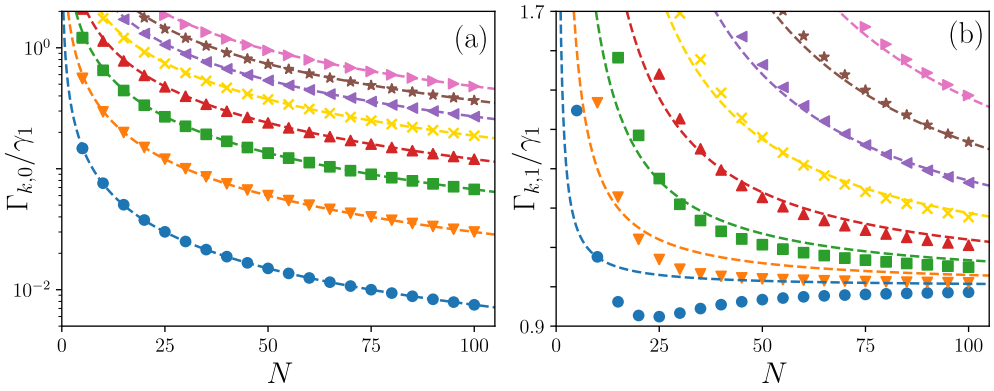

Figure J.1: (a) Comparison of the exact fundamental decay rates in points (Γ_k), and semiclassical expression in dashed lines ($\Gamma_{k,n=0}$). Blue circles $k = 1$, orange downward triangles $k = 2$, green squares $k = 3$, red upward triangles $k = 4$, yellow crosses $k = 5$, purple leftward triangles $k = 6$, brown stars $k = 7$, and ping rightwards triangles $k = 8$. (b) Same as panel (a) but considering the next excitations of each eigensector compared to $\Gamma_{k,n=1}$ in dashed lines. Parameters: $\eta/\gamma_1 = 0$.

correctly that the gap between the different bands of modes is of the order of $\sim \gamma_1$. Thus, Eq. (J.14) is truly valuable as it describes accurately the two features occurring in the limit $N \to \infty$ in which we are interested: it captures how the lifetime of the infinite fundamental eigenmodes diverges, and it predicts that the decay rate of the rest of eigenmodes saturate to a finite value at least as large as γ_1. These are the two basic features related to the spontaneous breaking of continuous time-translation symmetry that we have discussed in the chapter 7.

J.2 Non-zero squeezing strength

In the presence of squeezing and in the rotating frame with ω_s, the following terms must be added to right-hand side of Eq. (J.5):

$$\big[(2\eta\alpha^* + i\Delta\alpha)\partial_\alpha + (2\eta\alpha - i\Delta\alpha^*)\partial_{\alpha^*}\big]W(\alpha,\alpha^*,t). \tag{J.15}$$

In the same spirit as before, we can drop third order derivatives and approximate the term $|\alpha|^2$ in the diffusion coefficient by the *average* amplitude of the cycle with non-zero squeezing. Then, performing the same change of variables $\alpha = \sqrt{r}e^{i\phi}$, we obtain the following Fokker-Planck equation:

$$\begin{aligned}\partial_t P(r,\phi,t) = \Big\{ &-2\partial_r\Big[\frac{\gamma_1}{2} - \gamma_2 r - 2\eta\cos(2\phi)\Big]r \\ &+ \partial_\phi\big[\Delta - 2\eta\sin(2\phi)\big] + \frac{3\gamma_1}{2}\partial_r r\partial_r + \frac{3\gamma_1}{8r}\partial_\phi^2\Big\}P(r,\phi,t).\end{aligned} \tag{J.16}$$

Notice the following crucial differences/similitudes in the presence of squeezing: (i) the noiseless amplitude dynamics depends on the phase [coming from the drift term after ∂_r in Eq. (J.16)]; (ii) the noiseless phase dynamics is independent of the amplitude, but it is nonlinear; (iii) the diffusion terms are exactly the same as for the case $\eta/\gamma_1 = 0$. While the first two points constitute an important complication for any further analytical treatment, the third point still allows one to perform some approximations.

Small squeezing limit. In particular, let us consider the limit in which $N \to \infty$ while $\eta, |\Delta| \ll \gamma_1$. This is similar to what we have studied in chapter 7. Recall that since the bifurcation diagram only depends on the relation between Δ and η, the considered

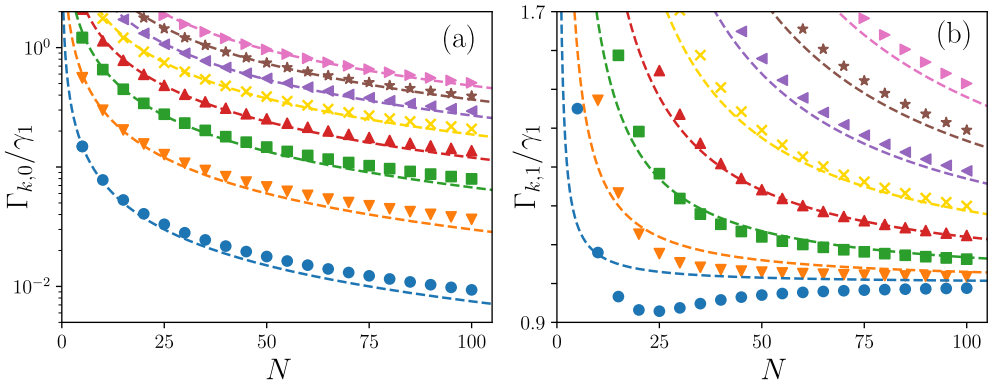

Figure J.2: (a) Comparison of the exact fundamental decay rates in points (Γ_k), and semiclassical expression in dashed lines ($\Gamma_{k,n=0}$). Blue circles $k = 1$, orange downward triangles $k = 2$, green squares $k = 3$, red upward triangles $k = 4$, yellow crosses $k = 5$, purple leftward triangles $k = 6$, brown stars $k = 7$, and ping rightwards triangles $k = 8$. (b) Same as panel (a) but considering the next excitations of each eigensector compared to $\Gamma_{k,n=1}$ in dashed lines. Parameters: $\eta/\gamma_1 = 0.02$ and $\Delta/\gamma_1 = 0.1$ (notice that $\eta_c/\gamma_1 = 0.05$).

limit does not preclude the observation of the bifurcation, as $\eta_c = |\Delta|/2$ can still be small compared to γ_1. Physically, we are assuming that the amplitude of the limit cycle is large compared to the squeezing strength, and thus, in a phase-space representation it looks essentially circular, with small elliptical deformations due to the non-zero squeezing. In these conditions, it seems reasonable to decouple amplitude and phase dynamics, similarly to what we have done before, i.e. by dropping the small phase dependence of the amplitude and approximating the diffusion terms as constant. It also seems reasonable to further linearize the amplitude dynamics. Hence, using the definition of the fluctuations given in Eq. (J.8), we arrive at:

$$\begin{aligned}\partial_t P(r_\delta,\phi,t) =& [\gamma_1\partial_{r_\delta} r_\delta + \frac{3\gamma_1^2}{4\gamma_2}\partial^2_{r_\delta}]P(r_\delta,\phi,t)\\ &+ \left[\partial_\phi\big(\Delta - 2\eta\sin(2\phi)\big) + \frac{3\gamma_2}{4}\partial^2_\phi\right]P(r_\delta,\phi,t).\end{aligned} \tag{J.17}$$

This equation displays the same amplitude fluctuations of the Gaussian process in the absence of squeezing; and the phase is now governed by a nonlinear drift with additive Gaussian fluctuations. This nonlinearity makes the phase dynamics non-Gaussian, and hence, it precludes us to make use of Eq. (J.11). However, we can still write down the following expression for the expectation values analogous to Eq. (J.13):

$$\langle(\alpha^*)^l\alpha^m(t)\rangle_c = \left[(\bar{r}^{\frac{l+m}{2}} + c_0) + \sum_{n\geq 1} c_n e^{-n\gamma_1 t}\right]\langle e^{i(m-l)\phi(t)}\rangle_c, \tag{J.18}$$

This approximate equation allows us to extract some qualitative conclusions. The first one is that the characteristic band structure due to 'pure-phase' and 'mixed amplitude-phase' fluctuations is still there, and the band gap should still be of the order of $\sim\gamma_1$ as the rest of the parameters entering in the phase dynamics are small compared to it. This agrees with what we have numerically observed in chapter 7. The second one is about the phase dynamics. Notice that no matter that it follows a more intricate nonlinear dynamics, for $\eta < |\Delta|/2$ the phase is still free or unlocked, and thus, the stochastic process corresponds to a random walk in a tilted washboard potential. This can be understood from the Langevin equation describing the phase dynamics of Eq. (J.17), which reads [88]:

$$\begin{aligned}\frac{d}{dt}\phi(t) = -\frac{d}{d\phi}V(\phi) + \xi_\phi(t), \quad \text{with} \quad V(\phi) = \Delta\phi + \eta\cos(2\phi),\\ \langle\xi_\phi(t)\rangle_c = 0, \quad \langle\xi_\phi(t)\xi_\phi(t')\rangle_c = \frac{3\gamma_2}{2}\delta(t-t'),\end{aligned} \tag{J.19}$$

where $V(\phi)$ is the tilted washboard potential and $\xi_\phi(t)$ is a zero mean Gaussian noise term. For zero squeezing, the constant drift Δ can be gauged away, and we find the same situation as before. For increasing squeezing strength, the washboard profile gets progressively activated, and the phase diffusion process gets accordingly modified, which should result in the decay rates of the fundamental band departing progressively from the zero squeezing case, as observed in chapter 7. Moreover, as the strength of the fluctuations in the phase dynamics is proportional to γ_2, they disappear in the infinite-excitation limit, explaining the increasing lifetime of the modes of the fundamental band.

These observations provide valuable physical insights and a qualitative understanding of the regime $\eta < \eta_c$. Moreover, they also provide intuition on why, for not to large squeezing strength, the theoretical results for $\eta/\gamma_1 = 0$, i.e. Eq. (J.14), are still close to the actual ones. This is shown in Fig. (J.2) (a) and (b), and considering the two lowest bands of eigenmodes for $\eta/\gamma_1 = 0.02$. Indeed, one needs to carefully compare the case $\eta/\gamma_1 = 0$ with $\eta/\gamma_1 = 0.02$, in order to spot the small differences, which are more noticeable for $n = 0$ and small k. Nevertheless, for larger squeezing strengths the differences become more evident, as the exponent δ significantly departs from one [see Fig. 7.3(d)].

APPENDIX K

Eigendecomposition of Hermitian eigenmodes

In chapter 7 we have commented that if an eigenmode is Hermitian it can be decomposed in terms of two density matrices, i.e. $\hat{\rho}_j \propto \hat{\rho}_j^+ - \hat{\rho}_j^-$ when λ_j is real. Here, we show how to obtain these density matrices. In fact, they are defined from the eigendecomposition of $\hat{\rho}_j$ as [35]:

$$\hat{\rho}_j = \sum_{n=0}^{D-1} p_n^{(j)} |\Psi_n^{(j)}\rangle\langle\Psi_n^{(j)}|, \tag{K.1}$$

where $p_n^{(j)}$ are real, and $\langle\Psi_n^{(j)}|\Psi_m^{(j)}\rangle = \delta_{nm}$, and D is the truncation dimension. Now since $\hat{\rho}_j$ is traceless, part of $p_n^{(j)}$ are positive and part are negative, while their sum is zero. We order them such that $p_n^{(j)} > 0$ for $n \leq \bar{n}$ and $p_n^{(j)} < 0$ for $n > \bar{n}$, obtaining

$$\hat{\rho}_j^+ = \frac{1}{\mathcal{N}} \sum_{n\leq\bar{n}} p_n^{(j)} |\Psi_n^{(j)}\rangle\langle\Psi_n^{(j)}|, \tag{K.2}$$

$$\hat{\rho}_j^- = \frac{1}{\mathcal{N}} \sum_{n>\bar{n}} |p_n^{(j)}| |\Psi_n^{(j)}\rangle\langle\Psi_n^{(j)}|, \tag{K.3}$$

with $\mathcal{N} = \sum_{n\leq\bar{n}} p_n^{(j)} = \sum_{n>\bar{n}} |p_n^{(j)}|$.

Bibliography

[1] A. Cabot, F. Galve, and R. Zambrini, *Dynamical and quantum effects of collective dissipation in optomechanical systems*, New J. Phys. **19**, 113007 (2017), doi: 10.1088/1367-2630/aa8b9c.

[2] A. Cabot, F. Galve, V. M. Eguíluz, K. Klemm, S. Maniscalco, and R. Zambrini, *Unveiling noiseless clusters in complex quantum networks* npj Quantum Inf. **4**, 57 (2018), doi: 10.1038/s41534-018-0108-9.

[3] A. Cabot, G. L. Giorgi, F. Galve, and R. Zambrini, *Quantum Synchronization in Dimer Atomic Lattices*, Phys. Rev. Lett. **123**, 023604 (2019), doi: 10.1103/PhysRevLett.123.023604.

[4] A. Cabot, G. L. Giorgi, S. Longhi, and R. Zambrini, *Exceptional points in 1D arrays of quantum harmonic oscillators*, EPL **127**, 20001 (2019), doi: 10.1209/0295-5075/127/20001.

[5] G. L. Giorgi, A. Cabot, and R. Zambrini, *Transient synchronization in open quantum systems* in *Advances in Open Systems and Fundamental Tests of Quantum Mechanics* (Eds.: B. Vacchini, H.-P. Breuer, A. Bassi), Springer, Cham, CH 2019, pp. 73-89.

[6] G. L. Giorgi, S. Longhi, A. Cabot, and R. Zambrini, *Quantum probing topological phase transitions by non-Markovianity*, Ann. Phys. (Berl.) **531**, 1900307 (2019), doi: 10.1002/andp.201900307.

[7] A. Cabot, G. L. Giorgi, and R. Zambrini, *Synchronization and coalescence in a dissipative two-qubit system*, Proc. R. Soc. A **477**, 20200850 (2021), doi: 10.1098/rspa.2021.0850.

[8] S. Lorenzo, S. Longhi, A. Cabot, R. Zambrini, and G. L. Giorgi, *Intermittent decoherence blockade in a chiral ring environment*, Sci. Rep. **11**, 12834 (2021), doi: 10.1038/s41598-021-92288-8.

[9] A. Cabot, G. L. Giorgi, and R. Zambrini, *Metastable quantum entrainment*, New J. Phys. **23**, 103017 (2021), doi: 10.1088/1367-2630/ac29fe.

[10] A. Cabot, G. L. Giorgi, and R. Zambrini, *From a continuous to a discrete time-crystal and the entrainment transition*, in preparation.

[11] J. R. Johansson, P.D. Nation, and F. Nori, *QuTiP: An open-source Python framework for the dynamics of open quantum systems* Comp. Phys. Comm. **183**, 1760 (2012), doi: 10.1016/j.cpc.2012.02.021.

[12] J. R. Johansson, P.D. Nation, and F. Nori, *QuTiP 2: A Python framework for the dynamics of open quantum systems* Comp. Phys. Comm. **184**, 1234 (2013), doi: 10.1016/j.cpc.2012.11.019.

[13] I. Carusotto and C. Ciuti, *Quantum fluids of light*, Rev. Mod. Phys. **85**, 299 (2013), doi: 10.1103/RevModPhys.85.299.

[14] H. Ritsch, P. Domokos, F. Brennecke, and T. Esslinger, *Cold atoms in cavity-generated dynamical optical potentials*, Rev. Mod. Phys. **85**, 553 (2013), doi: 10.1103/RevModPhys.85.553.

[15] M. J. Hartmann, *Quantum simulation with interacting photons* ,J. Opt. **18**, 104005 (2016), doi: 10.1088/2040-8978/18/10/104005.

[16] D. E. Chang, J. S. Douglas, A. González-Tudela, C. -L. Hung, and H. J. Kimble, *Colloquium: Quantum matter built from nanoscopic lattices of atoms and photons*, Rev. Mod. Phys. **90**, 031002 (2018), doi: 10.1103/RevModPhys.90.031002.

[17] M. Müller, S. Diehl, G. Pupillo, and P. Zoller, *Engineered open systems and quantum simulations with atoms and ions*, Adv. At. Mol. Opt. Phys. **61**, 1 (2012), doi: 10.1016/B978-0-12-396482-3.00001-6.

[18] I. Bloch, J. Dalibard, and W. Zwerger, *Many-body physics with ultracold gases*, Rev. Mod. Phys. **80**, 885 (2008), doi: 10.1103/RevModPhys.80.885.

[19] R. Blatt and C. F. Roos, *Quantum simulations with trapped ions*, Nature Phys **8**, 277 (2012), doi: 10.1038/nphys2252.

[20] A. A. Houck, H. E. Tureci, and J. Koch, *On-chip quantum simulation with superconducting circuits*, Nat. Phys. **8**, 292 (2012), doi: 10.1038/nphys2251.

[21] S. Schmidt and J. Koch, *Circuit QED lattices: Towards quantum simulation with superconducting circuits*, Ann. Phys. (Berlin) **525**, 395 (2013), doi: 10.1002/andp.201200261.

[22] C. Noh and D. G. Angelakis, *Quantum simulations and many-body physics with light*, Rep. Prog. Phys. **80**, 016401 (2017), doi: 10.1088/0034-4885/80/1/016401.

[23] M. Aspelmeyer, T. J. Kippenberg, and F. Marquardt, *Cavity optomechanics*, Rev. Mod. Phys. **86**, 1391 (2014), doi: 10.1103/RevModPhys.86.1391.

[24] P. Lodahl, S. Mahmoodian, and S. Stobbe, *Interfacing single photons and single quantum dots with photonic nanostructures*, Rev. Mod. Phys. **87**, 347 (2015), doi: 10.1103/RevModPhys.87.347.

[25] R. H. Dicke, *Coherence in Spontaneous Radiation Processes*, Phys. Rev. **93**, 99 (1954), doi: 10.1103/PhysRev.93.99.

[26] M. O. Araújo, I. Krešić, R. Kaiser, and W. Guerin, *Superradiance in a large and dilute cloud of cold atoms in the linear-optics regime*, Phys. Rev. Lett. **117**, 073002 (2016), doi: 10.1103/PhysRevLett.117.073002.

[27] W. Guerin, M. O. Araújo, and R. Kaiser, *Subradiance in a large cloud of cold atoms*, Phys. Rev. Lett. **116**, 083601 (2016), doi: 10.1103/PhysRevLett.116.083601.

[28] A. F. van Loo, A. Fedorov, K. Lalumière, B. C. Sanders, A. Blais, and A. Wallraff, *Photon-mediated interactions between distant artificial atoms*, Science **342**, 1494 (2013), doi: 10.1126/science.1244324.

[29] J. Mlynek, A. Abdumalikov, C. Eichler, and A. Wallraff, *Observation of Dicke superradiance for two artificial atoms in a cavity with high decay rate*, Nat. Commun. **5**, 5186 (2014), doi: 10.1038/ncomms6186.

[30] R. E. Evans, K. Bhaskar, D. D. Sukachev, C. T. Nguyen, A. Sipahigil, M. J. Burek, and B. Machielse, *Photon-mediated interactions between quantum emitters in a diamond nanocavity*, Science **362**, 662 (2018), doi: 10.1126/science.aau4691 .

[31] P. Domokos and H. Ritsch, *Collective cooling and self-organization of atoms in a cavity*, Phys. Rev. Lett. **89**, 253003 (2002), doi: 10.1103/PhysRevLett.89.253003.

[32] R. M. Kroeze, Y. Guo, V. D. Vaidya, J. Keeling, and B. L. Lev, *Spinor self-ordering of a quantum gas in a cavity*, Phys. Rev. Lett. **121**, 163601 (2018), doi: 10.1103/PhysRevLett.121.163601.

[33] G. Labeyrie, E. Tesio, P. M. Gomes, G.-L. Oppo, W. J. Firth,G. R. M. Robb, A. S. Arnold, R. Kaiser, and T. Ackemann, *Optomechanical self-structuring in a cold atomic gas*, Nat. Photonics **8**, 321 (2014), doi: 10.1038/nphoton.2014.52.

[34] E. M. Kessler, G. Giedke, A. Imamoglu, S. F. Yelin, M. D. Lukin, and J. I. Cirac, *Dissipative phase transition in a central spin system*, Phys. Rev. A **86**, 012116 (2012), doi: 10.1103/PhysRevA.86.012116.

[35] F. Minganti, A. Biella, N. Bartolo, and C. Ciuti, *Spectral theory of Liouvillians for dissipative phase transitions*, Phys. Rev. A **98**, 042118 (2018), doi: 10.1103/PhysRevA.89.022118.

[36] T. E. Lee, H. Häffner, and M. C. Cross, *Antiferromagnetic phase transition in a nonequilibrium lattice of Rydberg atoms*, Phys. Rev. A **84**, 031402(R) (2011), doi: 10.1103/PhysRevA.84.031402.

[37] P. Kirton, M. M. Roses, J. Keeling, and E. G. Dalla Torre, *Introduction to the Dicke model: From equilibrium to nonequilibrium, and vice versa*, Adv. Quantum Technol. **2**, 1800043 (2019), doi: 10.1002/qute.201800043.

[38] F. Iemini, A. Russomanno, J. Keeling, M. Schirò, M. Dalmonte, and R. Fazio, *Boundary time crystals*, Phys. Rev. Lett. **121**, 035301 (2018), doi: 10.1103/PhysRevLett.121.035301.

[39] Z. Gong, R. Hamazaki, and M. Ueda, *Discrete time-crystalline order in cavity and circuit QED systems*, Phys. Rev. Lett **120**, 040404 (2018), doi: 10.1103/PhysRevLett.120.040404.

[40] R. R. W. Wang, B. Xing, G. G. Carlo, D. Poletti, *Period doubling in period-one steady states*, Phys. Rev. E **97**, 020202(R) (2018), doi: 10.1103/PhysRevE.97.020202.

[41] H. Watanabe and M. Oshikawa, *Absence of quantum time crystals*, Phys. Rev. Lett. **114**, 251603 (2015), doi: 10.1103/PhysRevLett.114.251603.

[42] A. Balanov, N. Janson, D. Postnov, and O. Sosnovtseva, *Synchronization: From Simple to Complex* (Springer Science & Business Media, New York, 2008).

[43] A. S. Pikovsky, M. Rosenblum, and J. Kurths, *Synchronization: A Universal Concept in Nonlinear Science* (Cambridge University Press, New York, 2001).

[44] F. Galve, G. L. Giorgi, and R. Zambrini, *Quantum correlations and synchronization measures*, in *Lectures on General Quantum Correlations and their Applications*, edited by F. F. Fanchini, D. d. O. Soares Pinto, and G.Adesso (Springer International Publishing, Cham, 2017).

[45] G. L. Giorgi, F. Plastina, G. Francica, and R. Zambrini, *Spontaneous synchronization and quantum correlation dynamics of open spin systems*, Phys. Rev. A **88**, 042115 (2013), doi: 10.1103/PhysRevA.88.042115.

[46] M. Xu, D.A. Tieri, E.C. Fine, J. K. Thompson, and M.J. Holland, *Synchronization of two ensembles of atoms*, Phys. Rev. Lett. **113**, 154101 (2014), doi: 10.1103/PhysRevLett.113.154101.

[47] H. Xu, D. Mason, L. Jiang and J. G. E. Harris, *Topological energy transfer in an optomechanical system with exceptional points*, Nature **537**, 80 (2016), doi: 10.1038/nature18604.

[48] J. Doppler, A. A. Mailybaev, J. Böhm, U. Kuhl, A. Girschik,F. Libisch, T. J. Milburn, P. Rabl, N. Moiseyev, and S. Rotter, *Dynamically encircling an exceptional point for asymmetric mode switching*, Nature **537**,76 (2016), doi: 10.1038/nature18605.

[49] C. Huygens, *Horologium Oscillatorium* (Apud F. Muguet, Parisiis, France, 1673). English translation: *The Pendulum Clock*, (Iowa State University Press, Ames, 1986).

[50] E. V. Appleton, *The automatic synchronization of triode oscillator*, Proc. Cambridge Phil. Soc. (Math. and Phys. Sci.) **21**, 231 (1922).

[51] B. van der Pol, *Forced oscillations in a circuit with non-linear resistance (Reception with reactive triode)* Phil. Mag. **3**, 64 (1927), doi: 10.1080/14786440108564176.

[52] Z. Liu and R. Slavík, *Optical Injection Locking: From Principle to Applications*, J. Light. Technol **38**, 43 (2020), doi: 10.1109/JLT.2019.2945718.

[53] S. Bregni, *Synchronization of Digital Telecommunications Networks* (Wiley, Chichester, 2002).

[54] H. J. Carmichael, *Quantum trajectory theory for cascaded open systems*, Phys. Rev. Lett. **70**, 2273 (1993), doi: 10.1103/PhysRevLett.70.2273.

[55] S. H. Strogatz, *Nonlinear Dynamics and Chaos: With Applications to Physics, Biology, Chemistry, and Engineering* (Westview Press, Boulder, CO, 2014).

[56] S. Boccaletti, J. Kurths, G. Osipov, D.L. Valladares, C.S. Zhou, *The synchronization of chaotic systems*, Phys. Rep. 366, 1101 (2002), doi: 10.1016/S0370-1573(02)00137-0.

[57] A. Argyris, D. Syvridis, L. Larger, V. Annovazzi-Lodi, P. Colet, I. Fischer, J. García-Ojalvo, C. R. Mirasso, L. Pesquera, and K. Shore, *Chaos-based communications at high bit rates using commercial fibre-optic links*, Nature **438**, 343 (2005), doi: 10.1038/nature04275.

[58] H. -P. Breuer and F. Petruccione, *The theory of open quantum systems* (Oxford University Press, Oxford, 2007).

[59] H. Carmichael, *Statistical Methods in Quantum Optics I* (Springer, Berlin, 1999).

[60] C. W. Gardiner and P. Zoller, *Quantum Noise* (Springer-Verlag, Berlin, 2004).

[61] H. M. Wiseman and G. J. Milburn, *Quantum Measurement and Control*, (Cambridge University Press, Cambridge, England, 2009).

[62] I. Goychuk, J. Casado-Pascual, M. Morillo, J. Lehmann, and P. Hänggi, *Quantum Stochastic Synchronization*, Phys. Rev. Lett. **97**, 210601 (2006), doi: 10.1103/PhysRevLett.97.210601.

[63] O. V. Zhirov and D. L. Shepelyansky, *Synchronization and Bistability of a Qubit Coupled to a Driven Dissipative Oscillator*, Phys. Rev. Lett. **100**, 014101 (2008), doi: 10.1103/PhysRevLett.100.014101.

[64] P. P. Orth, D. Roosen, W. Hofstetter, and K. Le Hur, *Dynamics, synchronization, and quantum phase transitions of two dissipative spins*, Phys. Rev. B **82**, 144423 (2010), doi: 10.1103/PhysRevB.82.144423.

[65] G. L. Giorgi, F. Galve, G. Manzano, P. Colet, and R. Zambrini, *Quantum correlations and mutual synchronization*, Phys. Rev. A **85**, 052101 (2012), doi: 10.1103/PhysRevA.85.052101.

[66] M. Ludwig and F. Marquardt, *Quantum many-body dynamics in optomechanical arrays*, Phys. Rev. Lett. **111**, 073603 (2013), doi: 10.1103/PhysRevLett.111.073603.

[67] T. E. Lee and H. R. Sadeghpour, *Quantum synchronization of quantum van der Pol oscillators with trapped ions*, Phys. Rev. Lett. **111**, 234101 (2013), doi: 10.1103/PhysRevLett.111.234101.

[68] S. Walter, A. Nunnenkamp, C. Bruder, *Quantum synchronization of a driven self-sustained oscillator*, Phys. Rev. Lett. **112**, 094102 (2014), doi: 10.1103/PhysRevLett.112.094102.

[69] T. E. Lee, C.-K. Chan, and S. Wang, *Entanglement tongue and quantum synchronization of disordered oscillators*, Phys. Rev. E **89**, 022913 (2014), doi: 10.1103/PhysRevE.89.022913.

[70] S. Walter, A. Nunnenkamp, and C. Bruder, *Quantum synchronization of two Van der Pol oscillators*, Ann. Phys. **527**, 131 (2015), doi: 10.1002/andp.201400144

[71] G. Heinrich, M. Ludwig, J. Qian, B. Kubala, and F. Marquardt, *Collective dynamics in optomechanical arrays*, Phys. Rev. Lett. **107**, 043603 (2011), doi: 10.1103/PhysRevLett.107.043603.

[72] C. A. Holmes, C. P. Meaney, G. J. Milburn, *Synchronization of many nanomechanical resonators coupled via a common cavity field*, Phys. Rev. E **85**, 066203 (2012), doi: 10.1103/PhysRevE.85.066203.

[73] M. Zhang, G. S. Wiederhecker, S. Manipatruni, A. Barnard, P. McEuen, M. Lipson, *Synchronization of micromechanical oscillators using light*, Phys. Rev. Lett. **109**, 233906 (2012), doi: 10.1103/PhysRevLett.109.233906.

[74] M. Bagheri, M. Poot, L. Fan, F. Marquardt, and H.X. Tang, *Photonic cavity synchronization of nanomechanical oscillators*, Phys. Rev. Lett. **111**, 213902 (2013), doi: 10.1103/PhysRevLett.111.213902.

[75] S. Y. Shah, M. Zhang, R. Rand, and M. Lipson, *Master-slave locking of optomechanical oscillators over a long distance*, Phys. Rev. Lett. **114**, 113602 (2015), doi: 10.1103/PhysRevLett.114.113602.

[76] M. Zhang, S. Shah, J. Cardenas, and M. Lipson, *Synchronization and phase noise reduction in micromechanical oscillator arrays coupled through light*, Phys. Rev. Lett. **115**, 163902 (2015), doi: 10.1103/PhysRevLett.115.163902.

[77] E. Amitai, N. Lörch, A. Nunnenkamp, S. Walter, and C. Bruder, *Synchronization of an optomechanical system to an external drive*, Phys. Rev. A **95**, 053858 (2017), doi: 10.1103/PhysRevA.95.053858

[78] J. A. Acebrón, L. L. Bonilla, C. J. Pérez Vicente, F. Ritort, and R. Spigler, *The Kuramoto model: A simple paradigm for synchronization phenomena*, Rev. Mod. Phys. **77**, 137 (2005), doi: 10.1103/RevModPhys.77.137.

[79] I. H. de Mendoza, L. A. Pachón, J. Gómez-Gardeñes, and D. Zueco, *Synchronization in a semiclassical Kuramoto model*, Phys. Rev. E **90**, 052904 (2014), doi: 10.1103/PhysRevE.90.052904.

[80] B. Zhu, J. Schachenmayer, M. Xu, F. Herrera, J. G. Restrepo, M. J. Holland, and A. M. Rey, *Synchronization of interacting quantum dipoles*, New J. Phys. **17**, 083063 (2015), doi: 10.1088/1367-2630/17/8/083063.

[81] M. Ludwig, B. Kubala, F. Marquardt, *The optomechanical instability in the quantum regime*, New J. Phys. **10**, 095013 (2008), doi: 10.1088/1367-2630/10/9/095013.

[82] L. Ben Arosh, M. C. Cross, and R. Lifshitz, *Quantum limit cycles and the Rayleigh and van der Pol oscillators*, Phys. Rev. Research **3**, 013130 (2021), doi: 10.1103/PhysRevResearch.3.013130.

[83] M. R. Hush, W. Li, S. Genway, I. Lesanovsky, and A. D. Armour, *Spin correlations as a probe of quantum synchronization in trapped-ion phonon lasers*, Phys. Rev. A **91**, 061401(R) (2015), doi: 10.1103/PhysRevA.91.061401.

[84] C. Davis-Tilley and A. D. Armour, *Synchronization of micromasers*, Phys. Rev. A **94**, 063819 (2016), doi: 10.1103/PhysRevA.94.063819.

[85] M. R. Jessop, W. Li, and A. D. Armour, *Phase synchronization in coupled bistable oscillators*, Phys. Rev. Research **2**, 013233 (2020), doi: 10.1103/PhysRevResearch.2.013233.

[86] N. Lörch, E. Amitai, A. Nunnenkamp, and C. Bruder, *Genuine quantum signatures in synchronization of anharmonic self-oscillators*, Phys. Rev. Lett. **117**, 073601 (2016), doi: 10.1103/PhysRevLett.117.073601.

[87] T. Weiss, A. Kronwald, and F. Marquardt, *Noise-induced transitions in optomechanical synchronization*, New J. Phys. **18**, 013043 (2016), doi: 10.1088/1367-2630/18/1/013043.

[88] C. W. Gardiner, *Handbook of Stochastic Methods* (Springer, Berlin, 2004).

[89] G. L. Giorgi, F. Galve, and R. Zambrini, *Probing the spectral density of a dissipative qubit via quantum synchronization*, Phys. Rev. A **94**, 052121 (2016), doi: 10.1103/PhysRevA.94.052121.

[90] B. Bellomo, G. L. Giorgi, G. M. Palma, and R. Zambrini, *Quantum synchronization as a local signature of super- and subradiance*, Phys. Rev. A **95**, 043807 (2017), doi: 10.1103/PhysRevA.95.043807.

[91] A. Roulet and C. Bruder, *Synchronizing the smallest possible system*, Phys. Rev. Lett. **121**, 053601 (2018), doi: 10.1103/PhysRevLett.121.053601.

[92] A. Roulet and C. Bruder, *Quantum synchronization and entanglement generation*, Phys. Rev. Lett. **121**, 063601 (2018), doi: 10.1103/PhysRevLett.121.063601.

[93] J. Tindall, C. Sánchez Muñoz, B. Buča and D. Jaksch, *Quantum synchronisation enabled by dynamical symmetries and dissipation*, New J. Phys. **22**, 013026 (2020), doi: 10.1088/1367-2630/ab60f5.

[94] N. Jaseem, M. Hajdušek, V. Vedral, R. Fazio, L.-C. Kwek, and S. Vinjanampathy, *Quantum synchronization in nanoscale heat engines*, Phys. Rev. E **101**, 020201(R) (2020), doi: 10.1103/PhysRevE.101.020201.

[95] N. Lörch, S. E. Nigg, A. Nunnenkamp, R. P. Tiwari, and C. Bruder, *Quantum synchronization blockade: energy quantization hinders synchronization of identical oscillators*, Phys. Rev. Lett. **118**, 243602 (2017), doi: 10.1103/PhysRevLett.118.243602.

[96] A. Parra-López and J. Bergli, *Synchronization in two-level quantum systems*, Phys. Rev. A **101**, 062104 (2020), doi: 10.1103/PhysRevA.101.062104.

[97] C. Benedetti, F. Galve, A. Mandarino, M. G. A. Paris, and R. Zambrini, *Minimal model for spontaneous quantum synchronization*, Phys. Rev. A **94**, 052118 (2016), doi: 10.1103/PhysRevA.94.052118.

[98] G. Manzano, F. Galve, G. L. Giorgi, E. Hernández-García, and R. Zambrini, *Synchronization, quantum correlations and entanglement in oscillator networks*, Sci. Rep. **3**, 1439 (2013), doi: 10.1038/srep01439.

[99] S. Siwiak-Jaszek and A. Olaya-Castro, *Transient synchronisation and quantum coherence in a bio-inspired vibronic dimer*, Faraday Discuss. **216**, 38 (2019), doi: 10.1039/C9FD00006B.

[100] G. Garau Estarellas, G. L. Giorgi, M. C Soriano, and R. Zambrini, *Machine Learning Applied to Quantum Synchronization-Assisted Probing*, Adv. Quantum Technol. **2**, 1800085 (2019), doi: 10.1002/qute.201800085.

[101] G. Manzano, F. Galve, and R. Zambrini, *Avoiding dissipation in a system of three quantum harmonic oscillators*, Phys. Rev. A **87**, 032114 (2013), doi: 10.1103/PhysRevA.87.032114.

[102] B. Buča, J. Tindall and D. Jaksch, *Non-stationary coherent quantum many-body dynamics through dissipation*, Nat. Commun. **10**, 1730 (2019), doi: 10.1038/s41467-019-09757-y.

[103] D. A. Lidar and K. B. Whaley, *Decoherence-Free Subspaces and Subsystems* in *Irreversible Quantum Dynamics*, F. Benatti and R. Floreanini (Eds.), pp. 83-120 (Springer Lecture Notes in Physics vol. 622, Berlin, 2003).

[104] D. A. Lidar, *Review of Decoherence-Free Subspaces, Noiseless Subsystems, and Dynamical Decoupling*, Adv. Chem. Phys. **154**, 295 (2014), doi: 10.1002/9781118742631.ch11.

[105] P. Zanardi and M. Rasetti, *Noiseless quantum codes*, Phys. Rev. Lett. **79**, 3306 (1997), doi: 10.1103/PhysRevLett.79.3306.

[106] D. A. Lidar, I. L. Chuang, and K. B. Whaley, *Decoherence-free subspaces for quantum computation*, Phys. Rev. Lett. **81**, 2594 (1998), doi: 10.1103/PhysRevLett.81.2594.

[107] A. Beige, D. Braun, B. Tregenna, and P. L. Knight, *Quantum computing using dissipation to remain in a decoherence-free subspace*, Phys. Rev. Lett. **85**, 1762 (2000), doi: 10.1103/PhysRevLett.85.1762.

[108] L.-M. Duan and G.-C. Guo, *Preserving coherence in quantum computation by pairing quantum bits*, Phys. Rev. Lett. **79**, 1953 (1997), doi: 10.1103/PhysRevLett.79.1953.

[109] D. Braun, *Creation of entanglement by interaction with a common heat bath*, Phys. Rev. Lett. **87**, 277901 (2002), doi: 10.1103/PhysRevLett.89.277901.

[110] J. S. Prauzner-Bechcicki, *Two-mode squeezed vacuum state coupled to thecommon thermal reservoir*, J. Phys. A **37**, L173 (2004), doi: 10.1088/0305-4470/37/15/L04.

[111] J. P. Paz and A. J. Roncaglia, *Dynamics of the entanglement between two oscillators in the same environment*, Phys. Rev. Lett. **100**, 220401 (2008), doi: 10.1103/PhysRevLett.100.220401.

[112] V. Ameri, M. Eghbali-Arani, A. Mari, A. Farace, F. Kheirandish, V. Giovannetti, and R. Fazio, *Mutual information as an order parameter for quantum synchronization*, Phys. Rev. A **91**, 012301 (2015), doi: 10.1103/PhysRevA.91.012301.

[113] M. Koppenhöfer and A. Roulet, *Optimal synchronization deep in the quantum regime: Resource and fundamental limit*, Phys. Rev. A **99**, 043804 (2019), doi: 10.1103/PhysRevA.99.043804.

[114] N. Jaseem, M. Hajdušek, P. Solanki, L.-C. Kwek, R. Fazio, and S. Vinjanampathy, *Generalized measure of quantum synchronization*, Phys. Rev. Research **2**, 043287 (2020), doi: 10.1103/PhysRevResearch.2.043287.

[115] A. Mari, A. Farace, N. Didier, V. Giovannetti, and R. Fazio, *Measures of quantum synchronization in continuous variable systems*, Phys. Rev. Lett. **111**, 103605 (2013), doi: 10.1103/PhysRevLett.111.103605.

[116] N. Es'haqi-Sani, G. Manzano, R. Zambrini, and R. Fazio, *Synchronization along quantum trajectories*, Phys. Rev. Research **2**, 023101 (2020), doi: 10.1103/PhysRevResearch.2.023101.

[117] J. M. Weiner, K. C. Cox, J. G. Bohnet, and J. K. Thompson, *Phase synchronization inside a superradiant laser*, Phys. Rev. A **95**, 033808 (2017), doi: 10.1103/PhysRevA.95.033808.

[118] M. Xu and M. J. Holland, *Conditional Ramsey Spectroscopy with Synchronized Atoms*, Phys. Rev. Lett. **114**, 103601 (2015), doi: 10.1103/PhysRevLett.114.103601.

[119] M. Xu, S. B. Jäger, S. Schütz, J. Cooper, G. Morigi, and M.J. Holland, *Supercooling of atoms in an optical resonator*, Phys. Rev. Lett. **116**, 153002 (2016), doi: 10.1103/PhysRevLett.116.153002.

[120] A. W. Laskar, P. Adhikary, S. Mondal, P. Katiyar, S. Vinjanampathy, and S. Ghosh, *Observation of quantum phase synchronization in spin-1 atoms*, Phys. Rev. Lett. **125**, 013601 (2020), doi: 10.1103/PhysRevLett.125.013601.

[121] M. Koppenhöfer, C. Bruder, and A. Roulet, *Quantum synchronization on the IBM Q system*, Phys. Rev. Research **2**, 023026 (2020), doi: 10.1103/PhysRevResearch.2.023026.

[122] H. J. Carmichael, *Breakdown of photon blockade: a dissipative quantum phase transition in zero dimensions* Phys. Rev. X **5**, 031028 (2015), doi: 10.1103/PhysRevX.5.031028.

[123] M.-J. Hwang, R. Puebla, and M. B. Plenio, *Quantum phase transition and universal dynamics in the Rabi model*, Phys. Rev. Lett. **115**, 180404 (2015), doi: 10.1103/PhysRevLett.115.180404.

[124] S. Sachdev, *Quantum Phase Transitions* (Cambridge University Press, Cambridge, 1999).

[125] S. Diehl, A. Tomadin, A. Micheli, R. Fazio, and P. Zoller, *Dynamical phase transitions and instabilities in open atomic many-body systems*, Phys. Rev. Lett. **105**, 015702 (2010), doi: 10.1103/PhysRevLett.105.015702.

[126] R. K. Pathria and P.D. Beale, *Statistical Mechanics* (Academic, Boston, 2011).

[127] N. Goldenfeld, *Lectures on phase transitions and the renormalization group* (CRC Press, Boca Raton, 2018).

[128] T. E. Lee, S. Gopalakrishnan, and M. D. Lukin, *Unconventional magnetism via optical pumping of interacting spin systems*, Phys. Rev. Lett. **110**, 257204 (2013), doi: 10.1103/PhysRevLett.110.257204.

[129] T. E. Lee, C.-K. Chan, and S. F. Yelin, *Dissipative phase transitions: Independent versus collective decay and spin squeezing*, Phys. Rev. A **90**, 052109 (2014).

[130] J. Jin, A. Biella, O. Viyuela, L. Mazza, J. Keeling, R. Fazio, and D. Rossini, *Cluster Mean-Field Approach to the Steady-State Phase Diagram of Dissipative Spin Systems*, Phys. Rev. X **6**, 031011 (2016), doi: 10.1103/PhysRevX.6.031011.

[131] R. Rota, F. Storme, N. Bartolo, R. Fazio, and C. Ciuti, *Critical behavior of dissipative two-dimensional spin lattices*, Phys. Rev. B **95**, 134431 (2017), doi: 10.1103/PhysRevB.95.134431.

[132] J. Jin, D. Rossini, R. Fazio, M. Leib, and M. J. Hartmann, *Photon Solid Phases in Driven Arrays of Nonlinearly Coupled Cavities*, Phys. Rev. Lett. **110**, 163605 (2013), doi: 10.1103/PhysRevLett.110.163605.

[133] J. Jin, D. Rossini, M. Leib, M. J. Hartmann, and R. Fazio, *Steady-state phase diagram of a driven QED-cavity array with cross-Kerr nonlinearities*, Phys. Rev. A **90**, 023827 (2014), doi: 10.1103/PhysRevA.90.023827.

[134] N. Bartolo, F. Minganti, W. Casteels, and C. Ciuti, *Exact steady state of a Kerr resonator with one- and two-photon driving and dissipation: Controllable Wigner-function multimodality and dissipative phase transitions*, Phys. Rev. A **94**, 033841 (2016), doi: 10.1103/PhysRevA.94.033841.

[135] W. Casteels, F. Storme, A. Le Boité, and C. Ciuti, *Power laws in the dynamic hysteresis of quantum nonlinear photonic resonators*, Phys. Rev. A **93**, 033824 (2016), doi: 10.1103/PhysRevA.93.033824.

[136] W. Casteels, R. Fazio, and C. Ciuti, *Critical dynamical properties of a first-order dissipative phase transition*, Phys. Rev. A **95**, 012128 (2017), doi: 10.1103/PhysRevA.95.012128.

[137] W. Casteels and C. Ciuti, *Quantum entanglement in the spatial-symmetry-breaking phase transition of a driven-dissipative Bose-Hubbard dimer*, Phys. Rev. A **95**, 013812 (2017), doi: 10.1103/PhysRevA.95.013812.

[138] M. Foss-Feig, P. Niroula, J. T. Young, M. Hafezi, A. V. Gorshkov, R. M. Wilson, and M. F. Maghrebi, *Emergent equilibrium in many-body optical bistability*, Phys. Rev. A **95**, 043826 (2017), doi: 10.1103/PhysRevA.95.043826.

[139] V. Savona, *Spontaneous symmetry breaking in a quadratically driven nonlinear photonic lattice*, Phys. Rev. A **96**, 033826 (2017), doi: 10.1103/PhysRevA.96.033826.

[140] F. Vicentini, F. Minganti, R. Rota, G. Orso, and C. Ciuti, *Critical slowing down in driven-dissipative Bose-Hubbard lattices*, Phys. Rev. A **97**, 013853 (2018), doi: 10.1103/PhysRevA.97.013853.

[141] F. Dimer, B. Estienne, A. S. Parkins, and H. J. Carmichael, *Proposed realization of the Dicke-model quantum phase transition in an optical cavity QED system*, Phys. Rev. A **75**, 013804 (2007), doi: 10.1103/PhysRevA.75.013804.

[142] M. J. Bhaseen, J. Mayoh, B. D. Simons, and J. Keeling, *Dynamics of nonequilibrium Dicke models*, Phys. Rev. A **85**, 013817 (2012), doi: 10.1103/PhysRevA.85.013817.

[143] E. G. Dalla Torre, S. Diehl, M. D. Lukin, S. Sachdev, and P. Strack, *Keldysh approach for nonequilibrium phase transitions in quantum optics: Beyond the Dicke model in optical cavities*, Phys. Rev. A **87**, 023831 (2013), doi: 10.1103/PhysRevA.87.023831.

[144] J. Hannukainen and J. Larson, *Dissipation-driven quantum phase transitions and symmetry breaking*, Phys. Rev. A **98**, 042113 (2018), doi: 10.1103/PhysRevA.98.042113.

[145] S. Diehl, A. Micheli, A. Kantian, B. Kraus, H. P. Büchler, and P. Zoller, *Quantum states and phases in driven open quantum systems with cold atoms*, Nature Phys **4**, 878 (2008), doi: 10.1038/nphys1073.

[146] A. Tomadin, S. Diehl, and P. Zoller, *Nonequilibrium phase diagram of a driven and dissipative many-body system*, Phys. Rev. A **83**, 013611 (2011), doi: 10.1103/PhysRevA.83.013611.

[147] T. E. Lee, H. Häffner, and M. C. Cross, *Collective Quantum Jumps of Rydberg Atoms*, Phys. Rev. Lett. **108**, 023602 (2012), doi: 10.1103/PhysRevLett.108.023602.

[148] C. Ates, B. Olmos, J. P. Garrahan, and I. Lesanovsky, *Dynamical phases and intermittency of the dissipative quantum Ising model*, Phys. Rev. A **85**, 043620 (2012), doi: 10.1103/PhysRevA.85.043620.

[149] J. Qian, G. Dong, L. Zhou, and W. Zhang, *Phase diagram of Rydberg atoms in a nonequilibrium optical lattice*, Phys. Rev. A **85**, 065401 (2012), doi: 10.1103/PhysRevA.85.065401.

[150] M. Marcuzzi, E. Levi, S. Diehl, J. P. Garrahan, and I. Lesanovsky, *Universal Nonequilibrium Properties of Dissipative Rydberg Gases*, Phys. Rev. Lett. **113**, 210401 (2014), doi: 10.1103/PhysRevLett.113.210401.

[151] M. Marcuzzi, M. Buchhold, S. Diehl, and I. Lesanovsky, *Absorbing State Phase Transition with Competing Quantum and Classical Fluctuations*, Phys. Rev. Lett. **116**, 245701 (2016), doi: 10.1103/PhysRevLett.116.245701.

[152] M. Benito, C. Sánchez Muñoz, and C. Navarrete-Benlloch, *Degenerate parametric oscillation in quantum membrane optomechanics*, Phys. Rev. A **93**, 023846 (2016), doi: 10.1103/PhysRevA.93.023846.

[153] V. DeGiorgio and M. O. Scully, *Analogy between the laser threshold region and a second-order phase transition*, Phys. Rev. A **2**, 1170 (1970), doi: 10.1103/PhysRevA.2.1170.

[154] R. Bonifacio and L. A. Lugiato, *Optical bistability and cooperative effects in resonance fluorescence*, Phys. Rev. A **18**, 1129 (1978), doi: 10.1103/PhysRevA.18.1129.

[155] P. D. Drummond and D. F. Walls, *Quantum theory of optical bistability. I. Nonlinear polarisability model* J. Phys. A: Math. Gen. **13**, 725 (1980), doi: 10.1088/0305-4470/13/2/034.

[156] H. J. Carmichael, *Analytical and numerical results for the steady state in cooperative resonance fluorescence*, J. Phys. B **13**, 3551 (1980), doi: 10.1088/0022-3700/13/18/009.

[157] L. M. Sieberer, S. D. Huber, E. Altman, and S. Diehl, *Dynamical critical phenomena in driven-dissipative systems*, Phys. Rev. Lett. **110**, 195301 (2013), doi: 10.1103/PhysRevLett.110.195301.

[158] M.-J. Hwang, P. Rabl, and M. B. Plenio, *Dissipative phase transition in the open quantum Rabi model*, Phys. Rev. A **97**, 013825 (2018), doi: 10.1103/PhysRevA.97.013825.

[159] R. Rota, F. Minganti, C. Ciuti, and V. Savona, *Quantum critical regime in a quadratically driven nonlinear photonic lattice*, Phys. Rev. Lett. **122**, 110405 (2019), doi: 10.1103/PhysRevLett.122.110405.

[160] J. T. Young, A. V. Gorshkov, M. Foss-Feig, and M. F. Maghrebi, *Nonequilibrium fixed points of coupled ising models*, Phys. Rev. X **10**, 011039 (2020), doi: 10.1103/PhysRevX.10.011039.

[161] I. Lesanovsky, M. van Horssen, M. Guţă, and J. P. Garrahan, *Characterization of Dynamical Phase Transitions in Quantum Jump Trajectories Beyond the Properties of the Stationary State*, Phys. Rev. Lett. **110**, 150401 (2013), doi: 10.1103/PhysRevLett.110.150401.

[162] K. Macieszczak, M. Guta, I. Lesanovsky and J. P. Garrahan, *Towards a Theory of Metastability in Open Quantum Dynamics*, Phys. Rev. Lett **116**, 240404 (2016) doi: 10.1103/PhysRevLett.116.240404.

[163] C. Carr, R. Ritter, C. G. Wade, C. S. Adams, and K. J. Weatherill, *Nonequilibrium Phase Transition in a Dilute Rydberg Ensemble*, Phys. Rev. Lett. **111**, 113901 (2013), doi: 10.1103/PhysRevLett.111.113901.

[164] M. Fitzpatrick, N. M. Sundaresan, A. C. Y. Li, J. Koch, and A. A. Houck, *Observation of a Dissipative Phase Transition in a One-Dimensional Circuit QED Lattice*, Phys. Rev. X **7**, 011016 (2017), doi: 10.1103/PhysRevX.7.011016.

[165] T. Fink, A. Schade , S. Höfling, C. Schneider and A. Imamoglu, *Signatures of a dissipative phase transition in photon correlation measurements*, Nat. Phys. **14**, 365 (2018), doi: 10.1038/s41567-017-0020-9.

[166] S. Sonar, M. Hajdušek, M. Mukherjee, R. Fazio, V. Vedral, and S. Vinjanampathy, *Squeezing enhances quantum synchronization* Phys. Rev. Lett. **120**, 163601 (2018), doi: 10.1103/PhysRevLett.120.163601.

[167] F. Marquardt, J. G. E. Harris, S. M. Girvin, *Dynamical multistability induced by radiation pressure in high-finesse micromechanical optical cavities*, Phys. Rev. Lett. **96**, 103901 (2006), doi: 10.1103/PhysRevLett.96.103901.

[168] F. Minganti, I. I. Arkhipov, A. Miranowicz, and F. Nori, *Correspondence between dissipative phase transitions of light and time crystals*, arXiv preprint: 2008.08075.

[169] C.-K. Chan, T. E. Lee, and S. Gopalakrishnan, *Limit-cycle phase in driven-dissipative spin systems*, Phys. Rev. A **91**, 051601(R) (2015), doi: 10.1103/PhysRevA.91.051601.

[170] E. T. Owen, J. Jin, D. Rossini, R. Fazio, and M. J. Hartmann, *Quantum correlations and limit cycles in the driven-dissipative Heisenberg lattice*, New J. Phys. **20** 045004 (2018), doi: 10.1088/1367-2630/aab7d3.

[171] M. A. Armen and H. Mabuchi, *Low-lying bifurcations in cavity quantum electrodynamics*, Phys. Rev. A **73**, 063801 (2006), doi: 10.1103/PhysRevA.73.063801.

[172] F. Wilczek, *Quantum time crystals*, Phys. Rev. Lett. **109**, 160401 (2012), doi: 10.1103/PhysRevLett.109.160401.

[173] P. Bruno, *Comment on "Quantum Time Crystals"*, Phys. Rev. Lett. **110**, 118901 (2013), doi: 10.1103/PhysRevLett.110.118901.

[174] P. Bruno, *Comment on "Space-Time Crystals of Trapped Ions"*, Phys. Rev. Lett. **111**, 029301 (2013), doi: 10.1103/PhysRevLett.111.029301.

[175] P. Bruno, *Impossibility of spontaneously rotating time crystals: a no-go Theorem*, Phys. Rev. Lett. **111**, 070402 (2013), doi: 10.1103/PhysRevLett.111.070402.

[176] P. Noziéres, *Time crystals: Can diamagnetic currents drive a charge density wave into rotation?*, EPL **103**, 57008 (2013), doi: 10.1209/0295-5075/103/57008.

[177] D. V. Else, B. Bauer, and C. Nayak, *Floquet time crystals*, Phys. Rev. Lett. **117**, 090402 (2016), doi: 10.1103/PhysRevLett.117.090402.

[178] V. Khemani, A. Lazarides, R. Moessner, and S.L. Sondhi, *Phase structure of driven quantum systems*, Phys. Rev. Lett. **116**, 250401 (2013), doi: 10.1103/PhysRevLett.116.250401.

[179] K. Sacha, *Modeling spontaneous breaking of time-translation symmetry*, Phys. Rev. A **91**, 033617 (2015), doi: 10.1103/PhysRevA.91.033617.

[180] N. Y. Yao, A. C. Potter, I. -D. Potirniche, and A. Vishwanath, *Discrete Time Crystals: Rigidity, Criticality, and Realizations*, Phys. Rev. Lett. **118**, 030401 (2017), doi: 10.1103/PhysRevLett.118.030401.

[181] A. Russomanno, F. Iemini, M. Dalmonte, and R. Fazio, *Floquet time crystal in the Lipkin-Meshkov-Glick model*, Phys. Rev. B **95**, 214307 (2017), doi: 10.1103/PhysRevB.95.214307.

[182] K. Sacha and J. Zakrzewski, *Time crystals: a review*, Rep. Prog. Phys. **81**, 016401 (2018), doi: 10.1088/1361-6633/aa8b38.

[183] D. V. Else, C. Monroe, C. Nayak, and N. Y. Yao, *Discrete time crystals* Annu. Rev. Condens. Matter Phys. **11**, 467 (2020), doi: 10.1146/annurev-conmatphys-031119-050658.

[184] S. Choi, J. Choi, R. Landig, G. Kucsko, H. Zhou, J. Isoya, F. Jelezko, S. Onoda, H. Sumiya, V. Khemani, C. von Keyserlingk, N. Y. Yao, E. Demler, and M. D. Lukin, *Observation of discrete time-crystalline order in a disordered dipolar many-body system*, Nature (London) **543**, 221 (2017), doi: 10.1038/nature21426.

[185] J. Zhang, P. W. Hess, A. Kyprianidis, P. Becker, A. Lee, J. Smith, G. Pagano, I. D. Potirniche, A. C. Potter, A. Vishwanath, N. Y. Yao, and C. Monroe, *Observation of a discrete time crystal*, Nature (London) **543**, 217 (2017), doi: 10.1038/nature21413.

[186] A. Kyprianidis, F. Machado, W. Morong, P. Becker, K. S. Collins, D. V. Else, L. Feng, P. W. Hess, C. Nayak, G. Pagano, N. Y. Yao, C. Monroe, *Observation of a prethermal discrete time crystal*, Science **372**, 1192 (2021), doi: 10.1126/science.abg8102

[187] X. Mi, M. Ippoliti, C. Quintana et al., *Observation of Time-Crystalline Eigenstate Order on a Quantum Processor*, arXiv preprint: 2107.13571.

[188] J. Randall, C. E. Bradley, F. V. van der Gronden, A. Galicia, M. H. Abobeih, M. Markham, D. J. Twitchen, F. Machado, N. Y. Yao, and T. H. Taminiau, *Observation of a many-body-localized discrete time crystal with a programmable spin-based quantum simulator*, arXiv preprint: 2107.00736.

[189] F. M. Gambetta, F. Carollo, M. Marcuzzi, J. P. Garrahan, and I. Lesanovsky, *Discrete time crystals in the absence of manifest symmetries or disorder in open quantum systems*, Phys. Rev. Lett. **122**, 015701 (2019), doi: 10.1103/PhysRevLett.122.015701.

[190] A. Lazarides, S. Roy, F. Piazza, and R. Moessner, *Time crystallinity in dissipative Floquet systems*, Phys. Rev. Res. **2**, 022002(R) (2020), doi: 10.1103/PhysRevResearch.2.022002.

[191] A. Riera-Campeny, M. Moreno-Cardoner, and A. Sanpera, *Time crystallinity in open quantum systems*, Quantum **4**, 270 (2020), doi: 10.22331/q-2020-05-25-270.

[192] G. Buonaiuto, F. Carollo, B. Olmos, and I. Lesanovsky, *Dynamical Phases and Quantum Correlations in an Emitter-Waveguide System with Feedback*, Phys. Rev. Lett. **127**, 133601 (2021), doi: 10.1103/PhysRevLett.127.133601.

[193] K. Tucker, B. Zhu, R. J. Lewis-Swan, J. Marino, F. Jimenez, J. G. Restrepo and A. M. Rey, *Shattered time: can a dissipative time crystal survive many-body correlations?* New J. Phys. **20** 123003 (2018), doi: 10.1088/1367-2630/aaf18b.

[194] B. Zhu, J. Marino, N. Y. Yao, M. D. Lukin and E. A. Demler, *Dicke time crystals in driven-dissipative quantum many-body systems*, New J. Phys. **21**, 073028 (2019), doi: doi.org/10.1088/1367-2630/ab2afe.

[195] H. Keßler, J. G. Cosme, C. Georges, L. Mathey, and A. Hemmerich, *From a continuous to a discrete time crystal in a dissipative atom-cavity system*, New J. Phys. 22 085002 (2020), doi: 10.1088/1367-2630/ab9fc0.

[196] M. I. Dykman, C. Bruder, N. Lörch, and Y. Zhang, *Interaction-induced time-symmetry breaking in driven quantum oscillators*, Phys. Rev. B **98**, 195444 (2018), doi: 10.1103/PhysRevB.98.195444.

[197] C. Lledó, Th. K. Mavrogordatos, and M. H. Szymańska, *Emergent finite frequency criticality of driven-dissipative correlated lattice bosons*, Phys. Rev. B **100**, 054303 (2019), doi: 10.1103/PhysRevB.99.064511.

[198] O. Scarlatella, R. Fazio, and M. Schiró, *Emergent finite frequency criticality of driven-dissipative correlated lattice bosons*, Phys. Rev. B **95** 99, 064511 (2019), doi: 10.1103/PhysRevB.99.064511.

[199] C. Lledó and M. H. Szymańska, *A dissipative time crystal with or without Z_2 symmetry breaking*, New J. Phys. **22**, 075002 (2020), doi: 10.1088/1367-2630/ab9ae3.

[200] K. Seibold, R. Rota , and V. Savona, *Dissipative time crystal in an asymmetric nonlinear photonic dimer*, Phys. Rev. A **101**, 033839 (2020), doi: 10.1103/PhysRevA.101.033839.

[201] T. Shirai , S. Todo , and S. Miyashita, *Dynamical phase transition in Floquet optical bistable systems: An approach from finite-size quantum systems*, Phys. Rev. A **101**, 013809 (2020), doi: 10.1103/PhysRevA.101.013809.

[202] H. Alaeian, G. Giedke, I. Carusotto, R. Löw, and T. Pfau, *Limit cycle phase and Goldstone mode in driven dissipative systems*, Phys. Rev. A **103**, 013712 (2021), doi: 10.1103/PhysRevA.103.013712.

[203] C. Booker, B. Buča and D. Jaksch, *Non-stationarity and dissipative time crystals: spectral properties and finite-size effects*, New J. Phys. **22**, 085007 (2020), doi: 10.1088/1367-2630/ababc4.

[204] L. Feng, R. El-Ganainy and L. Ge, *Non-Hermitian photonics based on parity–time symmetry*, Nat. Photon. **11**, 752 (2017), doi: 10.1038/s41566-017-0031-1.

[205] R. El-Ganainy, K. G. Makris, M. Khajavikhan, Z. H. Musslimani, S. Rotter and D. N. Christodoulides, *Non-Hermitian physics and PT symmetry*, Nat. Phys. **14**, 11 (2018), doi: 10.1038/nphys4323.

[206] M. A. Miri and A. Alú, *Exceptional points in optics and photonnics*, Science **363**, 7709 (2019), doi: 10.1126/science.aar7709.

[207] S. K. Özdemir, S. Rotter, F. Nori, and L. Yang, *Parity-time symmetry and exceptional points in photonics*, Nat. Mater. **18**, 783 (2019), doi: 10.1038/s41563-019-0304-9.

[208] W. D. Heiss, *The physics of exceptional points* J. Phys. A: Math. Theor. **45**, 444016 (2012), doi: 10.1088/1751-8113/45/44/444016.

[209] F. Minganti, A. Miranowicz, R. W. Chhajlany, F. Nori, *Quantum exceptional points of non-Hermitian Hamiltonians and Liouvillians: The effects of quantum jumps*, Phys. Rev. A **100**, 062131 (2019), doi: 10.1103/PhysRevA.100.062131.

[210] A. Ruschhaupt, F. Delgado and J. G. Muga, *Physical realization of PT-symmetric potential scattering in a planar slab waveguide*, J. Phys. A: Math. Gen. **38**, L171 (2005), doi: 10.1088/0305-4470/38/9/L03.

[211] G. L. Giorgi, *Spontaneous PT symmetry breaking and quantum phase transitions in dimerized spin chains*, Phys. Rev. B **82**, 052404 (2010), doi: 10.1103/PhysRevB.82.052404.

[212] S. Longhi, *Spectral singularities and Bragg scattering in complex crystals*, Phys. Rev. A **81**, 022102 (2010) doi: 10.1103/PhysRevA.81.022102.

[213] C. E. Rüter, K. G. Makris, R. El-Ganainy, D. N. Christodoulides, M. Segev and D. Kip, *Observation of parity–time symmetry in optics*, Nat. Phys. **6**, 192 (2010) doi: 10.1038/nphys1515.

[214] W. Chen, Ş. K. Özdemir, G. Zhao, J. Wiersig and L. Yang, *Exceptional points enhance sensing in an optical microcavity*, Nature **548**, 192 (2017), doi: 10.1038/nature23281.

[215] S. Longhi, *Exceptional points and photonic catastrophe*, Opt. Lett. **43**, 2929 (2018) doi: 10.1364/OL.43.002929.

[216] T. J. Milburn, J. Doppler, C. A. Holmes, S. Portolan, S. Rotter, and P. Rabl, *General description of quasiadiabatic dynamical phenomena near exceptional points*, Phys. Rev. A **92**, 052124 (2015), doi: 10.1103/PhysRevA.92.052124.

[217] H. Cartarious and M. Moiseyev, *Fingerprints of exceptional points in the survival probability of resonances in atomic spectra*, Phys. Rev. A **84**, 013419 (2011), doi: 10.1103/PhysRevA.84.013419.

[218] S. Longhi, *Anomalous dynamics in multilevel quantum decay*, Phys. Rev. A **98**, 022134 (2018), doi: 10.1103/PhysRevA.98.022134.

[219] A. Ghatak and T. Das, *New topological invariants in non-Hermitian systems*, J. Phys.: Condens. Matter, **31**, 263001 (2019), doi: 10.1088/1361-648X/ab11b3.

[220] S. Longhi, *Parity-time symmetry meets photonics: A new twist in non-Hermitian optics* EPL **120**, 64001 (2017), doi: 10.1209/0295-5075/120/64001.

[221] C. Cohen-Tannoudji, J. Dupont-Roc, and G. Grynberg, *Atom-Photon Interactions* (Wiley, New York, 1992).

[222] A. Rivas and S. F. Huelga, *Open Quantum Systems. An Introduction* (Springer, Heidelberg, 2011).

[223] V. Gorini, A. Kossakowski, and E. C. G. Sudarshan, *Completely positive dynamical semigroups of N-level systems* J. Math. Phys. **17**, 821 (1976), doi: 10.1063/1.522979.

[224] G. Lindblad, *On the generators of quantum dynamical semigroups*, Commun. Math. Phys. **48**, 119 (1976), doi: 10.1007/BF01608499.

[225] M. Cattaneo, G. L. Giorgi, S. Maniscalco, and Roberta Zambrini, *Local versus global master equation with common and separate baths: superiority of the global approach in partial secular approximation*, New J. Phys. **21**, 113045 (2019), doi: 10.1088/1367-2630/ab54ac.

[226] A. Rivas, A. D. K. Plato, S. F. Huelga and M. B. Plenio, *Markovian master equations: a critical study*, New J. Phys. **12**, 113032 (2010), doi: 10.1088/1367-2630/12/11/113032.

[227] J. O. González, L. A. Correa, G. Nocerino, J. P. Palao, D. Alonso and G. Adesso, *Testing the Validity of the 'Local' and 'Global' GKLS Master Equations on an Exactly Solvable Model*, Open Syst. Inf. Dyn. **24**, 1740010 (2017), doi: 10.1142/S1230161217400108.

[228] P. P. Hofer, M. Perarnau-Llobet, L. D. M. Miranda, G. Haack, R. Silva, J. Bohr Brask, and N. Brunner, *Markovian master equations for quantum thermal machines: local versus global approach*, New J. Phys. **19**, 123037 (2017), doi: 10.1088/1367-2630/aa964f.

[229] M. T. Mitchison and M. B. Plenio, *Non-additive dissipation in open quantum networks out of equilibrium*, New J. Phys. **20**, 033005 (2018), doi: 10.1088/1367-2630/aa9f70.

[230] I. de Vega and D. Alonso, *Dynamics of non-Markovian open quantum systems*, Rev. Mod. Phys. **89**, 015001 (2017), doi: 10.1103/RevModPhys.89.015001.

[231] A. J. Legget, S. Chakravarty, A. T. Dorsey, M. P. A. Fisher, A. Garg, and W. Zwerger, *Dynamics of the dissipative two-state system*, Rev. Mod. Phys. **59**, 1 (1987), doi: 10.1103/RevModPhys.59.1.

[232] A. H. Safavi-Naeini, J. T. Hill, S. Meenehan, J. Chan, S. Gröblacher,and O. Painter, *Two-dimensional phononic-photonic band gap optomechanical crystal cavity*, Phys. Rev. Lett. **112**, 153603 (2014), doi: 10.1103/PhysRevLett.112.153603.

[233] A. H. Safavi-Naeini, D. van Thourhout, R. Baets, R. van Laer, *Controlling phonons and photons at the wavelength scale: integrated photonics meets integrated phononics*, Optica **6**, 213 (2019), doi: https://doi.org/10.1364/OPTICA.6.000213.

[234] F. Benatti, R. Floreanini, and M. Piani, *Environment induced entanglement in markovian dissipative dynamics*, Phys. Rev. Lett **91**, 070402 (2003), doi: 10.1103/PhysRevLett.91.070402.

[235] A. Gonzalez-Tudela, D. Martin-Cano, E. Moreno, L. Martin-Moreno, C. Tejedor, and F. J. García-Vidal, *Entanglement of two qubits mediated by one-dimensional plasmonic waveguides*, Phys. Rev. Lett. **106**,020501 (2011), doi: 10.1103/PhysRevLett.106.020501.

[236] R. G. DeVoe and R. G. Brewer, *Observation of superradiant and subradiant spontaneous emission of two trapped ions*, Phys. Rev. Lett. **76**, 2049 (1996), doi: 10.1103/PhysRevLett.76.2049.

[237] A. Goban, C.-L. Hung, J.D. Hood, S.-P. Yu, J.A. Muniz, O. Painter, and H.J. Kimble, *Superradiance for atoms trapped along a photonic crystal waveguide*, Phys. Rev. Lett. **115**, 063601 (2015), doi: 10.1103/PhysRevLett.115.063601.

[238] A. González-Tudela, V. Paulisch, D.E. Chang, H.J. Kimble, and J.I. Cirac, *Deterministic generation of arbitrary photonic states assisted by dissipation*, Phys. Rev. Lett. **115**, 163603 (2015), doi: 10.1103/PhysRevLett.115.163603.

[239] A. González-Tudela, V. Paulisch, H.J. Kimble, and J.I. Cirac, *Efficient multiphoton generation in waveguide quantum electrodynamics*, Phys. Rev. Lett. **118**, 213601 (2017), doi: 10.1103/PhysRevLett.118.213601.

[240] R. Doll, M. Wubs, P. Hänggi, and S. Kohler, *Limitation of entanglement due to spatial qubit separation*, EPL **76**, 547 (2006), doi: 10.1209/epl/i2006-10326-y.

[241] D. P. S. McCutcheon, A. Nazir, S. Bose, and A. J. Fisher, *Long-lived spin entanglement induced by a spatially correlated thermal bath*, Phys. Rev. A **80**, 022337 (2009), doi: 10.1103/PhysRevA.80.022337.

[242] Á. Rivas and M. Müller, *Quantifying spatial correlations of general quantum dynamics*, New J. Phys. **17**, 062001 (2015), doi: 10.1088/1367-2630/17/6/062001

[243] F. Galve, A. Mandarino, M. G. A. Paris, C. Benedetti, and R. Zambrini, *Microscopic description for the emergence of collective dissipation in extended quantum systems*, Sci. Rep. **7**, 42050 (2017), doi: 10.1038/srep42050.

[244] A. González-Tudela and J. I. Cirac, *Markovian and non-Markovian dynamics of quantum emitters coupled to two-dimensional structured reservoirs*, Phys. Rev. A **96**, 043811 (2017), doi: 10.1103/PhysRevA.96.043811.

[245] A. Asenjo-García, J. D. Hood, D. E. Chang, and H. J. Kimble, *Atom-light interactions in quasi-one-dimensional nanostructures: A Green's-function perspective*, Phys. Rev. A **95**, 033818 (2017), doi: 10.1103/PhysRevA.95.033818.

[246] P. W. Milonni and P. L. Knight, *Retardation in the resonant interaction of two identical atoms*, Phys. Rev. A **10**, 1096 (1974), doi: 10.1103/PhysRevA.10.1096.

[247] K. Sinha, P. Meystre, E. A. Goldschmidt, F. K. Fatemi, S.L. Rolston, and P. Solano, *Non-markovian collective emission from macroscopically separated emitters*, Phys. Rev. Lett. **124**, 043603 (2020), doi: 10.1103/PhysRevLett.124.043603.

[248] J. I. Cirac, R. Blatt, P. Zoller, and W. D. Philips, *Laser cooling of trapped ions in a standing wave*, Phys. Rev. A **46**, 2668 (1992), doi: 10.1103/PhysRevA.46.2668.

[249] D. Leibfried, R. Blatt, C. Monroe, and D. Wineland, *Quantum dynamics of single trapped ions*, Rev. Mod. Phys. **75**, 281 (2003), doi: 10.1103/RevModPhys.75.281.

[250] M. Wallquist, P. Rabl, M. D. Lukin, and P. Zoller, *Theory of cavity-assisted microwave cooling of polar molecules*, New J. Phys. **10**, 063005 (2008), doi: 10.1088/1367-2630/10/6/063005

[251] F. Marquardt, J. P. Chen, A. A. Clerk, and S. M. Girvin, *Quantum theory of cavity-assisted sideband cooling of mechanical motion*, Phys. Rev. Lett. **99**, 093902 (2007), doi: 10.1103/PhysRevLett.99.093902.

[252] I. Wilson-Rae, N. Nooshi, W. Zwerger, and T. J. Kippenberg, *Theory of ground state cooling of a mechanical oscillator using dynamical backaction*, Phys. Rev. Lett. **99**, 093901 (2007), doi: 10.1103/PhysRevLett.99.093901.

[253] J. Chan, T. P. Mayer Alegre, A. H. Safavi-Naeini, J. T. Hill, A. Krause, S. Gröblacher, M. Aspelmeyer, and O. Painter, *Laser cooling of a nanomechanical oscillator into its quantum ground state*, Nature **478**, 89 (2011), doi: 10.1038/nature10461.

[254] J. D. Teufel, T. Donner, D. Li, J. W. Harlow, M. S. Allman, K. Cicak, A. J. Sirois, J. D. Whittaker, K. W. Lehnert, R. W. Simmonds, *Sideband cooling of micromechanical motion to the quantum ground state*, Nature **475**, 359 (2011), doi: 10.1038/nature10261.

[255] I. Marzoli, J. I. Cirac, R. Blatt, and P. Zoller, *Laser cooling of trapped three-level ions: Designing two-level systems for sideband cooling*, Phys. Rev. A **49**, 2771 (1994), doi: 10.1103/PhysRevA.49.2771.

[256] A. Shankar, J. Cooper, J. G. Bohnet, J. J. Bollinger, and M. Holland, *Steady-state spin synchronization through the collective motion of trapped ions*, Phys. Rev. A 95, 033423 (2017), doi: 10.1103/PhysRevA.95.033423.

[257] B. Casabone, K. Friebe, B. Brandstätter, K. Schüppert, R. Blatt, and T.E. Northup, *Enhanced quantum interface with collective ion-cavity coupling*, Phys. Rev. Lett. **114**, 023602 (2015), doi: 10.1103/PhysRevLett.114.023602.

[258] R. Reimann, W. Alt, T. Kampschulte, T. Macha, L. Ratschbacher, N. Thau, S. Yoon, and D. Meschede, *Cavity-modified collective Rayleigh scattering of two atoms*, Phys. Rev. Lett. **114**, 023601 (2015), doi: 10.1103/PhysRevLett.114.023601.

[259] P. Samutpraphoot, T. Đorđević, P. L. Ocola, H. Bernien, C. Senko, V. Vuletić, and M. D. Lukin, *Strong coupling of two individually controlled atoms via a nanophotonic cavity*, Phys. Rev. Lett. **124**, 063602 (2020), doi: 10.1103/PhysRevLett.124.063602.

[260] I. Wilson-Rae, N. Nooshi, J. Dobrindt, T. J. Kippenberg, and W. Zwerger, *Cavity-assisted backaction cooling of mechanical resonators*, New J. Phys. **10**, 095007 (2008), doi: 10.1088/1367-2630/10/9/095007.

[261] M. Schmidt, M. Ludwig, and F. Marquardt, *Optomechanical circuits for nanomechanicalcontinuous variable quantum state processing*, New J. Phys. **14**, 125005 (2012), doi: 10.1088/1367-2630/14/12/125005.

[262] S. J. M. Habraken, K. Stannigel, M. D. Lukin, P. Zoller, and P. Rabl, *Continuous mode cooling and phonon routersfor phononic quantum networks*, New J. Phys. **14**, 115004 (2012), doi: 10.1088/1367-2630/14/11/115004.

[263] V. Peano, C. Brendel, M. Schmidt, and F. Marquardt, *Topological phases of sound and light*, Phys. Rev. X **5**, 031011 (2015), doi: 10.1103/PhysRevX.5.031011.

[264] D. Meiser and M. J. Holland, *Steady-state superradiance with alkaline-earth-metal atoms*, Phys. Rev. A **81**, 033847 (2010), doi: 10.1103/PhysRevA.81.033847.

[265] H. Schwager, J. I. Cirac, and G. Giedke, *Dissipative spin chains: Implementation with cold atoms and steady-state properties* Phys. Rev. A **87**, 022110 (2013), doi: 10.1103/PhysRevA.87.022110.

[266] A. Ferraro, S. Olivares, and M. G. A. Paris, *Gaussian States in Quantum Information* (Bibliopolis, Napoli, 2005).

[267] S. Olivares, *Quantum optics in the phase space*, Eur. Phys. J. ST **203**, 3 (2012), doi: 10.1140/epjst/e2012-01532-4.

[268] V. V. Albert and L. Jiang, *Symmetries and conserved quantities in Lindblad master equations*, Phys. Rev. A **89**, 022118 (2014), doi: 10.1103/PhysRevA.89.022118.

[269] M. Cattaneo, G. L. Giorgi, S. Maniscalco, and R. Zambrini, *Symmetry and block structure of the Liouvillian superoperator in partial secular approximation*, Phys. Rev. A 101, 042108, (2020), doi: https://doi.org/10.1103/PhysRevA.101.042108.

[270] N. Shammah, S. Ahmed, N. Lambert, S. De Liberato, and F. Nori, *Open quantum systems with local and collective incoherent processes: Efficient numerical simulations using permutational invariance*, Phys. Rev. A **98**, 063815, doi: https://doi.org/10.1103/PhysRevA.98.063815.

[271] F. Galve, G. L. Giorgi, and R. Zambrini, *Entanglement dynamics of nonidentical oscillators under decohering environments*, Phys. Rev. A **81**, 062117 (2010), doi: 10.1103/PhysRevA.81.062117.

[272] M. E. J. Newman, *Networks: An Introduction* (Oxford University Press, New York, 2010).

[273] D.J. Watts and S.H. Strogatz, *Collective dynamics of 'small-world' networks*, Nature **393**, 440 (1998), doi: 10.1038/30918.

[274] J. Biamonte, M. Faccin, and M. De Domenico, *Complex networks from classical to quantum* Commun. Phys. **2**, 53 (2019), doi: 10.1038/s42005-019-0152-6.

[275] A. Acin, J. I. Cirac, and M. Lewenstein, *Entanglement percolation in quantum networks*, Nat. Phys. **3**, 256 (2007), doi: 10.1038/nphys549.

[276] M. Cuquet, and J. Calsamiglia, *Entanglement percolation in quantum complex networks*, Phys. Rev. Lett. **103**, 240503 (2009), doi: 10.1103/PhysRevLett.103.240503.

[277] S. Perseguers, M. Lewenstein, A. Acin, and J. I. Cirac, *Quantum random networks*, Nat. Phys. **6**, 539 (2010), doi: 10.1038/nphys1665.

[278] S. Perseguers, G. J. Lapeyre, D. Cavalcanti, and M. Lewenstein, A. Acin, *Distribution of entanglement in large-scale quantum networks*, Rep. Prog. Phys. **76**, 096001 (2013), doi: 10.1088/0034-4885/76/9/096001.

[279] J. Roslund, R. Medeiros de Araujo, S. Jiang, C. Fabre, and N. Treps, *Wavelength-multiplexed quantum networks with ultrafast frequency combs*, Nat. Photonics **8**, 109 (2014), doi: 10.1038/nphoton.2013.340.

[280] H. J. Kimble, *The quantum internet*, Nature **453**, 1023 (2008), doi: 10.1038/nature07127.

[281] D. S. Wiersma, *Random quantum networks*, Science **327**, 1333 (2010), doi: 10.1126/science.1187084.

[282] S. Ritter, C. Nölleke, C. Hahn, A. Reiserer, A. Neuzner, M. Uphoff, M. Mücke, E. Figueroa, J. Bochmann, and G. Rempe, *An elementary quantum network of single atoms in optical cavities*, Nature **484**, 195 (2012), doi: 10.1038/nature11023.

[283] P. Kómár, E. M. Kessler, M. Bishof, L. Jiang, A- S. Sørensen, J. Ye, and M. D. Lukin, *A quantum network of clocks*, Nat. Phys. **10**, 582 (2014), doi: 10.1038/nphys3000.

[284] A. Xuereb, C. Genes, G. Pupillo, M. Paternostro, and A. Dantan, *Reconfigurable long-range phonon dynamics in optomechanical arrays*, Phys. Rev. Lett. **112**, 133604 (2014), doi: 10.1103/PhysRevLett.112.133604.

[285] A. Reiserer, N. Kalb, M. S. Blok, K. J.M. van Bemmelen, T. H. Taminiau, Ronald Hanson, D. J. Twitchen, and M. Markham, *Robust quantum-network memory using decoherence-protected subspaces of nuclear spins*, Phys. Rev. X **6**, 021040 (2016), doi: 10.1103/PhysRevX.6.021040.

[286] S. Goldstein, S. Korenblit, Y. Bendor, H. You, M. R. Geller, and N. Katz, *Decoherence and interferometric sensitivity of boson sampling in superconducting resonator networks*, Phys. Rev. B **95**, 020502(R) (2017), doi: 10.1103/PhysRevB.95.020502.

[287] M. Krenn, X. Gu, and A. Zeilinger, *Quantum experiments and graphs: multiparty states as coherent superpositions of perfect matchings*, Phys. Rev. Lett. **119**, 240403 (2017), doi: 10.1103/PhysRevLett.119.240403.

[288] L. Lodhal, *Quantum-dot based photonic quantum networks*, Quantum Sci. Technol. **3**, 013001 (2017), doi: 10.1088/2058-9565/aa91bb.

[289] A. J. Kollar, M. Fitzpatrick, and A. A. Houck, *Hyperbolic Lattices in Circuit Quantum Electrodynamics*, Nature **571**, 45 (2019), doi: 10.1038/s41586-019-1348-3

[290] E. Diamanti, H. -K. Lo, B. Qi, and Z. Yuan, *Practical challenges in quantum key distribution*, npj Quantum Inf. **2**, 16025 (2016), doi: 10.1038/npjqi.2016.25.

[291] J. I. Cirac, P. Zoller, H. J. Kimble, and H. Mabuchi, *Quantum state transfer and entanglement distribution among distant nodes in a quantum network*, Phys. Rev. Lett. **78**, 3221 (1997), doi: 10.1103/PhysRevLett.78.3221.

[292] G. D. Paparo, and M. A. Martin-Delgado, *Google in a quantum network*, Sci. Rep. **2**, 444 (2012), doi: 10.1038/srep00444.

[293] J. D. Noh, and H. Rieger, *Random Walks on Complex Networks*, Phys. Rev. Lett. **92**, 118701 (2004), doi: 10.1103/PhysRevLett.92.118701.

[294] M. B. Plenio and S. F. Huelga, *Dephasing-assisted transport: quantum networks and biomolecules*, New J. Phys. **10**, 113019 (2008), doi: 10.1088/1367-2630/10/11/113019.

[295] A. W. Chin, A. Datta, F. Caruso, S. F. Huelga, and M. B. Plenio, *Noise-assisted energy transfer in quantum networks and light-harvesting complexes*, New J. Phys. **12**, 065002 (2010), doi: 10.1088/1367-2630/12/6/065002.

[296] L. Campos Venuti, and P. Zanardi, *Excitation transfer through open quantum networks: Three basic mechanisms*, Phys. Rev B **84**, 134206 (2011), doi: 10.1103/PhysRevB.84.134206.

[297] D. I. Tsomokos, *Quantum walks on complex networks with connection instabilities and community structure*, Phys. Rev. A **83**, 052315 (2011), doi: 10.1103/PhysRevA.83.052315.

[298] S. F. Huelga, and M. B. Plenio, *Vibrations, Quanta and Biology*, Contemp. Phys. **54**, 181 (2013), doi: 10.1080/00405000.2013.829687.

[299] M. Faccin, P. Migda, T. H. Johnson, V. Bergholm, and J. D. Biamonte, *Community Detection in Quantum Complex Networks*, Phys. Rev. X **4**, 041012 (2014), doi: 10.1103/PhysRevX.4.041012.

[300] M. Galiceanu, and W. T. Strunz, *Continuous-time quantum walks on multilayer dendrimer networks*, Phys. Rev. E **94**, 022307 (2016), doi: 10.1103/PhysRevE.94.022307.

[301] O. Mulken, M. Dolgushev, and M. Galiceanu, *Complex quantum networks: From universal breakdown to optimal transport*, Phys. Rev. E **93**, 022304 (2016), doi: 10.1103/PhysRevE.93.022304.

[302] D. L. Underwood, W. E. Shanks, J. Koch, and A. A. Houck, *Low-disorder microwave cavity lattices for quantum simulation with photons*, Phys. Rev. A **86**, 023837 (2012), doi: 10.1103/PhysRevA.86.023837.

[303] P. Zanardi, *Dissipation and decoherence in a quantum register*, Phys. Rev. A, **57**, 3276 (1998), doi: 10.1103/PhysRevA.57.3276.

[304] D. Bacon, J. Kempe, D. A. Lidar and K. B. Whaley, *Universal Fault-Tolerant Quantum Computation on Decoherence-Free Subspaces*, Phys. Rev. Lett. **85**, 1758 (2000), doi: 10.1103/PhysRevLett.85.1758.

[305] J. M. Taylor, H.-A. Engel, W. Dür, A. Yacoby, C. M. Marcus, P. Zoller, and M. D. Lukin, *Fault-tolerant architecture for quantum computation using electrically controlled semiconductor spins*, Nat. Phys. **1**, 177 (2005), doi: 10.1038/nphys174.

[306] P. Erdős and P. Rényi, *On random graphs*, Publicationes Mathematicae Debrecen **6**, 290 (1959).

[307] B. Bollobás, Modern Graph Theory (Springer, New York, 1998).

[308] D. Leykam, A. Andreanov, and S. Flach, *Artificial flat band systems: from lattice models to experiments*, Adv. Phys. X, **66**, 1473052 (2018), doi: 10.1080/23746149.2018.1473052.

[309] B. Shutherland, *Localization of electronic wave functions due to local topology*, Phys. Rev. B **34**, 5208 (1986), doi: 10.1103/PhysRevB.34.5208.

[310] D. L. Bergman, C. Wu, and L. Balents, *Band touching from real-space topology in frustrated hopping models*, Phys. Rev. B **78**, 125104 (2008), doi: 10.1103/PhysRevB.78.125104.

[311] M. Nita, B. Ostahie, and A. Aldea, *Spectral and transport properties of the two-dimensional Lieb lattice*, Phys. Rev. B **87**, 125428 (2013), doi: 10.1103/PhysRevB.87.125428.

[312] J. Nokkala, F. Arzani, F. Galve, R. Zambrini, S. Maniscalco, J. Piilo, N. Treps, V. Parigi *Reconfigurable optical implementation of quantum complex networks*, New J. Phys. **20**, 053024 (2018), doi: 10.1088/1367-2630/aabc77.

[313] F. Arzani, C. Fabre, and N. Treps, *Versatile engineering of multimode squeezed states by optimizing the pump spectral profile in spontaneous parametric down-conversion*, Phys. Rev. A **97**, 033808 (2018), doi: 10.1103/PhysRevA.97.033808.

[314] M. V. Berry, *Physics of nonhermitian degeneracies*, Czech. J. Phys. **54**, 1039 (2004), doi: 10.1023/B:CJOP.0000044002.05657.04.

[315] S. Weis, R. Rivière, S. Deléglise, E. Gavartin, O. Arcizet, A. Schliesser, and T. J. Kippenberg, *Optomechanically induced transparency*, Science **330**, 1520 (2010), doi: 10.1126/science.1195596.

[316] A. H. Safavi-Naeini, T. P. Mayer Alegre, J. Chan, M. Eichenfield, M. Winger, Q. Lin, J. T. Hill, D. E. Chang, and O. Painter, *Electromagnetically induced transparency and slow light with optomechanics*, Nature **472**, 69 (2011), doi: 10.1038/nature09933.

[317] A. A. Clerk, M. H. Devoret, S. M. Girvin, Florian Marquardt, and R. J. Schoelkopf, *Introduction to quantum noise, measurement, and amplification*, Rev. Mod. Phys. **82**, 1155 (2010), doi: 10.1103/RevModPhys.82.1155.

[318] D. D. Smith, H. Chang, K. A. Fuller, A. T. Rosenberger, and R. W. Boyd, *Coupled-resonator-induced transparency*, Phys. Rev. A **69**, 063804 (2004), doi: 10.1103/PhysRevA.69.063804.

[319] K. Totsuka, N. Kobayashi, and M. Tomita, *Slow light in coupled-resonator-induced transparency*, Phys. Rev. Lett. **98**, 213904 (2007), doi: 10.1103/PhysRevLett.98.213904.

[320] J. D. Teufel, D. Li, M. S. Allman, K. Cicak, A. J. Sirois, J. D. Whittaker, and R. W. Simmonds, *Circuit cavity electromechanics in the strong-coupling regime*, Nature **471**, 204 (2011), doi: 10.1038/nature09898.

[321] M. Fleischhauer, A. Imamoglu, and J. P. Marangos, *Electromagnetically induced transparency: Optics in coherent media*, Rev. Mod. Phys. **77**, 633 (2005), doi: 10.1103/RevModPhys.77.633.

[322] B. Peng, Ş. Özdemir, W. Chen, F. Nori, and L. Yang, *What is and what is not electromagnetically induced transparency in whispering-gallery microcavities*, Nat. Commun. **5**, 5082 (2014), doi: 10.1038/ncomms6082.

[323] Q. Lin, J. Rosenberg, D. Chang, R. Camacho, M. Eichenfield, K. J. Vahala, and O. Painter, *Coherent mixing of mechanical excitations in nano-optomechanical structures* Nature Photon. **4**, 236 (2010), doi: 10.1038/nphoton.2010.5

[324] J. M. Dobrindt, I. Wilson-Rae, and T. J. Kippenberg, *Parametric normal-mode splitting in cavity optomechanics*, Phys. Rev. Lett. **101**, 263602 (2008), doi: 10.1103/PhysRevLett.101.263602.

[325] S. Gröblacher, K. Hammerer, M. R. Vanner, and M. Aspelmeyer, *Observation of strong coupling between a micromechanical resonator and an optical cavity field*, Nature **460**, 724 (2009), doi: 10.1038/nature08171.

[326] D. Meiser, J. Ye, D. R. Carlson, and M. J. Holland, *Prospects for a Millihertz-Linewidth Laser*, Phys. Rev. Lett. **102**, 163601 (2009), doi: 10.1103/PhysRevLett.102.163601.

[327] J. G. Bohnet, Z. Chen, J. M. Weiner, D. Meiser, M. J. Holland, J. K. Thompson, *A steady-state superradiant laser with less than one intracavity photon*, Nature **484**, 78 (2012), doi: 10.1038/nature10920.

[328] F. Le Kien, S. Dutta Gupta, K. P. Nayak, and K. Hakuta, *Nanofiber-mediated radiative transfer between two distant atoms*, Phys. Rev. A **72**, 063815 (2005), doi: 10.1103/PhysRevA.72.063815.

[329] K. Lalumière, B. C. Sanders, A. F. van Loo, A. Fedorov, A. Wallraff, and A. Blais, *Input-output theory for waveguide QED with an ensemble of inhomogeneous atoms*, Phys. Rev. A **88**, 043806 (2013), doi: 10.1103/PhysRevA.88.043806.

[330] I. I. Arkhipov, A. Miranowicz, F. Minganti, and F. Nori, *Liouvillian exceptional points of any order in dissipative linear bosonic systems: Coherence functions and switching between PT and anti-PT symmetries*, Phys. Rev. A **102**, 033715 (2020), doi: /10.1103/PhysRevA.102.033715.

[331] M. Soriente, T. L. Heugel, K. Arimitsu, R. Chitra, and O. Zilberberg, *Distinctive class of dissipation-induced phase transitions and their universal characteristics*, Phys. Rev. Research **3**, 023100 (2021), doi: 10.1103/PhysRevResearch.3.023100.

[332] C. Gross and I. Bloch, *Quantum simulations with ultracold atoms in optical lattices*, Science **357**, 995 (2017), doi: 10.1126/science.aal3837.

[333] M. Lewenstein, A. Sanpera, V. Ahufinger , B. Damski, A. Sen(De) and U. Sen, *Ultracold atomic gases in optical lattices: mimicking condensed matter physics and beyond*, Adv. Phys. **56**, 243 (2007), doi: 10.1080/00018730701223200.

[334] L.-M. Duan, E. Demler, and M. D. Lukin, *Controlling spin exchange interactions of ultracold atoms in optical lattices*, Phys. Rev. Lett. **91**, 090402 (2003), doi: 10.1103/PhysRevLett.91.090402.

[335] A. Imambekov, M. Lukin, and E. Demler, *Spin-exchange interactions of spin-one bosons in optical lattices: Singlet, nematic, and dimerized phases*, Phys. Rev. A **68**, 063602 (2003), doi: 10.1103/PhysRevA.68.063602.

[336] J. J. García-Ripoll, and J. I. Cirac, *Spin dynamics for bosons in an optical lattice*, New J. Phys. **5**, 76 (2003), doi: 10.1088/1367-2630/5/1/376.

[337] D. Porras and J. I. Cirac, *Effective quantum spin systems with trapped ions*, Phys. Rev. Lett. **92**, 207901 (2004), doi: 10.1103/PhysRevLett.92.207901.

[338] J. Simon, W. S. Bakr, R. Ma, M. Eric Tai, P. M. Preiss, and M. Greiner, *Quantum simulation of antiferromagnetic spin chains in an optical lattice*, Nature **472**, 307 (2011), doi: 10.1038/nature09994.

[339] H. Labuhn, D. Barredo, S. Ravets, S. de Léséleuc, T. Macrì, T. Lahaye, and A. Browaeys, *Tunable two-dimensional arrays of single Rydberg atoms for realizing quantum Ising models*, Nature **534**, 667 (2016), doi: 10.1038/nature18274.

[340] D. Jaksch, C. Bruder, J. I. Cirac, C. W. Gardiner, and P. Zoller, *Cold bosonic atoms in optical lattices*, Phys. Rev. Lett. **81**, 3108 (1998), doi: 10.1103/PhysRevLett.81.3108.

[341] D. Jaksch and P. Zoller, *The cold atom Hubbard toolbox*, Ann. Phys. **315**, 52 (2005), doi: 10.1016/j.aop.2004.09.010.

[342] J. Sebby-Strabley, M. Anderlini, P. S. Jessen, and J. V. Porto, *Lattice of double wells for manipulating pairs of cold atoms*, Phys. Rev. A **73**, 033605 (2006), doi: 10.1103/PhysRevA.73.033605.

[343] J. Sebby-Strabley, B. L. Brown, M. Anderlini, P. J. Lee, W. D. Phillips, J. V. Porto and P. R. Johnson, *Preparing and probing atomic number states with an atom interferometer*, Phys. Rev. Lett. **98**, 200405 (2007), doi: 10.1103/PhysRevLett.98.200405.

[344] S. Fölling, S. Trotzky, P. Cheinet, M. Feld, R. Saers, A. Widera, T. Müller and I. Bloch, *Direct observation of second-order atom tunnelling*, Nature **448**, 1029 (2007), doi: 10.1038/nature06112.

[345] M. Lohse, C. Schweizer, O. Zilberberg, M. Aidelsburger and I. Bloch, *A Thouless quantum pump with ultracold bosonic atoms in an optical superlattice*, Nat. Phys. **14**, 3584 (2016), doi: 10.1038/nphys3584.

[346] J. M. Torres, *Closed-form solution of Lindblad master equations without gain*, Phys. Rev. A **89**, 052133 (2014), doi: 10.1103/PhysRevA.89.052133.

[347] P. Coleman, *Introduction to Many Body Physics´* (Cambridge University Press, Cambridge, England, 2011).

[348] M. Gross and S. Haroche, *Superradiance: An essay on the theory of collective spontaneous emission*, Phys. Rep. **93**, 301 (1982), doi: 10.1016/0370-1573(82)90102-8.

[349] J. Gambetta, A. Blais, D. I. Schuster, A. Wallraff, L. Frunzio, J. Majer, M. H. Devoret, S. M. Girvin, and R. J. Schoelkopf, *Qubit-photon interactions in a cavity: Measurement-induced dephasing and number splitting*, Phys. Rev. A **74**, 042318 (2006), doi: 10.1103/PhysRevA.74.042318.

[350] P. M. Chaikin and T. C. Lubensky, *Principles of Condensed Matter Physics* (Cambridge University Press, Cambridge, 2000).

[351] N. G. van Kampen, *Stochastic Processes in Physics and Chemistry* (North Holland, Amsterdam, 1981).

[352] G. Biroli and J. P. Garrahan, *Perspective: The glass transition*, J. Chem. Phys. **138**, 12A301 (2013), doi: 10.1063/1.4795539.

[353] L. Berthier and M. D. Ediger, *Facets of glass physics*, Phys. Today **69**, 40 (2016), doi: 10.1063/PT.3.3052.

[354] D. C. Rose, K. Macieszczak, I. Lesanovsky and J. P. Garrahan, *Metastability in an open quantum Ising model*, Phys. Rev. E **94**, 052132 (2016), doi: 10.1103/PhysRevE.94.052132.

[355] A. Le Boité, M.-J. Hwang, and M. B. Plenio, *Metastability in the driven-dissipative Rabi model*, Phys. Rev. A **95**, 023829 (2017), doi: 10.1103/PhysRevA.95.023829.

[356] S. Wolff, A. Sheikhan, S. Diehl, and C. Kollath, *Nonequilibrium metastable state in a chain of interacting spinless fermions with localized loss*, Phys. Rev. B **101**, 075139 (2020), doi: 10.1103/PhysRevB.101.075139

[357] K. Vogel and H. Risken, *Quantum-tunneling rates and stationary solutions in dispersive optical bistability*, Phys. Rev. A **38**, 2409 (1988), doi: 10.1103/PhysRevA.38.2409.

[358] N. Bartolo, F. Minganti, J. Lolli, and C. Ciuti, *Homodyne versus photon-counting quantum trajectories for dissipative Kerr resonators with two-photon driving* Eur. Phys. J.: Spec. Top. **226**, 2705 (2017), doi: 10.1140/epjst/e2016-60385-8.

[359] F. Minganti, N. Bartolo, J. Lolli, W. Casteels, and C. Ciuti, *Exact results for Schrödinger cats in driven-dissipative systems and their feedback control* Sci. Rep. **6**, 26987 (2016), doi: 10.1038/srep26987.

[360] W.-K. Mok, L.-C. Kwek, and H. Heimonen, *Synchronization boost with single-photon dissipation in the deep quantum regime* Phys. Rev. Res. **2**, 033422 (2020), doi: 10.1103/PhysRevResearch.2.033422.

[361] Y. Kato, N. Yamamoto, and H. Nakao, *Semiclassical phase reduction theory for quantum synchronization*, Phys. Rev. Res. **1**, 033012 (2019), doi: https://doi.org/10.1103/PhysRevResearch.1.033012.

[362] Y. Kato and H. Nakao, *Quantum Coherence Resonance*, New. J. Phys. **23**, 043018 (2021), doi: 10.1088/1367-2630/abf1d7.

[363] T. Weiss, S. Walter, and F. Marquardt, *Quantum-coherent phase oscillations in synchronization*, Phys. Rev. A **94**, 41802(R) (2017), doi: 10.1103/PhysRevA.95.041802.

[364] J. I. Cirac, A. S. Parkins, R. Blatt, and P. Zoller, *"Dark" squeezed states of the motion of a trapped ion* Phys. Rev. Lett. **70**, 556 (1993), doi: 10.1103/PhysRevLett.70.556.

[365] D. M. Meekhof, C. Monroe, B. E. King, W. M. Itano, and D. J. Wineland, *Generation of Nonclassical Motional States of a Trapped Atom*, Phys. Rev. Lett. **76**, 1796 (1996), doi: 10.1103/PhysRevLett.76.1796.

[366] J. Gosner, B. Kubala , and J. Ankerhold, *Relaxation dynamics and dissipative phase transition in quantum oscillators with period tripling*, Phys. Rev. B **101**, 054501 (2020), doi: 10.1103/PhysRevB.101.054501.

[367] M. Marthaler, and M. I. Dykman, *Switching via quantum activation: A parametrically modulated oscillator*, Phys. Rev. A **73**, 042108 (2006), doi: 10.1103/PhysRevA.73.042108.

[368] M. I. Dykman, *Critical exponents in metastable decay via quantum activation*, Phys. Rev. E **75**, 011101 (2007), doi: 10.1103/PhysRevE.75.011101.

[369] K. Chinzei and T. N. Ikeda, *Time Crystals Protected by Floquet Dynamical Symmetry in Hubbard Models*, Phys. Rev. Lett. **125**, 060601 (2020), doi: 10.1103/PhysRevLett.125.060601.

[370] T. L. Heugel, 1, M. Oscity, A. Eichler, O. Zilberberg, and R. Chitra, *Classical Many-Body Time Crystals*, Phys. Rev. Lett. **123**, 124301 (2019), doi: 0.1103/PhysRevLett.123.124301.

[371] N. Y. Yao, C. Nayak, L. Balents and M. P. Zaletel, *Classical Discrete Time Crystals*, Nat. Phys. **16** 438, (2020), doi: 10.1038/s41567-019-0782-3.

[372] G. Karpat, İ. Yalçinkaya, B. Çakmak, G. L. Giorgi, and R. Zambrini, *Synchronization and non-Markovianity in open quantum systems*, Phys. Rev. A **103**, 062217 (2021), doi: 10.1103/PhysRevA.103.062217.

[373] A. J. Daley, *Quantum Trajectories and Open Many-Body Quantum Systems*, Adv. Phys. **63**, 77 (2014), doi: 10.1080/00018732.2014.933502.

[374] J. Lim, D. Paleček, F. Caycedo-Soler, C. N. Lincoln, J. Prior, H. von Berlepsch, S. F. Huelga, M. B. Plenio, D. Zigmantas and J. Hauer, *Vibronic origin of long-lived coherence in an artificial molecular light harvester*, Nat. Commun. **6**, 7755 (2015), doi: 10.1038/ncomms8755.

[375] J. Lim, D. J. Ing, J. Rosskopf, J. Jeske, J. H. Cole, S. F. Huelga, and M. B. Plenio, *Signatures of spatially correlated noise and non-secular effects in two-dimensional electronic spectroscopy*, J. Chem. Phys. **146**, 024109 (2017), doi: 10.1063/1.4973975.

[376] S. Mukamel, *Principles of Nonlinear Optical Spectroscopy* (Oxford University Press, New York, 1995).

[377] H. Carmichael, *Statistical Methods in Quantum Optics II* (Springer, New York, 2008).

[378] A.N. Pearson, Y. Guryanova, P. Erker, E.A. Laird, G.A.D. Briggs, M. Huber, and N. Ares, *Measuring the Thermodynamic Cost of Timekeeping*, Phys. Rev. X **11**, 021029 (2021), doi: 10.1103/PhysRevX.11.021029.

[379] O. Scarlatella, A. A. Clerk, R. Fazio, and M. Schiró, *Dynamical Mean-Field Theory for Markovian Open Quantum Many-Body Systems*, Phys. Rev. X **11**, 031018 (2021), doi: 10.1103/PhysRevX.11.031018.

[380] T. Tomita, S. Nakajima, I. Danshita, Y. Takasu, and Y. Takahashi, *Observation of the Mott Insulator to Superfluid Crossover of a Driven-Dissipative Bose-Hubbard System*, Sci. Adv. **3**, e1701513 (2017), doi: 10.1126/sciadv.1701513.

[381] H. Risken, *The Fokker–Planck Equation: Methods ofSolution and Applications* (Springer, New York, 1989).

[382] R. Toral and P. Colet, *Stochastic Numerical Methods* (Wiley-VCH, Weinheim, 2014).

[383] H. Risken, C. Savage, F. Haake, and D. F. Walls, *Quantum tunneling in dispersive optical bistability*, Phys. Rev. A **35**, 1729 (1987), doi: doi.org/10.1103/PhysRevA.35.1729.

[384] A. Polkovnikov, *Phase Space Representation of Quantum Dynamics*, Ann. Phys. (Amsterdam) **325**, 1790 (2010), doi: 10.1016/j.aop.2010.02.006.

[385] R. Taïeb, R. Dum, J. I. Cirac, P. Marte, and P. Zoller, *Cooling and localization of atoms in laser-induced potential wells* Phys. Rev. A **49**, 4876 (1994), doi: 10.1103/PhysRevA.49.4876.

[386] H. Risken, *Distribution- and correlation-functions for a laser amplitude*, Z. Phys. **186**, 85 (1965), doi: 10.1007/BF01383512.